# Rational ligand design in heteroleptic copper(I) complexes for application in light-emitting electrochemical cells

Inauguraldissertation
zur
Erlangung der Würde eines Doktors der Philosophie

vorgelegt der
Philosophisch-Naturwissenschaftlichen Fakultät
der Universität Basel

von

Fabian Brunner
aus Schopfheim, Deutschland

Basel, 2020

Genehmigt von der Philosophisch-Naturwissenschaftlichen Fakultät
auf Antrag von

Prof. Dr. Catherine E. Housecroft und Prof. Dr. Oliver S. Wenger

Basel, den 17.03.2020

Prof. Dr. Martin Spiess
Dekan

# Abstract

Light-emitting electrochemical cells are an emerging class of devices based on solid state lighting technology. The utilization of charged molecules as the main active component gives these devices inherent advantages over other modern lighting technologies such as low turn on voltage, easy device fabrication and the applicability on flexible substrates. These benefits make LECs an excellent candidate for display and large area low-tech lighting applications. Iridium based LECs are well established but face the problem of high material cost due to the low abundance of iridium. Using copper(I) based complexes as active material lower the production cost and therefore make LEC fabrication more affordable. This thesis takes a systematic approach to alter the luminescent properties of [Cu(N^N)(P^P)][$PF_6$] complexes, where N^N is a chelating diimine and P^P is a chelating bisphosphane ligand, and optimize them for LEC application. **Chapter 1** gives a brief history of artificial lighting technology, describes the rise of solid-state lighting and gives an introduction to modern OLED and LEC technology. **Chapter 2** describes the preparation of 2,2'-bipyridine ligands bearing large aromatic substituents in the 6-position. Complexation with copper(I) and suitable P^P ligands yields new heteroleptic complexes and their structural and photophysical properties are investigated in depth. **Chapter 3** presents the preparation of a new asymmetric methyl functionalized 2,2'-bipyridine ligand and the properties of the corresponding [Cu(N^N)(P^P)][$PF_6$] complexes. The particular substitution pattern is designed to optimize the steric demand of the N^N ligand and therefore increase LEC device performance. After in depth investigation of the N^N ligand in [Cu(N^N)(P^P)][$PF_6$] complexes, the development of new P^P ligands is describes in **Chapter 4**. Altering the bisphosphane ligand allows to influence the HOMO energy level, as well as the coordination sphere around the copper(I) centre. Five new complexes and their structural, photophysical and device properties are described. **Chapter 5** combines the previous findings in attempting to prepare a tetradentate N^N^P^P type ligand. Such a ligand is expected to give more stable copper(I) complexes and therefore increase the device lifetime of a corresponding light-emitting cell. Six synthetic approaches to prepare such a tetradentate ligand are described. The results of this thesis and a brief outlook on the project are given in **Chapter 6**.

# Parts of this work have been published

F. Brunner, S. Graber, Y. Baumgartner, D. Häussinger, A. Prescimone, E. C. Constable and C. E. Housecroft, *Dalton Trans.*, 2017, **46**, 6379–6391. DOI: 10.1039/c7dt00782e

F. Brunner, A. Babaei, A. Pertegás, J. M. Junquera-Hernández, A. Prescimone, E. C. Constable, H. J. Bolink, M. Sessolo, E. Ortí and C. E. Housecroft, *Dalton Trans.*, 2019, **48**, 446–460. DOI: 10.1039/C8DT03827A

# Table of Contents

# Acknowledgements

First of all, I would like to thank Prof. Dr. Catherine Housecroft and Prof. Dr. Edwin Constable. You made me feel welcome in the group from the first day on, supported me whenever I needed it and gave me the freedom to find my own path whenever I wanted it. Your ability to gather and lead the right people for a research group is truly amazing and it creates a positive and fun working atmosphere I have rarely seen elsewhere. Catherine, thank you so much for always having an open door, dealing with every question I had, no matter how detailed or tedious it might have been. The fact, that you care for every problem of you students, no matter if it concerns research, praktikum, maintenance or other things makes me feel appreciated and valued. Ed, thank you for all your guidance, for all the technical, and sometimes philosophical discussions and for being like an encyclopaedia when it comes to unconventional or crazy synthetic approaches. I could not have wished for better doctorate supervisors.

I would like to thank Prof. Dr. Oliver Wenger, not only for being my co-examiner, but also for having an open door when it came to tricky photophysical problems and for valuable discussion at the university and at conferences.

I would like to thank Dr. Henk Bolink and his team at the University of Valencia, namely, Dr. Antonio Pertegás, Dr. Michele Sessolo, Laura Martínez-Sarti and Azin Babaei for our fruitful collaboration, for all the LEC preparation and for hosting me during my stay at ICMol. I learned many new things about device fabrication in your lab and you greatly improved my understanding of materials chemistry. In addition, I would like to thank Prof. Dr. Enrique Ortí and his co-workers, especially José M. Junquera-Hernández for their calculations and contributions to our collaborations.

A huge thank you goes to all current and former members of the Constable/Housecroft research group. Since I joined the group the first time in spring 2014, I felt welcomed from the first day on. Many amazing people took their time to teach me, discuss research with me or were just there to have a good time in the lab. Since then people have come and gone and the group has changed many times, but the good spirit of the group was never lost and to this day it is a great environment to be in. I could not have wished for a more enjoyable working atmosphere than I had during the last years.

My special thanks go to the following people:

Dr. Steffen Müller, thank you for being my "gateway" to the Constable/Housecroft research group and for having me as a student. I really enjoyed our time together in the Lab and I am glad that we were able to maintain our friendship to this day. Sitting down with you and discussing politics and/or beer is always very enjoyable and I am happy to have you as my go-to chemist outside of the lab.

Dr. Sarah Keller, thank you so much for having me as a Wahlpraktikum and master student. I could not have wished for a better supervisor during this time. You got me hooked on LECs and I am so happy to have such great scientist as a colleague and a friend. Sharing a research topic with you always felt natural and I am grateful for the supportive relationship we had. Spending time with you has always been fun, no matter if in the lab, at conferences or just sitting by the Rhein.

Big thanks go to Dr. Paola Andrea Forero Cortés for teaching me how to properly do phosphorus chemistry and for our collaboration in the connected ligand project. My Schlenk skills have doubled since you joined the group.

Marco Meyer, thank you for being an amazing Master student, colleague and friend. Sharing a lab with you has always been a pleasure and you and Sven Freimann bring a good mood and that special sense of humour to the lab.

I would like to thank all the current and former members of the LEC subgroup and lab, namely, Dr. Andreas Bünzli, Dr. Cathrin Ertl, Dr. Sarah Keller, Isaak Nohara, Marco Meyer and Dr. Paola Andrea Forero Cortés for fruitful discussions and the great atmosphere in the lab.

Additionally, I want to thank Nina Arnosti, Francesca Mazzeo and Lukas Silber for being my students for various projects. Working with all of you was a great pleasure.

In addition, my special thanks for help with synthetic problem, photophysical discussion, joined projects or just a great time inside and outside the lab go to the following people: Isaak Nohara, Cedric Wobill, Dr. Markus Wilgert, Mariia Becker, Sven Freimann, Dr. Christina Wegeberg, Dr. Maximilian Klein, Dr. Roché Walliser, Dr. Stefan Graber, Dr. Cathrin Ertl, Dr. Annika Büttner, Dr. Nathalie Marinakis, Yann Baumgartner, Patrick Herr, Christoph Kerzig, Lucius Schmid, Miriam Schreier, Dr. Laura Büldt, Dr. Martin Kuss-Petermann, Dr. Christopher Larsen, Dr. Svenja Neumann, Dr. Andrea Pannewitz, Thomas Brandl, Alfredo Di Silvestro and Florian Degen.

I would like to thank Prof. Dr. Catherine Housecroft, Prof. Dr. Edwin Constable, Dr. Steffen Müller, Dr. Cathrin Ertl and Dr. Paola Andrea Forero Cortés for proofreading my thesis.

A special thank goes to the whole lumberjack group, aka Dr. Steffen Müller, Dr. Roché Walliser, Dr. Maximilian Klein, Dr. Heiko Gsellinger and Felix Brunner. I really enjoyed having a few hands-on guys around me and I am glad that we still manage to have a beer together every now and then.

Big thanks go to PD Dr. Daniel Häußinger and his former and current group members, namely Dr. Kaspar Zimmermann, Dr. Heiko Gsellinger, Dr. Roché Walliser, Dr. Thomas Müntener, Daniel Joss, Raphael Vogel and Yann Baumgartner for their tireless support with NMR and other measurements.

Dr. Alessandro Prescimone, thank you for all the crystal structures and the good times we had inside and outside the lab and at conferences.

Prof. Dr. Oliver Wenger and Dr. Christopher Larsen, thank you for letting me use your low temperature photophysical setup and for introducing me to the technique.

I would like to thank Dr. Bernhard Jung, firstly for having me as an assistant in the 1$^{st}$ and 2$^{nd}$ semester chemistry praktikum. I Enjoyed this part of the PhD life very much and we always had a good time when we were supervising students together. Secondly, I want to thank Bernhard and the IT team, namely Loreno Calisse and Manuel Sutter for their support with everything that was even remotely related to IT.

The analytics team, namely Sylvie Mittelheisser, Michael Pfeffer and Jonas Zurflüh are thanked for all their support regarding analytics and for measuring elemental analysis. It

has been a great pleasure working with you and I always liked learning some inside analytical skills from you.

A big thank you goes to Beatrice Erismann, for all her work regarding administrative tasks and answering all the questions I had about organisational issues. Thank you for always being there.

I would also like to thank the whole workshop team, namely Markus Ast, Pascal Andrek, Andreas Sohler, Andreas Koller and Hisni Meha for their tireless support. No matter how big or small a task is, we can count on you. Thank you for that.

Additionally, a big thank you goes to Markus Hauri, Susanne Foley and Oliver Ilg from the infrastructure team. Without you we would have nothing to do research with. Thank you for your support and for being there for us.

Special Thanks go to all my wonderful friends outside the University. You guys were always able to pull me back to the ground when my head was up in the clouds, filled with too many academic thoughts and problems and I am very grateful for that.

Mama, Papa and Martin, I can't thank you enough for all the support I had from you. No matter what I decided to do or where I decided to go, you supported me and my decisions in every way you could. Thank you so much.

And lastly, I want to thank my beautiful wife Keks. No matter where we go, I know you are there with me and for me. Thank you.

# Abbreviations

| | |
|---|---|
| ° | degree |
| °C | degree Celsius |
| A | ampere |
| Å | ångström |
| *a, b, c* | unit cell axes |
| *α, β, γ* | unit cell angle |
| $Alq_3$ | tris(quinolin-8-olato)aluminium(III) |
| au | atomic units |
| a.u. | arbitrary units |
| avg. | average |
| [BMIM][$PF_6$] | 1-butyl-3-methylimidazolium hexafluoridophosphate |
| bp | boiling point |
| bpy | 2,2'-bipyridine |
| br | broad |
| *n*BuLi | *n*-butyllithium |
| calc. | calculated |
| cd | candela |
| CFL | compact fluorescence lamp |
| CIE | Commission internationale de l'éclairage |
| cm | centimetre |
| COSY | correlation spectroscopy |
| CT | charge transfer |
| δ | chemical shift |
| d | day; doublet |
| DBU | 1,8-Diazabicyclo[5.4.0]undec-7-en |
| dd | doublet of doublets |
| ddd | doublet of doublets of doublets |
| DFT | density functional theory |
| dm | decimetre |
| DMF | *N,N*-dimethylformamide |
| DMSO | dimethyl sulfoxide |
| DPEPhos | bis(2-(diphenyl-phosphino)phenyl)ether |

| | |
|---|---|
| dt | doublet of triplets |
| *E* | half-cell potential; energy |
| $E^{pa}$ | anodic peak potential |
| $E^{pc}$ | cathodic peak potential |
| $\varepsilon$ | extinction coefficient |
| *e.g.* | for example |
| ECD | electrochemical doping |
| ED | electrodynamical |
| EDG | electron donating group |
| $H_4$EDTA | Ethylenediaminetetraacetic acid |
| EL | electroluminescence |
| [EMIM][$PF_6$] | 1-ethyl-3-methylimidazolium hexafluoridophosphate |
| eq. | equivalent |
| EQE | external quantum efficiency |
| ESI-MS | electron spray ionisation mass spectrometry |
| Et | ethyl, -$C_2H_5$ |
| *et al.* | and others |
| $Et_2O$ | diethyl ether |
| EtOH | ethanol |
| eV | electronvolt |
| EWG | electron-withdrawing group |
| EXSY | exchange spectroscopy |
| Fc | ferrocene |
| FWHM | full width at half maximum |
| g | gram |
| GS | ground state |
| h | hour |
| HOMO | highest occupied molecular orbital |
| HMBC | heteronuclear multiple bond correlation |
| HMQC | heteronuclear multiple quantum correlation |
| Hz | hertz |
| IL | ionic liquid |
| *i*Pr | isopropyl |
| IQE | internal quantum efficiency |

| | |
|---|---|
| ir | irreversible |
| IR | infrared |
| ISC | intersystem crossing |
| iTMC | ionic transition metal complex |
| ITO | indium tin oxide |
| $J$ | coupling constant |
| K | kelvin |
| kHz | kilohertz |
| kJ | kilojoule |
| $k_{nr}$ | non-radiative decay rate |
| $k_r$ | radiative decay rate |
| $\lambda$ | wavelength |
| $\lambda_{exc}$ | excitation wavelength |
| $\lambda_{em}{}^{max}$ | wavelength of emission maximum |
| $\lambda_{EL}{}^{max}$ | wavelength of electroluminescence maximum |
| L | litre |
| LC | ligand centred; liquid chromatography |
| LCD | liquid-crystal display |
| LEC | light-emitting electrochemical cell |
| LED | light-emitting diode |
| LLCT | ligand-to-ligand charge transfer |
| lm | lumen |
| $Lum_{\max}$ | maximal luminance |
| LUMO | lowest unoccupied molecular orbital |
| m | meter; multiplet |
| M | molarity |
| MALDI-TOF | matrix-assisted desorption ionization - time of flight |
| MC | metal-centred |
| Me | methyl |
| Mes | mesityl, 1,3,5-trimethylphenyl, -$C_6H_2Me_3$ |
| mg | milligram |
| µg | microgram |
| MHz | megahertz |
| min | minutes |

| | |
|---|---|
| ml | millilitre |
| µl | microlitre |
| MLCT | metal-to-ligand charge transfer |
| mmol | millimole |
| µmol | micromole |
| mol | mole |
| m.p. | melting point |
| MS | mass spectrometry |
| µs | microsecond |
| MW | microwave |
| *m/z* | mass to charge ratio |
| ν | frequency |
| NBS | *N*-Bromosuccinimide |
| NIS | *N*-Iodosuccinimide |
| nm | nanometre |
| NMR | nuclear magnetic resonance |
| NOESY | nuclear Overhauser effect spectroscopy |
| ns | nanosecond |
| OLED | organic light-emitting diode |
| ov. m | overlapping multiplet |
| PEDOT:PSS | poly(3,4-ethylenedioxythiophene):poly(styrenesulfonate) |
| Ph | phenyl, -$C_6H_5$ |
| Phen | 1,10-phenanthroline |
| PLQY | photoluminescence quantum yield |
| PMMA | poly(methyl methacrylate) |
| ppm | parts per million |
| qr | quasi reversible |
| quant. | quantitative |
| RT | room temperature |
| σ | Hammett parameter |
| s | second; singlet |
| $S_0$ | ground state |
| $S_1$ | lowest lying single excited state |
| sept | septet |

| | |
|---|---|
| sh | shoulder |
| SSL | solid-state lighting |
| τ | excited state lifetime |
| t | triplet |
| T | temperature |
| $T_1$ | lowest lying triplet excited state |
| $t_{1/2}$ | half lifetime (time to reach half of the maximum luminance) |
| $^t$Bu | *tert*-butyl |
| $^t$BuOH | *tert*-butanol |
| $^t$Bu-xantphos | 9,9-dimethyl-4,5-bis(di-*tert*-butylphosphino)xanthene |
| td | triplet of doublets |
| TD | time-dependent |
| THF | tetrahydrofuran |
| TMEDA | N,N,N',N'-tetramethylethylendiamin |
| TMS | trimethylsilyl group |
| $t_{on}$ | turn-on time (time to reach maximum luminance) |
| TWh | terawatt hour |
| UV | ultraviolet |
| V | volt |
| vpby | 4-vinyl-4'-methyl-2,2'-bipyridine |
| VT | variable temperature |
| Vis | visible |
| W | watt |
| ζ | spin-orbit coupling constant |
| xantphos | 4,5-bis(diphenylphosphino)-9,9-dimethylxanthene |
| Z | number of formula units in the unit cell |

# Materials and methods

Starting materials were obtained in reagent grade from Sigma-Aldrich, Alfa Aesar, Acros Organics, Fluorochem, Strem, Apollo Scientific, or TCI and used as received. Dry solvents (crown cap or AcroSeal®) were purchased from Sigma-Aldrich or Acros Organics and used for reactions carried out under inert atmosphere. For all other reactions, solvents used were of reagent grade or distilled. HPLC grade solvents were used for analyses. Column chromatography was performed using Fluka silica gel 60, Merck aluminium oxide 90 standardized or Aluminium oxide 90 activate basic.

Microwave reactions were performed in a Biotage Initiator 8 reactor. $^{1}H$, $^{13}C\{^{1}H\}$ and $^{31}P\{^{1}H\}$ NMR spectra were recorded on Bruker Avance III-400, 500 and 600 NMR spectrometers; spectra were recorded at 295 K unless otherwise stated. $^{1}H$ and $^{13}C\{^{1}H\}$ NMR chemical shifts were referenced to the residual solvent peaks with respect to $\delta$(TMS) = 0 ppm and $^{31}P\{^{1}H\}$ NMR chemical shifts with respect to $\delta$(85% aqueous $H_3PO_4$) = 0 ppm.

Solid-state IR spectra were recorded using a Perkin Elmer UATR Two spectrometer. Solution absorption spectra were measured using an Agilent 8453 spectrophotometer or a Shimadzu UV2600 spectrophotometer. Solution emission spectra were recorded using a Shimadzu RF-5301PC or a Shimadzu RF6000 spectrofluorometer. A Shimadzu LCMS-2020 instrument or a Bruker esquire 3000plus instrument was used to record electrospray ionization (ESI) mass spectra. Quantum yields ($CH_2Cl_2$ solution and powder) were measured using a Hamamatsu absolute photoluminescence quantum yield spectrometer C11347 Quantaurus-QY. Emission lifetimes and powder emission spectra were measured with a Hamamatsu Compact Fluorescence lifetime Spectrometer C11367 Quantaurus-Tau, using an LED light source with $\lambda_{exc}$ = 280 or 365 nm. Quantum yields and PL emission spectra in thin films were recorded using a Hamamatsu absolute quantum yield C9920. Low temperature emission and lifetime experiments were performed using an LP920-KS instrument from Edinburgh Instruments. 410 nm excitation was obtained from pulsed third-harmonic radiation from a Quantel Brilliant b Nd:YAG laser equipped with a Rainbow optical parameter oscillator (OPO). The laser pulse duration was ~10 ns and the pulse frequency 10 Hz, with a typical pulse energy of 7 mJ. Detection of the spectra occurred on an iCCD camera from Andor. Single-wavelength kinetics were recorded using a photomultiplier tube.

Electrochemical measurements were carried out using a CH Instruments 900B potentiostat with $[^{n}Bu_4N][PF_6]$ (0.1 M) as supporting electrolyte and at a scan rate of 0.1 V $s^{-1}$. The working electrode was glassy carbon, the reference electrode was a leakless $Ag^{+}$/AgCl (eDAQ ET069-1) and the counter-electrode was a platinum wire. Final potentials were internally referenced with respect to the $Fc/Fc^{+}$ couple.

Crystallographic data were collected on a Bruker Kappa Apex2[1] diffractometer with data reduction, solution and refinement using the programs APEX and CRYSTALS.[2] Structural analysis was carried out using Mercury v. 4.2.0.[3,4]

LEC devices were prepared in the Group of Henk Bolink at the university of Valencia. LECs were prepared on top of patterned indium tin oxide (ITO, 15 Ω $sq^{-1}$) coated glass substrates previously cleaned by chemical and UV-ozone methods. Prior to the deposition of the emitting layer, 80 nm thick films of poly-(3,4-ethylenedioxythiophene):poly(styrenesulfonate) (PEDOT:PSS) (CLEVIOS™ P VP AI 4083,

Heraeus) were coated in order to flatten the ITO electrode and to increase its work function. The emitting layer (100 nm thick) was prepared by spin-coating a dichloromethane solution of the emitting compound with the addition of the ionic liquid 1-ethyl-3-methylimidazolium hexafluoridophosphate [Emim][$PF_6$] (> 98.5%, Sigma-Aldrich), in a 4:1 molar ratio. The devices were then transferred to an inert atmosphere glovebox (< 0.1 ppm $O_2$ and $H_2O$), where the aluminium cathode (100 nm) was thermally deposited in high vacuum using an Edwards Auto500 chamber integrated in the glovebox. The thickness of all films was determined with an Ambios XP-1 profilometer. The active area of the devices was 6.5 $mm^2$. LECs were not encapsulated and were characterized inside the glovebox at room temperature. The device lifetime was measured by applying a pulsed current and monitoring the voltage and luminance versus time by a True Colour Sensor MAZeT (MTCSiCT Sensor) with a Botest OLT OLED Lifetime-Test System. The electroluminescence (EL) spectra were measured using an Avantes AvaSpec-2048 Fiber Optic Spectrometer during device lifetime measurement.

For Chapter 4: A set of density functional theory (DFT) calculations were performed for the $[Cu(P\hat{}P)(N\hat{}N)]^+$ cations (P^P = $^t$Bu$_2$xantphos and xantphosMes$_2$; N^N = bpy, 6'-Mebpy, and 6,6'-Me$_2$bpy) using the A.03 revision of Gaussian 16.[5] The Becke's three-parameter B3LYP exchange-correlation functional[6,7] was used in all the calculations. The "double-ζ" quality def2svp basis set was employed for C, H, P, N and O atoms, whereas the "triple-ζ" quality def2tzvp basis set was used for the Cu atom.[8,9] Intramolecular non-covalent interactions are expected to play a relevant role in determining the molecular geometry of the studied complexes owing to the presence of the bulky xantphos-derived ligands. To get a better description of those interactions, the D3 Grimme's dispersion term with Becke–Johnson damping was added to the B3LYP functional (B3LYP-D3).[10,11] The geometries of all the complexes in both their singlet ground electronic state ($S_0$) and their lowest-energy triplet excited state ($T_1$) were optimized without imposing any symmetry restriction. For $T_1$ the spin unrestricted UB3LYP approximation was used with a spin multiplicity of three. The lowest-lying excited states of each complex, both singlets and triplets, were computed at the minimum-energy geometry optimized for $S_0$ using the time-dependent DFT (TD-DFT) approach.[12–14] All calculations were performed in the presence of the solvent ($CH_2Cl_2$). Solvent effects were considered within the self-consistent reaction field (SCRF) theory using the polarized continuum model (PCM) approach.[15–17]

# Chapter 1: Introduction

## 1.1 The world´s need for energy

The world's population is growing. At the same time, the living standard of the average person is increasing. This leads to an ever-growing demand for energy. A large portion of this energy is supplied as electricity over the grid. The global electricity consumption of 2017 was 23 696 TWh and has more than doubled since 1990. Most of the electricity (75.1%) is generated by the combustion of fossil fuels such as coal, oil and natural gas or by nuclear power. Only 24.6% originates from renewable energy sources such as hydroelectric, wind or solar power plants.[18] Non-renewable sources of electricity (with the exception of nuclear power plants) release the greenhouse gas $CO_2$ into the atmosphere. These data show that our electricity consumption has a major impact on our carbon footprint and contribute massively to global warming. To counteract this trend, humanity has two major options: (i) We need to redesign our electricity generation system and (ii) base it on renewable sources. This is a long-term investment and often countries and companies fail to meet their declared carbon output goals.[19–21] Therefore, we need to decrease our energy consumption as a whole to loosen the strain on the grid and lower our carbon output. Electric consumers need to learn to become more efficient.

In 2017 10.1% of the consumed electricity in Switzerland was used for illumination.[22] In 2006 illumination accounted for 13.3% of the consumed electricity.[23] This decrease over the last eleven years is a direct result of the replacement of old inefficient lighting devices such as the incandescent light bulb with more energy efficient lighting sources like LEDs. This development needs to be pushed further and new energy-efficient lighting technologies are needed.

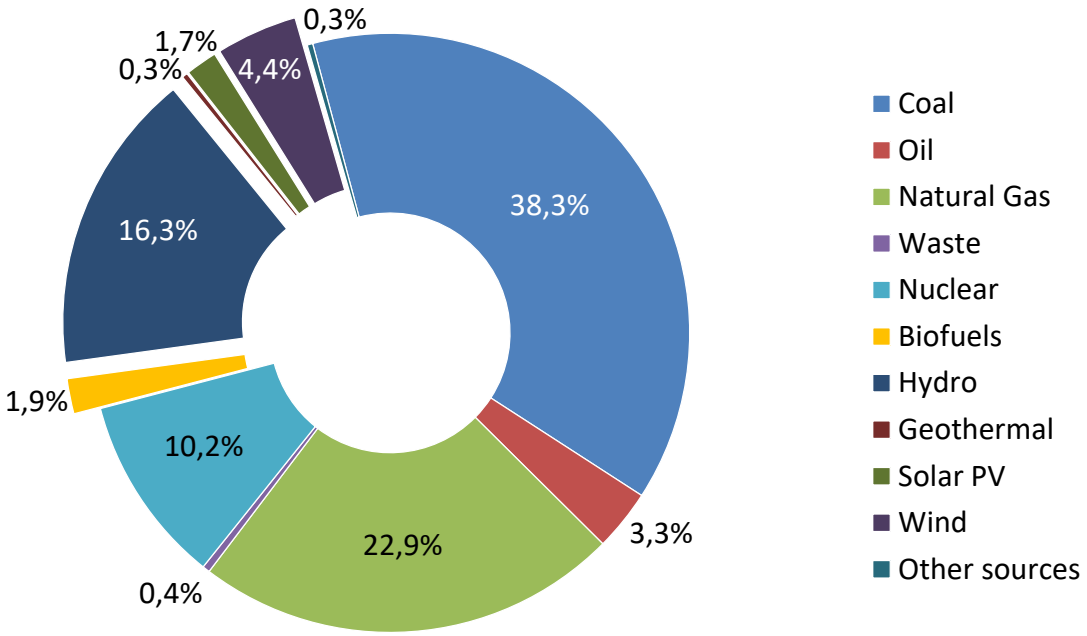


***Figure 1.1*** *Global electricity generation by source in 2017.*[18]

## 1.2 History of lighting

The use of artificial lighting devices is one of the most significant inventions of humanity. Even the earliest versions such as torches or campfires freed our ancestors from the limitations that the day-night cycle imposed on them and enabled humans to carry on with their daily business after nightfall. Since then our lighting technologies have greatly improved and our modern lifestyle would not be possible without the 24/7 availability of artificial light. The first lighting devices such as torches, candles or oil lamps, were based on the combustion of organic material. In the 19th century a more sophisticated lighting technologies were developed. It was found that by distilling coal, kerosene and "coal gas" could be extracted. The gas was used for illumination of streets and buildings in larger cities, by distributing it through a pipe system while kerosene was used in more rural areas, since transporting the liquid was more convenient than building extremely long gas pipes.[24] The efficiency of these devices was very low since most of the energy is converted into heat instead of light.

The first lighting device driven by electrical energy was invented by Joseph Swan, who obtained a patent for a carbon filament-based lighting device in a partial vacuum in 1860. Thomas Edison (who is commonly associated with the invention of the incandescent light bulb) patented an improved design in 1879 and was therefore sued by Swan for patent infringement. Later in 1883 Edison and Swan merged their companies to form the Edison and Swan United Electric Light Company in 1883 that sold an improved version of Swan's original light bulb.[25,26] An incandescent light bulb works based on the following principle: Current is passed through a thin filament with a high internal resistance, usually a tungsten wire. The wire heats up to around 3500 K and starts to glow. The emitted light covers most of the visible spectrum and is perceived as white light, generated with an efficacy of about 15 lm $W^{-1}$. For a lighting device, the efficacy defines how much light is emitted per consumed amount of energy. However, the device also emits strongly in the infrared, which leads to rather low electron to visible photon conversion of about 5%. 95% of the input energy is wasted as heat.[26,27]

In the 1930s the company General Electric commercialized a more efficient lighting device: the fluorescent tube. The principle of luminous electric discharge of mercury vapour had been known since the early 18th century, but it had not been used for lighting applications because the radiation consisted mostly of blue and ultraviolet (UV) light. General Electric developed a lamp that could convert this UV-radiation into visible light. The inside of a mercury vapour filled glass tube was coated with a mixture of phosphors that were known to emitted visible light. When a current was passed through the lamp, the mercury was excited and emit UV-radiation. This UV light was absorbed by the phosphors in the coating which led to the emission of visible light. Careful tuning of the phosphor mixture enabled device manufacturers to generate different shades of white light. Modern fluorescence tubes reach an efficiency of up to 25% with a typical efficacy of 60–100 lm $W^{-1}$. Compact fluorescence lamps (CFLs) are a smaller version of the fluorescent tube. They are mostly used in private homes and smaller scale lighting and show slightly lower efficiencies of around 20%. Fluorescent tubes have a significantly longer lifetime (up to 30'000 h) than incandescent light bulbs (around 1000 h) and are therefore more cost effective. However, the lifetime of a fluorescence tube is reduced

significantly when switched on and off many times. Fluorescence tubes are better suited for large area lighting with long turn-on periods.[24,26,28]

## 1.3 The emergence of solid-state lighting (SSL)

### *1.3.1 Light-emitting diodes (LEDs)*

All these previously mentioned methods of light generation rely on some form of an electronic discharge, which has one inherent disadvantage: A lot of energy is wasted as heat. This changed when the first example of a direct electron to photon conversion was observed by Holonyak and Bevacqua in 1962.[29] They described the emission of visible light from an GaAsP inorganic light-emitting diode (LED) under bias. The working principle of such LEDs is based on the combination of *p*- and *n*-doped semiconducting materials. When a bias is applied to such a device, holes and electrons are injected into the semiconductor and travel along the conduction and valence band levels. The band gap can be tuned by incorporating different doping atoms. Upon recombination of electrons and holes a photon is emitted with an energy corresponding to the wavelength of the band gap. In this direct electron to photon conversion no heat is generated as side product. The emitted light is monochromatic with a very narrow emission profile.[28,30–32] To generate white light, different device architectures can be developed. When the semiconductor emits light of high energy, different phosphors can be fabricated on top of it that absorb some of the high energy radiation and emit light of a different colour (similar to the working principle of a fluorescence tube). Careful tuning of the phosphor composition leads to LEDs with a high-quality white light emission and good colour rendering properties. Another way to generate white light is to simply combine two or more LEDs of different colours into a single cell. These LEDs show a lower colour rendering quality because the emitted light consists of multiple narrow emission bands instead of a broad band emission.[33] Modern consumer grade LEDs show an efficacy of up to 90 lm $W^{-1}$ [34] and are widely implemented in small scale lighting, public infrastructure and screen applications. The biggest drawback of LEDs is the fact that they are based on often brittle semiconducting materials which inhibits their use in flexible surfaces and increases the difficulty for continuous large-scale applications.

### *1.3.2 Organic light-emitting diodes (OLEDs)*

The first example of a light-emitting diode based on organic material was reported by Tang and VanSlyke in 1987.[35] They described the electroluminescence of a two-layered device with tris(quinolin-8-olato)aluminium(III) ($Alq_3$) as the photoactive species. The cell showed an external quantum efficiency (EQE) of 1% and a luminous efficiency of 1.5 lm $W^{-1}$. Some years later in 1990 Friend *et al.* presented the first organic light-emitting device that utilized an organic polymer as photoactive layer.[36] They used the delocalized π molecular orbitals of the polymer to inject electrons and described a working principle similar to that of a classical LED. The major advantage over an LED and the previously described OLED of Tang was the ease of processing the polymer layer to form a robust structure. This device emitted green-yellow light with a reported quantum efficiency of up to 0.05%. Since then the number of papers in the field of OLEDs has skyrocketed and nowadays OLEDs are widely used in modern electronics for display applications. OLEDs

have multiple advantages over traditional display technologies. They are generally thinner than conventional LCD displays and can be fabricated on flexible surfaces. At the same time, they do not rely on LED backlighting, since the coloured pixels themselves emit light. This results in very thin devices and better accuracy of dark colours.[37] In 2014 the Korean company LG released the first flexible OLED TV[38] followed by the presentation of a TV, that completely rolls up in its base in 2019.[39] In the same year, the company Royole released the world's first foldable smartphone, the FlexPai.[40] But even outside of cutting edge applications, OLEDs are widely used for their high picture quality, great colour accuracy, high contrast and viewing angle.

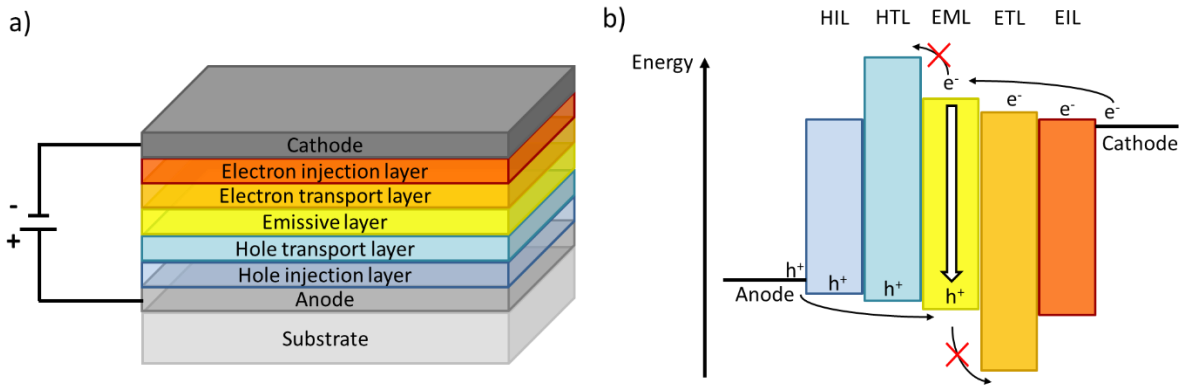


***Figure 1.2*** *a) Schematic representation of a typical OLED device architecture and b) representative energy level diagram of OLED layers.*

The general device architecture of an OLED is shown in **Figure 1.2 a)**. Historically, the complexity of the device has increased from simple two-layered approaches to multi-layer structures to tackle various performance issues. In a typical modern OLED the anode is fabricated on top of the substrate, followed by hole injection and transport layers. The emissive layer is then applied, followed by electron transport and injection layers and a cathode. The latter usually consists of a low work function metal such as Ca, Mg or Al.[41]

**Figure 1.2 b)** shows the operating principle of an OLED. When a bias is applied to the device electrons and holes are injected at the cathode and anode respectively. Careful tuning of HOMO and LUMO levels of injection and transport layers is needed to enable the charge carriers to travel when a potential is applied. When reaching the emissive layer, electrons and holes can recombine and form an exciton (molecule in its excited state). Upon relaxation to the ground state, light is emitted. It is crucial that electrons cannot enter the hole transport material nor that holes can enter the electron transport layer. To achieve this, the hole and electron transports materials need to incorporate high LUMO and low HOMO levels respectively. If this is not the case, additional electron and hole blocking layers are needed around the emissive layer to prevent charge migration further than intended.[42]

Fabrication methods for monochromatic OLEDs that emit light of lower energies (*e.g.* red, yellow or green) have been well established within the last decade. But what remains challenging is the fabrication of efficient deep blue emitters for OLEDs. Metal-organic blue emitters often show unsatisfactory performance due to triplet-polaron annihilation. One way to avoid this problem is the incorporation of purely organic blue-emitting small molecules or polymers[43–45]. To achieve multi-colour emission, different device architectures are possible: Single-colour emitting devices can be fabricated next to or on

top of each other while being electronically independent. This approach simplifies the architecture of the single cells but increases the complexity of the overall device and its driving electronics. Alternatively, multi-colour layers can be incorporated in one cell. This simplifies the cell architecture but complicates the design of the emissive layer. White light emission from a single cell can be achieved in different ways: Chromophores can be mixed within one emitting layer, multiple emitting layers can be fabricated within one cell or a single monochromic layer can be combined with a phosphor layer, similar to the approach for fluorescent tubes. All these approaches need careful engineering of the emissive layer in addition to the various injection, transport and blocking layers.[41,42]

The multi-layer structure of an OLED creates an additional challenge: Although devices and luminophores have been developed with an internal quantum yield (IQE) of close to 100%, the external quantum yield is usually significantly lower. The main reason for that is poor light outcoupling capability. When excitons relax to their ground state, photons are emitted unidirectionally. Light that travels in the intentioned direction leaves the device, but photons emitted at an angle get refracted at one of the many layer interfaces, travel to the edges or get re-absorbed, either by the layer molecules themselves or due to surface plasmon effects at the cathode interface. This results in a light outcoupling efficiency of about 20% for a standard multi-layer OLED.[41] The outcoupling efficiency can be increased by controlling the emitters dipole orientation, addition of interface materials on the layers or by surface modifications on the electrode or glass interface.[42,46–48] However, all these approaches make the devices even more complex and therefore more expensive.

Additionally, using a low work function metal as cathode is often a necessity for OLEDs, since the Fermi level of the electrode must match the LUMO of the electron injection layer.[31,41,49] Therefore, OLEDs must be sealed rigorously against oxygen and moisture or degeneration might occur, shortening the lifetime of the device. Their multi-layer architecture poses additional difficulties. Most of the active layers are applied by vapour deposition,[50] which requires high vacuum and a substantial amount of energy. Additionally, the materials must be volatile enough, which narrows the scope of available substances. Solution-based deposition methods can be suitable, but the solubility of previously applied layers need to be considered. All these details increase the complexity and cost of OLED production and have prevented them from being used in low-tech, large area lighting applications.

## 1.4 Light-emitting electrochemical cells

In 1995 Pei *et al.* developed a lighting device based on a luminescent polymer mixed with an electrolyte. The device could have been interpreted as a simplified version of an OLED at the time, but it showed some extraordinary properties. The voltage to trigger electroluminescence was very low compared to the OLEDs of the time and the device did not show a diode behaviour. No matter in which direction the current was flowing, electroluminescence was triggered. In a side by side configuration a thin luminescent zone could be observed within the thick main layer of 15 µm (**Figure 1.3**). This was the first example of a working light-emitting electrochemical cell. The key difference to previous lighting devices was the incorporation of mobile ions into a polymer matrix.[51]

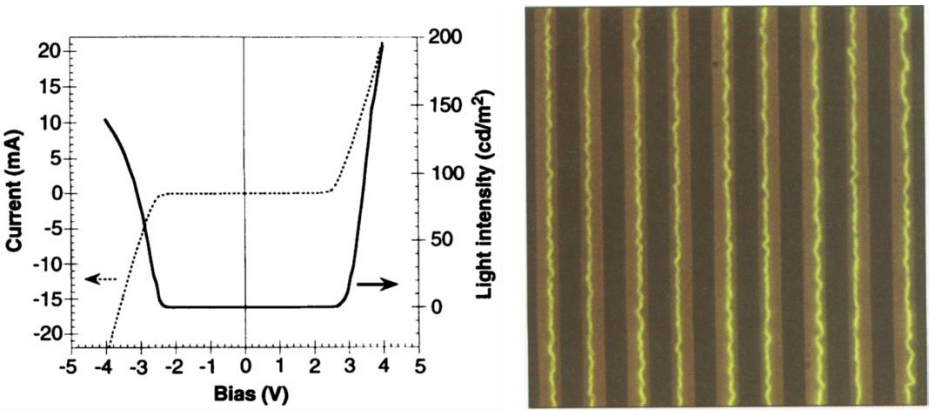


***Figure 1.3*** *Left: current and light emission vs. voltage behaviour of first LEC device. Right: Photograph of polymer LEC fabricated between interdigitated gold electrodes. Reprinted with permission from reference* 51*.*

Not long after Pei's first LEC, Maness *et al.* published a lighting device based on a polymer incorporating ionic transition metal complexes (iTMCs). They used poly $[Ru(vpby)_3][PF_6]_2$ based films that emitted light when biased with a relatively low voltage of −5.5 V.[52] In 1996 Lee *et al.* presented the first purely iTMC based LEC. They used $Ru(phen')_3^{2+}$ (where phen' is 4,7-diphenyl-1,10-phenanthrolinedisulfonic acid disodium salt) to fabricate multiple film devices. Sulfonate groups were used to enable film processing from polar solvents such as water, methanol and dimethylsulfoxide.[53]

### *1.4.1 LEC architecture and operation*

The biggest advantage of LECs compared to OLEDs is their simple device architecture. LECs usually consist of only one or two active layers sandwiched between two electrodes. The materials are air stable and various fabrication technics can be applied, such as spin coating, spray-on or roll-to-roll procedures.[31,49,54,55] A comparison of LECs and OLEDs can be found in **Table 1.1**. This simplification of the device architecture widens the field of applications and lowers the production costs at the same time, making LECs promising candidates for low-tech large area lighting applications. However, despite the many exotic examples of applications such as luminous fibres for wearable electronics[56], thin flexible films[57,58] and spray on fabrications,[59,60] LECs have not been able to make it into the market on a large scale yet. New fabrication methods based on roll-to-roll techniques have the potential to change this. Using this technique, large scale production of flexible luminescent surfaces is possible. The method allows the application of different luminophores and additional surface modifications, carrying the potential to enhance light outcoupling efficiencies.[61,62] A recent cost analysis by Sandström and Edman demonstrates the potential of this approach. Analysing different scenarios, they state that with a high initial cost for setting up large fabrication facilities a high output of 55 000 $m^2$ of luminescent material per week is possible. At this scale the cost per device drops to only 11 € $m^{-2}$. Driving these devices at 1000 cd $m^{-2}$ would result in a light-output cost of merely 0.0036 € per lumen, which would make them a serious competitor to current LED and OLED devices. However, the long term stability of such LEC devices is still a major issue and therefore remains the main challenge before such a large fabrication plant can be realized effectively.[63]

***Table 1.1*** *Comparison of OLED and LEC device parameters.*[55]

| Parameter | OLEDs | LECs | Benefit of LECs |
|---|---|---|---|
| Active layers | 4 or more | 1 or 2 | Simple device architecture |
| Typical thickness per layer | 1 – 40 nm | 100 – 500 nm | Thicker film promises robust processing |
| Cathode | Air sensitive | Air stable | Air stable metals such as Al, Ag or Au are suitable |
| Encapsulation requirements (permeation rate of $H_2O$) | High ($10^{-6}$ g m$^{-2}$ day$^{-1}$) | Low ($\gg 10^{-6}$ g m$^{-2}$ day$^{-1}$) | Air stable electrodes require less rigorous sealing |
| Processing of organic layer | Vacuum-based | Solution-based | More cost-efficient methods applicable |

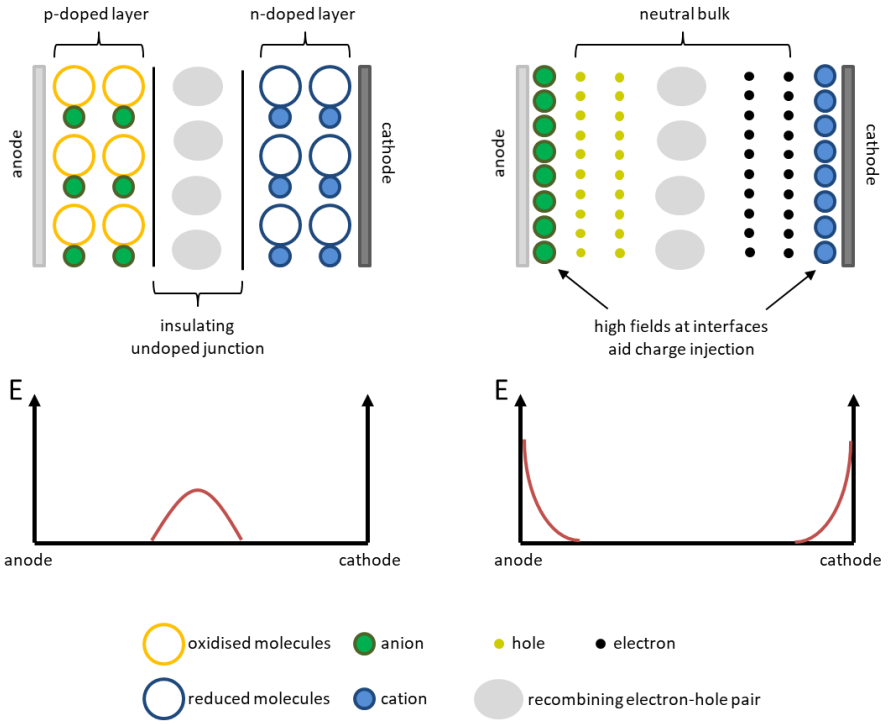


***Figure 1.4*** *Schematic representation of ECDM (electrochemical doping model, left) and electrodynamic model (EDM, right) of a LEC. (reproduced after reference* 49*)*

There are two major models to describe the operational mechanism of a LEC (see **Figure 1.4**). The electrochemical doping model (ECDM) was first proposed by Pei *et al.*[51,64] In this model, application of a potential leads to doping of the luminescent material. When this happens, counterions form charge pairs with the oxidised or reduced molecules. As more charges are injected the p- and n- doped regions grow towards each other. When these zones are close, an intrinsic region forms between them in the form of a p-i-n junction.

Within the intrinsic region, electrons and holes recombine to form excitons. These excitons can relax to their ground state with the emission of light. A strong electric field is only present in the intrinsic region, the doped regions are mostly field free. The presence of doped regions at the electrode interfaces leads to low resistance interfaces and therefore facilitates charge injection. This is one reason why LECs often need a high initial starting potential to dope the material and can then be driven at lower voltage. The alternative electrodynamic model (EDM) was first proposed by deMello.[65–67] In this description charged molecules move to the electrode surface and form electronic double layers, shielding the bulk of the material which is then left field free. The electric field still present at the interface enables charge injection into the bulk. The charge carriers then diffuse into the active layer. When electrons and holes recombine, excitons are formed and light is emitted.[31,49,55] Both models have been investigated experimentally and by numeric modelling and are believed to coexist.[64,68,69]

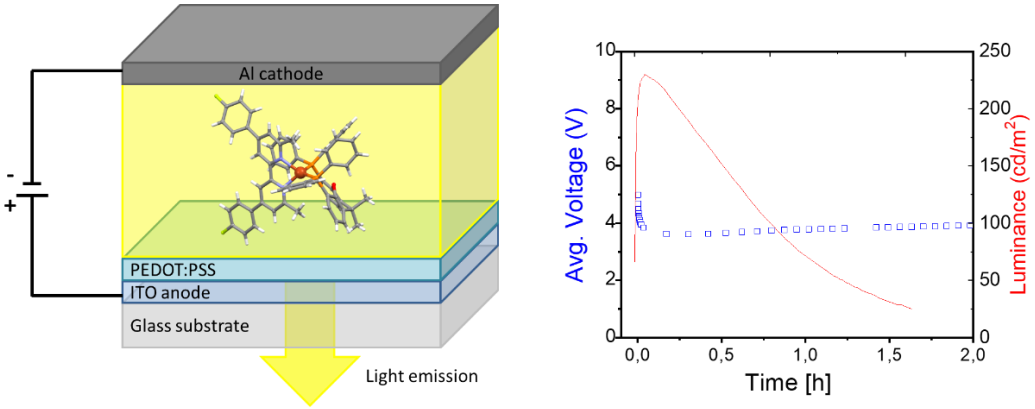


***Figure 1.5*** *Left: schematic representation of a typical iTMC-LEC. A PEDOT:PSS layer is spin-coated onto an ITO covered glass surface, followed by the active layer. The aluminium cathode is applied by vapour deposition. Right: voltage and luminance of LEC under bias over time. The device was driven at a constant current density of 50 A m$^{-2}$ with a duty cycle of 50%.*

The typical architecture of an iTMC-LEC is shown in **Figure 1.5** (left). Several device characteristics are recorded to evaluate the LEC performance. The turn-on time ($t_{on}$) describes the time which is needed until the device reaches a certain luminous intensity, usually the maximum luminance. Ideally this is low and the device turns on within seconds. The luminance (cd m$^{-2}$) gives a measure of the brightness of the device per unit area. The electroluminescent efficacy (in lm W$^{-1}$) gives information about how efficient the device is able to convert electrons into photons. Related to this is the external quantum efficiency (EQE in %) which describes how much of the input electrical energy is converted to luminous energy. The lifetime ($t_{1/2}$) describes the time after turn-on until the device reaches half of its luminous intensity. **Figure 1.5** (right) shows the voltage and luminous behaviour of a LEC under a pulsed current driving mode. This driving mode is beneficial over a constant current driving mode because a pulsed current leads to a reduced turn-on time due to the initially high voltage and therefore a fast formation of the double layer. Furthermore, the pulsed current results in a dynamic stabilization of the p-i-n junction, which results in an increased device lifetime.[54] After an initially high turn-on voltage, the device reaches a steady state. The luminance rises to a maximum after turn-on and then slowly decreases.

### *1.4.2 Improving LEC stability and performance*

Several factors affect device degradation: an imbalance in the doped regions, the stability of the electrode material in combination with contaminants such as water, oxygen or others, homogeneity of the emissive layer, temperature and the electrochemical stability of the luminous material.[70] Ions of different sizes are present in a LEC. In case of an iTMC-LEC the anions are usually small such as $[PF_6]^-$ or $[BF_4]^-$ while the majority of the cations consist of large photoactive coordinating complexes. Upon application of a bias the ions start to move through the active layer. Due to their larger size, the ionic conductivity of the larger cations is lower and the ion density at the respective electrodes is smaller. Therefore, charge imbalance exists and the intrinsic region is formed closer to one electrode. This can lead to enhanced exciton quenching and a lower EQE. To tackle this, small cations such as lithium, that move fast through the active material, can be added. This creates a more balanced charge distribution and the recombination zone forms more centrally. Additionally, due to faster formation of the electronic double layer at the cathode, charge injection is facilitated and the turn on time is reduced.[71,72] The same effect of improved positioning of the intrinsic region can be achieved by incorporating a hole transport material.[73] Bolink *et al.* additionally demonstrated the effect of lithium salts with different anions such as $[BF_4]^-$, $[PF_6]^-$, $[TFSI]^-$ and $[ClO_4]^-$. A high ionic conductivity of the additive results in a faster turn on time and a more balanced ion mobility leads to enhanced device lifetime. At the same time the additive needs to be chemically innocent. The most suitable additive in their study (with an iridium iTMC-LEC) was found to be $LiBF_4$.[74] Especially in polymer-based LECs (p-LECs), the homogeneity of the emissive layer plays an important role. Careful optimisation of the film morphology (*e.g.* by using polymer supporting electrolytes of different molecular weights) is needed to gain an optimal emissive layer formation and therefore light output.[75] The choice of electrode material plays a crucial role for the performance and especially the lifetime of a LEC. First and foremost, the material needs to be electrochemically suitable for the use case. Gold shows great electrochemical stability over a large potential window and can be used as cathode or anode material. This makes gold a suitable candidate to be used in symmetric LEC configurations. Aluminium on the other hand can be oxidised at rather low potentials.[76] In a classical LEC configuration this is not a problem, because aluminium is mostly used as cathode material, which means only negative potentials are applied. Recently, Edman *et al.* widened the scope of suitable electrode materials by investigating different metals and their performance in LECs. They found Ca, Mn, Cu, Ag and ITO to be suitable cathode materials, although the reflective and absorptive properties of *e.g*. Cu, Au and Mn need to be taken into account.[77] Nevertheless, contaminants such as water or oxygen can influence the long-term stability of aluminium electrodes. Oxygen can diffuse through imperfections and pinholes in the electrode and form an oxide layer between the electrode and active material, decreasing the contact. Water that enters the same way or might even be present from film fabrication can be reduced under bias and form molecular hydrogen. This can lead to the formation of bubbles under the electrode. Both these processes lead to delamination of the electrode over time and negatively influence the device lifetime.[78] Consequently, it is always beneficial to seal LECs, although the materials are in principle air stable. However, the sealing does not need to be as rigorous as for OLEDs and simply gluing on a glass plate is mostly sufficient. On the other hand, a rigorous removal of water from the active layer can have negative effects on the device

performance, since this reduces the ionic mobility and increases the necessary turn-on voltage.[79] Joule-heating of electroluminescent devices can lead to enhanced degradation of the luminescent material. Therefore it can be beneficial to apply the device on a substrate that is able to disperse heat away easily and therefore cool the device passively.[80] The electrolyte plays a crucial role in LECs. It assists with various processes such as ion transport, double layer formation, charge injection and doping, and ionic conductivity. To fulfil these requirements, the electrolyte must possess some crucial properties, such as a high ionic mobility, high conductivity, electrochemical stability over a large potential window and mixability with the active compounds. The latter two requirements are especially challenging to meet for many polymer-based electrolytes in p-LECs.[81,82] Ionic liquids, such as [EMIM][$PF_6$] or [BMIM][$PF_6$] show great stability and turn-on times and are therefore often used in iTMC-LECs.[83–87] Lastly, to achieve stable, long-lived devices the emitting species must be chemically and electrochemically stable. A low electrochemical stability leads to irreversible oxidation or reduction reaction and therefore decomposition of the emitting species. However, this is difficult to evaluate from degraded cells and varies greatly with the chemical nature of the emitting species.[88]

### *1.4.3 Applications of LECs*

Due to their simple architecture and large selection of suitable materials LECs can be applied for various tasks. Here we present only a few extraordinary use cases and applications to demonstrate the flexibility of these devices.

Edman *et al.* presented a LEC with a blue co-polymer and a red ruthenium complex blended together in the active layer. Since these luminophores showed emissive states of different nature there was no energy transfer observed, hence no host-guest system present. Charge injection varied on the applied voltage which enabled colour tuning from red to blue by voltage control. An intermediate voltage of 5 V resulted in the emission of white light.[89] Later the same year the group reported an optimized design with a polymer-iTMC blend that operated in a host-guest manner. At the ideal ratio of 0.5% red emitting iridium complex mixed into the polymer, white light emission with a good colour rendering index of 79 was observed.[90] The colour rendering index gives a measure from 1 to 100% of how accurate colours appear to the human eye when illuminated with a given light source.[33] In a different study, incorporation of various fluorophores within one co-polymer blend led to the emission of white light from LECs on hard and flexible surfaces. The immobilization of the fluorophores with a certain spatial separation from each other prevented energy transfers and therefore quenching of the higher excited states, which would have resulted in light emission from lower energetic states.[91] Wu *et al.* presented a white light-emitting cell with a tuneable colour temperature by applying a pulsed current with varying pulse length. The active layer in their study consisted of red and blue emitting iridium complexes that formed a host-guest complex. Depending on the pulse length, the voltage build-up on the electrode interfaces varied. Lower potential resulted in the dominant guest emission, rendering a warm white light emission. With longer pulses, the effective voltage was higher, resulting in a more dominant host emission and therefore cold white light.[92] LECs can be fabricated on various surfaces. This makes them especially suitable for wearable electronics applications. In 2015 Pei *et al.* presented the prototype of an electroluminescent fibre. The LEC was manufactured onto a steel wire as substrate and used zinc oxide and carbon nanotubes as electrodes.

Differently coloured fibres could be prepared and the fibre could be woven into a piece of fabric.[56] One year later, Edman *et al.* presented a LEC fabricated onto a transparent fabric-based electrode containing silver plated copper wires as electrode. The emissive layer was applied by a spray-coating technique.[58] This method had been developed before in the research group and they showed the applicability of the technique on various surfaces, including a steel fork that functioned as anode.[59] An unusual application of LECs was demonstrated by Chen *et al.* They fabricated a LEC using carbohydrate-based block co-polymers that showed memristive behaviour. The device was able to adapt one of three states and maintain this information over time.[93]

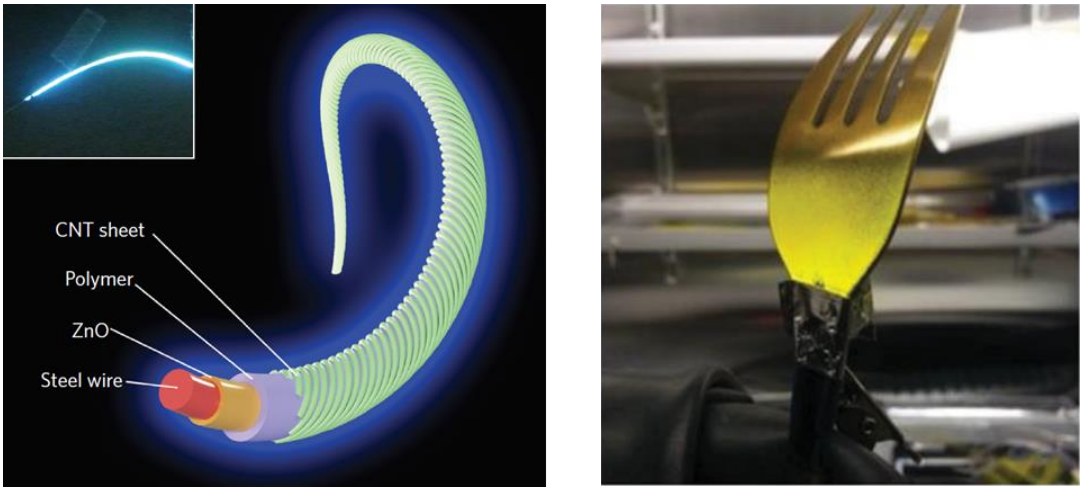


***Figure 1.6*** *Left: Schematic representation of a flexible LEC fabricated onto a steel wire. Inset: Fibre-LEC under bias of 10 V Right: LEC fabricated onto a stainless-steel fork with an active layer and a top cathode. Reprinted with permission from* [56] *and* [59]*.*

### *1.4.4 The era of iridium*

Although the first iTMC-LEC was based on a luminescent ruthenium complex,[53] poor device stability and low luminescence efficiency shifted the development towards more promising iridium-based LECs. Today, iridium complexes are well established and many examples for Ir-iTMC-LECs exist. Iridium complexes of the type $[Ir(C^N)_2(N^N)]^+$ (where N^C is a cyclometallating ligand and N^N is a diimine or related chelating ligand) show properties that are crucial for LEC performances. First and foremost, synthetic procedures to prepare the target complexes are well established and generally straight forward to perform. The majority of complexes is prepared via a chlorido-bridged $[Ir_2(C^N)_4(\mu\text{-}Cl)_2]$ dimer which is treated with the desired ancillary ligand to yield the target compound.[94–96] However, it is crucial to remove all residual chloride ions by ion exchange and/or precipitation of $Cl^-$ with $Ag^+$,[97,98] as residual chloride ions affect the LEC performance significantly.[99] $[Ir(C^N)_2(N^N)]^+$ complexes show a spatial separation of the HOMO and LUMO where the HOMO lies on the $[Ir(C^N)_2]$ moiety and the LUMO is localized on the N^N ligand. This allows for systematic alteration of the HOMO-LUMO gap and therefore colour tuning of the material.[88] The emitting state often shows a strong MLCT (metal-to-ligand charge transfer) character. Simple complexes of the type $[Ir(ppy)_2(bpy)]^+$ and $[Ir(ppy)_2(phen)]^+$ show yellow electroluminescence in a LEC configuration.[100] Introduction of strongly electron-donating substituents to the N^N ligand leads to a destabilization of the LUMO and, therefore, to a blue shift in emission.[101] Another way to reach bluer emission is to stabilize the HOMO. This can be done either by

introducing electron-withdrawing groups such as fluorine[102,103] or methylsulfonyl groups[104] to the C^N ligand, or by using nitrogen rich heterocycles as C^N ligands.[105,106] In a similar manner, the emission can be pushed to the red by either using more electron-donating substituents such as aryl-silyl groups[107] on the C^N ligand or electron-withdrawing substituents such as ester groups on the N^N ligand[108]. Alternatively, extension of the aromatic system on the N^N yields the same effect by stabilizing the LUMO level of the complex.[109,110] Introduction of large aromatic moieties can also lead to inter-ligand π-stacking interaction. This stabilizing effect showed a positive influence on the device lifetime.[111,112] Although iridium LECs generally show respectable luminance and occasionally impressive device lifetimes, reasonably fast turn-on times are often difficult to achieve. To tackle this, ionic liquids are used to enhance ion mobility and facilitate faster double layer formation.[82,113]

Iridium complexes are already in use in commercial OLED devices,[114,115] but they still possess one inherent disadvantage. Iridium is one of the rarest elements on earth. In the earth's crust there are only about 2 parts per billion of iridium present.[116] This results in the tremendous price of 47'580 US$ per kg as of the end of 2019.[117] Iridium is also used in the fabrication of extremely hard and durable alloys,[116] which is a potential competitor for the OLED and LEC industry. This shows clearly that more abundant and therefore sustainable base-materials are needed for large area lighting applications.

### *1.4.5 The rise of copper*

A cheaper and more abundant base material compared to iridium is copper. The Earth's crust contains about 68 ppm copper,[118] which is more than four orders of magnitude higher than iridium. This results in a relatively low price of 5.87 US$ per kg (2019).[119] Metallic copper has a low resistance and because of this property it is one of the most widely used materials in the electronics industry. This demand led to the development of a huge copper mining and recycling industry,[120] so the supply of this metal is secured for many decades to come. Cationic copper(I) complexes of the type $[Cu(N^N)_2]^+$ were studied intensively by McMillin in the 1970s and 1980s.[121–123] He elucidated structural features such as the tetrahedral geometry of the complexes and their emissive luminescent properties. Theses complexes showed intense absorption bands in the UV region, attributed to ligand-centred states and lower intensity absorption bands in the visible region. Investigation confirmed the MLCT nature of these excited states. Excitation in the MLCT level triggered an emission. It was demonstrated that the preservation of the tetrahedral geometry was crucial for this emission. Due to the formal oxidation of the copper centre to copper(II) in the excited state, the complex would undergo a flattening of the tetrahedral geometry, leaving the copper centre accessible to solvent molecules, which enabled vibrational quenching. Although these homoleptic copper complexes were emissive, they were never incorporated in a LEC architecture. Later work of McMillin demonstrated a new class of copper complexes. Instead of using two diimine ligands, one N^N type ligand was used in combination with phosphanes. In early investigations he demonstrated emission from a low lying MLCT state in frozen glass matrix of $[Cu(bpy)(PPh_3)_2]^+$.[124] Later studies widened the field of investigation to other diimine and phosphane ligands.[125,126] The use of chelating di-phosphane ligands boosted the emissive properties to higher luminescence quantum yields and longer excited state lifetimes. Complexes of the type [Cu(N^N)(P^P)][X] usually feature intense absorption bands below

350 nm arising from ligand centred π*←π and π*←σ transitions and MLCT absorption bands around 350–450 nm making them often appear yellow to orange-red in solution and in the solid state.[127–130] The copper centre adopts a distorted tetrahedral geometry. After excitation into an MLCT level, these complexes show emissions ranging from green to red, depending on the ligand's nature. Because an MLCT excitation equals a formal copper(I) oxidation, the complexes tend to adopt a flattened geometry similar to the previously discussed $[Cu(N^N)_2]^+$ complexes. Flattening enables nonradiative quenching of the excited state either through access of quenching molecules such as solvent or through enabling non-radiative decay pathways. To prevent this, sterically demanding groups need to be introduced around the copper centre, to avoid a flattening motion and protect the copper centre from solvent access. In this sense, chelating phosphane ligands with wide bite angles have been shown to protect the coordination sphere successfully.[131–133] In most cases, aryl-substituted phosphanes are used because of their relatively high stability against oxidation and established preparation methods.[131,134,135] Substituents on the N^N ligand can additionally stabilize the geometry although the steric bulk needs to be adjusted carefully. A too-crowded environment often prevents a successful complex formation or leads to ligand redistribution. Preventing this redistribution is one of the major challenges when preparing these complexes and can result in a mixture of $[Cu(N^N)(P^P)]^+$, $[Cu(N^N)_2]^+$ and $[Cu(P^P)_2]^+$ complexes.[49]

It has been demonstrated that these complexes often show thermally activated delayed fluorescence (**Figure 1.7**). Upon excitation the molecule is excited into its singlet excited state $S_1$. This state is generally short lived and in some cases radiative decay in the form of fluorescence (FL) can occurs. Alternatively, a fast inter-system crossing (ISC, enabled by spin orbit coupling due to the presence of copper) occurs and the molecule ends up in its triplet excited state $T_1$. From this long lived $T_1$ state the molecule can relax to its ground state by emission of light (phosphorescence, PH). If the energy difference ΔE between $S_1$ and $T_1$ is sufficiently small, a reverse inter-system crossing (RISC) can occur. This means the $S_1$ state is thermally repopulated from the $T_1$ state at room temperature, leading to a thermally activated delayed fluorescence (TADF).[136–139] This is a beneficial feature for lighting devices. When electrons and holes recombine, the nature of the excited states form according to spin-statistics. This means 25% of exciton form as singlet, 75% as triplet states. TADF enables harvesting of all spin states, leading to a theoretically possible IQE of 100%.[44,45]

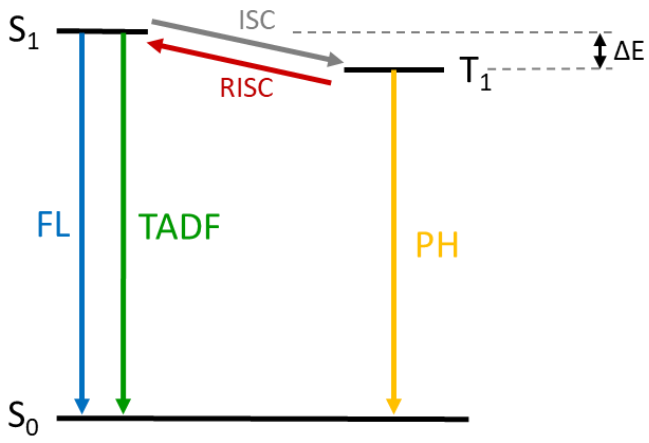


***Figure 1.7*** *Schematic illustration of possible luminescence mechanisms.*[137]

Two methods of complex preparation have been established.[83,84,127–129] In both cases $[Cu(MeCN)_4][X]$ salts are used as precursor complexes. These materials are easily prepared from copper(I) oxide by treatment with inorganic acids such as $HPF_6$ or $HBF_4$ in acetonitrile (**Scheme 1.1**). The ligands are added to a $[Cu(MeCN)_4]^+$ solution in parallel or sequentially. In the case of a sequential addition the phosphane ligand is added first, sometimes in a slight excess. This is only suitable for ligands that are known to not form a stable homoleptic $[Cu(P\hat{}P)_2]^+$ complex, such as DPEPhos. In this particular case, a tridentate complex of the type $[Cu(P\hat{}P)(P\hat{}P)']^+$ forms instead.[140,141] Upon addition of the diimine ligand, the non-chelating P^P ligand is exchanged and a heteroleptic complex is formed. In cases when both ligands show similar affinity to copper, a sequential addition is not necessary and both ligands can be added at the same time. The complex formation can even be carried out under air, provided the ligands possess a reasonable stability to oxygen. Complex formation is completed within minutes to hours. Purification can often be carried out by precipitation or crystallization in suitable solvents. This synthetic approach has the advantage of being easy, straight forward and chlorine free, which lowers the risk of carrying through chloride ions that could later disturb LEC performance (see chapter 1.4.4).

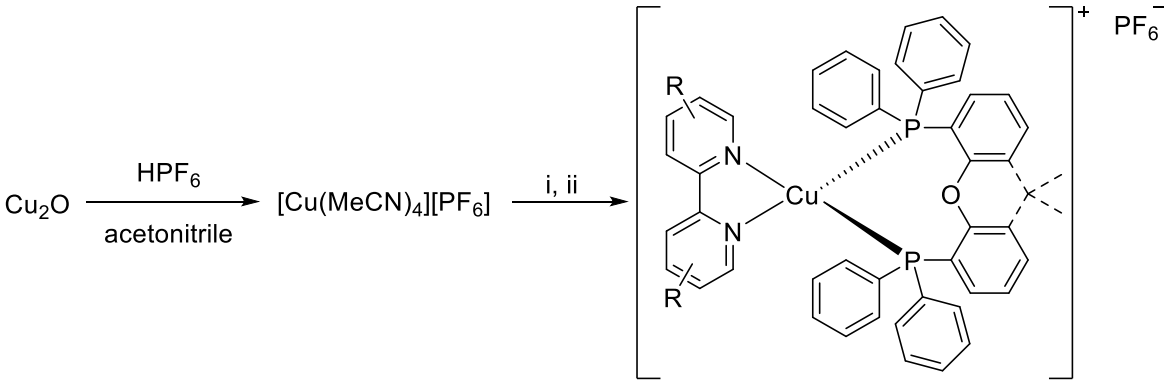


***Scheme 1.1*** *Synthetic preparation of heteroleptic copper(I) complexes, by either (i) stepwise addition of the P^P ligand followed by addition of the N^N ligand after some time, or (ii) simultaneous addition of N^N and P^P ligands.*

Heteroleptic complexes of the type $[Cu(N\hat{}N)(P\hat{}P)]^+$ have seen some unconventional applications in the recent past. Sauvage *et al.* used the complex scaffold to prepare multiple rotaxanes and pseudorotaxanes. They used phenanthroline with a cyclized glycol chain to create a macrocycle in which they were able to embed a diphosphane ligand. Absorption and emission spectra were recorded to confirm the formation of the desired complexes.[142,143] Besides such exotic applications luminescent copper(I) complexes are widely used in homogeneous catalysis as photosensitizers. Karnal *et al.* investigated the applicability of these complexes for water reduction,[144,145] especially in combination with large π-systems.[146,147] Other researchers used copper(I) complexes as photosensitizers in $CO_2$ reduction[148,149] or reductive cyclization reactions.[150,151] The first application of a luminescent copper complex in a lighting device was reported by Fu *et al.* in 2005. They used a linear dinuclear copper(I) complex in an OLED configuration.[152] The first LEC based on a mononuclear heteroleptic copper complex was presented by Armaroli *et al.* in 2006.[153] After this discovery the research field gained in popularity and today many groups are working on the optimization of copper complexes and LECs. One of the most significant studies in recent years was presented by Costa *et al.*[154] They investigated the

electronic influence of different 2,2'-bipyridine ligands in [Cu(4,4'-$R_2$-bpy)(xantphos)][$BF_4$] complexes by introducing substituents with different σ-Hammett parameters – different σ-donation abilities – in the 4,4'-positions of the bpy ligand. By doing so, they were able to alter the energy level of the LUMO, which calculations showed was localized on the bpy ligand. It was shown that more electron-donating substituents increased the HOMO-LUMO gap and shifted the emission maximum to higher energies. Even more important, they were able to demonstrate a linear relationship between the electron-donation ability of the substituent and the luminance and efficacy of the LEC device. However, since the used bpy ligands did not carry any substituents in the 6-position, stabilization of the tetrahedral geometry was not sufficient and device performance was therefore poor. Keller *et al.* have shown the positive effect of substitutions in these positions. Introduction of methyl groups in the 6-position led to higher quantum yields and longer excited state lifetimes of [Cu(N^N)(DPEPhos)][$PF_6$] complexes. When N^N was 6-methyl-2,2'-bipyridine the complex showed a respectable solid state quantum yield of 9.5% and with 6,6'-methyl-2,2'-bipyridine it increased to 43.2%.[129] However, a later study found that just increasing the steric bulk on the bpy side does not necessarily led to better performance. Introduction of a phenyl group in the 6-position of a [Cu(N^N)(P^P)][$PF_6$] complex decreased the quantum yield. This demonstrated that careful tuning of the coordination sphere around the copper is needed to tailor highly luminescent materials. The same study also showed another interesting feature: Highly luminescent materials did not necessarily lead to good LEC performance. The complex [Cu(6,6'-$Me_2$bpy)(xantphos)][$PF_6$] with a high PLQY of 37% in the solid state gave the highest light output (145 cd $m^{-2}$), but these devices had by far the lowest lifetime of only 0.8 h. Other devices with more moderate light outputs proved to be more stable.[84] This indicates that there are many more factors to take into account than just luminescence output when designing molecules for lighting applications. Electrochemical stability does certainly play an important role as well. Besides this, other factors also need to be carefully optimized during device fabrication, for example Bolink *et al.* found that a ratio of iTMC to IL of 4:1 was optimal for LEC performance and showed a good balance of turn-on time and lifetime in iridium iTMC-LECs.[100] But other factors, such as device thickness and driving modes (see chapter 1.4.1) also play a crucial role.

In recent years, the development of blue emitting copper complexes has become of major interest to the science community. An early attempt was presented by Costa *et al.* They prepared copper(I) complexes where the N^N ligand was imipy (3-(2-methoxyphenyl)-1-(pyridine-2-yl)imidazo[1,5-*a*]pyridine) in combination with DPEPhos as P^P ligand. The complex showed blue photoluminescence in the solid state and excellent redox stability. But upon incorporation of the material into a LEC device, the electroluminescence spectra showed a yellow emission. Further investigation led to the conclusion that the observed photoluminescence arose from a ligand centred singlet excited state and was therefore fluorescence. The electroluminescence emission arouse from a lower lying triplet state. The lack of any TADF due to a large energy difference between the $S_1$ and $T_1$ state prevented a RISC and led to these unexpected results.[155] In 2016, the same group presented a successful attempt to prepare blue copper LECs based on N-heterocyclic carbene ligands.[156] Later studies attempted to optimize these structures since degradation in common solvents can occur and therefore careful ligand tuning is necessary.[157,158]

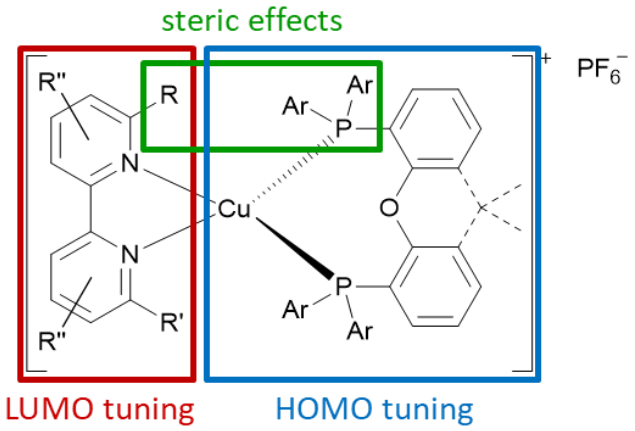


***Figure 1.8*** *Schematic representation of a [Cu(N^N)(P^P)][PF$_6$] complex and outlines for systematic variations.*

Copper complexes of the type [Cu(N^N)(P^P)][PF$_6$] provide an ideal scaffold for systematic investigation of structural properties of different substituents and their influence on the photophysical behaviour and device performance (**Figure 1.8**). Calculations have shown that the HOMO is mainly localized on the copper atom and partly on the P^P ligand, while the LUMO is localized on the N^N ligand.[83,84,127] This allows for systematic variation of these levels independently. At the same time the steric bulk around the copper centre has a major influence on the luminescence properties. In this thesis we present a systematic approach to alter the HOMO and LUMO levels separately and attempt to enhance device performance by increasing the steric bulk of both ligands.

# Chapter 2: Nitrogen ligand tuning - Introducing sterically demanding aryl substituents

## 2.1 Motivation

The content of this chapter from section 2.2 onwards was reproduced from Reference 159 with permission from the Royal Society of Chemistry.

As discussed above, stabilization of the tetrahedral geometry of the copper centre is crucial for the stability and photophysical behaviour of [Cu(N^N)(P^P)][$PF_6$] type complexes. Keller *et al.* studied the influence of various alkyl groups in the 6-position of the bpy ligand and found, that substituents larger than methyl groups, such as ethyl groups yield enhanced device performance. They also demonstrated that the 6-position could host large substituents such as a phenyl group. This introduced interesting structural properties because of the asymmetric nature of the $[Cu(N^N)(P^P)]^+$ complex. In solution two conformers were observed, one where the phenyl substituent was located beneath the xanthene bowl and a second one where it was opposite of the P^P ligand. The two conformers could be interconverted by inversion of the xanthene unit. This was confirmed by the observation of EXSY signals between the inequivalent methyl groups on the xanthene backbone and the significant change in magnetic environment for proton A6 (**Figure 2.1**). The device performance however, was poor compared to complexes with alkyl substituents in the 6-position of the 2,2'-bipyridine ligand.[84]

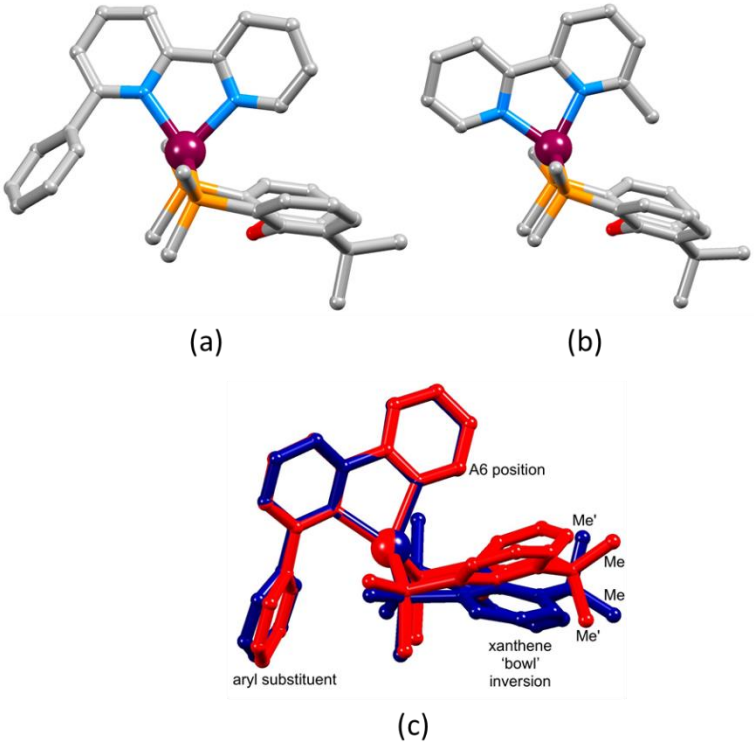


***Figure 2.1*** *Structures of (a) [Cu(Phbpy)(xantphos)]$^+$ and (b) [Cu(Mebpy)(xantphos)]$^+$ (c) Overlay of the structures of two conformers of [Cu(Phbpy)(xantphos)]$^+$ which are related by inversion of the xanthene unit. Only the ipso-C atoms of each $PPh_2$ phenyl rings are shown and H atoms are omitted. The relevance of the 'A6 position' and the positions of the methyl groups (Me and Me') are discussed later. Data for the figure are from reference* 84.

The aim of this project was to introduce large sterically demanding aryl substituents such as naphthyl or pyrenyl in the 6-position of a 2,2'-bipyridine ligand and to investigate their dynamic behaviour in solution as well as their effect on the solid-state structure in [Cu(N^N)(P^P)][$PF_6$] complexes (**Scheme 2.1**). Bünzli *et al.* have investigated the photophysical behaviour of [Ir(C^N)$_2$(N^N)][$PF_6$] compounds (C^N = cyclometallating ligand and N^N = derivative of 2,2'-bipyridine) that carried a remote naphthyl functionalization on the C^N ligands. They found that the introduction of this functionalization did not significantly alter the emissive behaviour or device operation when the compound was incorporated into the emissive layer of a LEC.[160] Therefore, we did not expect a significant influence on the photophysical behaviour of copper complexes carrying a naphthyl functionalization. However, introduction of a pyrenyl group was expected to alter the emissive behaviour of a [Cu(N^N)(P^P)][$PF_6$] type complex significantly because of a low lying, non-emissive triplet excited state of the pyrenyl moiety.[161] The synthesis, structural, electrochemical and photophysical properties of six copper(I) complexes are presented in this chapter.

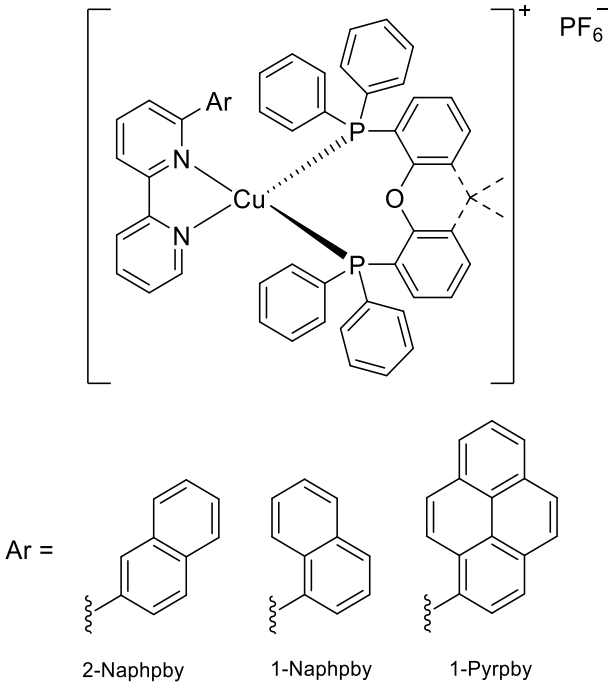


***Scheme 2.1*** *Chemical structures of [Cu(N^N)(P^P)][$PF_6$] complexes with large aromatic moieties in the 6-position of the 2,2'-bipyridine ligand.*

## 2.2 Synthesis

### *2.2.1 Ligand synthesis*

The ligand 2-Naphbpy has been reported previousely.[162,163] However, we found that the palladium-catalysed coupling of 6-bromo-2,2'-bipyridine with 2-naphthaleneboronic acid (using the second generation Suzuki-Miyaura precatalyst SPhosPd G2) was a more convenient synthetic strategy than the methods reported in literature. An analogous procedure was used to prepare 2-Naphbpy and 1-Pyrbpy. Each ligand was characterized by $^1$H and $^{13}$C{$^1$H} NMR spectroscopy and mass spectrometry (see experimental section 2.6).

### *2.2.2 Copper complex synthesis*

Two different strategies are typically used to prepare the heteroleptic complexes [Cu(N^N)(P^P)][$PF_6$] (P^P = DPEPhos or xantphos). The addition of DPEPhos to a solution of [Cu(MeCN)$_4$][$PF_6$] leads to the formation of three-coordinate complexes [Cu(DPEPhos)(MeCN)]$^+$ or [Cu(DPEPhos-*P,P'*)(DPEPhos-*P*)]$^+$.[141] The steric demands of DPEPhos prevent the formation of the four-coordinate [Cu(DPEPhos-*P,P'*)$_2$]$^+$. The monodentate ligand in the three-coordinate intermediate is readily substituted by an N^N ligand such as bpy.[164] With the less sterically demanding ligand xantphos, the formation of a homoleptic bis-chelate complex [Cu(xantphos-*P,P'*)$_2$]$^+$ is more likely. The optimized strategy for [Cu(N^N)(DPEPhos)][$PF_6$] complexes is sequential addition of 1–1.2 equivalents of DPEPhos followed by a bpy ligand after ≈2 hours to a solution of [Cu(MeCN)$_4$][$PF_6$]. For [Cu(N^N)(xantphos)][$PF_6$], a 1:1 solution of N^N and xantphos is added to a solution of [Cu(MeCN)$_4$][$PF_6$]. Immediately after mixing, the solution may appear red, indicating the presence of some [Cu(N^N)$_2$]$^+$ complex. However, after stirring for 2 hours, equilibration yields yellow [Cu(N^N)(xantphos)]$^+$ as the preferred species in solution.

The complexes [Cu(1-Naphbpy)(DPEPhos)][$PF_6$], [Cu(2-Naphbpy)(DPEPhos)][$PF_6$], [Cu(1-Pyrbpy)(DPEPhos)][$PF_6$], [Cu(1-Naphbpy)(xantphos)][$PF_6$], [Cu(2-Naphbpy)(xantphos)][$PF_6$] and [Cu(1-Pyrbpy)(xantphos)][$PF_6$] were isolated as yellow solids in yields of between 38% and 98%. The electrospray mass spectrum of each complex showed a peak corresponding to [M–$PF_6$]$^+$ with a characteristic isotope pattern. The presence of the [$PF_6$]$^-$ counterion was confirmed by the appearance of a septet at $\delta$ −144.4 ppm in the $^{31}P\{^1H\}$ NMR spectrum, in addition to the signals for the DPEPhos or xantphos ligands.

## 2.3 Structural Discussion

### *2.3.1 Single crystal structures*

Single crystals of [Cu(1-Naphbpy)(DPEPhos)][$PF_6$]·0.25THF, [Cu(2-Naphbpy)(DPEPhos)][$PF_6$]·$Me_2CO$, [Cu(1-Pyrbpy)(DPEPhos)][$PF_6$]·0.5$Et_2O$·$CH_2Cl_2$, [Cu(2-Naphbpy)(xantphos)][$PF_6$] and [Cu(1-Pyrbpy)(xantphos)][$PF_6$]·0.5$Et_2O$ were grown by diffusion of $Et_2O$ into solutions of the complexes in THF ([Cu(1-Naphbpy)(DPEPhos)][$PF_6$]), $Me_2CO$ ([Cu(2-Naphbpy)(DPEPhos)][$PF_6$]) or $CH_2Cl_2$ (the remaining complexes). The structures exhibit many similarities and it is appropriate to discuss them in a comparative manner. **Figure 2.5** - **Figure 2.9** show the structures of the [Cu(1-Naphbpy)(DPEPhos)]$^+$, [Cu(2-Naphbpy)(DPEPhos)]$^+$, [Cu(2-Naphbpy)(xantphos)]$^+$, [Cu(1-Pyrbpy)(DPEPhos)]$^+$ and [Cu(1-Pyrbpy)(xantphos)]$^+$ cations, respectively, and parameters describing the copper(I) coordination environments are given in the figure captions. In each complex, the copper(I) atom is in a distorted tetrahedral environment with Cu–P and Cu–N bond lengths in the ranges 2.2453(10)–2.3101(11) and 2.085(4)–2.143(3) Å, respectively. The P–Cu–P angles fall in the range 109.97(3)–116.83(4)°, the largest being for the [Cu(2-Naphbpy)(xantphos)]$^+$ cation. As expected, the N–Cu–N bond angles vary little across the series (79.16(14)–

79.88(13)°). The asymmetry of the 6-substituted bpy ligand means that there are two possible orientations of the N^N ligand with respect to the P^P ligand, one with the 6-substituent lying over the 'xanthene bowl' and one with it positioned remotely from the bowl as shown in **Figure 2.1**. The two orientations are related by a 180° rotation of the bpy unit. Keller *et al.* have previously reported the solid-state structures of [Cu(6-Mebpy)(xantphos)]$^+$ and [Cu(6-Etbpy)(xantphos)]$^+$ in which the 6-alkyl substituent lies over the 'bowl' of the xanthene unit (**Figure 2.1b**); in contrast, the 6-phenyl substituent in [Cu(6-Phbpy)(xantphos)]$^+$ is remote from the xanthene 'bowl' (**Figure 2.1a**).[84] Each of the cations shown in **Figure 2.5** - **Figure 2.9** exhibits the same N^N ligand orientation with the sterically-demanding naphthyl or pyrenyl group positioned away from the $(C_6H_4)_2O$ unit of DPEPhos or the xanthene 'bowl' of xantphos (**Figure 2.2a**). We return to this point in the NMR spectroscopic discussion.

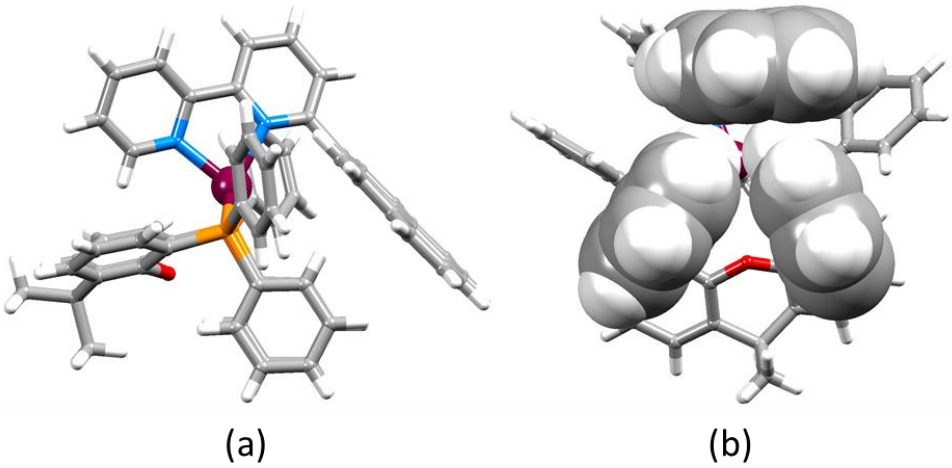


***Figure 2.2*** *(a) The [Cu(1-Pyrbpy)(xantphos)]$^+$ cation showing the orientation of the 1-pyrenyl substituent (right) remote from the xanthene 'bowl' (left). (b) Edge-to-face positioning of the two phenyl rings of xantphos and the naphthyl unit in [Cu(2-Naphbpy)(xantphos)]$^+$.*

The interannular twist within the bpy unit varies significantly across the series of structures with the angle between the planes through the pyridine rings ranging from 5.8 to 26.0° (**Table 2.1**). This twist is coupled with the orientation of the pendant aryl unit with respect to the phenyl substituents of the DPEPhos or xantphos ligand. In [Cu(1-Pyrbpy)(xantphos)]$^+$ and [Cu(2-Naphbpy)(xantphos)]$^+$, one phenyl ring of each $PPh_2$ group engages in an edge-to-face interaction with the pyrenyl or naphthyl group (**Figure 2.2**). The closest CH...π contacts[165] (measured to the centroid of the closest $C_6$ ring) are 2.75 Å in [Cu(2-Naphbpy)(xantphos)]$^+$ and 2.45 and 2.58 Å in [Cu(1-Pyrbpy)(xantphos)]$^+$. Each DPEPhos-containing complex exhibits face-to-face π-stacking between one arene ring of the $(C_6H_4)_2O$ unit and one phenyl ring (**Figure 2.3**). In [Cu(1-Naphbpy)(DPEPhos)]$^+$ (**Figure 2.3a**), this interaction is characterized by an angle between ring planes, centroid...centroid distance, and centroid...plane separation of 12.0°, 3.56 Å and 3.53 Å. The angles between the ring planes in [Cu(1-Pyrbpy)(DPEPhos)]$^+$ and [Cu(2-Naphbpy)(DPEPhos)]$^+$ are, however, 26.0 and 23.4°, respectively. This deviation from a coplanar orientation is associated with edge-to-face CH...π contacts involving the 6-substituted pyrenyl or naphthyl group (**Figure 2.3b and c**).

Interestingly, intermolecular face-to-face π-contacts play an insignificant role in packing in the solid state. Pyrenyl-units of adjacent cations in [Cu(1-

Pyrbpy)(DPEPhos)][$PF_6$]·0.5$Et_2O$·$CH_2Cl_2$ approach closely (**Figure 2.4**), but the orientation of the two arene moieties is not optimal for efficient stacking. The angle between the least squares planes through the two pyrenyl units is 21.8° and the centroid...centroid separation of the two closest $C_6$-rings is 3.80 Å.

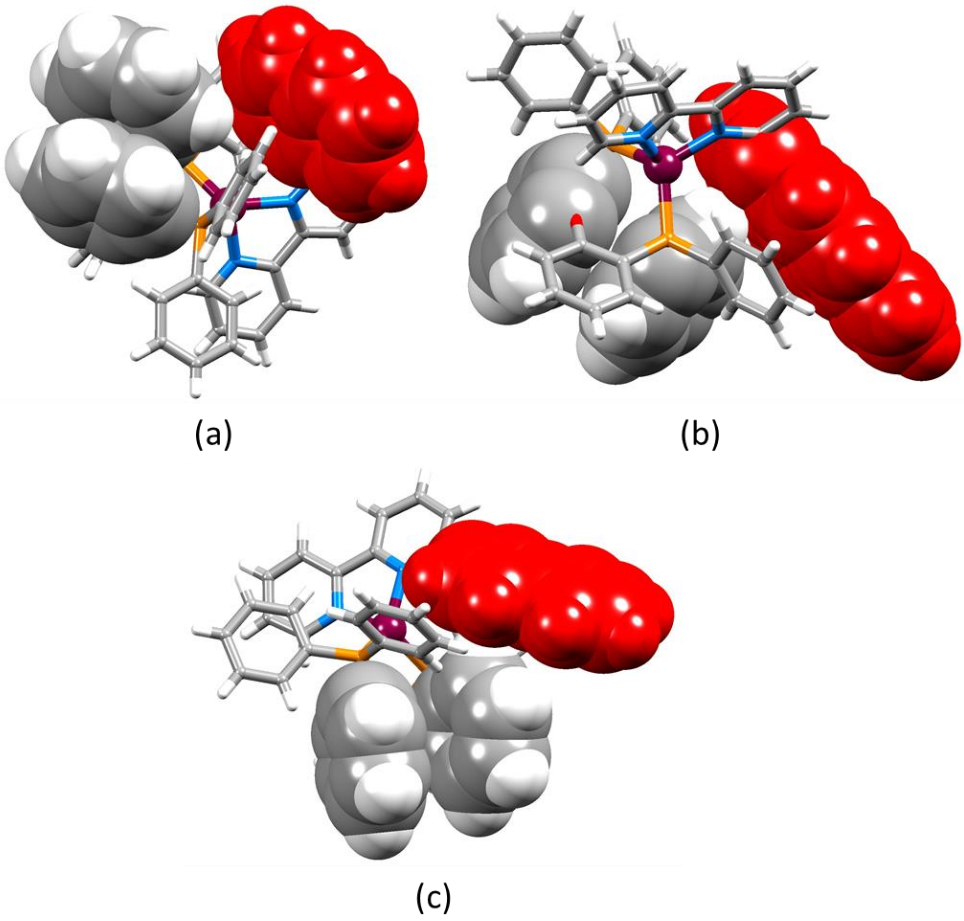


***Figure 2.3*** *Structures of (a) [Cu(1-Naphbpy)(DPEPhos)]⁺, (b) [Cu(1-Pyrbpy)(DPEPhos)]⁺ and (c) [Cu(2-Naphbpy)(DPEPhos)]⁺ showing π-stacking of arene rings within the DPEPhos ligand. The 6-substituted naphthyl or pyrenyl group is shown in red.*

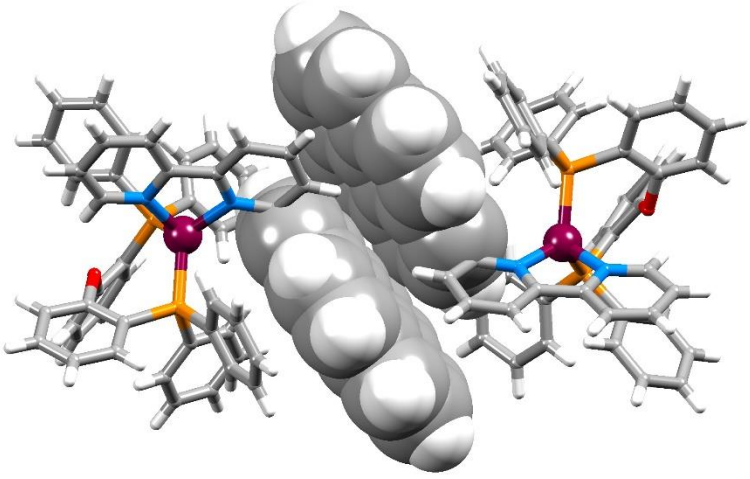

***Figure 2.4*** *Close approach of adjacent pyrenyl-units of adjacent [Cu(1-Pyrbpy)(DPEPhos)]⁺ cations (symmetry codes* x, y, z *and 1*–x, y, *1*–z*).*

***Table 2.1*** *Angular distortions of the N^N ligands in the [Cu(N^N)(P^P)]⁺ cations.*

| Complex cation | Angle between planes of pyridine rings / ° | Angle between plane of pyridine ring and attached arene unit / ° |
|---|---|---|
| [Cu(1-Naphbpy)(DPEPhos)]⁺ | 16.0 | 69.0 |
| [Cu(2-Naphbpy)(DPEPhos)]⁺ | 18.4 | 50.5 |
| [Cu(1-Pyrbpy)(DPEPhos)]⁺ | 5.8 | 66.6 |
| [Cu(2-Naphbpy)(xantphos)]⁺ | 22.8 | 44.0 |
| [Cu(1-Pyrbpy)(xantphos)]⁺ | 26.0 | 60.8 |

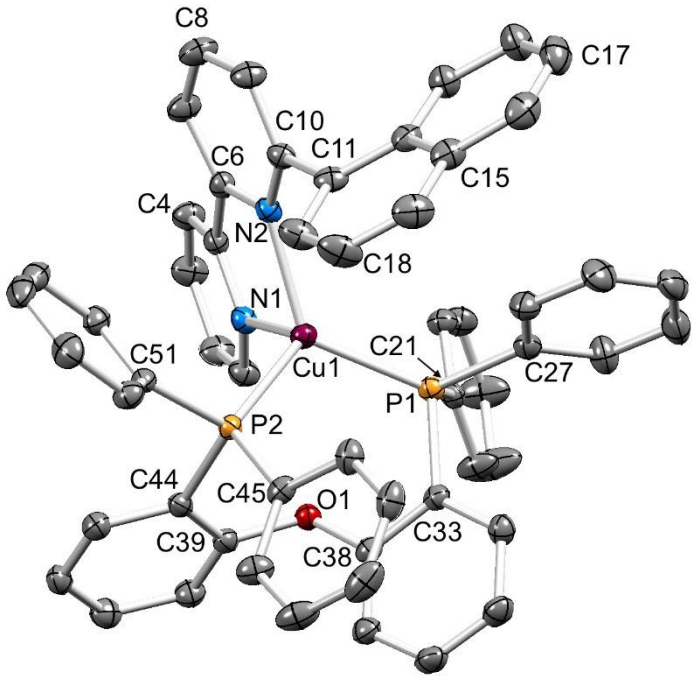


***Figure 2.5*** *Structure of the [Cu(1-Naphbpy)(DPEPhos)]⁺ cation in [Cu(1-Naphbpy)(DPEPhos)][$PF_6$]·0.25THF with ellipsoids plotted at 40% probability level. H atoms and solvent molecules are omitted for clarity. Selected bond parameters: Cu1–P1 = 2.2723(8), Cu1–P2 = 2.2833(8), Cu1–N1 = 2.118(2), Cu1–N2 = 2.111(2) Å; P1–Cu1–P2 = 109.97(3), P1–Cu1–N1 = 106.14(7), P2–Cu1–N1 = 109.85(7), P1–Cu1–N2 = 128.14(7), P2– Cu1–N2 = 116.14(7), N1–Cu1–N2 = 79.68(9)°.*

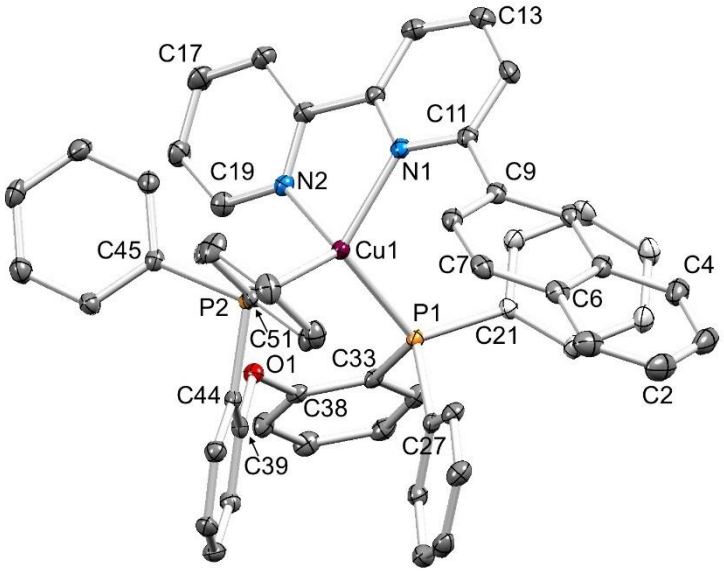


***Figure 2.6*** *Structure of the [Cu(2-Naphbpy)(DPEPhos)]⁺ cation in [Cu(2-Naphbpy)(DPEPhos)][PF₆]·Me₂CO with ellipsoids plotted at 40% probability level. H atoms and solvent molecules are omitted for clarity. Selected bond parameters: Cu1–P1 = 2.2600(8), Cu1–P2 = 2.2716(8), Cu1–N1 = 2.105(2), Cu1–N2 = 2.099(2) Å; P1–Cu1–P2 = 112.01(3), P1–Cu1–N1 = 109.59(6), P2–Cu1–N1 = 131.94(6), P1–Cu1–N2 = 113.42(7), P2–Cu1–N2 = 104.26(7), N1–Cu1–N2 = 79.68(9)°.*

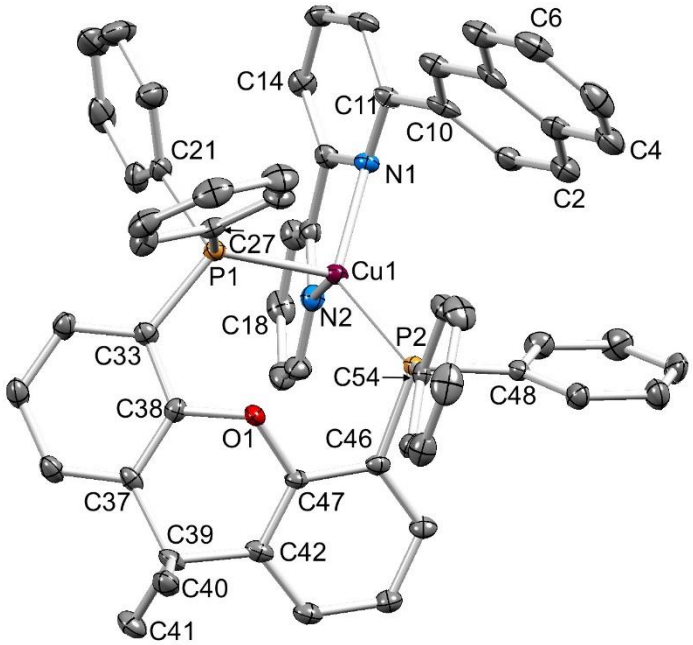


***Figure 2.7*** *Structure of the [Cu(2-Naphbpy)(xantphos)]⁺ cation in [Cu(2-Naphbpy)(xantphos)][PF₆] with ellipsoids plotted at 30% probability level. H atoms omitted for clarity. Selected bond parameters: Cu1–P2 = 2.2453(10), Cu1–P1 = 2.3101(11), Cu1–N2 = 2.085(4), Cu1–N1 = 2.143(3) Å; P2–Cu1–P1 = 116.83(4), P2–Cu1–N2 = 113.47(10), P1–Cu1–N2 = 105.84(10), P2–Cu1–N1 = 130.15(10), P1–Cu1–N1 = 103.74(10), N2–Cu1–N1 = 79.16(14)°.*

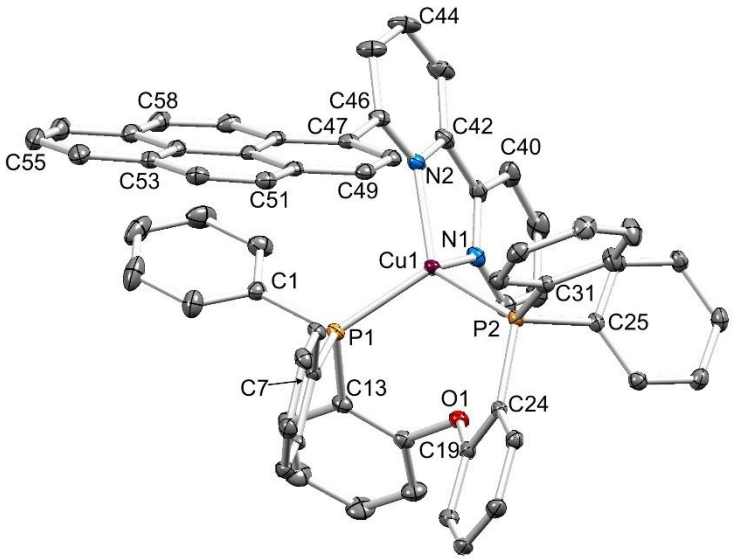


***Figure 2.8*** *Structure of the [Cu(1-Pyrbpy)(DPEPhos)]⁺ cation in [Cu(1-Pyrbpy)(DPEPhos)][PF₆]·0.5Et₂O·CH₂Cl₂ with ellipsoids plotted at 30% probability level. H atoms and solvent molecules omitted for clarity. Selected bond parameters: Cu1–P1 = 2.2543(7), Cu1–P2 = 2.2876(7), Cu1–N1 = 2.098(2), Cu1–N2 = 2.089(2) Å; P1–Cu1–P2 = 112.04(2), P1–Cu1–N1 = 111.02(6), P2–Cu1–N1 = 104.99(6), P1–Cu1–N2 = 114.25(6), P2–Cu1–N2 = 127.85(6), N1–Cu1–N2 = 79.52(8)°.*

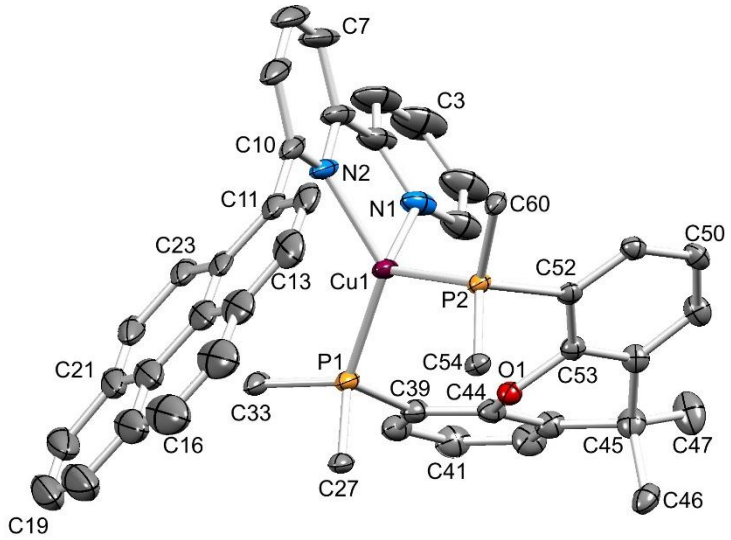


***Figure 2.9*** *Structure of the [Cu(1-Pyrbpy)(xantphos)]⁺ cation in [Cu(1-Pyrbpy)(xantphos)][PF₆]·0.5Et₂O with ellipsoids plotted at 30% probability level. H atoms and solvent molecules omitted for clarity, and only the ipso-C atom of each of the four P-attached phenyl rings is shown. Selected bond parameters: Cu1–P2 = 2.2576(7), Cu1–P1 = 2.2649(8), Cu1–N2 = 2.098(2), Cu1–N1 = 2.104(3) Å; P2–Cu1–P1 = 112.20(3), P2–Cu1–N2 = 110.70(8), P1–Cu1–N2 = 130.64(7), P2–Cu1–N1 = 112.49(8), P1–Cu1–N1 = 104.67(8), N2–Cu1–N1 = 79.88(13)°.*

***Table 2.2*** *Crystallographic parameters of [Cu(N^N)(P^P)][$PF_6$] complexes.*

| Compound | [Cu(1-Naphbpy)(DPEPhos)][$PF_6$]·0.25 THF | [Cu(2-Naphbpy)(DPEPhos)][$PF_6$]·$Me_2CO$ | [Cu(2-Naphbpy)(xantphos)][$PF_6$] | [Cu(1-Pyrbpy)(DPEPhos)][$PF_6$]·0.5$Et_2O$·$CH_2Cl_2$ | [Cu(1-Pyrbpy)(xantphos)][$PF_6$]·0.5$Et_2O$ |
|---|---|---|---|---|---|
| Formula | $C_{57}H_{44}CuF_6N_2O_{1.25}P_3$ | $C_{59}H_{48}CuF_6N_2O_2P_3$ | $C_{59}H_{46}CuF_6N_2OP_3$ | $C_{65}H_{51}Cl_2CuF_6N_2O_{1.5}P_3$ | $C_{67}H_{53}CuF_6N_2O_{1.5}P_3$ |
| Formula weight | 1047.44 | 1087.50 | 1069.48 | 1225.49 | 1180.63 |
| Crystal colour and habit | Yellow block | Yellow block | Yellow plate | Yellow block | Yellow block |
| Crystal system | Orthorhombic | Monoclinic | Monoclinic | Monoclinic | Triclinic |
| Space group | *Pccn* | $P2_1/c$ | *Pn* | *C*2/*m* | *P*–1 |
| *a, b, c* / Å | 22.6154(14)<br>20.0116(12)<br>21.8373(14) | 22.2781(11)<br>14.7143(8)<br>15.4481(7) | 11.4374(8)<br>13.1660(9)<br>16.8565(12) | 23.5648(17)<br>43.959(3)<br>12.3463(9) | 13.0030(9)<br>14.4788(10)<br>16.9143(11) |
| $\alpha, \beta, \gamma$ / ° | 90<br>90<br>90 | 90<br>99.249(3)<br>90 | 90<br>98.647(3)<br>90 | 90<br>94.788(3)<br>90 | 72.110(3)<br>84.932(4)<br>75.976(4) |
| *U* / Å$^3$ | 9882.9(11) | 4998.1(4) | 2509.5(3) | 12744.7(16) | 2939.8(4) |
| *Dc* / Mg m$^{-3}$ | 1.408 | 1.445 | 1.415 | 1.277 | 1.334 |
| *Z* | 8 | 4 | 2 | 8 | 2 |
| $\mu$(Cu-K$\alpha$) / mm$^{-1}$ | 2.103 | 2.112 | 2.079 | 2.464 | 1.834 |
| *T* / K | 123 | 123 | 123 | 123 | 123 |
| Refln. collected ($R_{int}$) | 70584 (0.060) | 52879 (0.055) | 16429 (0.024) | 44681 (0.032) | 39266 (0.030) |
| Unique refln. | 9287 | 9320 | 7635 | 11839 | 10819 |
| Refln. for refinement | 7830 | 7470 | 7511 | 11247 | 9691 |
| Parameters | 645 | 661 | 650 | 257 | 748 |
| Threshold | 2$\sigma$ | 2$\sigma$ | 2$\sigma$ | 2$\sigma$ | 2$\sigma$ |
| *R*1 (*R*1 all data) | 0.0605 (0.0713) | 0.0432 (0.0572) | 0.0472 (0.0476) | 0.0603 (0.0622) | 0.0698 (0.0761) |
| *wR*2 (*wR*2 all data) | 0.1485 (0.1530) | 0.0866 (0.1067) | 0.1120 (0.1121) | 0.1527 (0.1531) | 0.1719 (0.1737) |
| Goodness of fit | 1.0589 | 0.8433 | 0.7142 | 1.0572 | 1.0983 |
| CCDC deposition‡ | 1528552 | 1528550 | 1528551 | 1528548 | 1528549 |

## *2.3.2 NMR spectroscopy and dynamic behaviour*

Acetone-$d_6$ was chosen as the solvent for NMR spectroscopic studies because previous studies revealed that some [Cu(N^N)(P^P)]$^+$ complexes are prone to ligand dissociation in $CD_2Cl_2$ after several days in solution.[84,155] **Figure 2.10** shows the room temperature $^1$H NMR spectra of the six complexes. Although the resonances arising from the bpy domain are sharp in all cases, those from the 6-aryl substituent are only sharp at 298 K for the 2-Naphthyl group. Signals from the DPEPhos and xantphos ligands are broadened in [Cu(2-Naphbpy)(DPEPhos)][$PF_6$] and [Cu(2-Naphbpy)(xantphos)][$PF_6$], and are very broad for the remaining complexes (**Figure 2.10**). NMR spectroscopic characterization of [Cu(2-Naphbpy)(DPEPhos)][$PF_6$] and [Cu(2-Naphbpy)(xantphos)][$PF_6$] was carried out by recording COSY, NOESY, HMBC and HMQC spectra at 298 K. For the remaining complexes, ROESY, TOCSY, HSQC, HMBC and $^1$H-$^{31}$P-HSQC (only for the complexes containing 1-Pyrbpy) spectra were measured at lower temperatures. Use of these 2D methods permitted full assignment of the $^1$H and $^{13}$C{$^1$H} NMR spectra and atom labelling is given in the experimental section 2.6.

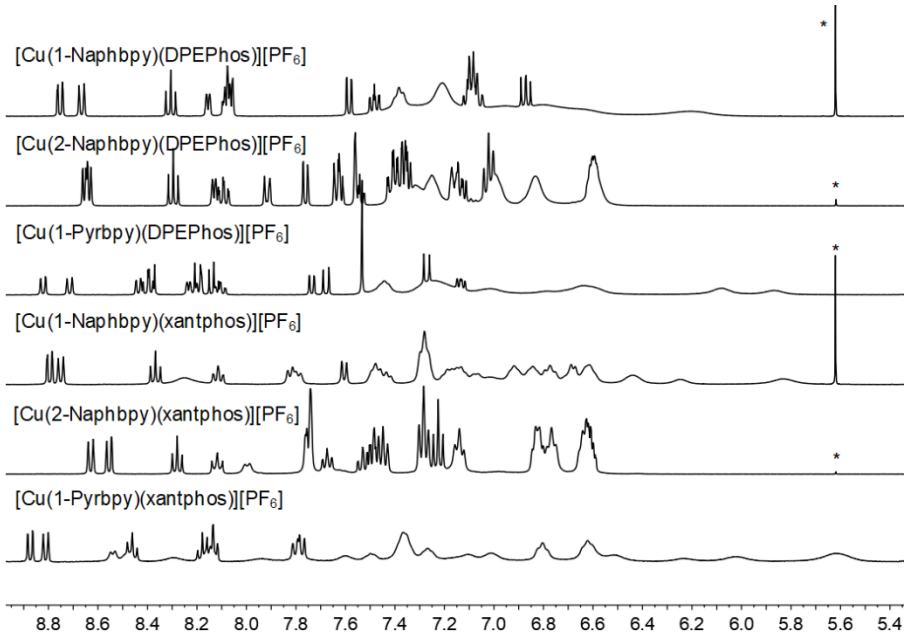


***Figure 2.10*** *Room temperature 400 MHz $^1$H NMR spectra of acetone-$d_6$ solutions of the six complexes. The alkyl regions of the spectra are omitted. * = residual $CH_2Cl_2$. Chemical shifts in δ/ppm.*

In the discussion below, we assume that dynamic behaviour arises from non-dissociative processes[84] and initially consider the three complexes containing DPEPhos. In [Cu(2-Naphbpy)(DPEPhos)][$PF_6$], one set of signals arising from the DPEPhos-backbone ring-C protons (correlating in the HMQC spectrum to one set of $^{13}C\{^1H\}$ NMR signals) is observed at 298 K. This is consistent with the [Cu(2-Naphbpy)(DPEPhos)]$^+$ cation having $C_2$ symmetry. Each $PPh_2$ group of the DPEPhos ligand gives two sets of signals, one each for the phenyl rings (labelled Da and Db) pointing towards or away from the aryl group on the 6-position of the bpy. The conformational flexibility of the 8-membered chelate {CuPCCOCCP}-ring can exchange these positions as confirmed by exchange peaks (EXSY) in the ROESY spectrum between pairs $H^{D2a}/H^{D2b}$,$H^{D3a}/H^{D3b}$ and $H^{D4a}/H^{D4b}$ (**Figure 2.11**). Low temperature $^{13}C\{^1H\}$ and $^1H$ NMR spectra of [Cu(1-Naphbpy)(DPEPhos)][$PF_6$] and [Cu(1-Pyrbpy)(DPEPhos)][$PF_6$] indicated loss of $C_2$ symmetry and as an example, we focus on [Cu(1-Naphbpy)(DPEPhos)][$PF_6$]. Two sets of signals for the C rings of the DPEPhos-backbone are observed (labelled Ca and Cb, see experimental section 2.6.5) along with four sets of signals for the P-bonded phenyl rings (labelled Da, Db, Dc and Dd). The ROESY spectrum (at 253 K) is shown in **Figure 2.12**, and from this, EXSY cross-peaks show the exchange of rings Ca/Cb, Da/Db and Dc/Dd at higher temperatures.

We now turn to the solution dynamic behaviour of [Cu(1-Naphbpy)(xantphos)]$^+$, [Cu(2-Naphbpy)(xantphos)]$^+$ and [Cu(1-Pyrbpy)(xantphos)]$^+$ and **Figure 2.10** shows the room temperature $^1H$ NMR spectra. As observed for the DPEPhos complexes, the spectra for [Cu(1-Naphbpy)(xantphos)][$PF_6$] and [Cu(1-Pyrbpy)(xantphos)][$PF_6$] are very broad at 298 K, indicating dynamic behaviour. **Figure 2.14** shows the effect of cooling an acetone-$d_6$ solution of [Cu(1-Pyrbpy)(xantphos)][$PF_6$]; similar changes are observed for [Cu(1-Naphbpy)(xantphos)][$PF_6$]. The spectra at 238 K (N^N = 1-Pyrbpy) or 223 K (N^N = 1-Naphbpy) were fully assigned using 2D methods (see experimental section 2.6).

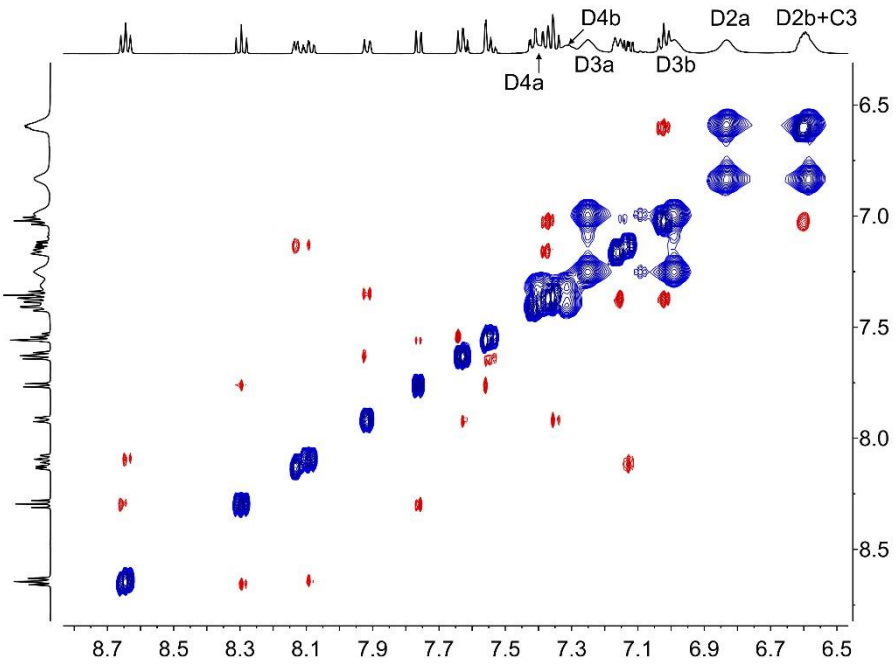


***Figure 2.11*** *400 MHz ROESY spectrum of [Cu(2-Naphbpy)(DPEPhos)][PF$_6$] at 298 K in acetone-d$_6$. Signals in phase with the diagonal (blue) correspond to EXSY peaks and signals with opposite phase relative to the diagonal (red) correspond to NOESY peaks. Chemical shifts in δ/ppm.*

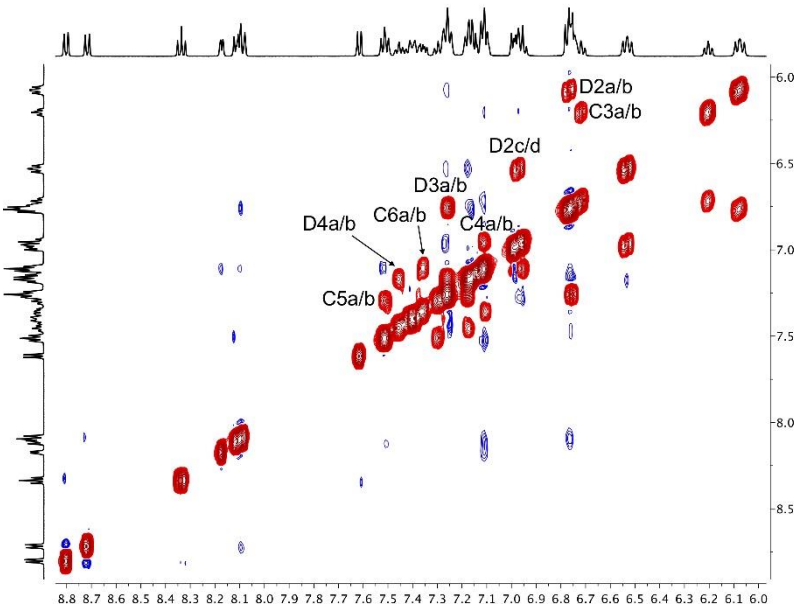


***Figure 2.12*** *500 MHz ROESY spectrum of [Cu(1-Naphbpy)(DPEPhos)][PF$_6$] at 253 K in acetone-d$_6$. Signals in phase with the diagonal (red) correspond to EXSY peaks, and signals with opposite phase relative to the diagonal (blue) correspond to NOESY peaks. Clearly resolved EXSY peaks between pairs of protons on phenyl rings D or DPEPhos-backbone rings C are labelled; EXSY peaks for D3c/d and D3c/d lie close to the diagonal.*

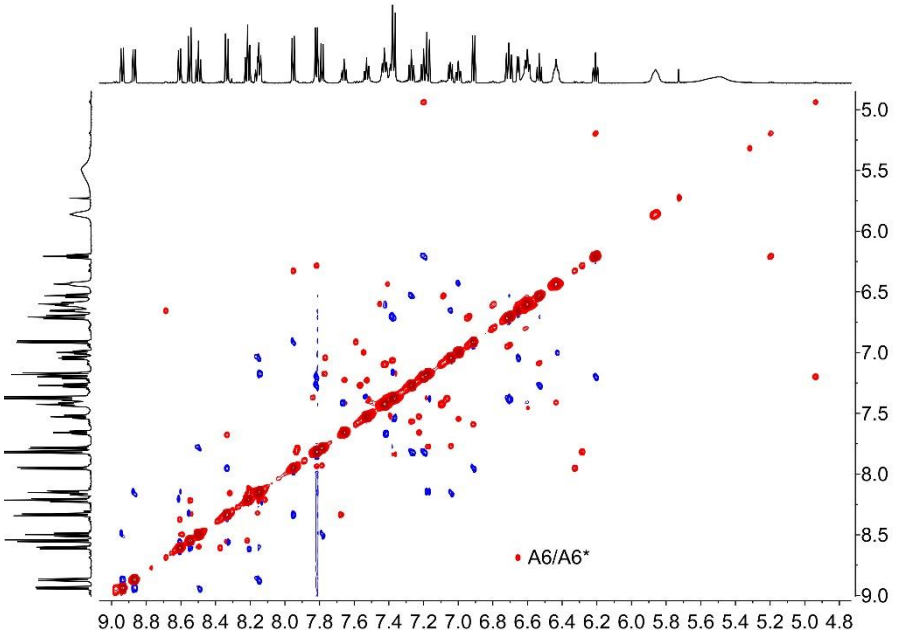


***Figure 2.13*** *600 MHz ROESY spectrum of [Cu(1-Pyrbpy)(xantphos)][$PF_6$] at 238 K in acetone-$d_6$. Signals in phase with the diagonal (red) correspond to EXSY peaks, and signals with opposite phase relative to the diagonal (blue) are NOESY peaks. Full assignment of the spectrum of the major conformer is given in the Experimental Section.*

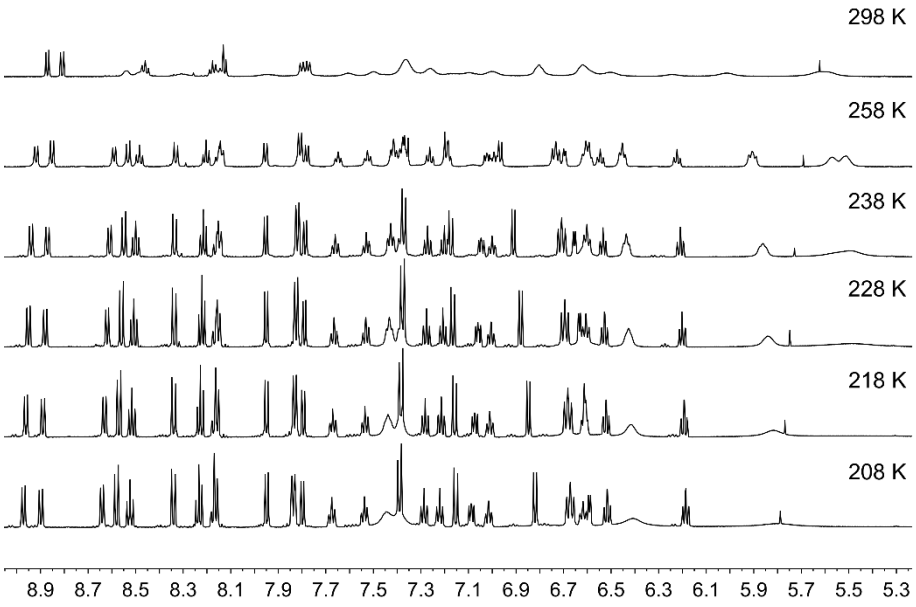


***Figure 2.14*** *Variable temperature 600 MHz $^1$H NMR spectra of an acetone-$d_6$ solution of [Cu(1-Pyr)(xantphos)][$PF_6$]. The alkyl region of the spectrum is omitted. Chemical shifts in δ/ppm.*

Although xantphos is more rigid than DPEPhos, the xanthene 'bowl' may undergo inversion (see for example references 166 and 167). Keller *et al.* previously reported that in solution, [Cu(Phbpy)(xantphos)]$^+$ (Phbpy = 6-phenyl-2,2'-bipyridine) exists as two conformers which are related by the inversion of the xanthene 'bowl' (**Figure 2.1**). The relative population of the conformers of [Cu(Phbpy)(xantphos)]$^+$ in $CD_2Cl_2$ was ~1.0 : 0.9, and the calculated energy difference was 3.57 kcal mol$^{-1}$. The characteristic $^1$H NMR signal distinguishing the two conformers is that for $H^{A6}$ (see experimental section 2.6 and **Figure 2.1c** for labelling) which appeared at $\delta$ 8.42 ppm in one conformer and $\delta$ 6.35 ppm in the

other.[84] In the low temperature $^{1}$H NMR spectra of [Cu(1-Naphbpy)(xantphos)][$PF_6$] and [Cu(1-Pyrbpy)(xantphos)][$PF_6$], a second set of signals with much lower intensity with respect to the dominant peaks (~0.05 : 1.0) was observed. This is shown for [Cu(1-Pyrbpy)(xantphos)][$PF_6$] in **Figure 2.15**. For the major and minor components in the spectrum, the signal for $H^{A6}$ (which exhibits a characteristic coupling constant of ~5 Hz) appears at $\delta$ 6.65 and 8.69 ppm, respectively. These values are similar to those observed in [Cu(Phbpy)(xantphos)][$PF_6$] ($\delta$ 6.35 and 8.42 ppm)[84] (see above) and are consistent with the presence of two conformers of [Cu(1-Pyrbpy)(xantphos)]$^+$ which interconvert through inversion of the xanthene 'bowl'. EXSY cross-peaks observed in the ROESY spectrum (**Figure 2.13**) confirmed an exchange process. As Keller *et al.* discussed in detail[84] for [Cu(Phbpy)(xantphos)]$^+$, the methyl region of the $^{1}$H NMR spectrum is very informative. The boat conformation (**Figure 2.7** and **Figure 2.9**)[84,168] of the xanthene unit forces one methyl group to be in the plane of the xantphos ligand backbone, whereas the second methyl is out-of-plane. This is clear in the projection of the [Cu(1-Pyrbpy)(xantphos)]$^+$ cation in **Figure 2.2**. Interconversion of the conformers (**Figure 2.1c**) places the two methyl groups in different magnetic environments. In the dominant conformer, signals for the two Me groups are at $\delta$ 2.03 and 1.28 ppm, whereas in the second conformer, the corresponding resonances are $\delta$ 1.14 and 1.87 ppm, EXSY cross-peaks ($\delta$ 1.14 with 2.03 ppm, and $\delta$ 1.87 with 1.28 ppm) confirmed exchange. These observations are consistent with those described for [Cu(Phbpy)(xantphos)][$PF_6$].[84] The significantly different populations of the conformers in the case of [Cu(Phbpy)(xantphos)][$PF_6$] (~1.0 : 0.9) versus [Cu(1-Pyrbpy)(xantphos)][$PF_6$] (~0.05 : 1.0) is consistent with the sterically more demanding pyrenyl group.

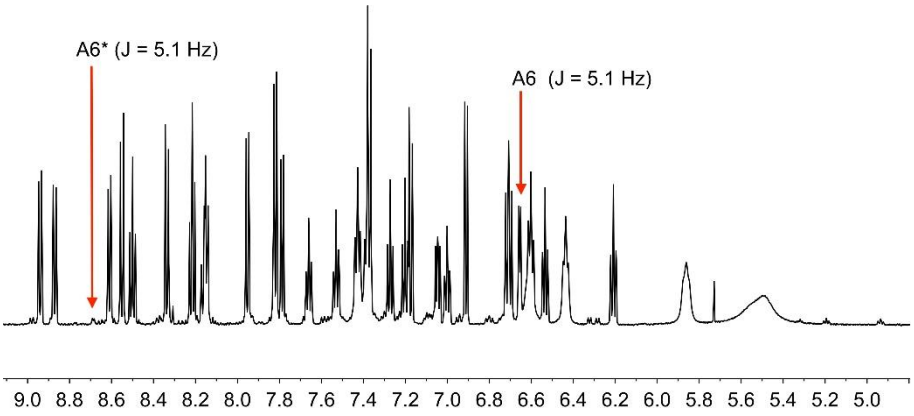


***Figure 2.15*** *Part of the solution 600 MHz $^{1}$H NMR spectrum of [Cu(1-Pyrbpy)(xantphos)][$PF_6$] (acetone-$d_6$) at 238 K. Chemical shifts in δ/ppm.*

The room temperature $^{31}P\{^{1}H\}$ spectra of [Cu(2-Naphbpy)(DPEPhos)][$PF_6$] and [Cu(2-Naphbpy)(xantphos)][$PF_6$] show broad signals at $\delta$ –13.4 and –12.8 ppm, respectively. A similar broad signal at $\delta$ –14.5 ppm is observed for [Cu(1-Pyrbpy)(DPEPhos)][$PF_6$] at 238 K. In contrast, [Cu(1-Pyrbpy)(xantphos)][$PF_6$] shows two doublets at 238 K ($^{2}J_{PP}$ = 95 Hz) at $\delta$ –10.9 and –13.5 ppm. A similar pattern is observed in the low temperature spectrum of [Cu(1-Naphbpy)(xantphos)][$PF_6$] ($^{2}J_{PP}$ = 110 Hz). Two $^{31}P\{^{1}H\}$ NMR signals ($\delta$ –12.7 and –15.5 ppm) are observed for [Cu(1-Naphbpy)(DPEPhos)][$PF_6$] at 253 K, but the coupling could not be resolved. These observations are consistent with desymmetrization of the P^P ligand on the $^{1}$H NMR time-scale at low temperatures.

# 2.4 Electrochemical and photophysical properties

## *2.4.1 Electrochemistry*

The [Cu(N^N)(P^P)][$PF_6$] complexes are redox-active and cyclic voltammetry was used to investigate the processes. Each complex undergoes a reversible copper-centred oxidation (**Table 2.3**), and the $E_{1/2}^{ox}$ values are similar to those of +0.82 and +0.81 V reported for [Cu(6,6'-$Me_2$bpy)(DPEPhos)][$BF_4$] and [Cu(6,6'-$Me_2$bpy)(xantphos)][$BF_4$] (MeCN solution, *vs.* $Fc/Fc^+$).[169] For each compound, reduction processes within the solvent accessible window were very poorly defined.

***Table 2.3*** *Cyclic voltammetric data for [Cu(N^N)(P^P)][$PF_6$] complexes referenced to internal $Fc/Fc^+$ = 0 V; $CH_2Cl_2$ (freshly distilled) solutions with [$^nBu_4N$][$PF_6$] as supporting electrolyte and scan rate of 0.1 V $s^{-1}$.*

| Complex cation | $E_{1/2}^{ox}$ / V ($E_{pc} - E_{pa}$ / mV) |
|---|---|
| [Cu(1-Naphbpy)(DPEPhos)]$^+$ | +0.79 (97) |
| [Cu(1-Naphbpy)(xantphos)]$^+$ | +0.82 (101) |
| [Cu(2-Naphbpy)(DPEPhos)]$^+$ | +0.77 (96) |
| [Cu(2-Naphbpy)(xantphos)]$^+$ | +0.81 (101) |
| [Cu(1-Pyrbpy)(DPEPhos)]$^+$ | +0.77 (99) |
| [Cu(1-Pyrbpy)(xantphos)]$^+$ | +0.82 (88) |

## *2.4.2 Solution absorption and emission properties*

The solution absorption spectra of [Cu(N^N)(xantphos)][$PF_6$] and [Cu(N^N)(DPEPhos)][$PF_6$] are shown in **Figure 2.16**. The intense absorption bands below 340 nm correspond to spin-allowed ligand-centred $\pi^* \leftarrow \pi$ transitions. For [Cu(1-Naphbpy)(P^P)][$PF_6$] and [Cu(2-Naphbpy)(P^P)][$PF_6$] (P^P = DPEPhos or xantphos), a broad absorption of low intensity appears at ~390 nm arising from metal-to-ligand charge transfer (MLCT). For the complexes containing 1-Pyrbpy (dotted curves in **Figure 2.16**), the profile of the bands between 225 and ~335 nm reflects that of the absorption spectrum of the free 1-Pyrbpy ligand (**Figure 2.18**) which in turn is similar to, but broader than, that of pyrene. We assign the broad absorption around 350 nm to a charge-transfer from the pyrenyl to bpy unit.[170,171]

Dichloromethane solutions of the [Cu(N^N)(P^P)][$PF_6$] complexes were poorly emissive. Emission data for powder samples are given in **Table 2.4**. The complexes are all orange emitters with values of $\lambda_{max}^{em}$ in the range 582 to 617 nm. The emission spectra of the complexes containing 1-Naphby and 2-Naphbpy are shown in **Figure 2.17**. Photoluminescence quantum yields (PLQY) were <6% and the emission lifetimes ($\tau_{1/2}$) were all ~ 2 μs (**Table 2.4**). Both [Cu(1-Pyrbpy)(DPEPhos)][$PF_6$] and [Cu(1-Pyrbpy)(xantphos)][$PF_6$] are extremely weak emitters in the solid state.

***Table 2.4*** *Emission maxima and PLQY for powder samples of [Cu(P^P)(N^N)][PF$_6$] complexes ($\lambda_{exc}$ = 365 nm).*

| Compound | $\lambda_{em}^{max}$ / nm | PLQY /% | $\tau_{1/2}$(1)/μs (A1) | $\tau_{1/2}$(2)/μs (A2) | $\tau_{1/2}$(av)/μs |
|---|---|---|---|---|---|
| [Cu(1-Naphbpy)(DPEPhos)][PF$_6$] | 595 | 4.0 | 2.9 (0.3812) | 1.1 (0.4664) | 1.9[a] |
| [Cu(2-Naphbpy)(DPEPhos)][PF$_6$] | 586 | 4.6 | 2.5 (0.4636) | 0.8 (0.4101) | 1.7[a] |
| [Cu(1-Pyrbpy)(DPEPhos)][PF$_6$] | 617 | 0.3 | [b] | [b] | [b] |
| [Cu(1-Naphbpy)(xantphos)][PF$_6$] | 582 | 5.6 | 2.9 (0.4547) | 1.1 (0.3933) | 2.1[a] |
| [Cu(2-Naphbpy)(xantphos)][PF$_6$] | 586 | 3.6 | 2.7 (0.4644) | 1.0 (0.3951) | 1.9[a] |
| [Cu(1-Pyrbpy)(xantphos)][PF$_6$] | 576 | 0.3 | [b] | [b] | [b] |

[a] Biexponential fit using the equation $\tau_{1/2}(av) = \sum A_i\tau_i/\sum A_i$ where $A_i$ is the pre-exponential factor for the lifetime [b]Not measured.

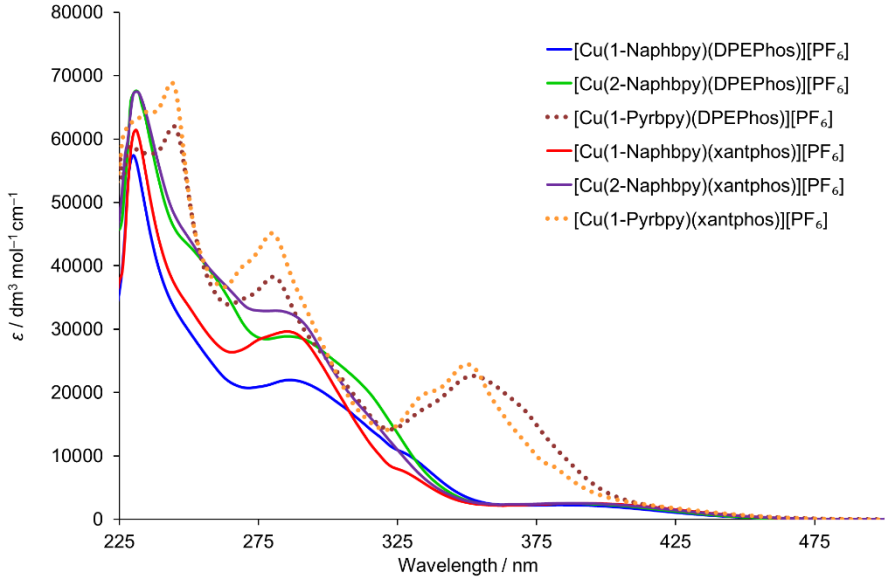


***Figure 2.16*** *Absorption spectra of the [Cu(N^N)(P^P)][PF$_6$] complexes ($CH_2Cl_2$, 2.5 x 10$^{-5}$ mol dm$^{-3}$)*

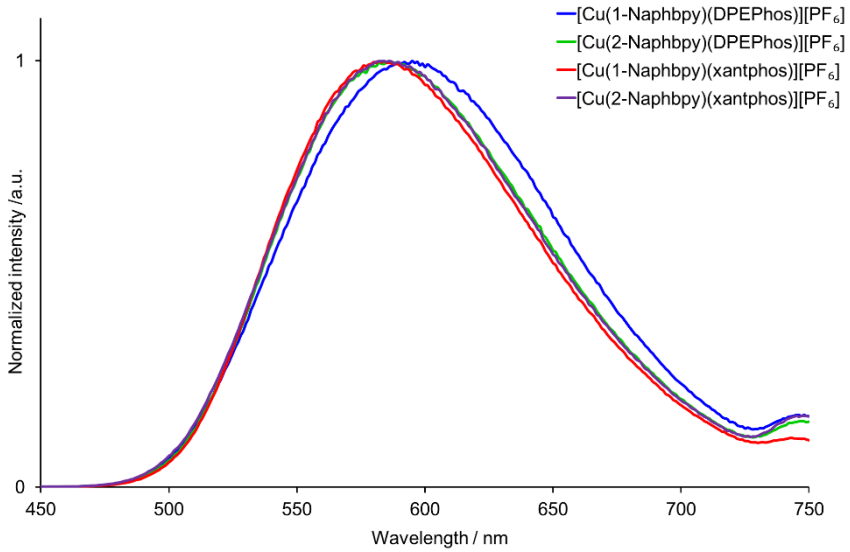


***Figure 2.17*** *Emission spectra of powder samples of [Cu(N^N)(P^P)][PF$_6$] complexes containing 1-Naphby and 2-Naphbpy ($\lambda_{exc}$ = 365 nm).*

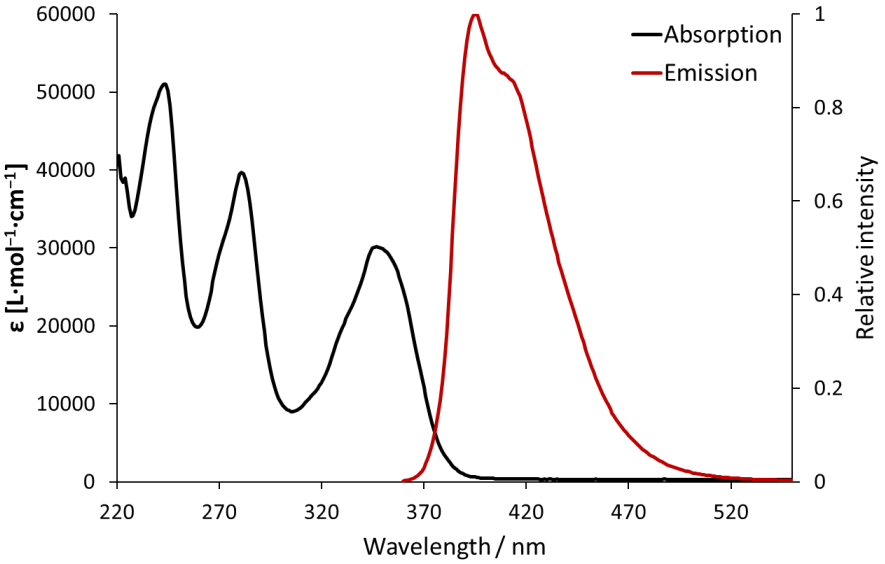


***Figure 2.18*** *Solution absorption and emission spectra of 1-Pyrbpy in $CH_2Cl_2$ ($2.5 \times 10^{-5}$ mol dm$^{-3}$). For the emission spectrum, $\lambda_{exc}$ = 340 nm. Deaerated solution.*

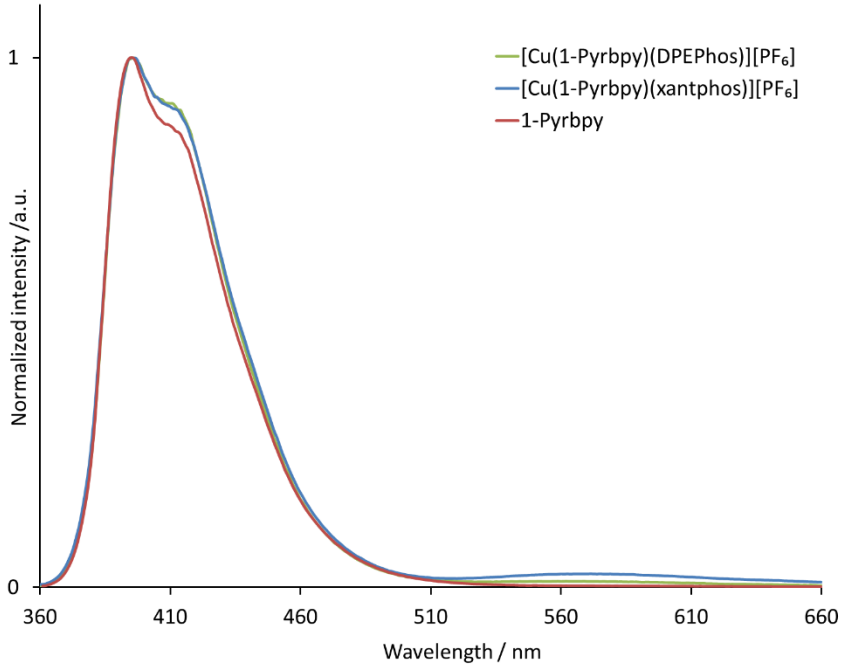


***Figure 2.19*** *Emission spectra of [Cu(1-Pyrbpy)(DPEPhos)][$PF_6$] and [Cu(1-Pyrbpy)(xantphos)][$PF_6$] ($CH_2Cl_2$, 2.5 x $10^{-5}$ mol dm$^{-3}$, $\lambda_{exc}$ = 340 nm), compared to the emission spectrum of 1-Pyrbpy in $CH_2Cl_2$ ($2.5 \times 10^{-5}$ mol dm$^{-3}$, $\lambda_{exc}$ = 340 nm).*

## 2.5 Conclusion

We were able to show, that [Cu(N^N)(P^P)][$PF_6$] type complexes can be prepared and are stable when large aromatic moieties are introduced in the 6-position of the 2,2'-bipyridine ligand. Complexes containing DPEPhos show intramolecular π-stacking of one arene moiety with a phenyl ring. The complex [Cu(1-Pyrbpy)(DPEPhos)][$PF_6$] shows intermolecular face-to-face π-stacking in the crystal lattice.

Variable temperature NMR spectroscopic studies elucidated the dynamic behavior of the complexes in solution. Complexes containing DPEPhos show two sets of $PPh_2$ signals at low temperatures (one pointing towards, the other away from the large aromatic moiety on the 2,2'-bipyridine ligand) that interchange due to flexibility in the DPEPhos backbone. Xantphos-containing complexes also show two sets of $PPh_2$ signals, although they do not interchange on the NMR time scale; the two sets of signals correspond to being on the same or opposite side of the large aromatic substituent. At low temperature, a second conformer is observed for $[Cu(1\text{-}Pyrbpy)(xantphos)]^+$ that is present in a ratio of ~0.05 : 1.0. The conformers are interchangeable by inversion of the xantphos boat conformation and are identified by a characteristic shift of proton A6 in the $^1H$ NMR spectrum.

Complexes containing naphthyl functionalization show a characteristic MLCT absorption and emission behaviour as expected for $[Cu(N^N)(P^P)][PF_6]$ type complexes. However, the PLQY is low, which is in agreement with former studies with a phenyl group in the 6-position of a 2,2'-bipyridine ligand.[84] Complexes with pyrenyl moieties do not show significant emission, most likely due to a low lying triplet state localized on the pyrenyl moiety quenching the $^3MLCT$ excited state.

## 2.6 Experimental

### *2.6.1 6-Bromo-2,2'-bipyridine*

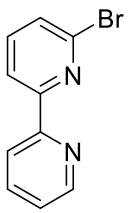


2,6-Dibromopyridine (1.27 g, 5.38 mmol, 1.0 eq.) and $[Pd(PPh_3)_4]$ (311 mg, 0.27 mmol, 0.05 eq.) were placed in a 10-20 ml microwave vial. The vial was evacuated and refilled with $N_2$ three times before dry THF (5 ml) was added. $N_2$ was bubbled through the solution for 20 min before a solution of 2-pyridylzinc bromide (0.5 M in THF, 14.0 ml, 7.00 mmol, 1.3 eq.) was added and the vial was sealed. The reaction was performed in a microwave reactor (90 °C, 2.5 h). Saturated aqueous $NaHCO_3$ (30 ml) was added and the crude mixture was extracted with $CH_2Cl_2$ (3 × 70 ml). The combined organic layers were washed with water (3 × 180 ml) and dried over $MgSO_4$. The solvent was removed in vacuo and the crude material was purified by column chromatography (Alox 90, hexane : ethyl acetate 50 : 1) to give 6-bromo-2,2'-bipyridine (462 mg, 2.39 mmol, 44%) as a white powder. $^1H$ NMR spectroscopic data were consistent with the literature data[172]. ESI MS: *m/z* 234.7 $[M + H]^+$ (base peak, calc. 235.0).

### *2.6.2 6-(Naphthalen-1-yl)-2,2'-bipyridine (1-Naphbpy)*

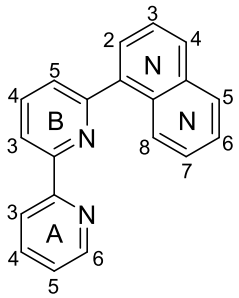


6-(Naphthalen-1-yl)-2,2'-bipyridine was prepared based on a methodology described in the literature.[173] A mixture of 6-bromo-2,2'-bipyridine (325 mg, 1.38 mmol, 1.0 eq.), 1-naphthaleneboronic acid (261 mg, 1.51 mmol, 1.1 eq.) and SPhosPd G2 (49.7 mg, 0.07 mmol, 0.05 eq.) in toluene (15 ml), EtOH (7 ml) and aqueous $Cs_2CO_3$ (2 M, 1.5 ml, 2.2 eq.) were heated at 80 °C under inert conditions for 23 h. The mixture was allowed to cool to room temperature before toluene (30 ml) was added. The organic layer was washed with water (3 × 50 ml) dried over $MgSO_4$ and filtered. The solvent was removed in vacuo and the product was purified by column chromatography (Alox 90, cyclohexane : ethyl acetate 25 : 1) to give

6-(naphthalen-1-yl)-2,2'-bipyridine (259 mg, 0.92 mmol, 67%) as a white powder. $^{1}$H NMR (500 MHz, DMSO-$d_6$) $\delta$/ppm: 8.74 (ddd, $J$ = 4.8, 1.8, 0.9 Hz, 1H, $H^{A6}$), 8.47 (dd, $J$ = 7.9, 1.0 Hz, 1H, $H^{B3}$), 8.37 (dt, $J$ = 8.0, 1.1 Hz, 1H, $H^{A3}$), 8.17 (m, 1H, $H^{N8}$), 8.13 (t, $J$ = 7.8 Hz, 1H, $H^{B4}$), 8.07 – 8.03 (overlapping m, 2H, $H^{N4+N5}$), 7.93 (ddd, $J$ = 8.0, 7.5, 1.8 Hz, 1H, $H^{A4}$), 7.74 (dd, $J$ = 7.7, 1.0 Hz, 1H, $H^{B5}$), 7.72 (dd, $J$ = 7.1, 1.3 Hz, 1H, $H^{N2}$), 7.64 (dd, $J$ = 8.2, 7.1 Hz, 1H, $H^{N3}$), 7.58 (ddd, $J$ = 8.2, 6.8, 1.5 Hz, 1H, $H^{N6}$), 7.54 (ddd, $J$ = 8.2, 6.8, 1.6 Hz, 1H, $H^{N7}$), 8.74 (ddd, $J$ = 7.5, 4.8, 1.2 Hz, 1H, $H^{A5}$). $^{13}$C{$^{1}$H} NMR (126 MHz, DMSO-$d_6$) $\delta$/ppm: 157.9 ($C^{B6}$), 155.3 ($C^{A2}$), 154.9 ($C^{B2}$), 149.4 ($C^{A6}$), 138.2 ($C^{B4}$), 137.9 ($C^{N1}$), 137.3 ($C^{A4}$), 133.5 ($C^{N4a}$), 130.6 ($C^{N8a}$), 128.9 ($C^{N4}$), 128.4 ($C^{N5}$), 127.6 ($C^{N2}$), 126.7 ($C^{N7}$), 126.0 ($C^{N6}$), 125.5 ($C^{N3}$), 125.3 ($C^{N8}$), 125.2 ($C^{B5}$), 124.3 ($C^{A5}$), 120.6 ($C^{A3}$), 118.9 ($C^{B3}$). MALDI-TOF MS: $m/z$ 283.0 $[M + H]^+$ (base peak, calc. 283.1). Found: C 84.78, H 5.37, N 9.73; $C_{20}H_{14}N_2$ requires C 85.08, H 5.00, N 9.92%.

### *2.6.3 6-(Naphthalen-2-yl)-2,2'-bipyridine (2-Naphbpy)*

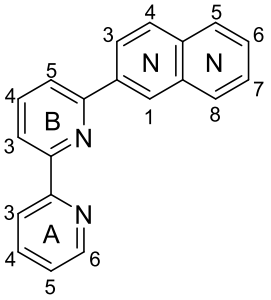


6-(Naphthalen-2-yl)-2,2'-bipyridine was prepared using the same procedure as for 6-(naphthalen-1-yl)-2,2'-bipyridine but starting with 6-bromo-2,2'-bipyridine (350 mg, 1.49 mmol, 1.0 eq.), 2-naphthaleneboronic acid (282 mg, 1.64 mmol, 1.1 eq.) and SPhosPd G2 (53.6 mg, 0.07 mmol, 0.05 eq.) in toluene (15 ml), EtOH (7 ml) and aqueous $Cs_2CO_3$ (2 M, 1.7 ml, 2.2 eq.). 6-(Naphthalen-2-yl)-2,2'-bipyridine (288 mg, 1.02 mmol, 69%) was isolated as a white powder. $^{1}$H and $^{13}$C{$^{1}$H} NMR data were consistent with the literature data.[162] ESI MS: $m/z$ 305.0 $[M + Na]^+$ (base peak, calc. 305.1). Found: C 84.73, H 5.48, N 10.11; $C_{20}H_{14}N_2$ requires C 85.08, H 5.00, N 9.92%.

### *2.6.4 6-(Pyrene-1-yl)-2,2'-bipyridine (1-Pyrbpy)*

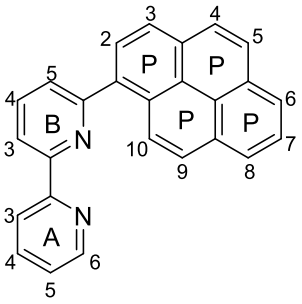


This synthesis has been performed by Dr. Stefan Graber. 6-Bromo-2,2'-bipyridine (1.50 g, 4.89 mmol, 1.0 eq.), pyrene-1-boronic acid (1.32 g, 5.38 mmol, 1.1 eq.) and $Na_2CO_3$ (1.04 g, 9.78 mmol, 2.0 eq.) were dissolved in toluene (200 ml) and water (50 ml). The mixture was degassed with $N_2$ for 50 min before $[Pd(PPh_3)_4]$ (282 mg, 0.24 mmol, 0.05 eq.) was added. The reaction mixture was heated at reflux for 69 h under rigorous exclusion of light. The reaction mixture was cooled to room temperature and the aqueous phase was separated. The organic layer was washed with water (50 ml), dried over $MgSO_4$ and evaporated to dryness. The crude product was purified by column chromatography (Alox 90, hexane : $CH_2Cl_2$ 4 : 1 to pure $CH_2Cl_2$, then Silica 60, toluene : ethyl acetate 10 : 1 to 5:1, then Alox 90, pure $CH_2Cl_2$, then Silica 60 pure $CH_2Cl_2$ to $CH_2Cl_2$ : ethyl acetate 10:1) to give 6-(pyrene-1-yl)-2,2'-bipyridine (1.25 g, 3.51 mmol, 72%) as a yellow powder. $^{1}$H NMR (500 MHz, acetone-$d_6$) $\delta$/ppm: 8.75 (ddd, $J$ = 4.8, 1.8, 0.9 Hz, 1H, $H^{A6}$), 8.62 (overlapping dd, $J$ = 7.9, 0.9 Hz, 1H, $H^{B6}$), 8.62 (overlapping d, $J$ = 9.1 Hz, 1H, $H^{P10}$), 8.59 (d, $J$ = 8.0 Hz, 1H, $H^{A3}$), 8.42 (d, $J$ = 7.9 Hz, 1H, $H^{P3}$), 8.34 (d, $J$ = 7.6 Hz, 1H, $H^{P6}$), 8.33 (d, $J$ = 7.9 Hz, 1H, $H^{P2}$), 8.31 (d, $J$ = 7.6 Hz, 1H, $H^{P8}$), 8.26 (s, 2H, $H^{P4+P5}$), 8.22 (d, $J$ = 9.1 Hz, 1H, $H^{P9}$), 8.18 (t, $J$ = 7.8 Hz, 1H, $H^{B4}$), 8.11 (t, $J$ = 7.6 Hz, 1H, $H^{P7}$), 7.93 (td, $J$ = 7.8, 1.8 Hz, 1H, $H^{A4}$), 7.91 (dd, $J$ = 7.6, 0.9 Hz, 1H, $H^{B5}$), 7.45 (ddd, $J$ = 7.5, 4.8, 1.2 Hz, 1H, $H^{A5}$). $^{13}$C{$^{1}$H} NMR (126 MHz, acetone-$d_6$) $\delta$/ppm: 159.8 ($C^{B6}$), 156.9 ($C^{A2}$), 156.7 ($C^{B2}$),

150.2 ($C^{A6}$), 138.7 ($C^{B4}$), 137.9 ($C^{A4}$), 132.4 ($C^{P5}$), 131.9 ($C^{P8a}$), 129.6 ($C^{P10c}$), 128.8 ($C^{P9}$), 128.7 ($C^{P2}$), 128.6 ($C^{P4+P5}$), 128.4 ($C^{P1}$), 127.2 ($C^{P7}$), 126.6 ($C^{B5}$), 126.4 ($C^{P6}$), 126.1 ($C^{A10a}$), 126.1 ($C^{P8}$), 126.0 ($C^{P10}$), 125.8 ($C^{P10b}$), 125.7 ($C^{P3}$), 125.6 ($C^{P3a}$), 125.0 ($C^{A5}$), 121.7 ($C^{A3}$), 119.8 ($C^{B3}$). ESI MS: m/z 357.1 $[M + H]^+$ (base peak, calc. 357.1). Found: C 87.37, H 4.48, N 7.50; $C_{26}H_{16}N_2$ requires C 87.62, H 4.52, N 7.86%.

### *2.6.5 [Cu(1-Naphbpy)(DPEPhos)][PF$_6$]*

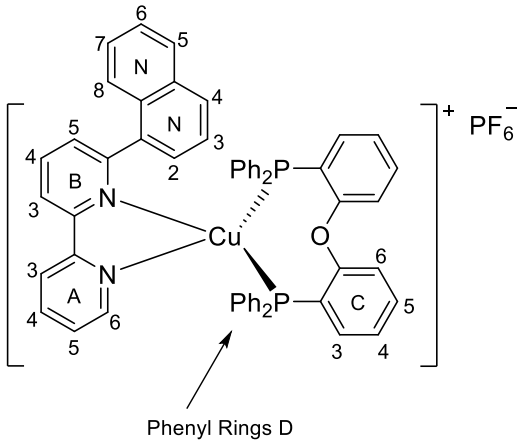


$[Cu(MeCN)_4][PF_6]$ (93.2 mg, 0.25 mmol, 1.0 eq.) and DPEPhos (135 mg, 0.25 mmol, 1.0 eq.) were dissolved in $CH_2Cl_2$ (30 ml) and the mixture was stirred for 2 h at room temperature. 1-Naphbpy (70.6 mg, 0.25 mmol, 1.0 eq.) was added and stirring was continued for 2 h. The yellow solution was filtered and the solvent was removed from the filtrate under vacuum. The solid product was washed with hexane (2 × 30 ml) and dried under vacuum. [Cu(1-Naphbpy)(DPEPhos)][$PF_6$] (244 mg, 0.21 mmol, 82%) was isolated as a yellow solid. $^1$H NMR (500 MHz, acetone-$d_6$, 253 K) $\delta$/ppm: 8.80 (dd, $J$ = 8.1, 1.1 Hz, 1H, $H^{B3}$), 8.72 (dt, $J$ = 8.3, 1.0 Hz, 1H, $H^{A3}$), 8.34 (t, $J$ = 7.9 Hz, 1H, $H^{B4}$), 8.17 (dd, $J$ = 5.2, 0.9 Hz, 1H, $H^{A6}$), 8.13-8.06 (overlapping m, 3H, $H^{A4+N4+N6}$), 7.62 (dd, $J$ = 7.7, 1.0 Hz, 1H, $H^{B5}$), 7.54-7.49 (overlapping m, 2H, $H^{C5a+N7}$), 7.45 (td, $J$ = 7.4, 1.3 Hz, 1H, $H^{D4a}$), 7.42-7.39 (overlapping m, 2H, $H^{D4c+D4d}$), 7.36 (m, 1H, $H^{C6a}$), 7.30-7.22 (overlapping m, 5H, $H^{D3a+C5b+D3c}$), 7.20-7.14 (overlapping m, 4H, $H^{N2+D3d+D4b}$), 7.14-7.08 (overlapping m, 4H, $H^{A5+C4a+C6b+N5}$), 7.01-6.93 (overlapping m, 4H, $H^{C4b+D2c+N8}$), 6.79-6.69 (overlapping m, 6H, $H^{C3a+D2a+D3b+N3}$), 6.53 (m, 2H, $H^{D2d}$), 6.20 (td, $J$ = 7.8, 1.6 Hz, 1H, $H^{C3b}$), 6.08 (m, 2H, $H^{D2b}$). $^{13}$C{$^1$H} NMR (126 MHz, acetone-$d_6$, 253 K) $\delta$/ppm: 159.5 ($C^{B6}$), 157.8 ($C^{C1a}$), 157.4 ($C^{C1b}$), 154.1 ($C^{B2}$), 153.0 ($C^{A2}$), 149.3 ($C^{A6}$), 139.2 ($C^{A4}$), 139.0 ($C^{B4}$), 138.8 ($C^{N1}$), 135.5 ($C^{C3a}$), 134.4 ($C^{C3b}$), 134.4 ($C^{D2a}$), 134.3 ($C^{N4a}$), 133.6 ($C^{D2c}$), 133.5 ($C^{D2b}$), 132.9 ($C^{D2d}$), 132.8 ($C^{C5a}$), 132.5 ($C^{C5b}$), 131.0 ($C^{N8a}$), 130.6 ($C^{D4a}$), 130.5 ($C^{D4c+D4d}$), 130.4 ($C^{D4b}$), 130.0 ($C^{N4}$), 129.4 ($C^{B5}$), 129.4 ($C^{D3c}$), 129.3 ($C^{D3a}$), 129.2 ($C^{D3d}$), 129.0 ($C^{N6}$), 128.9 ($C^{D3b}$), 127.8 ($C^{N5}$), 127.8 ($C^{N8}$), 127.7 ($C^{N2}$), 127.0 ($C^{N7}$), 126.4 ($C^{N3}$), 126.0 ($C^{A5}$), 125.8 ($C^{C2a}$), 125.6 ($C^{C4b}$), 125.5 ($C^{C4a}$), 124.1 ($C^{C2b}$), 123.5 ($C^{A3}$), 122.8 ($C^{B3}$), 120.5 ($C^{C6b}$), 119.9 ($C^{C6a}$). $^{31}$P{$^1$H} NMR (202 MHz, acetone-$d_6$, 253 K) δ/ppm –12.7 (broad, FWHM = 200 Hz), –15.5 (br, FWHM = 220 Hz), –144.5 (septet, $J_{PF}$ = 710 Hz, $[PF_6]^-$). ESI MS: $m/z$ 883.0 $[M\text{-}PF_6]^+$ (base peak, calc. 883.2). UV-Vis ($CH_2Cl_2$, 2.5 × $10^{-5}$ mol $dm^{-3}$): $\lambda$/nm ($\varepsilon$/$dm^3$ $mol^{-1}$ $cm^{-1}$) 230 (57400), 287 (21900), 327sh (10500), 383 (2300). Found: C 64.94, H 4.49, N 3.05; $C_{56}H_{42}CuF_6N_2OP_3$ requires C 65.34, H 4.11, N 2.72%.

## *2.6.6 [Cu(1-Naphbpy)(xantphos)][PF$_6$]*

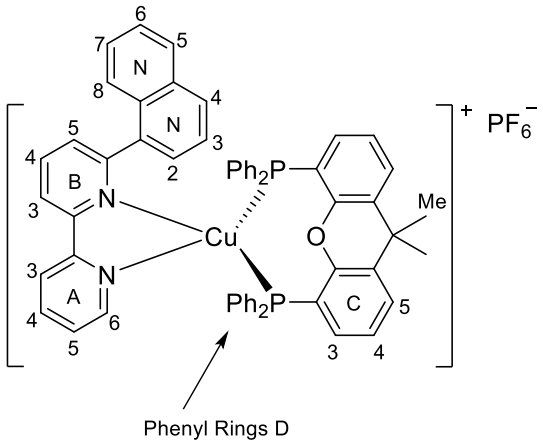


[Cu(MeCN)$_4$][PF$_6$] (93.2 mg, 0.25 mmol, 1.0 eq.) was dissolved in $CH_2Cl_2$ (15 ml). A solution of xantphos (148 mg, 0.25 mmol, 1.0 eq.) and 1-Naphbpy (70.6 mg, 0.25 mmol, 1.0 eq.) was added and the mixture turned red then yellow while it was stirred for 2 h at room temperature. The yellow solution was filtered and the solvent was removed from the filtrate. The solid material was washed with hexane (2 × 30 ml) and dried under vacuum. [Cu(1-Naphbpy)(xantphos)][PF$_6$] (251 mg, 0.24 mmol, 94%) was isolated as a yellow solid. $^1$H NMR (500 MHz, acetone-$d_6$, 223 K) $\delta$/ppm: 8.87 (dd, $J$ = 8.1, 1.1 Hz, 1H, H$^{B3}$), 8.83 (d, $J$ = 8.2 Hz, 1H, H$^{A3}$), 8.41 (t, $J$ = 7.9 Hz, 1H, H$^{B4}$), 8.17 (d, $J$ = 8.3 Hz, 1H, H$^{N5}$), 8.30 (d, $J$ = 8.3 Hz, 1H, H$^{N4}$), 8.14 (td, $J$ = 7.9, 1.7 Hz, 1H, H$^{A4}$), 7.84 (dt, $J$ = 8.0, 1.6 Hz, 2H, H$^{C5a+C5b}$), 7.61 (dd, $J$ = 7.7, 1.0 Hz, 1H, H$^{B5}$), 7.57-7.49 (overlapping m, 2H, H$^{D4a+N6}$), 7.46 (td, $J$ = 7.4, 1.3 Hz, 1H, H$^{D4b}$), 7.37-7.26 (overlapping m, 5H, H$^{D3a+D3b+C4a}$), 7.25-7.13 (overlapping m, 4H, H$^{C4b+N3+D4c+D4d}$), 7.08-7.03 (overlapping m, 2H, H$^{A5+N8}$), 6.90-6.82 (overlapping m, 4H, H$^{D3c+D3d}$), 6.69-6.53 (overlapping m, 7H, H$^{A6+D2a+D2b+C3a+N7}$), 6.46 (d, $J$ = 6.5 Hz, 1H, H$^{N2}$), 6.30-6.20 (overlapping m, 3H, H$^{C3b+D2c}$), 5.66 (broad m, 2H, H$^{D2d}$), 2.06 (s, H$^{Me}$, overlaps with acetone-$d_6$ and assigned from 2D spectra), 1.32 (s, 3H, H$^{Me'}$). $^{13}$C{$^1$H} NMR (126 MHz, acetone-$d_6$, 223 K) $\delta$/ppm: 160.2 (C$^{B6}$), 155.0 (C$^{C1a}$), 154.4 (C$^{C1b}$), 153.5 (C$^{A2}$), 153.0 (C$^{B2}$), 147.5 (C$^{A6}$), 139.7 (C$^{A4+B4}$), 139.0 (C$^{N1}$), 134.6 (C$^{N4a}$), 134.5 (C$^{C6a+C6b}$), 134.4 (C$^{D2a}$), 134.0 (C$^{D2c}$), 133.3 (C$^{D2b}$), 132.4 (C$^{D2d}$), 131.3 (C$^{C3b}$), 131.2 (C$^{D4a}$), 131.1 (C$^{N8a}$), 130.9 (C$^{C3a}$), 130.7 (C$^{D4b}$), 130.1 (C$^{D4c}$), 130.1 (C$^{N4}$), 129.7 (C$^{D4d}$), 129.6 (C$^{D1a}$), 129.5 (C$^{D3a+D3b}$), 129.4 (C$^{B5}$), 129.3 (C$^{N5}$), 128.9 (C$^{D1c+D1d}$), 128.7 (C$^{D3c+D3d}$), 128.0 (C$^{C5a+C5b}$), 127.5 (C$^{N7}$), 127.4 (C$^{N2}$), 127.3 (C$^{N6}$), 126.8 (C$^{N3}$), 126.1 (C$^{C4b}$), 125.9 (C$^{C4a}$), 125.8 (C$^{N8+A5}$), 124.5 (C$^{A3}$), 123.3 (C$^{B3}$), 121.5 (C$^{C2a}$), 120.2 (C$^{C2b}$), 36.7 (C$^{q}$), 32.0 (C$^{Me}$), 23.0 (C$^{Me'}$). $^{31}$P{$^1$H} NMR (202 MHz, acetone-$d_6$, 223 K) δ/ppm –10.9 (broad d, $J$ = 110 Hz), –13.4 (broad d, $J$ = 110 Hz), –144.5 (septet, $J_{PF}$ = 710 Hz, [PF$_6$]$^-$). ESI MS: $m/z$ 923.1 [M-PF$_6$]$^+$ (base peak, calc. 923.2). UV-Vis ($CH_2Cl_2$, 2.5 × 10$^{-5}$ mol dm$^{-3}$): $\lambda$/nm ($\varepsilon$/dm$^3$ mol$^{-1}$ cm$^{-1}$) 230 (60800), 289 (29900), 328sh (7800), 392 (2500). Found: C 66.29, H 4.78, N 2.86; $C_{59}H_{46}CuF_6N_2OP_3$ requires C 66.26, H 4.34, N 2.62%.

## *2.6.7 [Cu(2-Naphbpy)(DPEPhos)][PF$_6$]*

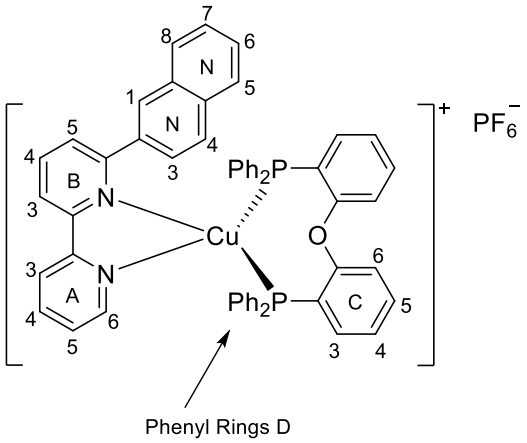


[Cu(2-Naphbpy)(DPEPhos)][PF$_6$] was prepared according to the procedure for [Cu(1-Naphbpy)(DPEPhos)][PF$_6$] using 2-Naphbpy (70.6 mg, 0.25 mmol, 1.0 eq.) in place of 1-Naphbpy. [Cu(2-Naphbpy)(DPEPhos)][PF$_6$] was isolated as a yellow powder (251 mg, 0.24 mmol, 98%). $^1$H NMR (500 MHz, acetone-$d_6$) $\delta$/ppm: 8.67-8.62 (overlapping m, 2H, H$^{A3+B3}$), 8.30 (t, $J$ = 7.9 Hz, 1H, H$^{B4}$), 8.12 (d, $J$ = 5.1 Hz, 1H, H$^{A6}$), 8.09 (td, $J$ = 7.9, 1.7 Hz, 1H, H$^{A4}$), 7.91 (m, 1H, H$^{N5}$), 7.76 (dd, $J$ = 7.7, 1.0 Hz, 1H, H$^{B5}$), 7.65-7.61 (overlapping m, 2H, H$^{N6+N8}$), 7.57-7.52 (overlapping m, 2H, H$^{N1+N7}$), 7.44-7.33 (overlapping m, 6H, H$^{N3+C5+D4a+N4}$), 7.31 (m, 2H, H$^{D4b}$), 7.25 (m, 4H, H$^{D3a}$), 7.16 (m, 2H, H$^{C6}$), 7.13 (ddd, $J$ = 7.6, 5.2, 1.1 Hz, 1H, H$^{A5}$), 7.05-6.95 (overlapping m, 6H, H$^{C4+D3b}$), 6.83 (m, 4H, H$^{D2a}$), 6.64-6.54 (overlapping m, 6H, H$^{C3+D2b}$). $^{13}$C{$^1$H} NMR (126 MHz, acetone-$d_6$) $\delta$/ppm: 161.8 (C$^{B6}$), 158.2 (t, $J$ = 5.9 Hz, C$^{C1}$), 154.4 (C$^{B2}$), 153.8 (C$^{A2}$), 149.7 (C$^{A6}$), 140.3 (C$^{B4}$), 139.7 (C$^{A4}$), 139.0 (C$^{N2}$), 135.3 (C$^{C3}$), 134.6 (C$^{D2b}$), 134.4 (C$^{N4a}$), 133.5 (C$^{N8a+D2a}$), 133.1 (C$^{C5}$), 131.0 (C$^{D4a}$), 130.8 (C$^{D4b}$), 130.1 (C$^{N4}$), 129.7 (C$^{D3a}$), 129.5 (C$^{N8}$), 129.3 (C$^{D3b}$), 128.8 (C$^{N1+N5}$), 128.1 (C$^{N6}$), 128.0 (C$^{B5}$), 127.9 (C$^{N7}$), 126.4 (C$^{A5+N3}$), 125.9 (t, $J$ = 2.1 Hz, C$^{C4}$), 124.6 (t, $J$ = 14.2 Hz, C$^{C2}$), 124.0 (C$^{A3}$), 123.0 (C$^{B3}$), 120.6 (C$^{C6}$). $^{31}$P{$^1$H} NMR (202 MHz, acetone-$d_6$) δ/ppm –13.4 (broad, FWHM = 200 Hz), –144.3 (septet, $J_{PF}$ = 710 Hz, [PF$_6$]$^-$). ESI MS: $m/z$ 883.1 [M-PF$_6$]$^+$ (base peak, calc. 883.2). UV-Vis (CH$_2$Cl$_2$, 2.5 × 10$^{-5}$ mol dm$^{-3}$): $\lambda$/nm ($\varepsilon$/dm$^3$ mol$^{-1}$ cm$^{-1}$) 232 (67600), 288 (28800), 389 (2600). Found: C 64.94, H 4.61, N 2.92; C$_{56}$H$_{42}$CuF$_6$N$_2$OP$_3$ requires C 65.34, H 4.11, N 2.72%.

## *2.6.8 [Cu(2-Naphbpy)(xantphos)][PF$_6$]*

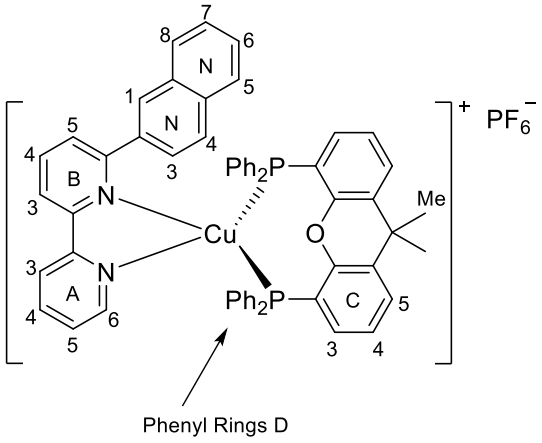


This compound was prepared by the same procedure as was used for [Cu(1-Naphbpy)(xantphos)][PF$_6$] using 2-Naphbpy (70.6 mg, 0.25 mmol, 1.0 eq.) instead of 1-Naphbpy. [Cu(2-Naphbpy)(xantphos)][PF$_6$] was isolated as a yellow powder (256 mg, 0.24 mmol, 96%). $^1$H NMR (500 MHz, acetone-$d_6$) $\delta$/ppm: 8.63 (dt, $J$ = 8.3, 1.0 Hz, 1H, H$^{A3}$), 8.55 (dd, $J$ = 8.0, 1.0 Hz, 1H, H$^{B3}$), 8.24 (t, $J$ = 7.9 Hz, 1H, H$^{B4}$), 8.12 (m 1H, H$^{A4}$), 8.00 (m, 1H, H$^{N5}$), 7.77-7.73 (overlapping m, 4H, H$^{C5+B5+N1}$), 7.67 (ddd, $J$ = 8.3, 6.8, 1.3 Hz, 1H, H$^{N6}$), 7.53 (ddd, $J$ = 8.1, 6.7, 1.2 Hz, 1H, H$^{N7}$), 7.50-7.42 (overlapping m Hz, 4H, H$^{N3+N8+D4a}$), 7.28 (t, $J$ = 7.7 Hz, 4H, H$^{D3a}$), 7.28 (t, $J$ = 7.7 Hz, 2H, H$^{C4}$), 7.17-7.11 (overlapping m, 3H, H$^{A5+D4b}$), 6.82 (m Hz, 4H, H$^{D2a}$), 6.80-6.73 (overlapping m, 5H, H$^{A6+D3b}$), 6.67-6.59 (overlapping m, 6H, H$^{C3+D2b}$), 1.91 (broad s, 3H, H$^{Me}$), 1.46 (s, 3H, H$^{Me'}$). $^{13}$C{$^1$H} NMR (126 MHz, acetone-$d_6$) $\delta$/ppm: 161.7 (C$^{B6}$), 155.5 (t, $J$ = 6.3 Hz, C$^{C1}$), 154.3 (C$^{A2}$), 154.0 (C$^{B2}$), 148.9 (C$^{A6}$), 140.3 (C$^{B4}$), 140.1 (C$^{A4}$), 139.2 (C$^{N2}$), 135.6 (C$^{D1a}$), 134.9 (C$^{C6}$), 134.5 (C$^{N4a}$), 134.1 (C$^{N8a}$), 133.9 (t, $J$ = 7.7 Hz,

$C^{D2a+D2b}$), 131.5 ($C^{C3}$), 131.1 ($C^{D4a}$), 130.8 ($C^{D1b}$), 130.6 ($C^{D4b}$), 129.8 (t, *J* = 4.5 Hz, $C^{D3a}$), 129.5 ($C^{N8}$), 129.1 (t, *J* = 4.7 Hz, $C^{D3a}$), 128.9 ($C^{N5}$), 128.7 ($C^{N1}$), 128.3 ($C^{C5}$), 128.2 ($C^{N6}$), 127.9 ($C^{B5}$), 126.4 ($C^{A5}$), 126.2 (t, *J* = 2.2 Hz, $C^{C4}$), 126.0 ($C^{N3}$), 124.5 ($C^{A3}$), 123.3 ($C^{B3}$), 121.9 ($C^{N7}$), 121.1 (t, *J* = 13.1 Hz, $C^{C2}$), 36.8 ($C^{q}$), 30.8 ($C^{Me'}$), 25.3 ($C^{Me}$). $^{31}P\{^{1}H\}$ NMR (202 MHz, acetone-$d_6$) δ/ppm −12.8 (broad, FWHM = 210 Hz), −144.3 (septet, $J_{PF}$ = 710 Hz, $[PF_6]^-$). ESI MS: *m/z* 923.2 $[M–PF_6]^+$ (base peak, calc. 923.2). UV-Vis ($CH_2Cl_2$, 2.5 × $10^{-5}$ mol $dm^{-3}$): λ/nm (ε/$dm^3$ $mol^{-1}$ $cm^{-1}$) 230 (67000), 284 (32800), 388 (2500). Found: C 66.18, H 4.79, N 2.90; $C_{59}H_{46}CuF_6N_2OP_3$ requires C 66.26, H 4.34, N 2.62%.

### *2.6.9 [Cu(1-Pyrbpy)(DPEPhos)][PF$_6$]*

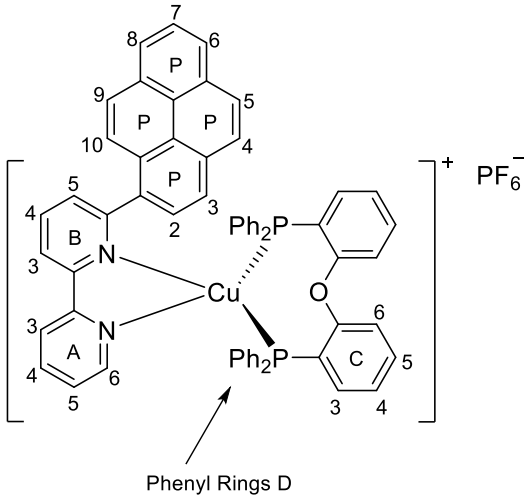


$[Cu(MeCN)_4][PF_6]$ (93.2 mg, 0.25 mmol, 1.0 eq.) and DPEPhos (148 mg, 0.27 mmol, 1.2 eq.) were dissolved in $CH_2Cl_2$ (30 ml) and the mixture was stirred for 2 h at room temperature. 1-Pyrbpy (89.6 mg, 0.25 mmol, 1.0 eq.) was added and stirring was continued for 2 h. The yellow solution was filtered and the solvent was removed from the filtrate. The solid material was washed with hexane (2 × 30 ml), dried under vacuum and redissolved in a small amount of acetone. The solution was layered with $Et_2O$ and left to crystallize for 2 days. The resulting yellow crystals were ground to a powder and dried under vacuum to give [Cu(1-Pyrbpy)(DPEPhos)][$PF_6$] (105 mg, 0.10 mmol, 38%) as a yellow powder. $^{1}H$ NMR (600 MHz, acetone-$d_6$, 238 K) δ/ppm: 8.89 (dd, *J* = 8.2, 1.0 Hz, 1H, $H^{B3}$), 8.78 (d, *J* = 8.3 Hz, 1H, $H^{A3}$), 8.47 (d, *J* = 7.6 Hz, 1H, $H^{P6}$), 8.45 (t, *J* = 7.8 Hz, 1H, $H^{B4}$), 8.42 (d, *J* = 8.9 Hz, 1H, $H^{P5}$), 8.32 (d, *J* = 5.1 Hz, 1H, $H^{A6}$), 8.23 (d, *J* = 7.6 Hz, 1H, $H^{P8}$), 8.19 (d, *J* = 8.9 Hz, 1H, $H^{P4}$), 8.14 (t, *J* = 7.6 Hz, 1H, $H^{P7}$), 8.13 (t, *J* = 8.3 Hz, 1H, $H^{A4}$), 7.80 (dd, *J* = 7.6, 1.0 Hz, 1H, $H^{B5}$), 7.70 (d, *J* = 7.2 Hz, 1H, $H^{P2}$), 7.69 (d, *J* = 9.4 Hz, 1H, $H^{P9}$), 7.62 (t, *J* = 7.5 Hz, 1H, $H^{D4a}$), 7.53 (t, *J* = 7.5 Hz, 1H, $H^{D4b}$), 7.45-7.42 (overlapping m Hz, 2H, $H^{D4c+C5b}$), 7.38-7.30 (overlapping m, 10H, $H^{C6a+C6b+C5a+D3a+D3b+D3c+P3}$), 7.16 (ddd, *J* = 7.6, 5.1, 1.1 Hz, 1H, $H^{A5}$), 7.09 (t, *J* = 8.2 Hz, 2H, $H^{D2c}$), 7.04-7.01 (overlapping m, 2H, $H^{C4b+P10}$), 6.95 (t, *J* = 7.7 Hz, 1H, $H^{C4a}$), 6.70 (t, *J* = 7.7 Hz, 1H, $H^{D4d}$), 6.66 (ddd, *J* = 7.8, 6.2, 1.7 Hz, 1H, $H^{C3b}$), 6.52 (t, *J* = 8.1 Hz, 2H, $H^{D2a}$), 6.39 (t, *J* = 8.2 Hz, 2H, $H^{D2b}$), 6.13 (dd, *J* = 7.8, 6.2, 1.7 Hz, 1H, $H^{C3a}$), 6.03 (m Hz, 2H, $H^{D3d}$), 5.63 (m Hz, 2H, $H^{D2d}$). $^{13}C\{^{1}H\}$ NMR (151 MHz, acetone-$d_6$, 238 K) δ/ppm: 159.8 ($C^{B6}$), 158.3 ($C^{C1b}$), 158.3 ($C^{C1b}$), 154.3 ($C^{B3}$), 152.9 ($C^{A2}$), 149.5 ($C^{A6}$), 139.7 ($C^{A4}$), 139.2 ($C^{B4}$), 136.0 ($C^{C3b}$), 135.5 ($C^{P1}$), 134.7 ($C^{C3a}$), 133.7 ($C^{D2a}$), 133.4 ($C^{D2c}$), 133.1 ($C^{D2b}$), 132.8 ($C^{C5b}$), 132.7 ($C^{D2d}$), 132.4 ($C^{C5a}$), 131.8 ($C^{P3a}$), 131.6 ($C^{P5a}$), 130.9 ($C^{P8a}$), 130.5 ($C^{D4b+D4c}$), 130.4 ($C^{D4a}$), 129.8 ($C^{B5+D4d}$), 129.4 ($C^{D3b}$), 129.3 ($C^{D3c}$), 129.2 ($C^{P9}$), 129.1 ($C^{D3a}$), 129.0 ($C^{P5}$), 128.4 ($C^{P10a}$), 128.0 ($C^{D3d}$), 127.9 ($C^{P4}$), 127.5 ($C^{P2}$), 127.1 ($C^{P7}$), 126.4 ($C^{P6}$), 126.1 ($C^{P8+C4a}$), 125.9 ($C^{A5}$), 125.7 ($C^{P3}$), 124.7 ($C^{C4b+P10b}$), 124.5 ($C^{P10c}$), 123.6 ($C^{A3}$), 123.5 ($C^{P10}$), 122.2 ($C^{C6a}$), 117.7 ($C^{C6b}$), 112.8 ($C^{B3}$). $^{31}P\{^{1}H\}$ NMR (162 MHz, acetone-$d_6$, 295 K) δ/ppm −13.7 (broad, FWHM = ~350 Hz), −144.3 (septet, $J_{PF}$ = 707 Hz, $[PF_6]^-$); (243 MHz, acetone-$d_6$, 238 K) δ/ppm −14.5 (broad, FWHM = 130 Hz). ESI MS: *m/z* 957.2 $[M–PF_6]^+$ (base peak, calc. 957.2). UV-Vis ($CH_2Cl_2$, 2.5 × $10^{-5}$ mol $dm^{-3}$): λ/nm (ε/$dm^3$ $mol^{-1}$ $cm^{-1}$)

230 (58800), 245 (62000), 282 (38000), 354 (22500). Found: C 66.72, H 4.47, N 2.60; $C_{62}H_{44}CuF_6N_2OP_3$ requires C 67.48, H 4.02, N 2.54%.

### *2.6.10[Cu(1-Pyrbpy)(xantphos)][PF$_6$]*

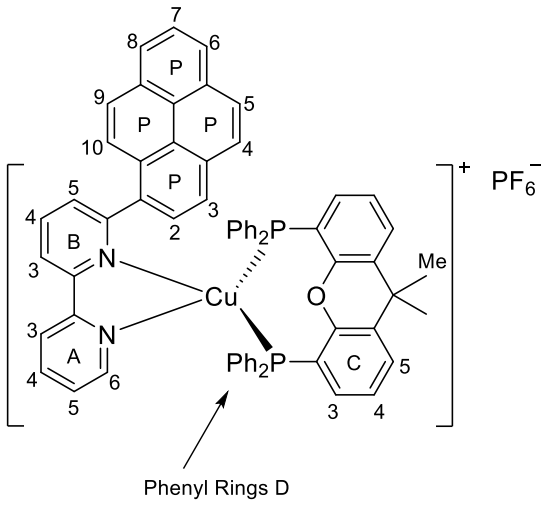


[Cu(MeCN)$_4$][PF$_6$] (93.2 mg, 0.25 mmol, 1.0 eq.) was dissolved in $CH_2Cl_2$ (15 ml). A solution of xantphos (148 mg, 0.25 mmol, 1.0 eq.) and 1-Pyrbpy (89.6 mg, 0.25 mmol, 1.0 eq.) was added and the mixture turned red then yellow while it was stirred for 2 h at room temperature. The yellow solution was filtered and the solvent was removed from the filtrate. The solid material was washed with hexane (2 × 30 ml) dried under vacuum and redissolved in a small amount of acetone. The solution was layered with $Et_2O$ and left to crystallize for 2 days. The resulting yellow crystals were ground to a powder and dried under vacuum to give [Cu(1-Pyrbpy)(xantphos)][PF$_6$] (115 mg, 0.10 mmol, 40%) as a yellow powder. $^1$H NMR (600 MHz, acetone-$d_6$, 238 K) $\delta$/ppm: 8.89 (dd, $J$ = 8.2, 1.1 Hz, 1H, $H^{B3}$), 8.87 (d, $J$ = 8.2 Hz, 1H, $H^{A3}$), 8.61 (d, $J$ = 7.6 Hz, 1H, $H^{P6}$), 8.55 (d, $J$ = 9.0 Hz, 1H, $H^{P5}$), 8.50 (d, $J$ = 7.8 Hz, 1H, $H^{B4}$), 8.34 (d, $J$ = 9.0 Hz, 1H, $H^{P4}$), 8.21 (t, $J$ = 7.6 Hz, 1H, $H^{P7}$), 8.16 (td, $J$ = 8.1, 1.1 Hz, 1H, $H^{A4}$), 8.14 (d, $J$ = 7.6 Hz, 1H, $H^{P8}$), 7.95 (d, $J$ = 7.8 Hz, 1H, $H^{P3}$), 7.82 (dd, $J$ = 7.9, 1.4 Hz, 2H, $H^{C5a+C5b}$), 7.79 (dd, $J$ = 7.5, 1.0 Hz, 1H, $H^{B5}$), 7.66 (m, 1H, $H^{D4d}$), 7.53 (m, 1H, $H^{D4}$), 7.43 (m, 2H, $H^{D3d}$), 7.38 (m, 2H, $H^{D3a}$), 7.37 (d, $J$ = 9.2 Hz, 1H, $H^{P10}$), 7.27 (td, $J$ = 7.8, 1.1 Hz, 1H, $H^{C4a}$), 7.20 (td, $J$ = 7.8, 1.2 Hz, 1H, $H^{C4b}$), 7.17 (dd, $J$ = 9.2 Hz, 1H, $H^{P9}$), 7.04 (ddd, $J$ = 7.6, 5.1, 1.1 Hz, 1H, $H^{A5}$), 7.00 (m, 1H, $H^{D4b}$), 6.91 (d, $J$ = 7.7 Hz, 1H, $H^{P2}$), 6.71 (m, 2H, $H^{D2a}$), 6.65 (d, $J$ = 5.1 Hz, 1H, $H^{A6}$), 6.64-6.58 (overlapping m, 3H, $H^{D4b+D2d}$), 6.53 (m, 1H, $H^{C3a}$), 6.43 (t, $J$ = 7.0 Hz, 2H, $H^{D3c}$), 6.21 (m, 1H, $H^{C3b}$), 5.85 (m, 2H, $H^{D2b}$), 5.49 (broad overlapping m, 4H, $H^{D2c+D3c}$), 2.03 (s, 3H, $H^{Me}$), 1.28 (s, 3H, $H^{Me'}$). $^{13}$C{$^1$H} NMR (151 MHz, acetone-$d_6$, 238 K) $\delta$/ppm: 160.3 ($C^{B6}$), 154.9 ($C^{C1b}$), 154.5 ($C^{C1a}$), 153.2 ($C^{A2}$), 152.9 ($C^{B2}$), 147.6 ($C^{A6}$), 139.7 ($C^{B4}$), 139.4 ($C^{A4}$), 135.9 ($C^{P1}$), 134.4 ($C^{D4c}$), 134.2 ($C^{C6a+C6b}$), 133.5 ($C^{D2b}$), 133.3 ($C^{D2a}$), 132.3 ($C^{P3a}$), 131.8 ($C^{P5a}$), 131.7 ($C^{D1d}$), 131.6 ($C^{D1a}$), 131.5 ($C^{D2c+D3c}$), 131.2 ($C^{D4d}$), 131.1 ($C^{C3b}$), 131.0 ($C^{P8a}$), 130.8 ($C^{C3a}$), 130.6 ($C^{D4a}$), 129.8 ($C^{D4b}$), 129.5 ($C^{B5}$), 129.46 ($C^{D3d}$), 129.4 ($C^{D3a}$), 129.0 ($C^{P5+D2d}$), 128.9 ($C^{P9}$), 128.5 ($C^{P10a}$), 128.3 ($C^{D1b}$), 128.0 ($C^{D3b+P4}$), 127.7 ($C^{C5a+C5b}$), 127.4 ($C^{P7}$), 127.1 ($C^{P2}$), 126.6 ($C^{P6}$), 126.4 ($C^{P8}$), 126.0 ($C^{P3}$), 125.8 ($C^{C4b}$), 125.7 ($C^{A5}$), 125.8 ($C^{C4a}$), 124.8 ($C^{P10b}$), 124.7 ($C^{P10c}$), 124.6 ($C^{P10}$), 124.3 ($C^{A3}$), 160.3 ($C^{B6}$), 123.1 ($C^{B3}$), 121.1 ($C^{C2a}$), 119.9 ($C^{C2b}$), 36.5 ($C^{q}$), 31.6 ($C^{Me}$), 22.6 ($C^{Me'}$). $^{31}$P{$^1$H} NMR (162 MHz, acetone-$d_6$, 295 K) $\delta$/ppm –12.0 (broad, FWHM = ~550 Hz), –144.2 (septet, $J_{PF}$ = 707 Hz, [PF$_6$]$^-$); (243 MHz, acetone-$d_6$, 238 K) $\delta$/ppm –10.9 (broad d, $J$ = 95 Hz), –13.5 (broad d, $J$ = 95 Hz). ESI MS: $m/z$ 997.3 [M–PF$_6$]$^+$ (base peak, calc. 997.2). UV-Vis ($CH_2Cl_2$, 2.5 × 10$^{-5}$ mol dm$^{-3}$): $\lambda$/nm ($\varepsilon$/dm$^3$ mol$^{-1}$ cm$^{-1}$) 243 (68000), 280 (45000), 337sh (20000), 351 (24000). Found: C 67.51, H 4.81, N 2.59; $C_{65}H_{48}CuF_6N_2OP_3$ requires C 68.27, H 4.23, N 2.45%.

# Chapter 3: Nitrogen ligand tuning - Moving the methyl group

## 3.1 Motivation

The results in the previous chapter show, that although the "space" around the copper centre of [Cu(N^N)(P^P)][$PF_6$] complexes is limited, it can still host fairly large substituents. However, this is only true if there are no additional substituents in 6-position on the second pyridine ring of the N^N ligand. Keller *et al.* have shown that in case of smaller substituents, a simultaneous modification of the 6- and 6'-position of a 2,2'-bipyridine ligand can still lead to complex formation.[84,128,174] The complex [Cu(6,6'-$Me_2$bpy)(xantphos)[$PF_6$] showed a high PLQY of 37% in the solid state and yielded LECs with a high peak brightness of 145 cd $m^{-2}$. However, the devices showed a rather short lifetime of only 0.8 h. In the case of asymmetric 2,2'-bipyridine complexes with no substitution in 6'-position (such as 6-Mebpy and 6-Etbpy) the PLQY in the solid state as well as the device peak brightness were generally lower, but devices prepared from these complexes showed much longer lifetimes of up to 82 h in the case of [Cu(6-Etbpy)(DPEPhos)[$PF_6$]. It seems that the asymmetric nature of the 2,2'-bipyridine complex is beneficial for device performance while still incorporating decent luminescence properties. Keller also presented photophysical data for 5,5'-$Me_2$bpy containing complexes. However the PLQYs of these were low (see **Table 3.5**). It seems that at least one substituent in the 6-position is crucial for good luminescence properties and PLQYs.

In an attempt to combine the beneficial properties such as the high brightness of 6,6'-$Me_2$bpy and long device lifetime of 6-Mebpy containing complexes, we designed a 2,2'-bipyridine ligand with sterically demanding methyl groups in 5- and 6'-position for application in [Cu(N^N)(P^P)][$PF_6$]. Complexes formed with this ligand were expected to be able to stabilize the tetrahedral geometry of the copper centre more efficiently than 6-Mebpy. At the same time, we wanted to limit the risk of ligand redistribution in solution and therefore complex degradation in the device. This is observed as a result of large steric effects around the copper centre, as is the case when using 6,6'-$Me_2$bpy[84,128,129] (see also section 4.2.2). The structural, electrochemical and photophysical properties of [Cu(5,6'-$Me_2$bpy)(DPEPhos)][$PF_6$] and [Cu(5,6'-$Me_2$bpy)(xantphos)][$PF_6$] are presented in this chapter. At the time of writing of this thesis, testing of these complexes in lighting devices has not yet taken place.

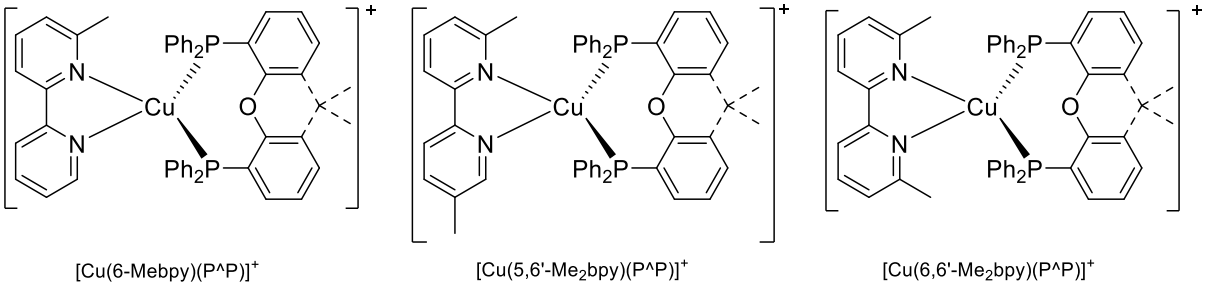


[Cu(6-Mebpy)(P^P)]$^+$ [Cu(5,6'-$Me_2$bpy)(P^P)]$^+$ [Cu(6,6'-$Me_2$bpy)(P^P)]$^+$

***Scheme 3.1*** *Structures of [Cu(6-Mebpy)(P^P)]$^+$,[174] [Cu(5,6'-$Me_2$bpy)(P^P)]$^+$ and [Cu(6,6'-$Me_2$bpy)(P^P)]$^{+}$[174] complexes. Additional methyl groups close to the copper centre leads to an increased steric demand and preservation of the tetrahedral geometry upon excitation.*

## 3.2 Synthesis

The asymmetric 2,2'-bipyridine ligand was synthesized via a palladium catalysed cross coupling reaction. The pyridyl-zinc bromide species was generated in-situ from the respective bromo pyridine (**Scheme 3.2**). The ligand was isolated in moderate yield of 48%.

The two complexes [Cu(5,6'-$Me_2$bpy)(DPEPhos)][$PF_6$] and[Cu(5,6'-$Me_2$bpy)(xantphos)][$PF_6$] were prepared by a sequential and simultaneous addition of ligands respectively. The chosen synthetic strategies were previously discussed for copper complexes with large aromatic substituents in section 2.2.2. The complexes were isolated in good yields of 74 and 90% respectively.

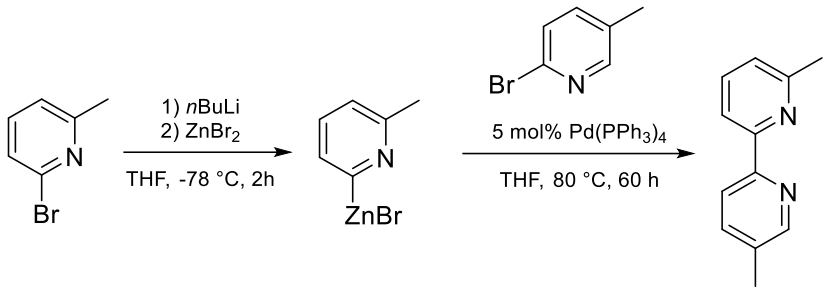


***Scheme 3.2*** *Preparation of asymmetric 5,6'-$Me_2$bpy ligand.*

## 3.3 Structural Discussion

### *3.3.1 Single crystal structure*

Single crystals of 5,6'-$Me_2$bpy, [Cu(5,6'-$Me_2$bpy)(DPEPhos)][$PF_6$]·$Me_2CO$ and [Cu(5,6'-$Me_2$bpy)(xantphos)][$PF_6$]·0.5$CH_2Cl_2$·0.75$Et_2O$ were obtained by diffusion of cyclohexane into an ethyl acetate solution of 5,6'-$Me_2$bpy and by diffusion of $Et_2O$ into acetone or dichloromethane solutions of [Cu(5,6'-$Me_2$bpy)(DPEPhos)][$PF_6$] and [Cu(5,6'-$Me_2$bpy)(xantphos)][$PF_6$], respectively (**Figure 3.4** - **Figure 3.6**). Crystallographic parameters are summarized in **Table 3.2** The ligand 5,6'-$Me_2$bpy crystallizes in the monoclinic space group $P2_1/n$ with the pyridine rings rotated towards each other to minimize steric train. The rings are slightly twisted with a dihedral angle of 16.5° between the ring planes (**Table 3.1**). π-Stacking interactions between molecules and σ-π interactions of the methyl groups with pyridine rings of neighbouring molecules lead to a zigzag packing in the crystal lattice (**Figure 3.1**).

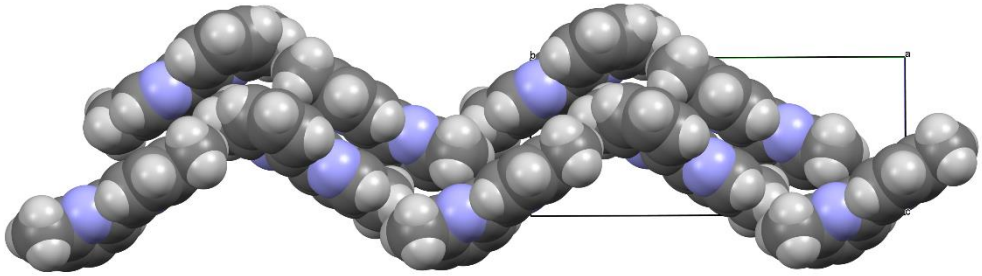

***Figure 3.1*** *π-Stacking packing of zigzag arrangements of 5,6'-$Me_2$bpy molecules.*

[Cu(5,6'-$Me_2$bpy)(DPEPhos)][$PF_6$] shows intermolecular π-stacking of one phenyl ring of the backbone with $PPh_2$ phenyl ring, similar to [Cu(2-Naphbpy)(DPEPhos)][$PF_6$] (see chapter 2.3.1). Packing of the molecules involves some intermolecular σ-π interactions of H-atoms with phenyl rings (*i.e.* C–H…π) of neighbouring molecules, but no intermolecular π-π interactions are observed. The 2,2'-bipyridine ligand is arranged in a way that the 6-methyl group sits opposite of the DPEPhos backbone, leaving the 5-methyl group on the backbone side, which seems to be sterically beneficial (**Figure 3.2**).

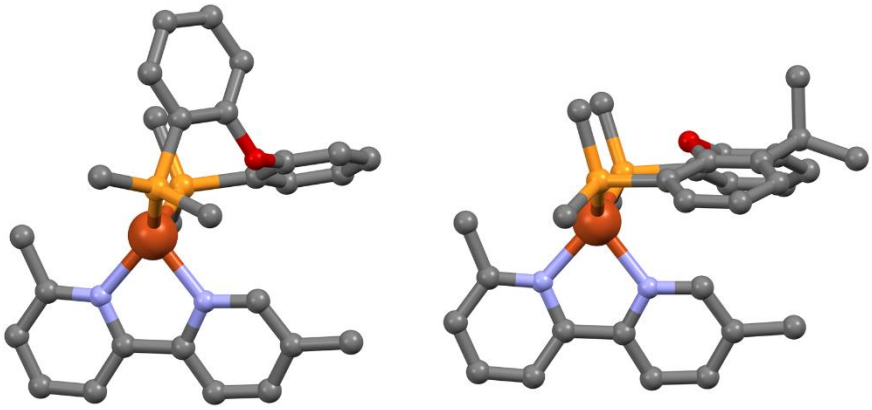

***Figure 3.2*** *Side view of the [Cu(5,6'-$Me_2$bpy)(DPEPhos)]$^+$ (left) and [Cu(5,6'-$Me_2$bpy)(xantphos)]$^+$ cations (right). Only the ipso-C of the phenyl rings is shown. Hydrogens are omitted for clarity.*

[Cu(5,6'-$Me_2$bpy)(xantphos)][$PF_6$] shows no intramolecular π-π interactions. Two phenyl rings of the $PPh_2$ groups point upwards but are twisted with an angle of 39.5° with respect to each other. The 5-methyl substituted pyridine ring is involved in an intermolecular π-π interactions with a $PPh_2$ phenyl ring of a neighbouring molecule (**Figure 3.3**). The xantphos backbone adopts a boat conformation as expected.[84,128] Similarly to the structure of [Cu(2-Naphbpy)(DPEPhos)][$PF_6$], the 6'-methyl sits opposite of the xanthene backbone, leaving the 5-methyl substituent beneath the boat conformation of the backbone (**Figure 3.2**).

In both copper(I) cations the pyridine rings of the 2,2'-bipyridine ligand are slightly twisted out of plane with respect to each other (9.8 and 11.7°), although the distortion from planarity in the complexes is smaller than in the free ligand (16.5°). The N-Cu-N and

P-Cu-P planes are almost perpendicular in both complexes, showing the distorted tetrahedral coordination geometry of the copper atom (**Table 3.1**). A perfect tetrahedral geometry cannot be achieved, because of the different bite angle of the N^N and P^P ligand.

***Table 3.1*** *Angular distortions of the N^N ligands in the [Cu(N^N)(P^P)]⁺ cations.*

| Compound | Angle between planes of pyridine rings / ° | Angle between N-Cu-N and P-Cu-P planes /° |
|---|---|---|
| 5,6'-$Me_2$bpy | 16.5 | - |
| [Cu(5,6'-$Me_2$bpy)(DPEPhos)][$PF_6$] | 9.8 | 87.0 |
| [Cu(5,6'-$Me_2$bpy)(xantphos)][$PF_6$] | 11.7 | 85.1 |

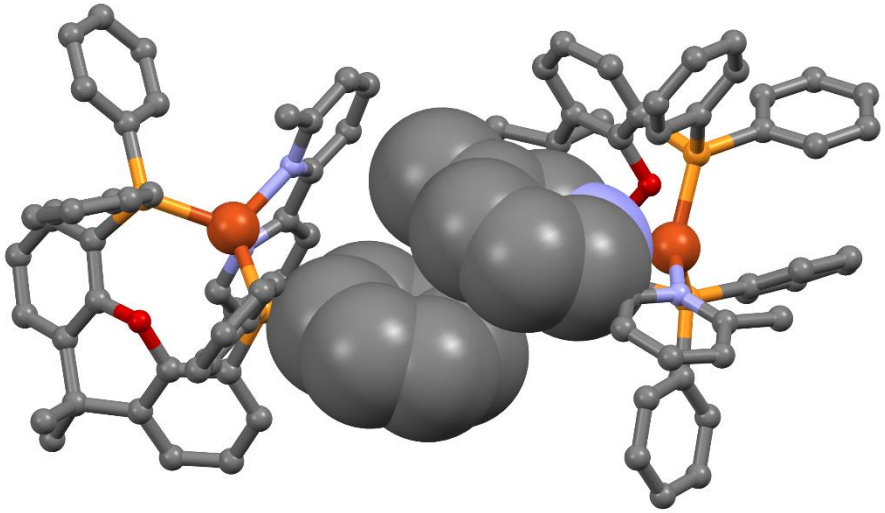

***Figure 3.3*** *Intermolecular π-π interactions of two [Cu(5,6'-$Me_2$bpy)(xantphos)]⁺ cations. Hydrogen atoms are omitted for clarity.*

***Table 3.2*** *Crystallographic parameters of ligand 5,6'-$Me_2$bpy and [Cu(N^N)(P^P)][$PF_6$] complexes.*

| Compound | 5,6'-$Me_2$bpy | [Cu(5,6'-$Me_2$bpy)(DPEPhos)][$PF_6$] ·$Me_2CO$ | [Cu(5,6'-$Me_2$bpy)(xantphos)][$PF_6$] ·0.5$CH_2Cl_2$·0.75$C_4H_{10}O$ |
|---|---|---|---|
| Formula | $C_{12}H_{12}N_2$ | $C_{51}H_{46}CuF_6N_2O_2P_3$ | $C_{55}$ $H_{52.5}CuF_6N_2O_{1.75}P_3$ |
| Formula weight | 184.24 | 989.39 | 1069.38 |
| Crystal colour and habit | Colourless plate | Orange needle | Yellow block |
| Crystal system | Monoclinic | Monoclinic | Monoclinic |
| Space group | *P* $2_1/n$ | *P*$2_1/c$ | *P* $2_1/n$ |
| *a, b, c* / Å | 6.4300(2)<br>19.2147(4)<br>8.0931(2) | 9.5613(9)<br>14.8515(13)<br>32.472(3) | 17.6502(15)<br>16.8504(15)<br>18.4582(16) |
| *α, β, γ* / ° | 90<br>91.147(2)<br>90 | 90<br>90.338(4)<br>90 | 90<br>104.685(3)<br>90 |
| *U* / Å³ | 999.71(4) | 4611.0(7) | 5310.4(8) |
| *Dc* / Mg m⁻³ | 1.224 | 1.425 | 1.338 |
| *Z* | 4 | 4 | 4 |
| *μ*(Cu-Kα) / mm⁻¹ | 0.369 | 2.227 | 2.422 |
| *T* / K | 130 | 130 | 130 |
| Refln. collected ($R_{int}$) | 13711 (0.0291) | 31246 (0.029) | 55278 (0.0319) |
| Unique refln. | 2030 | 8211 | 9603 |
| Refln. for refinement | 2030 | 8211 | 9603 |
| Parameters | 130 | 586 | 608 |
| Threshold | 2*σ* | 2*σ* | 2*σ* |
| *R*1 (*R*1 all data) | 0.0564 (0.0574) | 0.0392 (0.0420) | 0.0544 (0.0575) |
| *wR*2 (*wR*2 all data) | 0.1686 (0.1698) | 0.0529 (0.0536) | 0.1728 (0.1768) |
| Goodness of fit | 1.190 | 0.9967 | 1.025 |
| CCDC deposition | - | - | - |

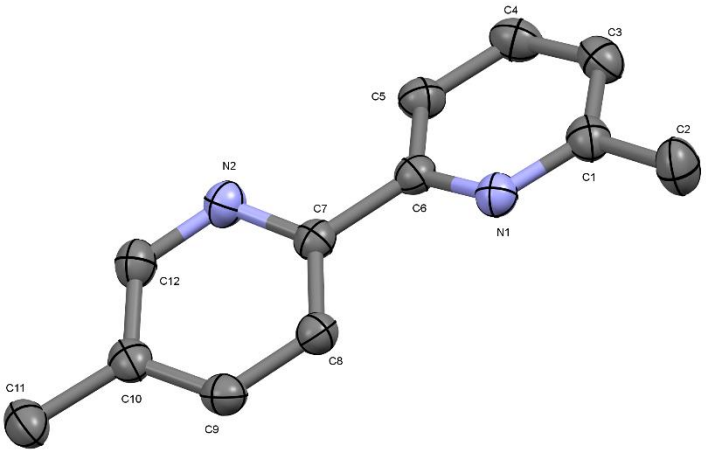


***Figure 3.4*** *Structure of 5,6'-$Me_2$bpy with ellipsoids plotted at 50% probability level. H atoms are omitted for clarity.*

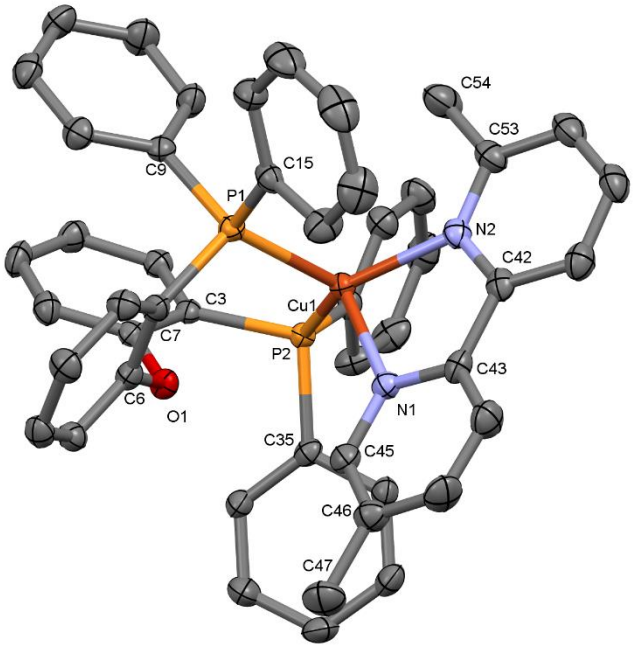


***Figure 3.5*** *Structure of the [Cu(5,6'-$Me_2$bpy)(xantphos)]$^+$ cation in [Cu(5,6'-$Me_2$bpy)(xantphos)][$PF_6$]·$Me_2CO$ with ellipsoids plotted at 50% probability level. H atoms and solvent molecules omitted for clarity. Selected bond parameters: Cu1–P2 = 2.2516(7), Cu1–P1 = 2.2967(7), Cu1–N2 = 2.089(2), Cu1–N1 = 2.075(2) Å; P2–Cu1–P1 = 113.48(2), P2–Cu1–N2 = 131.83(6), P1–Cu1–N2 = 108.62(6), P2–Cu1–N1 = 110.64(6), P1–Cu1–N1 = 103.81(6), N2–Cu1–N1 = 79.90(8)°.*

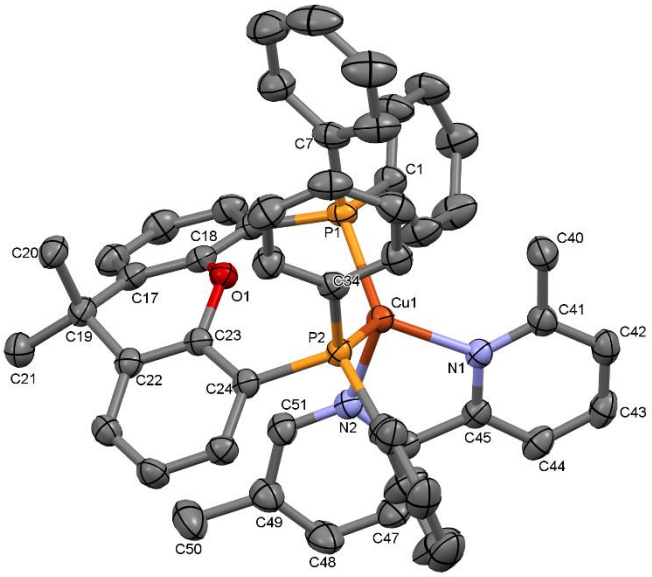


***Figure 3.6*** *Structure of the [Cu(5,6'-Me₂bpy)(xantphos)]⁺ cation in [Cu(5,6'-Me₂bpy)(xantphos)][PF₆]·0.5CH₂Cl₂·0.75Et₂O with ellipsoids plotted at 50% probability level. H atoms and solvent molecules omitted for clarity. Selected bond parameters: Cu1–P2 = 2.2555(8), Cu1–P1 = 2.2490(9), Cu1–N2 = 2.105(3), Cu1–N1 = 2.053(2) Å; P2–Cu1–P1 = 117.36(3), P2–Cu1–N2 = 103.55(7), P1–Cu1–N2 = 110.47(7), P2–Cu1–N1 = 120.61(7), P1–Cu1–N1 = 116.04(7), N2–Cu1–N1 = 80.02(9)°. SQUEEZE was used to refine solvent molecules.*

## *3.3.2 NMR spectroscopic behaviour*

$^{1}H$, $^{13}C\{^{1}H\}$, $^{31}P\{^{1}H\}$, COSY, NOESY, HMBC and HMQC NMR spectra were recorded to fully assign the signals in the spectra of [Cu(5,6'-Me₂bpy)(DPEPhos)][PF₆] and [Cu(5,6'-Me₂bpy)(xantphos)][PF₆]. Part of the NOESY spectrum of [Cu(5,6'-Me₂bpy)(DPEPhos)][PF₆] is shown in **Figure 3.7**. Two sets of signals are observed for the phenyl protons (D and D' rings, for assignment see section 3.6.2 and 3.6.3) that show exchange peaks. This indicates a dynamic behaviour in solution. We propose that configuration of the DPEPhos backbone with one phenyl ether ring in and the other one out of the P-Cu-P plane leaves two phenyl groups in an equatorial and two in an axial position. Upon interchange of the phenyl ether rings on the backbone the former axial phenyl rings change to an equatorial position and vice versa. (**Scheme 3.3**). A similar behaviour has been observed before in [Cu(N^N)(P^P)][PF₆] complexes with asymmetric N^N ligands (see reference 84 and chapter 2.3.2). The $^{1}H$ spectrum of [Cu(5,6'-Me₂bpy)(xantphos)][PF₆] also shows two set of D-signals, but no exchange peaks between them. This indicates that the xanthene backbone does not invert at room temperature on an NMR timescale, effectively locking the D rings in either an equatorial or axial position. This is in agreement with the single crystal structure of [Cu(5,6'-Me₂bpy)(xantphos)][PF₆], where the sterically less demanding 5-substituted pyridine ring is located beneath the xanthene boat conformation.

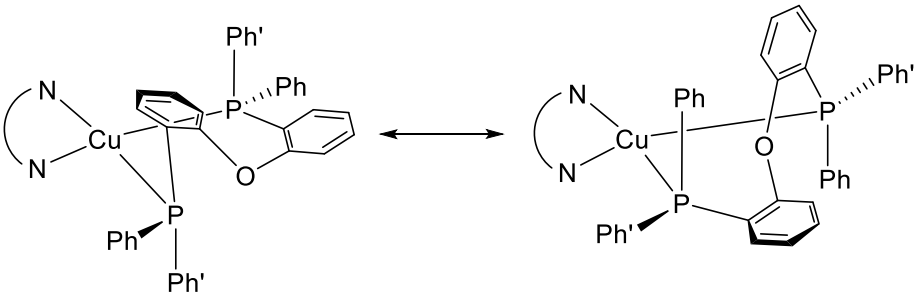


***Scheme 3.3*** *Dynamic behaviour of [Cu(N^N)(DPEPhos)][$PF_6$] complexes in solution. The flip of the diphenyl backbone changes the position of the former axial phenyl groups (Ph on the left) to the equatorial position and opposite (Ph on the right) and vice versa for phenyl groups in former axial position (Ph' on the left).*

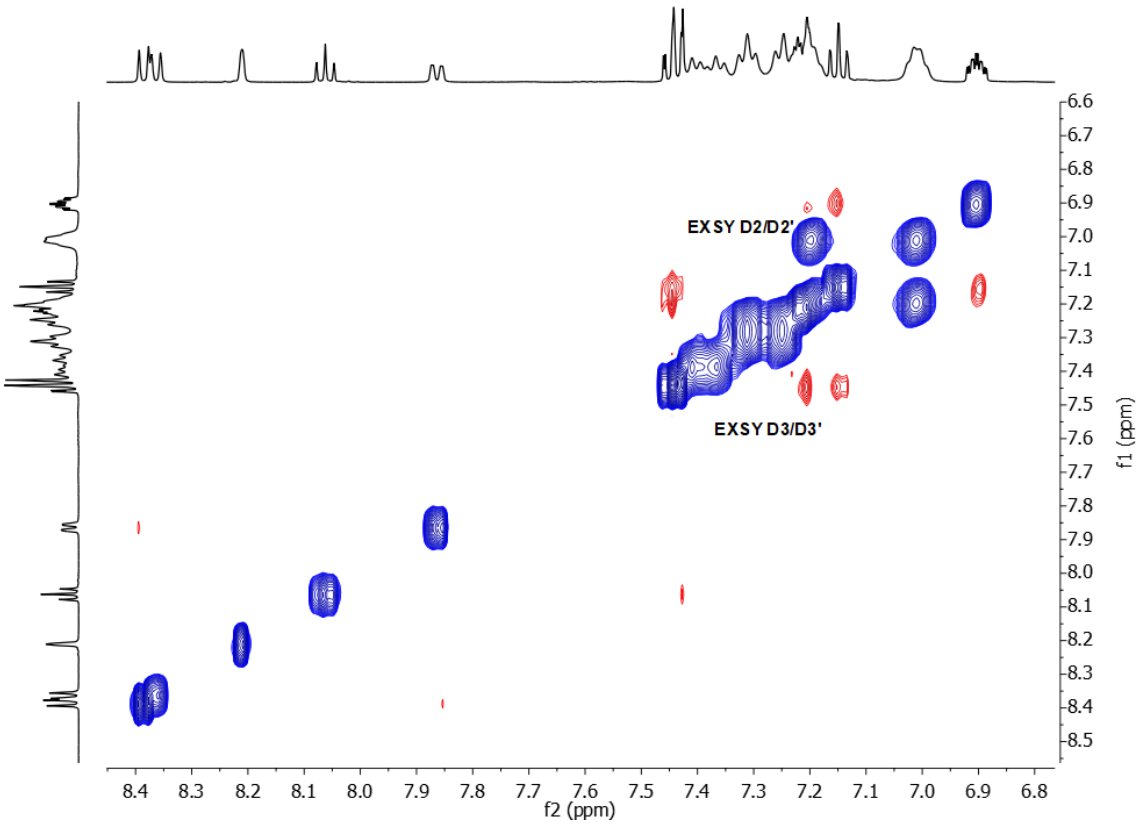


***Figure 3.7*** *500 MHz NOESY spectrum of [Cu(5,6'-$Me_2$bpy)(DPEPhos)][$PF_6$] at 298 K in acetone-$d_6$. Cross-peaks in phase with the diagonal (blue) correspond to EXSY peaks and signals with opposite phase (red) relative to the diagonal correspond to NOESY peaks. Chemical shifts in δ/ppm.*

## 3.4 Electrochemical and photophysical properties

### *3.4.1 Electrochemistry*

Both complexes are redox active and show an irreversible oxidation and a reversible reduction in propylene carbonate solution (**Table 3.3**). The oxidation is assigned to a copper centred oxidation, whereas the reduction is most likely based on the N^N ligand, assuming an orbital distribution close to similar complexes.[83,84,164] Redox potentials for

similar copper complexes bearing DPEPhos and xantphos in combination with 6-Mebpy, 6,6'-$Me_2$bpy and 5,5'-$Me_2$bpy were investigated by Keller[174] and are summarized in **Table 3.4**. Values in **Table 3.4** were obtained by cyclic voltammetry in dichloromethane solution but do not show reduction processes due to the limited negative potential range of this solvent. Complexes containing 6,6'-$Me_2$bpy as the N^N ligand show the highest oxidation potentials, followed by 6-Mebpy and then 5,5'-$Me_2$bpy containing complexes. Oxidation potentials for xantphos containing complexes are similar or slightly higher than for DPEPhos containing complexes. This observation is also true for [Cu(5,6'-$Me_2$bpy)(P^P)][$PF_6$] complexes. Although, reversible oxidation signals were not observed, $E_{pc}^{ox}$ values of [Cu(5,6'-$Me_2$bpy)(P^P)][$PF_6$] complexes lie between the values obtained for 5,5'-$Me_2$bpy and 6,6'-$Me_2$bpy for DPEPhos containing complexes and between 5,5'-$Me_2$bpy and 6-Mebpy for xantphos containing complexes.

Reduction potentials are similar for [Cu(5,6'-$Me_2$bpy)(DPEPhos)][$PF_6$] and [Cu(5,6'-$Me_2$bpy)(xantphos)][$PF_6$]. Cyclic voltammetry indicates a slightly higher HOMO-LUMO gap for [Cu(5,6'-$Me_2$bpy)(xantphos)][$PF_6$] compared to [Cu(5,6'-$Me_2$bpy)(DPEPhos)][$PF_6$], although the values are very close with a difference for $\Delta(E_{pc}^{ox} - E_{1/2}^{red})$ of only 60 mV.

***Table 3.3*** *Cyclic voltammetric data for [Cu(5,6'-$Me_2$bpy)(P^P)][$PF_6$] complexes referenced to internal $Fc/Fc^+$ = 0 V; Propylene carbonate solutions with [$^nBu_4N$][$PF_6$] as supporting electrolyte and scan rate of 0.1 V $s^{-1}$.*

| Complex cation | $E_{pc}^{ox}$ / V | $E_{1/2}^{red}$ / V ($E_{pa} - E_{pc}$ / mV) |
|---|---|---|
| [Cu(5,6'-$Me_2$bpy)(DPEPhos)]$^+$ | +0.81 | −2.12 (100) |
| [Cu(5,6'-$Me_2$bpy)(xantphos)]$^+$ | +0.89 | −2.10 (100) |

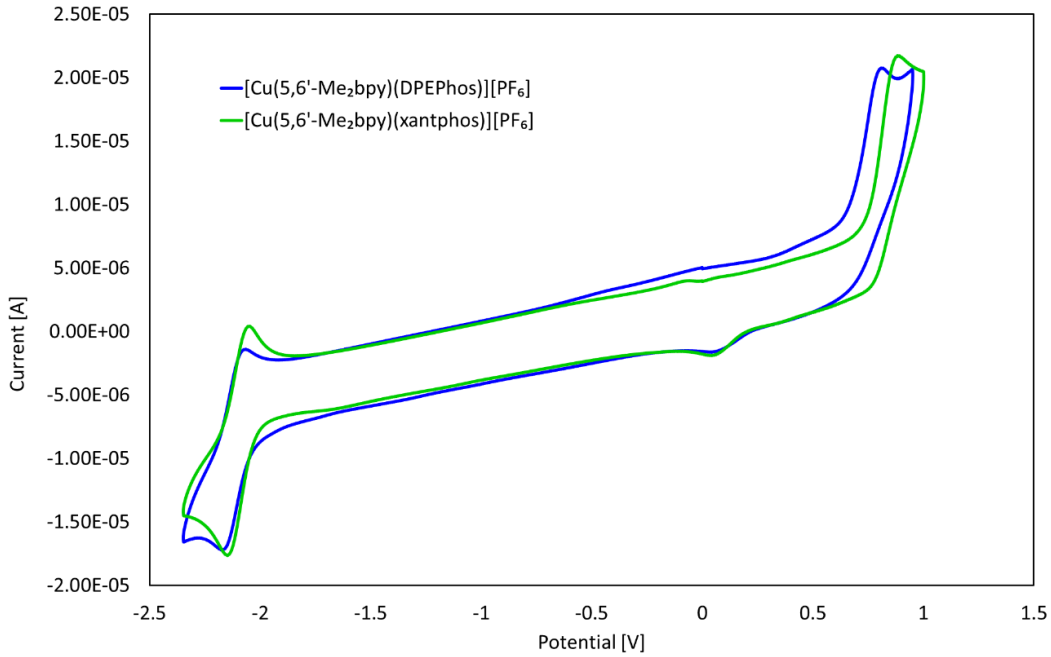


***Figure 3.8*** *Cyclic voltammogram of [Cu(5,6'-$Me_2$bpy)(DPEPhos)][$PF_6$] and [Cu(5,6'-$Me_2$bpy)(xantphos)][$PF_6$] in propylene carbonate at a scan rate of 0.1 V $s^{-1}$ referenced to internal $Fc/Fc^+$ = 0V. The second of three reproducible cycles is shown.*

***Table 3.4*** *Cyclic voltammetric data for [Cu(N^N)(P^P)][$PF_6$] complexes referenced to internal Fc/Fc+ = 0.V; $CH_2Cl_2$ (freshly distilled) solutions with [$nBu_4N$][$PF_6$] as supporting electrolyte and scan rate of 0.1 V $s^{-1}$. Reproduced from reference* 174*.*

| Complex cation | $E_{1/2}^{ox}$ / V | ($E_{pc}$ – $E_{pa}$ / mV) | $E_{pc}^{ox}$ / V[a] |
|---|---|---|---|
| [Cu(6-Mebpy)(DPEPhos)]$^+$ | +0.69 | 125 | 0.75 |
| [Cu(6-Mebpy)(xantphos)]$^+$ | +0.85 | 100 | 0.90 |
| [Cu(6,6'-$Me_2$bpy)(DPEPhos)]$^+$ | +0.92 | 183 | 1.01 |
| [Cu(6,6'-$Me_2$bpy)(xantphos)]$^+$ | +0.89 | 145 | 0.96 |
| [Cu(5,5'-$Me_2$bpy)(DPEPhos)]$^+$ | +0.70 | 127 | 0.76 |
| [Cu(5,5'-$Me_2$bpy)(xantphos)]$^+$ | +0.75 | 131 | 0.82 |

[a] Values calculated from $E_{1/2}^{ox}$ and $E_{pc}$ – $E_{pa}$.

## *3.4.2 Absorption and emission properties*

The photophysical properties of [Cu(5,6'-$Me_2$bpy)(DPEPhos)][$PF_6$] and [Cu(5,6'-$Me_2$bpy)(xantphos)][$PF_6$] are summarized in **Table 3.5**. The absorption spectra of these complexes show intense bands below 330 nm which are assigned to ligand-based $\pi^*\leftarrow n$ and $\pi^*\leftarrow\pi$ transitions. The broad absorption around 375 nm arises from a metal-to-ligand charge transfer (MLCT) excitation (**Figure 3.9**). Solution emission is weak for both complexes with quantum yields of only 1 and 2% in degassed solution and are even lower (>1%) in non-degassed solutions. Keller similarly reported low solution quantum yields for complexes containing 6-Mebpy and 5,5'-$Me_2$bpy. However, complexes containing 6,6'-$Me_2$bpy showed high solution quantum yields of 13.8% for [Cu(6,6'-$Me_2$bpy)(DPEPhos)][$PF_6$] and 10.0% for [Cu(6,6'-$Me_2$bpy)(xantphos)][$PF_6$] (**Table 3.5**).[174] This illustrates the importance of the second methyl group in the 6-position to prevent quenching of the excited state in solution. Her data show that only one methyl group in 6- position or two methyl groups in 5,5'-position are not sufficient to shield the copper centre from solvent access. Our findings indicate that even a 5,6'-substitution pattern on the 2,2'-bipyridine ligand is not sufficient and a 6,6'-dimethyl substitution is critical to achieve reasonably high quantum yields in solution. Excited state lifetimes are short for [Cu(5,6'-$Me_2$bpy)(P^P)][$PF_6$] in solution and increase only slightly when degassed. In solid state both [Cu(5,6'-$Me_2$bpy)(P^P)][$PF_6$] complexes show a yellow emission with moderate quantum yields of 12 and 11% (**Figure 3.10**). This is somewhat surprising because Keller found solid state quantum yields of 9.5% for [Cu(6-Mebpy)(DPEPhos)][$PF_6$], 33.4% for [Cu(6-Mebpy)(xantphos)][$PF_6$], 43.2% for [Cu(6,6'-$Me_2$bpy)(DPEPhos)][$PF_6$] and 37.3% for Cu(6,6'-$Me_2$bpy)(xantphos)][$PF_6$] (see **Table 3.5**). It was initially thought that 5,6'-$Me_2$bpy would lie between 6-Mebpy and 6,6'-$Me_2$bpy in terms of steric demands and therefore also beneficial in stabilizing the tetrahedral geometry of the copper centre upon excitation, leading to a higher PLQY in the solid state. But clearly, the steric bulk of the substituents on the bpy ligand is only one factor that influences the photophysical behaviour of the [Cu(N^N)(P^P)$^+$ complex. Introduction of a methyl group in the 5-position tends to red-shift the emission of the complex (as can be seen for complexes containing 5,6'-$Me_2$bpy and 5,5'-$Me_2$bpy compared to 6,6'-$Me_2$bpy in **Table 3.5**). This indicates that introduction of an electron-donating methyl group in a position meta to the nitrogen atom stabilizes the LUMO of the complex. At the same time this seems to diminish the radiative decay of the excited state, leading to only a moderate PLQY increase when going from 6-Mebpy to 5,6'-$Me_2$bpy, although the stabilization of the tetrahedral geometry of the complex seems to be increased.

***Table 3.5*** *Photophysical properties of [Cu(5,6'-Me$_2$bpy)(P^P)][PF$_6$] complexes.*

| Complex cation | $CH_2Cl_2$ solution[a,b] | | | | Powder | | |
|---|---|---|---|---|---|---|---|
| | UV-Vis MLCT $\lambda_{max}$/nm | $\lambda_{em}^{max}$ /nm | PLQY (non-degassed/ degassed)% | $\tau_{1/2}$(av)(non-degassed/ degassed)/µs | $\lambda_{em}^{max}$/nm | PLQY/% | $\tau_{1/2}$(av)[c]/µs |
| [Cu(5,6'-Me$_2$bpy)(DPEPhos)]$^+$ | 375 | 626 | >1/1 | 0.23/0.80 | 553 | 12 | 6 |
| [Cu(5,6'-Me$_2$bpy)(xantphos)]$^+$ | 374 | 622 | >1/2 | 0.24/1.36 | 555 | 11 | 5 |
| [Cu(6-Mebpy)(DPEPhos)]$^+$[d] | 378 | 610, 639 | 0.6/1.2 | 0.126/0.172 | 567 | 9.5 | 2.6 |
| [Cu(6-Mebpy)(xantphos)]$^+$[d] | 379 | 605, 635 | 1.0/1.8 | 0.272/0.784 | 547 | 33.8 | 9.7 |
| [Cu(6,6'-Me$_2$bpy)(DPEPhos)]$^+$[d] | 372 | 564, 645 | 1.3/13.8 | 0.310/4.032 | 535 | 43.2 | 10.5 |
| [Cu(6,6'-Me$_2$bpy)(xantphos)]$^+$[d] | 379 | 606, 635 | 1.6/10.0 | 0.451/3.406 | 539 | 37.3 | 11.4 |
| [Cu(5,5'-Me$_2$bpy)(DPEPhos)]$^+$[d] | 390 | 622, 643 | 0.5/0.7 | 0.057/0.108 | 585 | 2.7 | 2.3 |
| [Cu(5,5'-Me$_2$bpy)(xantphos)]$^+$[d] | 390 | 616, 642 | 0.4/0.9 | 0.153/0.338 | 571 | 6.3 | 5.1 |

[a] Solution concentration = 2.5 x $10^{-5}$ mol $dm^{-3}$. [b] $\lambda_{exc}$ = 365 nm. [c] Biexponential fit using the equation $\tau_{1/2}(av) = \Sigma A_i\tau_i/\Sigma A_i$ where $A_i$ is the pre-exponential factor for the lifetime. [d] Values taken from reference 174.

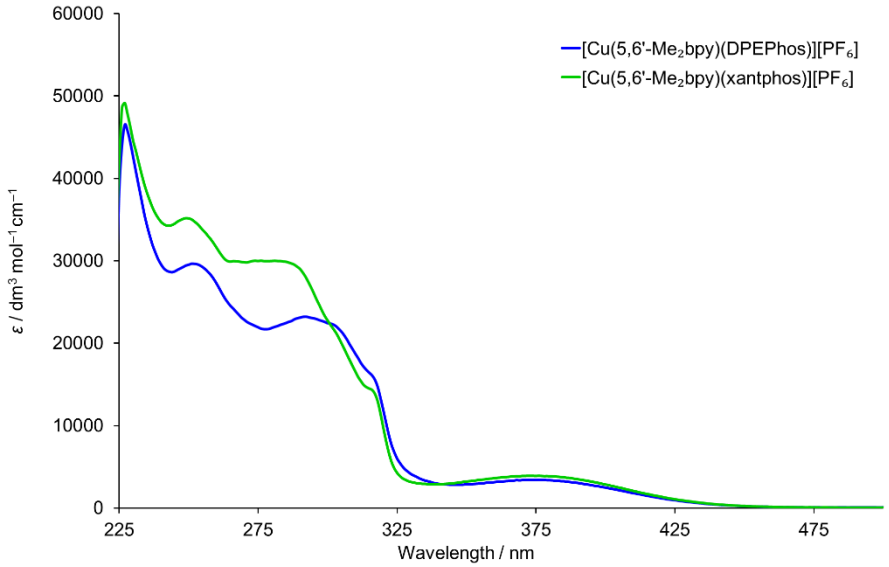


***Figure 3.9*** *Absorption spectra of the [Cu(5,6'Me$_2$bpy)(P^P)][PF$_6$] complexes ($CH_2Cl_2$, 2.5 x $10^{-5}$ mol $dm^{-3}$).*

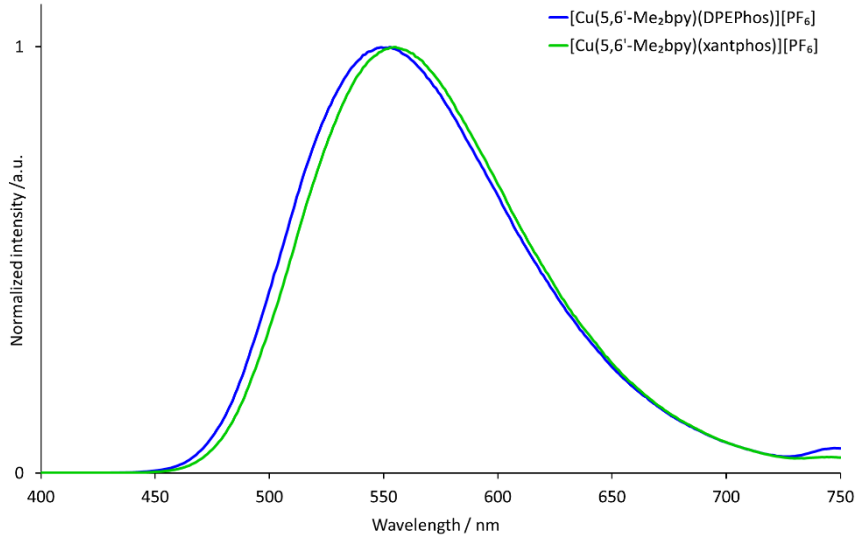


***Figure 3.10*** *Emission spectra of powder samples of [Cu(5,6'Me$_2$bpy)(P^P)][PF$_6$] complexes ($\lambda_{exc}$ = 365 nm).*

## 3.5 Conclusion

We were able to successfully prepare and characterize the complexes [Cu(5,6'-$Me_2$bpy)(DPEPhos)][$PF_6$] and[Cu(5,6'-$Me_2$bpy)(xantphos)][$PF_6$]. Both complexes are redox active and show a yellow emission in solution and in the solid state. PLQYs in degassed solution are low for both complexes. In the solid state, a moderately high PLQY of 12 and 11% is observed for the DPEPhos and xantphos complexes, respectively. This is surprising because an increase in radiative decay was expected compared to 6-Mebpy containing complexes. It is proposed that the electron-donating effect of the methyl group in the 5-position of the 2,2'-bipyridine is unfavourable towards the emissive properties. However, testing in a LEC configuration is still needed.

## 3.6 Experimental

### *3.6.1 5,6'-Dimethyl-2,2'-bipyridine (5,6'-$Me_2$bpy)*

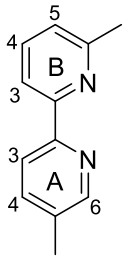


*n*BuLi (4.66 mL, 11.7 mmol, 2.5 M in hexane, 1.1 eq.) was added to a degassed solution of 2-bromo-6-methylpyridine (2.01 g, 11.7 mmol, 1.1 eq.) in dry THF (10 mL) at -78 °C under nitrogen atmosphere. The mixture was stirred for 30 min while it turned deep red. A solution of $ZnCl_2$ (10.6 ml, 10.6 mmol, 1.0 M in diethyl ether, 1.0 eq.) was added dropwise and the mixture was stirred for additional 1.5 h. The solution was allowed to warm to RT and was added dropwise to a degassed solution of Palladium-tetrakis(triphenylphosphine) (612 mg, 0.53 mmol, 0.05 eq.) and 2-bromo-5-methylpyridine (2.01 g, 11.7 mmol, 1.1 eq.) in dry THF (30 ml) and the mixture was heated to 80 °C for 60 h. The reaction mixture was allowed to cool to RT and a solution of NaOH in water (ca. 100 ml, 3 M) was added until most of the precipitate had dissolved. The mixture was extracted with $CH_2Cl_2$ (3 × 50 ml) and the combined organic fractions were washed with NaOH (aq.) and dried over $MgSO_4$. The solvent was removed under reduced pressure. The crude material was purified by column chromatography (Alox neutral, cyclohexane : ethyl acetate 40 : 1, then silica, cyclohexane : ethyl acetate 20 : 1) to give 5,6'-dimethyl-2,2'-bipyridine (937 mg, 5.08 mmol, 48%) as a white solid. $^1$H NMR (500 MHz, $CDCl_3$) $\delta$/ppm: 8.52 – 8.48 (m, 1H, $H^{A6}$), 8.29 (d, $J$ = 8.1 Hz, 1H, $H^{A3}$), 8.13 (d, $J$ = 7.9 Hz, 1H, $H^{B3}$), 7.68 (t, $J$ = 7.7 Hz, 1H, $H^{B4}$), 7.61 (ddd, , $J$ = 8.1, 2.2, 0.7 Hz, 1H, $H^{A4}$), 7.14 (d, $J$ = 7.6 Hz, 1H, $H^{B5}$), 2.63 (s, 3H, $H^{MeB6}$), 2.39 (s, 3H, $H^{MeA5}$). $^{13}$C{$^1$H} NMR (126 MHz, $CDCl_3$) $\delta$/ppm: 158.0($C^{B6}$), 155.8($C^{B2}$), 154.0($C^{A2}$), 149.7($C^{A6}$), 137.6($C^{A4}$), 137.2($C^{B4}$), 133.3($C^{A5}$), 123.1($C^{B5}$), 120.9($C^{A3}$), 118.0($C^{B3}$), 24.8($C^{MeB6}$), 18.5($C^{MeA5}$). ESI MS: m/z 184.1 $[M + H]^+$ (base peak, calc. 184.1). Found: C 78.01, H 6.75, N 15.40; $C_{12}H_{12}N_2$ requires C 78.23, H 6.57, N 15.21%.

## *3.6.2 [Cu(5,6'-Me$_2$bpy)(DPEPhos)][PF$_6$]*

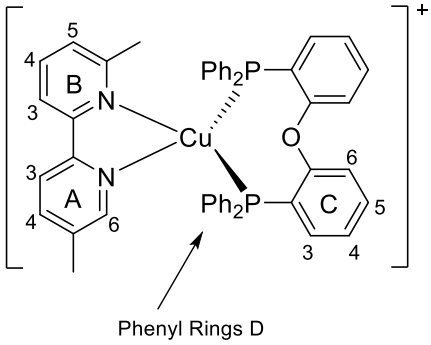


[Cu(MeCN)$_4$][PF$_6$] (93.2 mg, 0.25 mmol, 1.0 eq.) and DPEPhos (148 mg, 0.27 mmol, 1.1 eq.) were dissolved in $CH_2Cl_2$ (30 ml) and the mixture was stirred for 1.5 h at room temperature. 5,6'-Me$_2$bpy (46.1 mg, 0.25 mmol, 1.0 eq.) was added and stirring was continued for 1.5 h. The yellow solution was filtered and the solvent volume was reduced and added to hexane to precipitate the product. The solid material was washed with hexane (4 × 10 ml) by sonication and dried under vacuum to yield [Cu(5,6'-Me$_2$bpy)(DPEPhos)][PF$_6$] (173 mg, 0.19 mmol, 74%) as a yellow solid. $^1$H NMR (500 MHz, acetone-$d_6$) $\delta$/ppm: 8.39 (d, $J$ = 8.4 Hz, 1H, H$^{A3}$), 8.36 (d, $J$ = 8.3 Hz, 1H, H$^{B3}$), 8.21 (s, 1H, H$^{A6}$), 8.06 (t, $J$ = 7.8 Hz, 1H, H$^{B3}$), 7.86 (dd, $J$ = 8.4, 2.1 Hz, 1H, H$^{A4}$), 7.48 – 7.42 (m, 3H, H$^{B5+C5}$), 7.42 – 7.33 (m, 4H, H$^{D4+D4'}$), 7.31 (t, J = 7.5 Hz, 4H, H$^{D3}$), 7.28 – 7.18 (m, 10H, H$^{C6+D2+D3'}$), 7.15 (td, J = 7.5, 1.1 Hz, 2H, H$^{C4}$), 7.05 – 6.97 (m, 4H, H$^{D2'}$), 6.90 (dtd, J = 7.9, 4.0, 1.6 Hz, 2H, H$^{D3}$), 2.48 (s, 3H, H$^{MeB6}$), 2.11 (s, 3H, H$^{MeA5}$). $^{13}$C{$^1$H} NMR (126 MHz, acetone-$d_6$) $\delta$/ppm: 159.6(C$^{B6}$), 158.9 (t, $J$ = 6.1 Hz, C$^{C1}$), 152.8 (t, $J$ = 2.0 Hz, C$^{B2}$), 150.9 (t, $J$ = 2.0 Hz, C$^{A2}$), 150.4 (C$^{A6}$), 140.0 (C$^{B4}$), 139.9 (C$^{A4}$), 137.0, (C$^{A5}$) 135.0 (C$^{C3}$), 134.2 (t, $J$ = 7.8 Hz, C$^{D2}$), 133.7 (t, $J$ = 7.8 Hz, C$^{D2'}$), 133.2 (C$^{C5}$), 132.1 (C$^{D1'}$), 132.0 (C$^{D1}$), 131.2 (br, C$^{D4}$), 130.8 (br, C$^{D4'}$), 129.8 (t, $J$ = 4.4 Hz, C$^{D3}$), 129.6 (t, $J$ = 4.4 Hz, C$^{D3'}$), 126.6 (C$^{B5}$), 126.1 (t, $J$ = 2.2 Hz, C$^{C4}$), 125.0 (t, $J$ = 14.5 Hz, C$^{C2}$), 123.0 (C$^{A3}$), 121.2 (C$^{C6}$), 120.5 (C$^{B3}$), 26.8 (C$^{MeB6}$), 18.2 (C$^{MeA5}$). $^{31}$P{$^1$H} NMR (202 MHz, acetone-$d_6$) $\delta$/ppm: –12.5 (broad, FWHM = ~450 Hz), –144.2 (septet, $J_{PF}$ = 707 Hz, [PF$_6$]$^-$); ESI MS: $m/z$ 785.2 [M–PF$_6$]$^+$ (base peak, calc. 785.2). UV-Vis ($CH_2Cl_2$, 2.5 × 10$^{-5}$ mol dm$^{-3}$): $\lambda$/nm ($\varepsilon$/dm$^3$ mol$^{-1}$ cm$^{-1}$) 253 (29600), 293 (23000), 316 (16000) 376 (3400). Found: C 60.77, H 4.55, N 2.96; $C_{48}H_{40}CuF_6N_2OP_3$ requires C 61.90, H 4.33, N 3.01%.

## *3.6.3 [Cu(5,6'-Me$_2$bpy)(xantphos)][PF$_6$]*

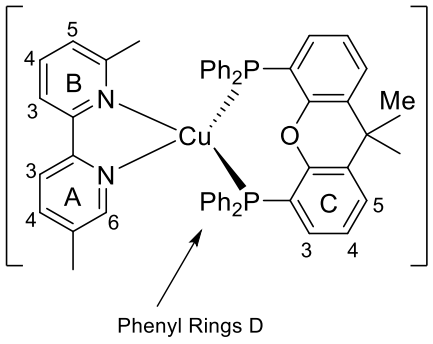


[Cu(MeCN)$_4$][PF$_6$] (93.2 mg, 0.25 mmol, 1.0 eq.) was dissolved in $CH_2Cl_2$ (15 ml). A solution of xantphos (145 mg, 0.25 mmol, 1.0 eq.) and 5,6'-Me$_2$bpy (46.1 mg, 0.25 mmol, 1.0 eq.) was added and the mixture turned orange then yellow while it was stirred for 1.5 h at room temperature. The yellow solution was filtered and the solvent volume was reduced under vacuum. Diethyl ether was added to precipitate the product. The solid material was washed with diethyl ether (4 × 10 ml) by sonication and dried under vacuum. [Cu(5,6'-Me$_2$bpy)(xantphos)][PF$_6$] (218 mg, 0.23 mmol, 90%) was isolated as a yellow solid. $^1$H NMR (500 MHz, acetone-$d_6$) $\delta$/ppm: 8.45 (d, $J$ = 8.0 Hz, 1H, H$^{A3}$), 8.43 (d, $J$ = 7.5 Hz, 1H, H$^{B3}$), 8.13 (t, $J$ = 7.8 Hz, 1H, H$^{B4}$), 7.90 – 7.86 (ov. m, 3H, H$^{A4+C5}$), 7.62 (s, 1H, H$^{A6}$), 7.52 (d, $J$ = 7.7 Hz, 1H, H$^{B5}$), 7.438 (t, $J$ = 7.6 Hz, 2H, H$^{D4'}$), 7.35 (t, $J$ = 7.2 Hz, 2H, H$^{D4}$), 7.29 (t, $J$ = 7.7 Hz, 2H, H$^{D4}$), 7.23 (m, 4H, H$^{D3'}$), 7.20 (m, 4H, H$^{D3}$), 7.08 (m, 4H, H$^{D2}$), 7.01 (m, 4H, H$^{D2'}$), 6.60 (dtd, $J$ = 7.6, 3.8, 1.4 Hz, 2H, H$^{C3}$), 2.40 (s, 3H, H$^{MeB6}$), 2.05 (s, 2H, H$^{MeA5}$), 1.87 (s, 3H, H$^{MeCq}$), 1.77 (s, 3H, H$^{MeCq'}$). $^{13}$C{$^1$H} NMR (126 MHz, acetone-$d_6$) $\delta$/ppm: 159.2 (C$^{B6}$),

155.9 (t, *J* = 6.2 Hz, $C^{C1}$), 152.5 (t, *J* = 2.0 Hz, $C^{B2}$), 151.0 (t, *J* = 2.2 Hz, $C^{A2}$), 149.6 ($C^{A6}$), 140.3 ($C^{B4}$), 140.2 ($C^{A4}$), 137.1 ($C^{A5}$), 135.1 (t, *J* = 1.7 Hz, $C^{C6}$), 133.8 (t, *J* = 8.1 Hz, $C^{D2'}$), 133.6 (t, *J* = 7.8 Hz, $C^{D2}$), 132.6 (t, *J* = 17.2 Hz, $C^{D1'}$), 132.3 (t, *J* = 17.1 Hz, $C^{D1}$), 131.6 ($C^{C3}$), 131.2 ($C^{D4'}$), 131.0 ($C^{D4}$), 129.8 (t, *J* = 4.8 Hz, $C^{D3'}$), 129.8 (t, *J* = 4.8 Hz, $C^{D3}$), 128.4 ($C^{C5}$), 126.6 ($C^{B5}$), 126.37 (t, *J* = 2.4 Hz, $C^{C4}$), 123.3 ($C^{A3}$), 121.36 (dd, *J* = 14.1, 12.9 Hz, $C^{C2}$), 120.7 ($C^{B3}$), 37.0 ($C^{Cq}$), 28.7 ($C^{MeCq'}$), 27.8 ($C^{MeCq}$), 26.9 ($C^{MeB6}$), 18.1 ($C^{MeA5}$). $^{31}P\{^{1}H\}$ NMR (202 MHz, acetone-$d_6$) $\delta$/ppm: –12.1 (broad, FWHM = ~330 Hz), –144.2 (septet, $J_{PF}$ = 707 Hz, $[PF_6]^-$); ESI MS: *m/z* 825.3 $[M–PF_6]^+$ (base peak, calc. 825.2). UV-Vis ($CH_2Cl_2$, $2.5 \times 10^{-5}$ mol $dm^{-3}$): $\lambda$/nm ($\varepsilon$/$dm^3$ $mol^{-1}$ $cm^{-1}$) 251 (35000), 287 (29700), 315 (14000) 374 (3900). Found: C 62.82, H 4.54, N 2.97; $C_{51}H_{44}CuF_6N_2OP_3$ requires C 63.06, H 4.57, N 2.88%.

# Chapter 4: Phosphane ligand tuning - Increasing steric demand

## 4.1 Motivation

The content of this chapter has been reproduced from reference 175.

In the previous chapters attention has been focused on modification of the N^N ligand of [Cu(N^N)(P^P)][$PF_6$] complexes. Many examples of N^N modified copper(I) complexes are known in the literature:[86,147,176–178] Costa *et al.* demonstrated a systematic study of different electron-withdrawing and -releasing groups in 4,4'-positions of a 2,2'-bipyridine ligand in [Cu(N^N)(xantphos)][$PF_6$] complexes.[154] Keller *et al.* investigated the influence of one or two methyl groups in the 6- and 6'-positions of 2,2'-bipyridine ligands in copper(I) complexes.[84,129,174] The P^P ligands DPEPhos and xantphos are often used because of their commercial availability and established complexation protocols. Copper(I) complexes where the P^P ligand is 1,2-bis(diphenylphosphino)benzene,[164] 1,1'-biphenyl-2,2'-diylbis(diphenylphosphane)[179] or 9,9-dimethyl-4,5-bis(di-*tert*-butylphosphino)xanthene[180] are known but most complexes incorporating these ligands showed poor emissive properties. The aromatic nature of the phosphorus substituents in combination with a backbone that allows for a wide bite angle P^P ligands seem to be crucial properties for luminescent copper(I) complexes.

In this chapter, we report on the effects of modifying the xantphos ligand and investigate the influence on both the structural and electronic properties. It has previously been reported that in [Cu(N^N)(DPEPhos)]$^+$ and [Cu(N^N)(xantphos)]$^+$ complexes, the HOMO is mainly centred on copper with small contributions from phosphorus, while the LUMO is localized on the N^N ligand.[83,84] Thus, structural modifications made to the backbone of the P^P ligand will have little if any effect on the energy level of the HOMO and any structural tuning should lead primarily to changes in steric effects. We decided to introduce *tert*-butyl groups into the 2,7-positions of xantphos to give $^t$Bu$_2$xantphos (**Scheme 4.1**); $^t$Bu$_2$xantphos has previously been used in combination with palladium(II) in vinylarene hydroamination catalysis.[181] The introduction of peripheral *tert*-butyl groups was expected to additionally result in a larger spatial separation of complex ions in the active layer in a LEC. Therefore its influence on the electroluminescent properties was anticipated.

Other bisphosphane ligands investigated in this work were 4,5-bis(dimesitylphosphino)-9,9-dimethylxanthene (xantphosMes$_4$) and 4,5-bis(mesitylphenylphosphino)-9,9-dimethylxanthene (xantphosMes$_2$), in which the $PPh_2$ groups in xantphos were replaced by either $PMes_2$ or PPhMes units (**Scheme 4.1**), thereby tuning the Tolman cone angle[182] of the phosphane. The N^N ligands chosen for the investigation were bpy, 6-Mebpy and 6,6'-$Me_2$bpy (**Scheme 4.1**). The photophysical properties of [Cu(N^N)(xantphos)][$PF_6$] (N^N = bpy, 6-Mebpy and 6,6'-$Me_2$bpy) have been previously reported,[83,84,129] giving a benchmark series for the present investigation.

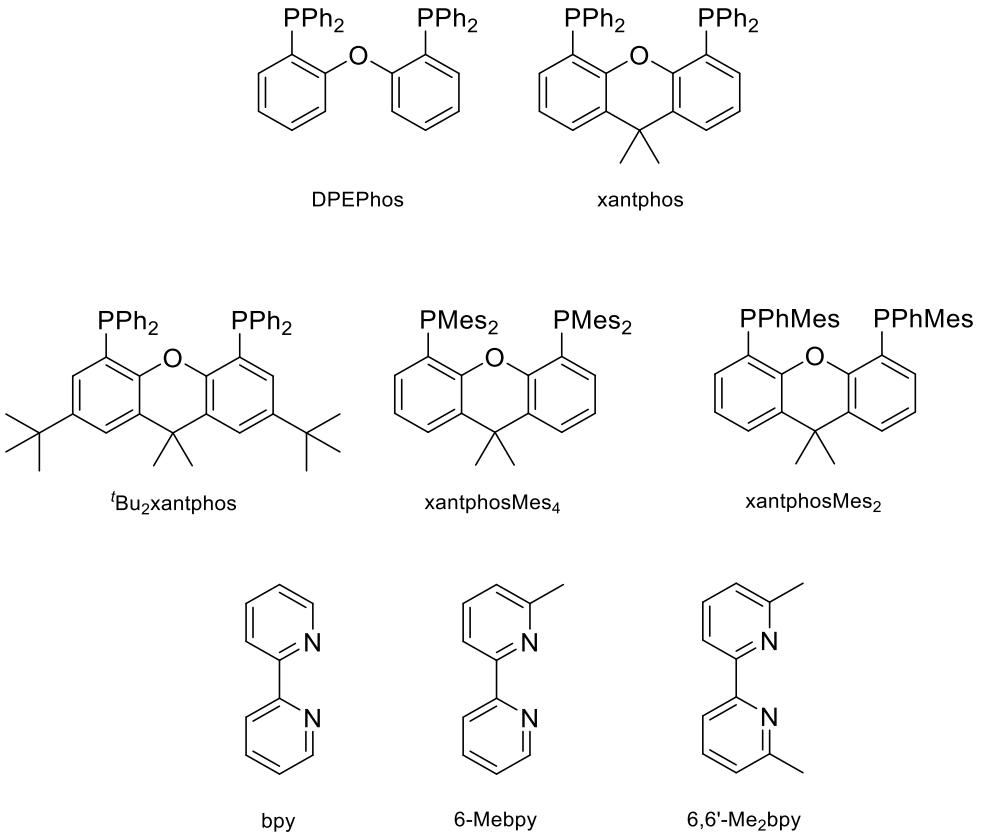


***Scheme 4.1*** *Structures of the P^P and N^N ligands.*

## 4.2 Synthesis

### *4.2.1 Ligand synthesis*

The P^P ligand $^{t}$Bu$_2$xantphos was synthesized using the literature procedure.[181] The synthetic routes to xantphosMes$_4$ and xantphosMes$_2$ were based on the strategy of Hamann and Hartwig to prepare bidentate phosphanes with varying steric properties.[183] The syntheses of xantphosMes$_4$ and xantphosMes$_2$ are summarized in **Scheme 4.2**. Both compounds were isolated as white solids, but facile oxidation to the phosphane oxides made it difficult to obtain analytically pure samples. The electrospray (ESI) mass spectra of xantphosMes$_4$ and xantphosMes$_2$ showed base peaks at *m/z* 747.3 and 663.5, respectively, arising from the $[M+H]^+$ ions. Single crystals of xantphosMes$_2$ were grown from an Et$_2$O solution of the compound by slow evaporation. **Figure 4.1** shows an ORTEP-style plot of the molecule and important bond parameters are given in the figure caption. Few chiral xantphos-derived ligands have been reported in the literature,[184,185] and the solid-state structure of xantphosMes$_2$ represents the (*rac*)-form of xantphosMes$_2$. It crystallizes in the monoclinic $P2_1/n$ space group with both the (*R,R*)- and (*S,S*)-enantiomers in the unit cell; the (*S,S*)-enantiomer is shown in **Figure 4.1**. The xanthene unit deviates very slightly from planarity, in contrast to the 'bowl' shape that is commonly adopted.

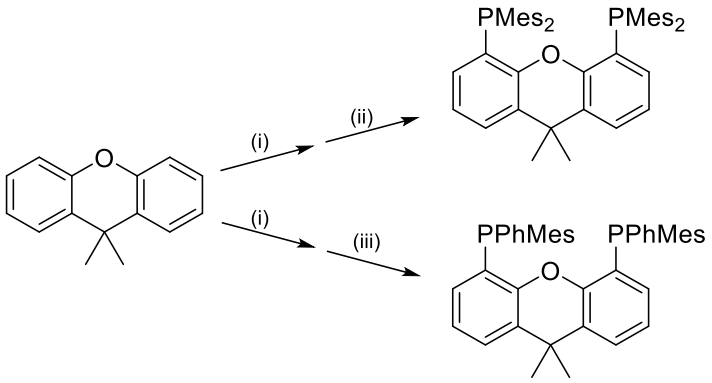


***Scheme 4.2*** *Syntheses of xantphosMes4 and xantphosMes2. Conditions: (i) nBuLi, dry heptane, TMEDA, reflux, 20 min; (ii) Mes2PCl, THF, 0 °C, 1 h; (iii) MesPhPCl, THF, 0 °C, 1 h.*

The $^{31}P\{^{1}H\}$ NMR spectra of xantphosMes4 and xantphosMes2 exhibit resonances at $\delta$ –36.2 and –25.8 ppm, respectively, consistent with one phosphorus environment in each compound. $^{1}H$ and $^{13}C\{^{1}H\}$ NMR spectra (see section 4.6) were assigned by 2D methods and were in accordance with functionalization in the 4,5-positions of the xanthene unit (**Scheme 4.2**). The $^{1}H$ NMR spectra are shown in **Figure 4.2** and **Figure 4.3**. The $^{1}H$ NMR spectrum of xantphosMes2 (**Figure 4.3**) also shows the presence of a subspecies in solution, present in <10% based on integration. The chemical shifts of the low intensity signals and the presence of diagnostic NOESY peaks suggest the major and minor species are structurally related, and we assign them to the (*rac*)- and (*meso*)-forms, respectively. Based on the preference seen in the solid-state, we propose that the dominant species is the (*rac*)-form. Thus, the bisphosphane is preorganized to give particular diastereoisomers upon complexation with copper(I) and this is indeed the case as discussed later.

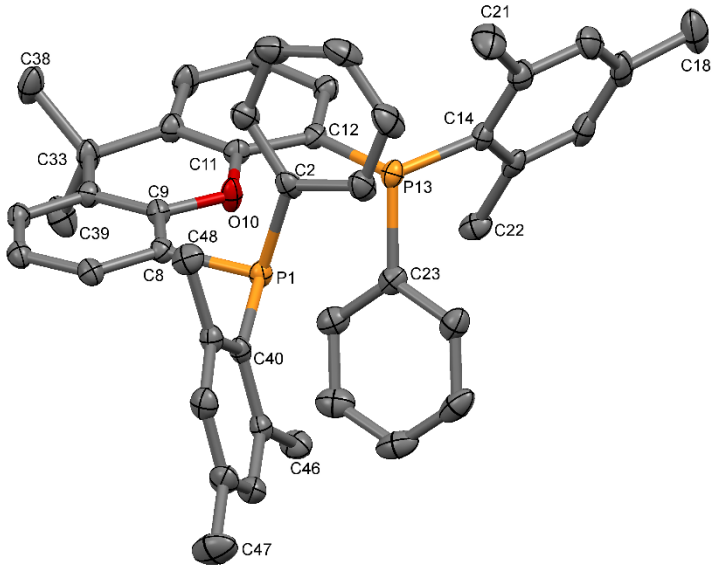


***Figure 4.1*** *Molecular structure of xantphosMes2 with ellipsoids plotted at 50% probability level; H atoms are omitted for clarity. Selected bond parameters: P1–C2 = 1.8326(14), P1–C8 = 1.8432(13), P1–C40 = 1.8492(14), P13–C12 = 1.8357(13), P13–C14 = 1.8417(14), P13–C23 = 1.8378(15), C9–O10 = 1.3758(16), O10–C11 = 1.3746(16) Å; C2–P1–C8 = 103.30(6), C2–P1–C40 = 106.26(6), C8–P1–C40 = 102.94(6), C12–P13–C14 = 102.10(6), C12–P13–C23 = 103.57(6), C14–P13–C23 = 104.92(6), C9–O10–C11 = 120.07(10)°.*

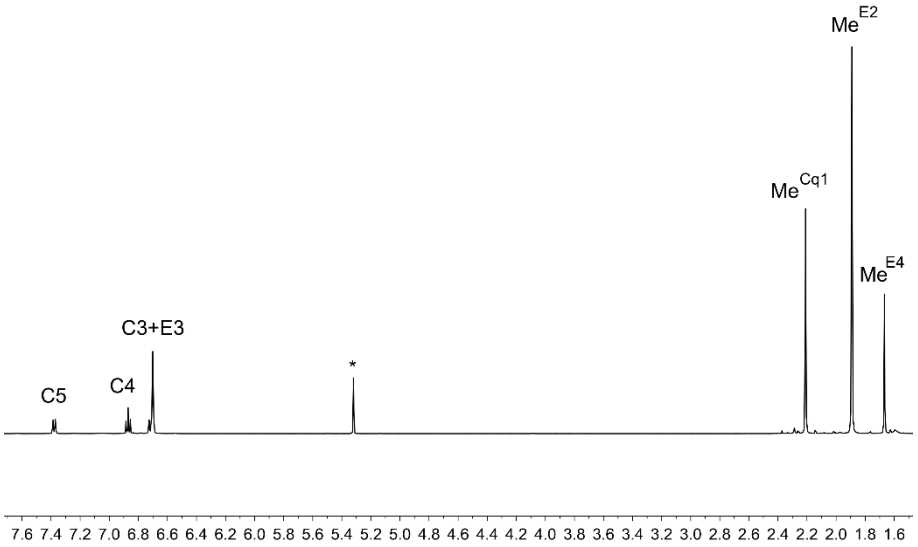


***Figure 4.2*** *$^1$H NMR spectrum (500 MHz, $CD_2Cl_2$) of xantphosMe$_4$, assigned by 2D methods. See section 4.6 for atom labels. * = residual $CDHCl_2$.*

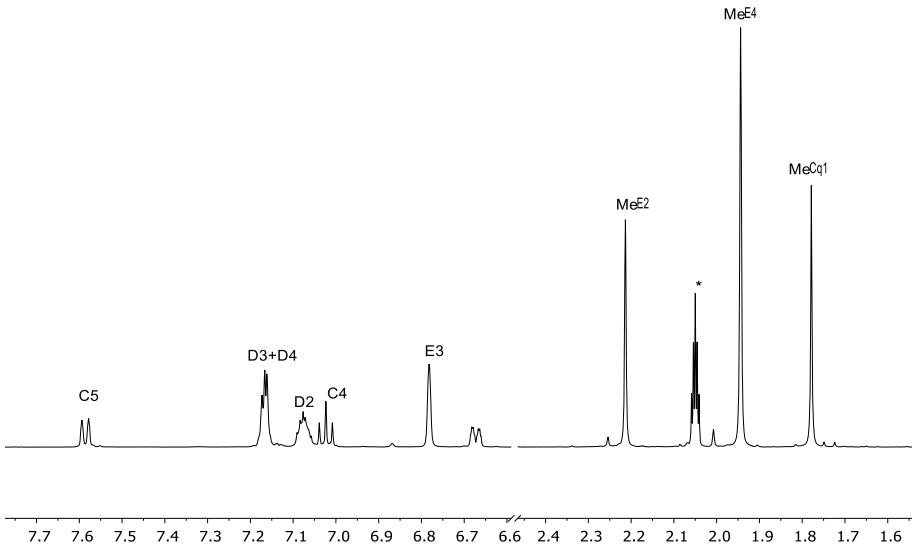


***Figure 4.3*** *Part of the $^1$H NMR spectrum (500 MHz, acetone-$d_6$) of xantphosMes$_2$, assigned by 2D methods. See section 4.6 for atom labels. * = residual acetone-$d_5$.*

## *4.2.2 Copper complex synthesis*

Attempts to prepare [Cu(bpy)(xantphosMes$_4$)][$PF_6$], [Cu(6-Mebpy)(xantphosMes$_4$)][$PF_6$] and [Cu(6,6'-Mebpy)(xantphosMes$_4$)][$PF_6$] by reaction of [Cu(MeCN)$_4$][$PF_6$] and xantphosMes$_4$ followed by the corresponding 2,2'-bipyridine ligand failed to yield the desired heteroleptic complexes. The $^{31}P\{^1H\}$ spectrum of each crude reaction mixture was dominated by a signal for the free ligand ($\delta$ –36.2 ppm), and also exhibited several other unassigned signals. Evidence for the formation of [Cu(xantphosMes$_4$)]$^+$ came from ESI mass spectrometry with a peak envelope at *m/z* 809.5. Mononuclear [Cu(P^P)]$^+$ complexes containing sterically demanding substituents attached to the phosphorus atoms are known, for example [Cu($^t$Bu-xantphos-$\kappa^{P,O,P}$)][$PF_6$][180] ($^t$Bu-xantphos = 9,9-dimethyl-4,5-bis(di-*tert*-butylphosphino)xanthene) and 3-coordinate copper(I) complexes with P^N^P pincer ligands.[186] Since xantphosMes$_4$ proved to be too sterically

demanding for the formation of $[Cu(N^N)(xantphosMes_4)]^+$ species, we turned our attention to the use of $xantphosMes_2$.

Heteroleptic $[Cu(N^N)(P^P)]^+$ complexes with P^P = $^tBu_2$xantphos or $xantphosMes_2$ were prepared using the established procedure[83] by the addition of a mixture of the xantphos and bpy ligands to a solution of $[Cu(MeCN)_4][PF_6]$ in $CH_2Cl_2$. This procedure avoids competitive formation of homoleptic $[Cu(P^P)_2]^+$ complexes.[141] Homoleptic $[Cu(N^N)_2]^+$ complexes where N^N is a bpy derivative, and heteroleptic $[Cu(N^N)(xantphos)]^+$ species are typically red and yellow, respectively. In all cases, the reaction mixture remained orange after being stirred for 1–2 hours, suggesting incomplete conversion to the heteroleptic complex. To force full conversion, an additional 0.2 equivalents of the bisphosphane ligand were added, resulting in the solution turning yellow. After being stirred for a further 2.5 hours, the solvent was removed and the excess ligand was removed by washing with $Et_2O$. This procedure yielded $[Cu(bpy)(^tBu_2xantphos)][PF_6]$, $[Cu(6\text{-}Mebpy)(^tBu_2xantphos)][PF_6]$, $[Cu(6,6'\text{-}Me_2bpy)(^tBu_2xantphos)][PF_6]$, $[Cu(bpy)(xantphosMes_2)][PF_6]$ and $[Cu(6\text{-}Mebpy)(xantphosMes_2)][PF_6]$ as yellow powders. In the reaction between $[Cu(MeCN)_4][PF_6]$, $xantphosMes_2$ and 6,6'-$Me_2$bpy, the yellow colour corresponding to a heteroleptic complex was not observed and only a red solid, identified by NMR spectroscopy and mass spectrometry as $[Cu(6,6'\text{-}Me_2bpy)_2][PF_6]$,[187] could be isolated. We suggest that the steric demands of the substituents in 6,6'-$Me_2$bpy combined with the two mesityl groups in $xantphosMes_2$ militate against the formation of $[Cu(6,6'\text{-}Me_2bpy)(xantphosMes_2)][PF_6]$.

The five heteroleptic compounds were characterized by $^1H$, $^{13}C\{^1H\}$ and $^{31}P\{^1H\}$ NMR spectroscopies, elemental analysis, ESI mass spectrometry and IR spectroscopy, as well as representative single crystal structures. The ESI mass spectrum of each complex containing $^tBu_2$xantphos exhibited a base peak corresponding to the $[M–PF_6]^+$ ion. The ESI mass spectrum of $[Cu(bpy)(xantphosMes_2)][PF_6]$ showed a base peak envelope at *m/z* 725.4 assigned to $[Cu(xantphosMes_2)]^+$ and a lower intensity peak envelope at *m/z* 881.5 arising from $[M–PF_6]^+$. For $[Cu(6,6'\text{-}Me_2bpy)(xantphosMes_2)][PF_6]$, the ESI mass spectrum exhibited only a peak envelope for the $[Cu(xantphosMes_2)]^+$ ion (*m/z* 725.4). Elemental analysis and the NMR spectra confirmed the formation of a heteroleptic complex. The solution NMR spectroscopic properties are discussed in section 4.3.2.

## 4.3 Structural Discussion

### *4.3.1 Single crystal structures*

Single crystals of $[Cu(bpy)(^tBu_2xantphos)][PF_6]\cdot0.5Et_2O$, $[Cu(6\text{-}Mebpy)(^tBu_2xantphos)][PF_6]\cdot1.5CH_2Cl_2\cdot0.5H_2O$, $[Cu(bpy)(xantphosMes_2)][PF_6]$ and $[Cu(6\text{-}Mebpy)(xantphosMes_2)][PF_6]$ were obtained by layering $Et_2O$ over a $CH_2Cl_2$ solution of each complex. The $^tBu_2$xantphos-containing compounds crystallized in the triclinic space group *P*–1, whereas $[Cu(bpy)(xantphosMes_2)][PF_6]$ and $[Cu(6\text{-}Mebpy)(xantphosMes_2)][PF_6]$ crystallized in the monoclinic space group *C*2/*c*. **Figure 4.6** - **Figure 4.9** show ORTEP-style plots of the $[Cu(^tBu_2xantphos)]^+$, $[Cu(bpy)(^tBu_2xantphos)(6\text{-}Mebpy)]^+$, $[Cu(bpy)(xantphosMes_2)]^+$, and $[Cu(6\text{-}Mebpy)(xantphosMes_2)]^+$ cations. Selected structural parameters are given in the captions to **Figure 4.6** - **Figure 4.9**, and important parameters are compared in **Table**

**4.1**. In each cation, the copper(I) centre is in a distorted tetrahedral geometry and the xanthene backbone adopts a 'bowl' (boat) conformation, which is observed for the majority of free and coordinated xantphos ligands. A search of the Cambridge Structural Database (CSD[188] v. 5.39, Conquest[3] v. 1.2, search 10 August 2018) revealed 254 xantphos-containing structures, with flattening of the xanthene unit usually being associated with a $\kappa^{P,O,P}$ coordination mode. The angle between the P–Cu–P and N–Cu–N planes (**Table 1.1**) is close to 90° in [Cu(6-Mebpy)(P^P)][$PF_6$] and slightly smaller in [Cu(bpy)(P^P)][$PF_6$]. The bite angle of the P^P ligand increases slightly on going from $^t$Bu$_2$xantphos to xantphosMes$_2$ (**Table 4.1**), consistent with the increased steric effects of PPhMes *versus* $PPh_2$.

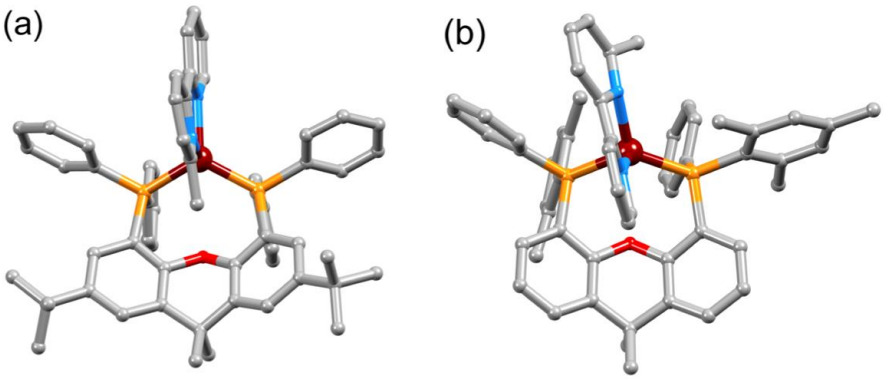


***Figure 4.4*** *(a) Structure of the [Cu(6-Mebpy)($^t$Bu$_2$xantphos)]$^+$ cation. (b) Structure of one conformer of [Cu(6-Mebpy)(xantphosMes$_2$)]$^+$ in [Cu(6-Mebpy)(xantphosMes$_2$)][$PF_6$] in which the 6-Mebpy ligand is disordered over two sites. H atoms are omitted.*

On going from [Cu(bpy)(P^P)]$^+$ to [Cu(6-Mebpy)(P^P)]$^+$, the introduction of the 6-methyl group in the bpy unit lowers the symmetry of the cation. The methyl substituent can, in principle, lie over the xanthene 'bowl' or be remote from it.[84] **Figure 4.4a** shows that in [Cu(6-Mebpy)($^t$Bu$_2$xantphos)][$PF_6$], the methyl group lies over the xanthene unit. In contrast, in [Cu(6-Mebpy)(xantphosMes$_2$)][$PF_6$], the 6-Mebpy ligand is orientationally disordered over two sites, each with 50% occupancy. **Figure 4.4b** depicts the conformer in which the Me group is remote from the xanthene unit; the second conformer is structurally related to [Cu(6-Mebpy)($^t$Bu$_2$xantphos)]$^+$ (**Figure 4.4a**). The N–C–C–N torsion angles in **Table 1.1** demonstrate that the bpy unit is significantly more twisted in the cations containing the xantphosMes$_2$ ligand than those with $^t$Bu$_2$xantphos. This appears to be associated with the fact that in both [Cu(bpy)(xantphosMes$_2$)][$PF_6$] (**Figure 4.5**) and [Cu(6-Mebpy)(xantphosMes$_2$)][$PF_6$] one methyl group of one mesityl substituent is directed towards the middle of the bpy domain (**Figure 4.5b**). This spatial proximity is characterized by $C_{Me(Mes)}\cdots centroid_{pyridine}$ distances of 3.98 and 4.37 Å ($H_{Me(Mes)}\cdots centroid_{pyridine}$ = 3.16 and 3.56 Å) in the [Cu(bpy)(xantphosMes$_2$)]$^+$ cation. Corresponding separations in [Cu(6-Mebpy)(xantphosMes$_2$)]$^+$ are 4.00 and 4.38 Å (3.24 and 3.57 Å) and 3.85 and 4.39 Å (3.27 and 3.48 Å) for the two partial occupancy 6-Mebpy sites.

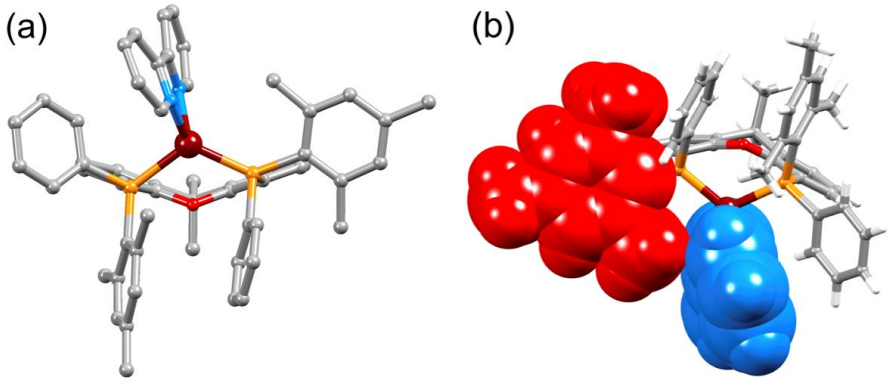


***Figure 4.5*** *Structure of the [Cu(bpy) (xantphosMe$_2$)]$^+$ cation (a) emphasizing the relative positions of the phenyl and mesityl substituents with respect to the bpy unit, and (b) with the bpy (blue) and one mesityl group (red) shown in space-filling representation to emphasize their spatial proximity.*

***Table 4.1*** *Selected structural parameters of [Cu(P^P)(N^N)]$^+$ complex cations.*

| complex cation | P-Cu-P chelating angle/° | N-Cu-N chelating angle/° | Angle between P-Cu-P and N-Cu-N planes /° | N-C-C-N torsion angle/° |
|---|---|---|---|---|
| [Cu(bpy)($^t$Bu$_2$xantphos)]$^+$ | 113.56(2) | 79.90(7) | 84.1 | −0.4(3) |
| [Cu(6-Mebpy)($^t$Bu$_2$xantphos)]$^+$ | 112.70(7) | 80.1(2) | 89.3 | 2.5(8) |
| [Cu(bpy)(xantphosMes$_2$)]$^+$ | 115.96(2) | 79.08(6) | 86.1 | 15.0(2) |
| [Cu(6-Mebpy)(xantphosMes$_2$)]$^+$ | 115.25(3) | 78.6(1)$^a$ | 89.3$^a$ | −23.3(6)$^a$ |
| | | 79.4(1)$^b$ | 89.0$^b$ | −22.5(6)$^b$ |

$^a$ Values for the conformer with 6-Mebpy oriented with the 6-Me group away from the xanthene bowl as in Fig. 2b. $^b$ Values for the conformer with 6-Mebpy oriented with the 6-Me group lying over the xanthene bowl.

***Table 4.2*** *Crystallographic parameters of [Cu(N^N)(P^P)][PF$_6$] complexes.*

| Compound | xantphosMes2 | [Cu(bpy)($^t$Bu$_2$xantphos)][PF$_6$] ·0.5Et$_2$O | [Cu(6-Mebpy)($^t$Bu$_2$xantphos)][PF$_6$] ·1.5CH$_2$Cl$_2$·0.5H$_2$O | [Cu(bpy) (xantphosMes$_2$)] [PF$_6$] | [Cu(6-Mebpy) (xantphosMes$_2$)] [PF$_6$] |
|---|---|---|---|---|---|
| Formula | $C_{45}H_{44}OP_2$ | $C_{59}H_{61}CuF_6N_2O_{1.5}P_3$ | $C_{59.5}H_{62}Cl_3CuF_6N_2O_{1.5}P_3$ | $C_{55}H_{52}CuF_6N_2OP_3$ | $C_{56}H_{54}CuF_6N_2OP_3$ |
| Formula weight | 662.79 | 1092.60 | 1205.97 | 1027.49 | 1041.51 |
| Crystal colour and habit | Colourless plate | Yellow block | Yellow block | Yellow block | Yellow block |
| Crystal system | Monoclinic | Triclinic | Triclinic | Monoclinic | Monoclinic |
| Space group | $P2_1/n$ | $P\bar{1}$ | $P\bar{1}$ | $C2/c$ | $C2/c$ |
| $a, b, c$ / Å | 10.6380(9)<br>15.0841(13)<br>23.545(2) | 12.0991(12)<br>13.3253(13)<br>18.6750(18) | 10.7080(9)<br>13.4475(12)<br>22.167(2) | 38.341(2)<br>11.8342(7)<br>26.5208(14) | 38.1932(19)<br>12.0648(6)<br>26.5270(13) |
| $\alpha, \beta, \gamma$ / ° | 90<br>102.585(3)<br>90 | 91.353(3)<br>90.939(3)<br>115.475(2) | 73.142(6)<br>79.483(6)<br>86.606(6) | 90<br>126.4524(19)<br>90 | 90<br>127.0427(19)<br>90 |
| $U$ / Å$^3$ | 3687.4(5) | 2716.2(5) | 3003.4(5) | 9679.2(10) | 9756.6(9) |
| $Dc$ / Mg m$^{-3}$ | 1.194 | 1.336 | 1.33 | 1.410 | 1.418 |
| $Z$ | 4 | 2 | 2 | 8 | 8 |
| $\mu$(Cu-Kα) / mm$^{-1}$ | 1.317 | 1.932 | 2.997 | 2.126 | 2.117 |
| $T$ / K | 123 | 123 | 123 | 123 | 123 |
| Refln. collected ($R_{int}$) | 40993 (0.035) | 35686 (0.029) | 35561 (0.082) | 29726 (0.027) | 31926 (0.033) |
| Unique refln. | 6810 | 9826 | 10903 | 8726 | 8749 |
| Refln. for refinement | 6264 | 9540 | 7619 | 7795 | 7701 |
| Parameters | 433 | 664 | 700 | 613 | 685 |
| Threshold | $2\sigma$ | $2\sigma$ | $2\sigma$ | $2\sigma$ | $2\sigma$ |
| $R1$ ($R1$ all data) | 0.0336 (0.0365) | 0.0416 (0.0423) | 0.1178 (0.1490) | 0.0320 (0.0362) | 0.0467 (0.0531) |
| $wR2$ ($wR2$ all data) | 0.0776 (0.0794) | 0.1012 (0.1016) | 0.1151 (0.1470) | 0.0851 (0.0870) | 0.0586 (0.0623) |
| Goodness of fit | 0.9775 | 0.9707 | 1.0317 | 1.0356 | 0.9991 |
| CCDC deposition‡ | 1860879 | 1844060 | 1844063 | 1844062 | 1844061 |

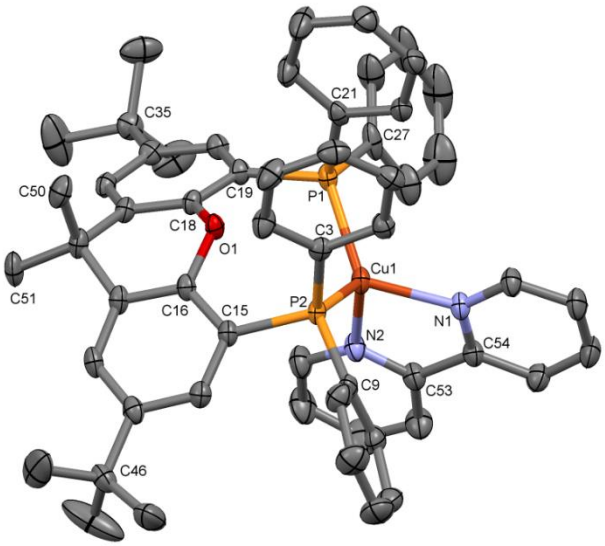


***Figure 4.6*** *Structure of the [Cu(bpy)(tBu2xantphos)]+ cation in [Cu(bpy)(tBu2xantphos)][PF6]·0.5Et2O with ellipsoids plotted at 50% probability level; H atoms are omitted for clarity. Selected bond parameters: Cu1–P1 = 2.2580(6), Cu1–P2 = 2.2522(6), Cu1–N1 = 2.056(2), Cu1–N2 = 2.070(2) Å; P1–Cu1–P2 = 113.56(2), P1–Cu1–N1 = 118.71(5), P2–Cu1–N1 = 112.59(5), P1–Cu1–N2 = 110.19(5), P2–Cu1–N2 = 117.97(5), N1–Cu1–N2 = 79.90(7)°.*

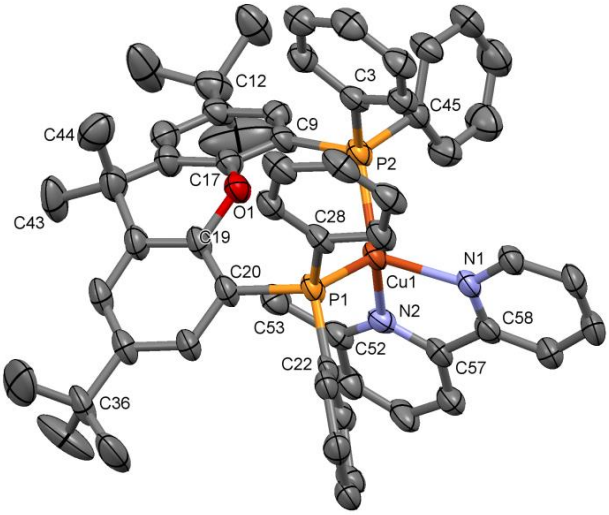


***Figure 4.7*** *Structure of the [Cu(6-Mebpy) (tBu2xantphos)]+ cation in [Cu(6-Mebpy)(tBu2xantphos)][PF6]·1.5CH2Cl2·0.5H2O with ellipsoids plotted at 50% probability level; H atoms are omitted for clarity. Selected bond parameters: Cu1–P1 = 2.277(2), Cu1–P2 = 2.254(2), Cu1–N1 = 2.065(6), Cu1–N2 = 2.081(4) Å; P1–Cu1–P2 = 112.70(7), P1–Cu1–N1 = 112.1(2), P2–Cu1–N1 = 115.9(2), P1–Cu1–N2 = 114.9(1), P2–Cu1–N2 = 117.3(1), N1–Cu1–N2 = 80.1(2)°.*

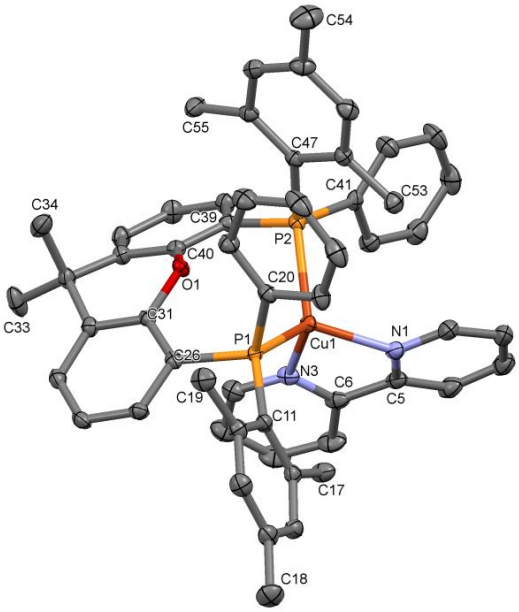


***Figure 4.8*** *Structure of the [Cu(bpy)(xantphosMes$_2$)]$^+$ cation in [Cu(bpy)(xantphosMes$_2$)][PF$_6$] with ellipsoids plotted at 50% probability level; H atoms are omitted for clarity. Selected bond parameters: Cu1–P1 = 2.2808(6), Cu1–P2 = 2.3343(5), Cu1–N1 = 2.098(1), Cu1–N3 = 2.106(1) Å; P1–Cu1–P2 = 115.96(2), P1–Cu1–N1 = 128.48(4), P2–Cu1–N1 = 106.96(4), P1–Cu1–N3 = 112.79(4), P2–Cu1–N3 = 106.11(4), N1–Cu1–N3 = 79.08(6)°.*

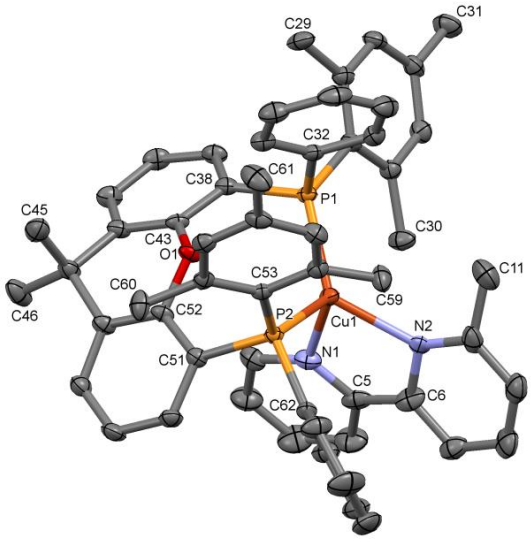


***Figure 4.9*** *Structure of one conformer of the [Cu(6-Mebpy)(xantphosMes$_2$)]$^+$ cation in [Cu(6-Mebpy)(xantphosMes$_2$)][PF$_6$] with ellipsoids plotted at 50% probability level; H atoms are omitted for clarity. The 6-Mebpy ligand is disordered and has been modelled over two sites, each with 50% occupancy. Selected bond parameters for one conformer: Cu1–P1 = 2.2993(7), Cu1–P2 = 2.3718(8), Cu1–N1 = 2.070(3), Cu1–N2 = 2.182(3) Å; P1–Cu1–P2 = 115.25(3), P1–Cu1–N1 = 112.3(1), P2–Cu1–N1 = 104.7(1), P1–Cu1–N2 = 126.3(1), P2–Cu1–N2 = 111.6(1), N1–Cu1–N2 = 78.6(1)°. The values are similar for the second conformer.*

### *4.3.2 Solution NMR spectroscopy*

The aromatic regions of the solution $^{1}$H NMR spectra of [Cu(bpy)($^{t}$Bu$_2$xantphos)][PF$_6$], [Cu(bpy)(xantphosMes$_2$)][PF$_6$] and [Cu(6,6'-Me$_2$bpy)($^{t}$Bu$_2$xantphos)][PF$_6$] show sharp signals, are well-resolved at room temperature and were assigned using COSY, NOESY, HMBC and HMQC methods. The $^{t}$Bu-substituents give rise to a singlet at $\delta$ 1.11 ppm in [Cu(bpy)($^{t}$Bu$_2$xantphos)][PF$_6$] and $\delta$ 1.16 ppm in [Cu(6,6'-Me$_2$bpy)($^{t}$Bu$_2$xantphos)][PF$_6$]. The two pyridine rings of bpy in [Cu(bpy)($^{t}$Bu$_2$xantphos)][PF$_6$] and [Cu(bpy)(xantphosMes$_2$)][PF$_6$] are magnetically equivalent. Similarly, the 6,6'-Me$_2$bpy ligand in [Cu(6,6'-Me$_2$bpy)($^{t}$Bu$_2$xantphos)][PF$_6$] is symmetric on the NMR timescale at room temperature. Keller *et al.* have previously detailed a solution dynamic behaviour for [Cu(N^N)(xantphos)]$^{+}$ complexes involving inversion of the xanthene unit ('bowl'),[84] and this is depicted in the first dynamic process illustrated in **Figure 4.10**. The scheme demonstrates that inversion of the xanthene bowl exchanges the environments of the xanthphos methyl groups (green and magenta in **Figure 4.10**) between axial and equatorial sites, but does not render pyridine rings A and B (represented by N$_A$ and N$_B$) equivalent. By invoking a second process involving movement of the {Cu(bpy)} unit (*i.e.*, a change in conformation of the chelate ring, **Figure 4.10**), N$_A$ and N$_B$ experience both sides of the xanthene bowl and are equivalent on the NMR timescale.

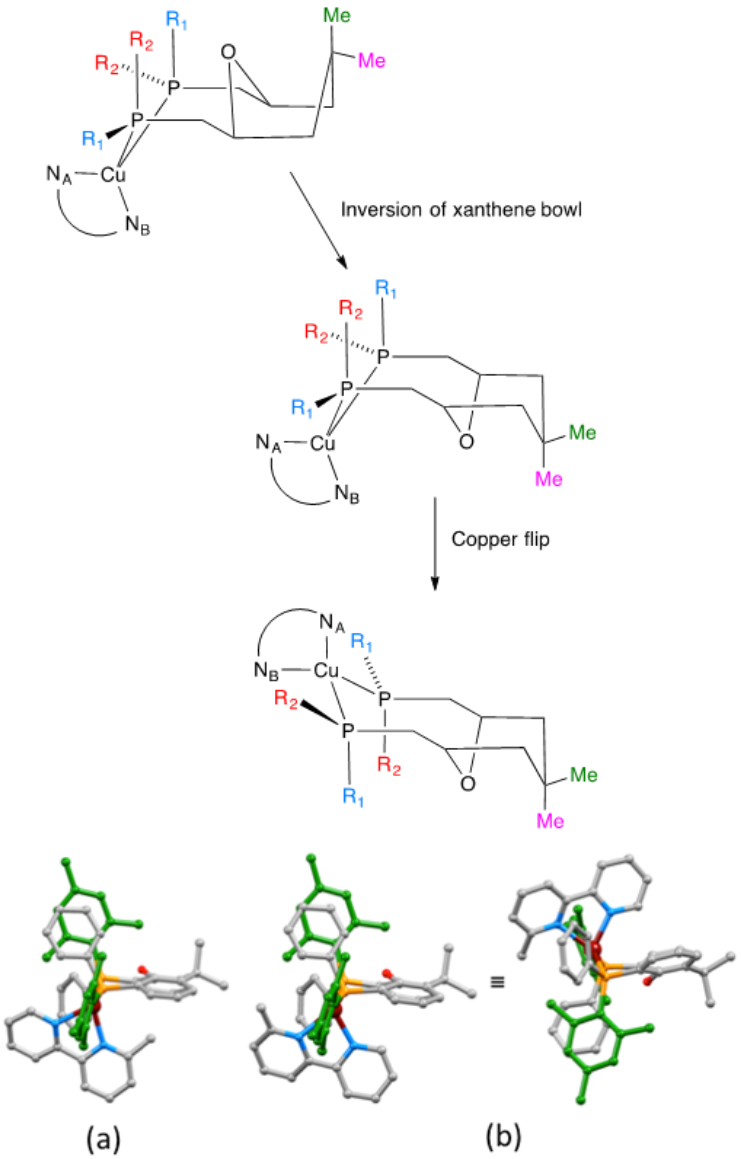


***Figure 4.10*** *Upper: Proposed dynamic processes in [Cu(bpy)(xantphos)]⁺ type compounds. $N_A$ and $N_B$ represent pyridine rings A and B. For $^t$Bu$_2$xantphos, $R_1$ = $R_2$ = Ph. For xantphosMes$_2$. $R_1$ = Mes, $R_2$ = Ph. Lower: Crystallographically determined structure of the [Cu(6-Mebpy)(xantphosMes$_2$)]⁺ cation in which the 6-Mebpy is orientationally disordered: (a) orientation 1 of 6-Mebpy, and (b) orientation 2 of 6-Mebpy shown in two views of the cation.*

On going from [Cu(bpy)($^t$Bu$_2$xantphos)][PF$_6$] to [Cu(6-Mebpy)($^t$Bu$_2$xantphos)][PF$_6$], the symmetry of the cation is lowered and phenyl rings D (experimental section 4.6) split into two sets, those proximate to the methyl group of 6-Mebpy and those on the side of the unsubstituted pyridine ring (**Figure 4.4 a**). **Figure 4.11** shows the aromatic region of the solution $^1$H NMR spectrum of [Cu(6-Mebpy)($^t$Bu$_2$xantphos)][PF$_6$], in which the sets of D rings are labelled D and D'. In the NOESY spectrum at 298 K, exchange (EXSY) peaks are observed between pairs of signals for protons D2/D2' and D3/D3'; the D4/D4' EXSY peaks appear too close to the diagonal in the NOESY spectrum to be clearly resolved. NOESY cross peaks (no EXSY) are observed between MeCq1 and MeCq1' (**Figure 4.12**). These observations are consistent with inversion of the chelate ring ('copper flip' in **Figure 4.10**) and no inversion of the xanthene bowl.

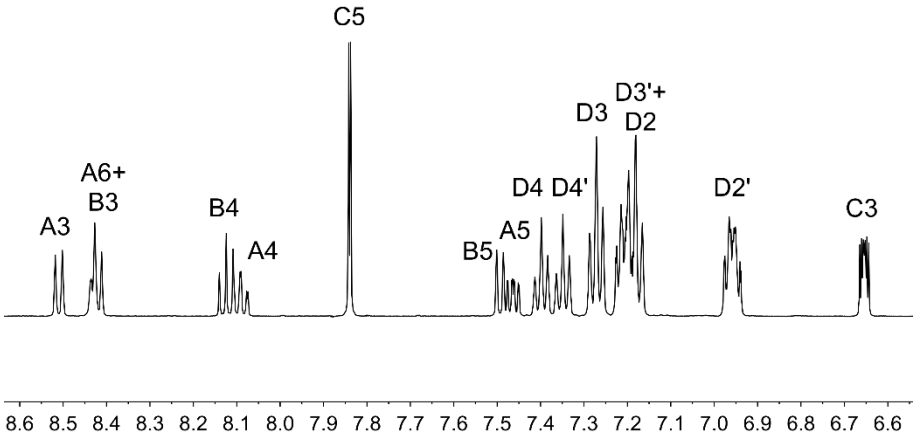


***Figure 4.11*** *Aromatic region of the $^{1}H$ NMR spectrum (500 MHz, acetone-$d_6$) of [Cu(6-Mebpy)($^{t}Bu_2$xantphos)][$PF_6$]. See section 4.6.6 for atom labelling.*

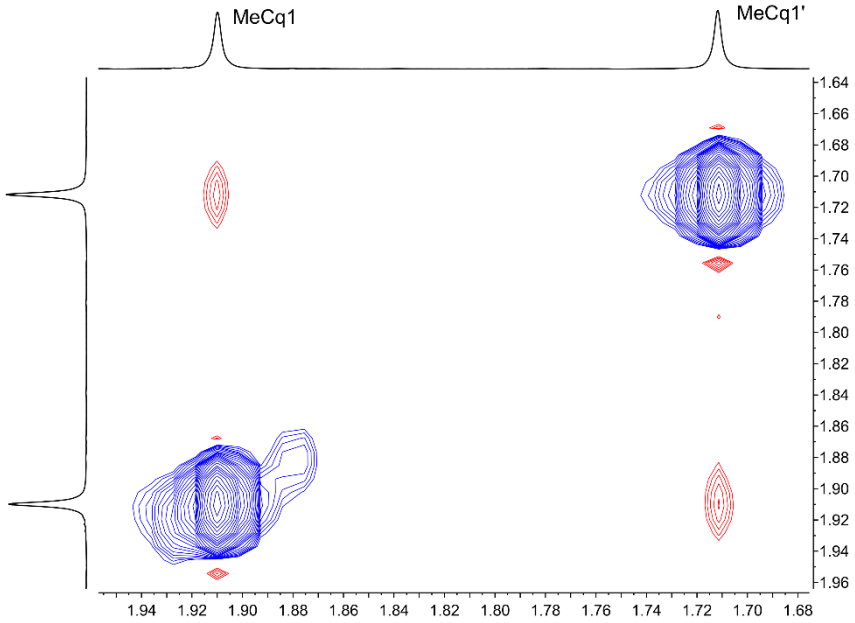


***Figure 4.12*** *Part of the NOESY spectrum (500 MHz, acetone-$d_6$) of [Cu(6-Mebpy)($^{t}Bu_2$xantphos)][$PF_6$] showing NOESY peaks between the two xanthene methyl groups Cq1/Cq1'.*

The single crystal structures of [Cu(bpy)(xantphosMes$_2$)][$PF_6$] and [Cu(6-Mebpy)(xantphosMes$_2$)][$PF_6$] reveal that the two PPhMes groups of the xantphosMes$_2$ ligand are mutually oriented as shown in **Figure 4.5a** and **Figure 4.10**. This desymmetrizes the xanthene unit (labelled rings C and C'). In addition, the equatorial and axial positions of the Ph and Mes substituents with respect to the chelate ring leads to chemical shift differences in the $^{1}H$ NMR spectrum for pairs of phenyl rings (D and D') and mesityl groups (E and E'). **Figure 4.13** shows the $^{1}H$ NMR spectrum of [Cu(6-Mebpy)(xantphosMes$_2$)][$PF_6$], and **Figure 4.14** and **Figure 4.15** show exchange peaks observed in the NOESY spectrum. Exchange peaks between the signals for phenyl proton D2/D2' and D4/D4' is consistent with the 'copper flip' shown in **Figure 4.10**. This leads to equivalence of the outer rings of the xanthene unit as confirmed by the EXSY peak between the signals for protons C3/C3'. The EXSY peak between signals for the xanthene methyl groups MeCq1 and MeCq1' (**Figure 4.15**) confirms the inversion of the xanthene

bowl (**Figure 4.10**). This contrasts with [Cu(6-Mebpy)($^t$Bu$_2$xantphos)][PF$_6$] where no exchange (only NOESY) peaks are observed (see above and **Figure 4.12**).

Earlier, we noted an orientational disorder of the 6-Mebpy ligand in the solid-state structure of [Cu(6-Mebpy)(xantphosMes$_2$)][PF$_6$]. The disorder was modelled with a 50% occupancy of each orientation and **Figure 4.10a** and **b** show the [Cu(6-Mebpy)(xantphosMes$_2$)]$^+$ with the two orientations of 6-Mebpy. The structure in **Figure 4.10a** corresponds to the top diagram in the scheme in **Figure 4.10**, while **Figure 4.10b** corresponds to the bottom diagram in the scheme. The disorder therefore parallels a combination of the two dynamic processes which we propose the cation undergoes in solution.

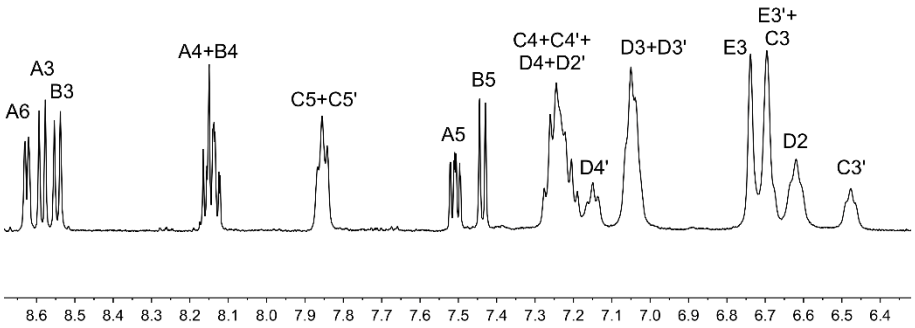


***Figure 4.13*** *Aromatic region of the $^1$H NMR spectrum (500 MHz, acetone-d$_6$) of [Cu(6-Mebpy)(xantphosMes$_2$)][PF$_6$]. See section 4.6.9 for atom labelling.*

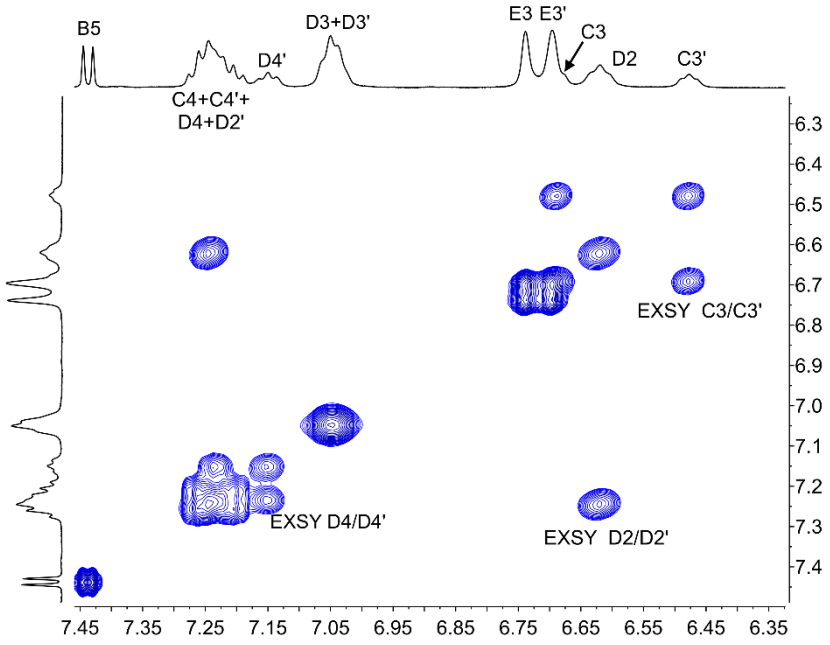


***Figure 4.14*** *Part of the NOESY spectrum (500 MHz, acetone-d$_6$) of [Cu(6-Mebpy)(xantphosMes$_2$)][PF$_6$] showing exchange (EXSY) peaks between pairs of protons C3 and C3', D2 and D2', and D4 and D4'.*

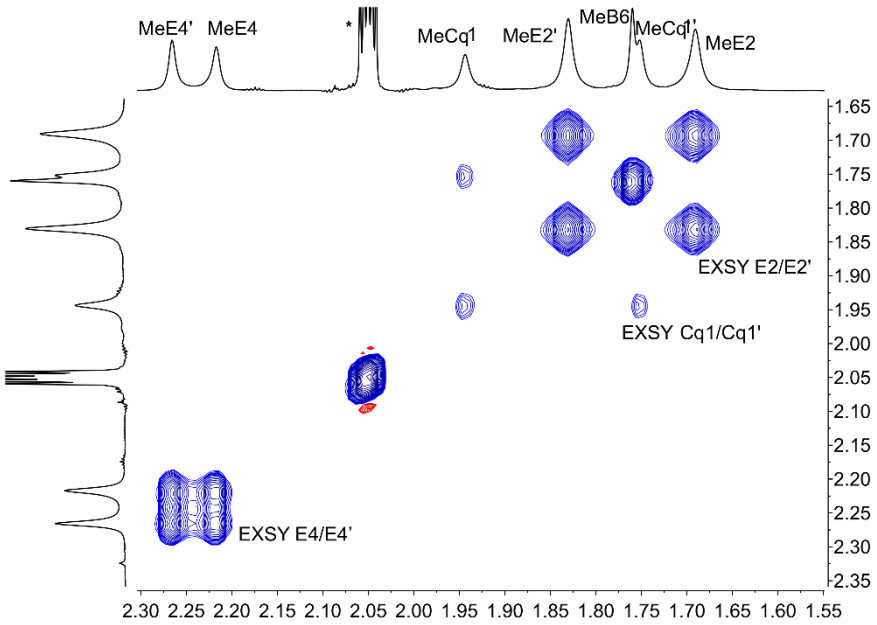


***Figure 4.15*** *Part of the NOESY spectrum (500 MHz, acetone-$d_6$) of [Cu(6-Mebpy)(xantphosMes$_2$)][PF$_6$] showing exchange (EXSY) peaks between pairs of mesityl methyl protons E2 and E2', E4/E4', and xanthene methyl protons Cq/Cq'. See section 4.6.9 for atom labelling. * = residual acetone-$d_5$.*

Variable temperature (VT) NMR spectra were recorded for an acetone-$d_6$ solution of [Cu(6-Mebpy)(xantphosMes$_2$)][PF$_6$]. The $^{31}$P{$^1$H} NMR spectrum (**Figure 4.18**) shows only one signal over the range 298–180 K. **Figure 4.16** shows the effect of temperature on the alkyl region of the $^1$H NMR spectrum of [Cu(6-Mebpy)(xantphosMes$_2$)][PF$_6$]. The collapse of the signals for mesityl-methyl protons MeE2 and MeE2' and appearance of four signals for these methyl groups below 218 K are consistent with freezing out the rotation of the mesityl groups. A similar temperature dependence is observed for the mesityl E3 protons in the aromatic region of the spectrum (**Figure 4.17**). Significant shifting of the xanthene methyl protons MeCq1 and MeCq1' (**Figure 4.16**) and 6-Mebpy protons A6 and MeB6 (**Figure 4.17**) can be attributed to changes in their magnetic environments as the mesityl groups adopt a static configuration. Both $^{31}$P{$^1$H} and $^1$H VT NMR spectra are consistent with the presence of only one conformer in solution.

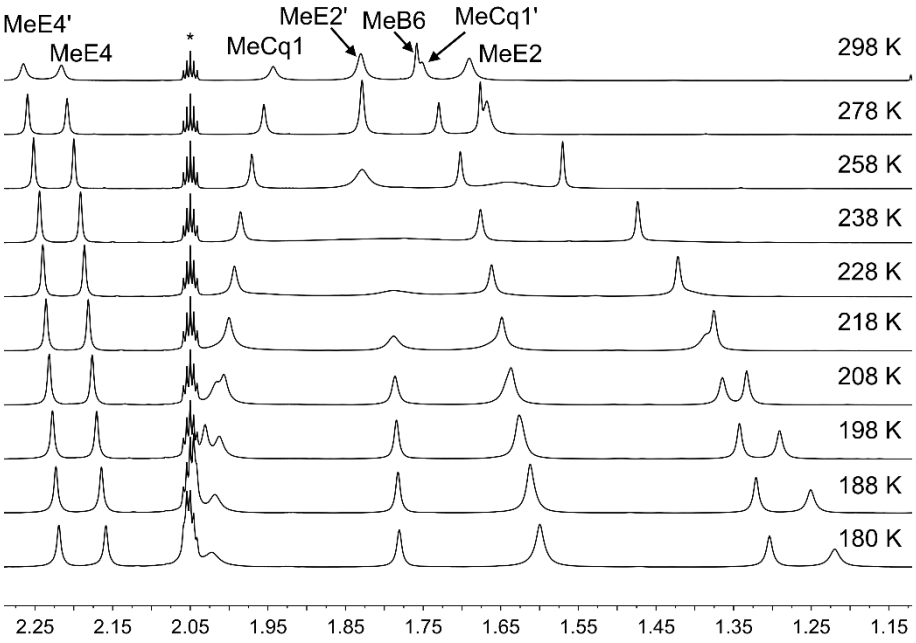


***Figure 4.16*** *Alkyl regions of the variable temperature $^{1}H$ NMR spectra (500 MHz, acetone-$d_6$) of [Cu(6-Mebpy)($^{t}Bu_2$xantphos)][$PF_6$]. See section 4.6.6 for atom labelling.*

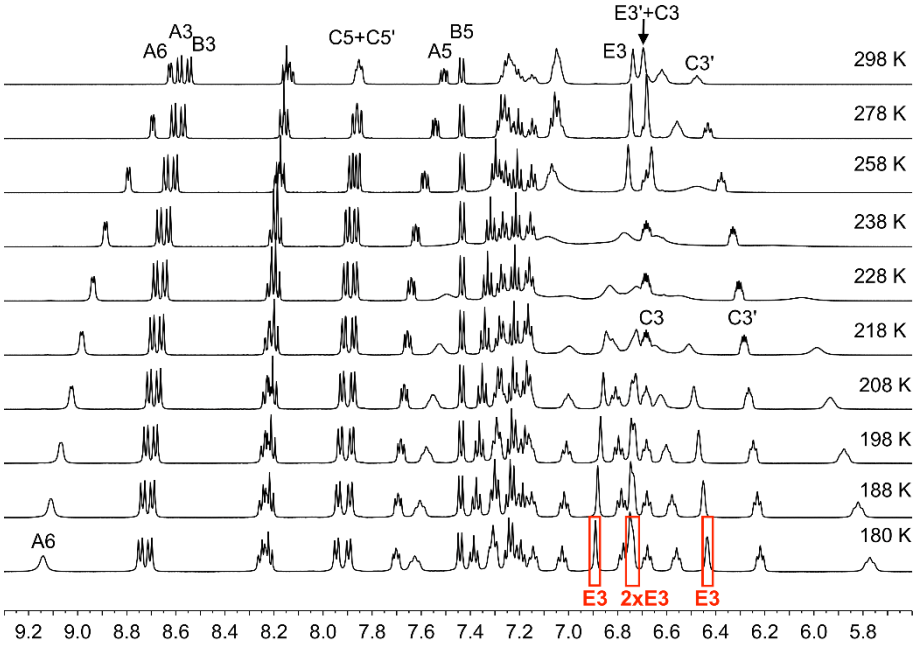


***Figure 4.17*** *Aromatic regions of the variable temperature $^{1}H$ NMR spectra (500 MHz, acetone-$d_6$) of [Cu(6-Mebpy)($^{t}Bu_2$xantphos)][$PF_6$]. See section 4.6.6 for atom labelling. The signals at 180 K highlighted in red correspond to those assigned to the four independent mesityl E3 protons with rotation of the mesityl groups frozen out.*

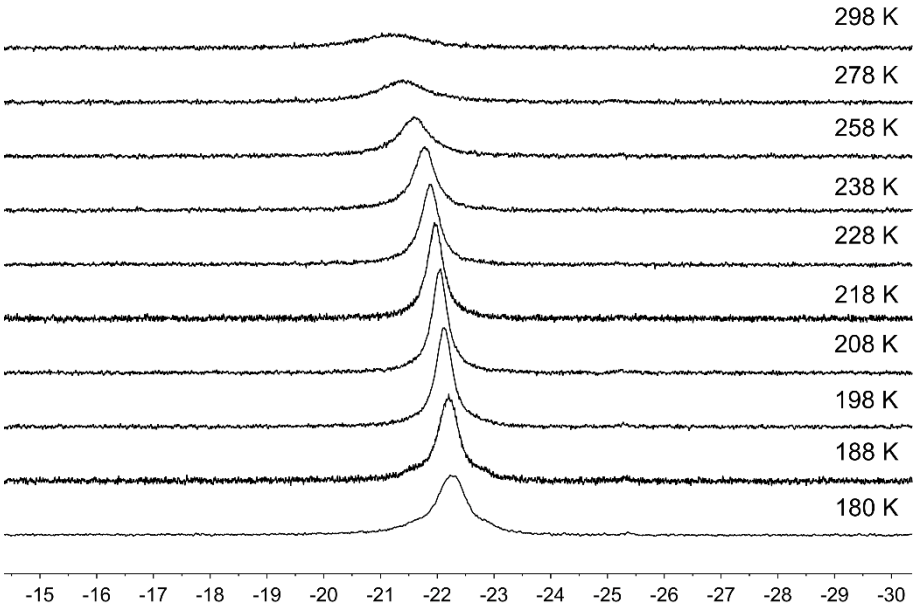


***Figure 4.18*** *Variable temperature $^{31}P\{^1H\}$ NMR spectra (202 MHz, acetone-$d_6$) of [Cu(6-Mebpy)($^t$Bu$_2$xantphos)][PF$_6$]. The [PF$_6$]$^-$ signal was observed as a septet at δ –144.6 ppm and was independent of the temperature.*

## 4.4 Electrochemical and photophysical properties

### *4.4.1 Electrochemistry*

The electrochemical behaviour of the [Cu(N^N)(P^P)][PF$_6$] complexes was studied using cyclic voltammetry and the results are summarized in **Table 4.3** and **Figure 4.19**. All compounds with the exception of [Cu(bpy)(xantphosMes$_2$)][PF$_6$] exhibit a quasi-reversible process in the range +0.76 to +0.85 V, which is assigned to a copper-centred oxidation. For [Cu(bpy)(xantphosMes$_2$)][PF$_6$] the oxidation at +0.80 V is irreversible. Although the corresponding reduction peak could not be resolved, the position of this oxidation peak ($E^{ox}_{pc}$) is similar to the one observed for [Cu(bpy)($^t$Bu$_2$xantphos)][PF$_6$] (+0.80 V, **Figure 4.19**). When scanning beyond +1.0 V, additional oxidation waves appear and the copper oxidation is no longer reversible. Instead a reduction signal appears at around +0.25 V. This indicates decomposition of the complexes at potentials higher than +1.0 V. Complexes containing $^t$Bu$_2$xantphos also show an irreversible reduction wave at around −2.2 V (**Table 4.3**) arising from a ligand-based process. For the complexes containing xantphosMes$_2$, no reduction processes were observed within the solvent accessible window.

Along the series [Cu(N^N)($^t$Bu$_2$xantphos)][PF$_6$] with N^N = bpy to 6-Mebpy to 6,6'-Me$_2$bpy, the copper oxidation shifts to higher potentials (as observed for the analogous [Cu(N^N)(xantphos)][PF$_6$] series, **Table 4.3**[83]) while the reduction moves towards more negative potentials. This demonstrates an increase in the HOMO-LUMO gap as the steric demand of the bpy ligand increases. This trend was also observed for a related series of compounds and has been rationalized using DFT calculations.[83]

***Table 4.3*** *Cyclic voltammetric data for [Cu(N^N)(P^P)][PF$_6$] complexes referenced to internal Fc/Fc$^+$ = 0 V; degassed HPLC grade CH$_2$Cl$_2$ solution with [nBu$_4$N][PF$_6$] as supporting electrolyte and a scan rate of 0.1 V s$^{-1}$. Processes are quasi-reversible unless otherwise stated (ir = irreversible). Data for [Cu(N^N)(xantphos)][PF$_6$] (N^N = bpy, 6-Mebpy, 6,6'-Me$_2$bpy) are also included.*

| Complex cation | $E_{1/2}^{ox}$ / V ($E_{pc} - E_{pa}$ / mV) | $E^{ox}_{pc}$/V | $E^{red}_{pa}$ /V |
|---|---|---|---|
| [Cu(bpy)($^t$Bu$_2$xantphos)]$^+$ | +0.76 (90) | | −2.20 |
| [Cu(6-Mebpy)($^t$Bu$_2$xantphos)]$^+$ | +0.83 (90) | | −2.22 |
| [Cu(6,6'-Me$_2$bpy)($^t$Bu$_2$xantphos)]$^+$ | +0.85 (100) | | −2.28 |
| [Cu(bpy)(xantphosMes$_2$)]$^+$ | | +0.80$^{ir}$ | |
| [Cu(6-Mebpy)(xantphosMes$_2$)]$^+$ | +0.84 (70) | | |
| [Cu(bpy)(xantphos)]$^+$ [a] | +0.76 (110) | | |
| [Cu(6-Mebpy)(xantphos)]$^+$ [a] | +0.85 (100) | | |
| [Cu(6,6'-Me$_2$bpy)(xantphos)]$^+$ [a] | +0.90 (150) | | |

[a] Values are taken from reference 83

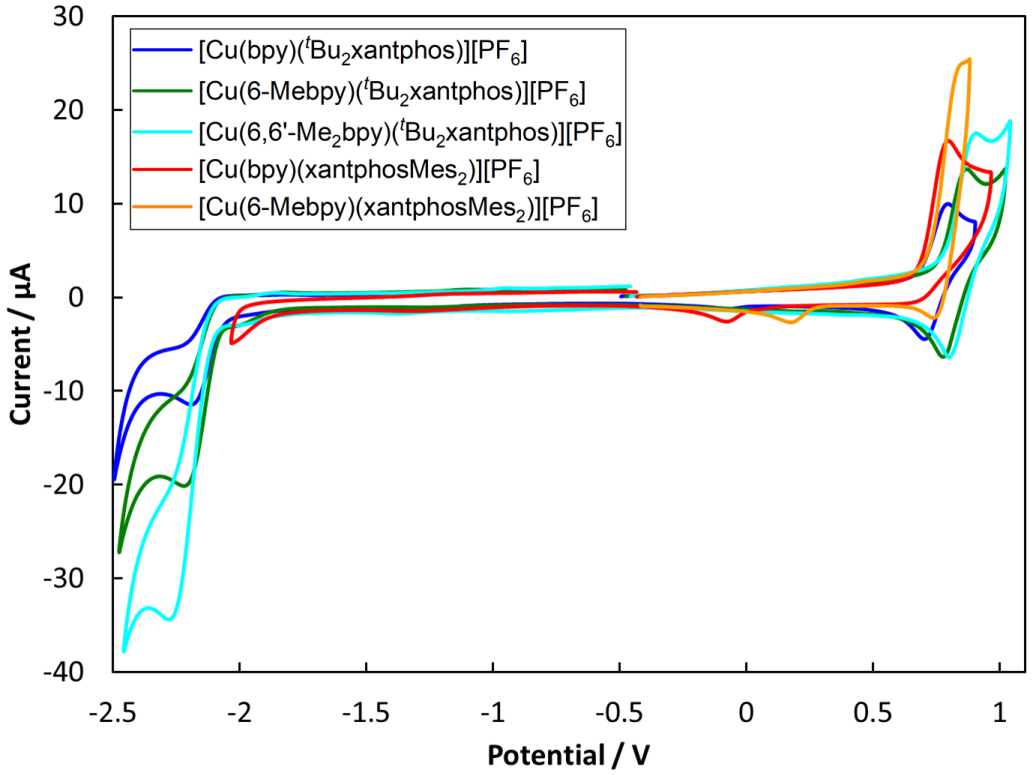


***Figure 4.19*** *Cyclic voltammograms of [Cu(N^N)(P^P)][PF$_6$] compounds in CH$_2$Cl$_2$ at a scan rate of 0.1 V s$^{-1}$ referenced to internal Fc/Fc$^+$ = 0 V.*

## *4.4.2 Theoretical Calculations: Geometry and Molecular Orbitals*

The results and discussion in the following section and in parts of section 4.4.3 were provided in collaboration with Prof. Enrique Ortí (University of Valencia).

The geometries of all the [Cu(N^N)(P^P)]$^+$ cations in their electronic ground state ($S_0$) were optimized at the DFT B3LYP-D3/(def2svp+def2tzvp) level in the presence of the solvent ($CH_2Cl_2$) and without imposing any symmetry restriction (see section Materials and Methods for full computational details). The values obtained for the most representative geometrical parameters defining the Cu(I) coordination sphere are summarized in **Table 4.4**. Calculations successfully reproduce the distorted tetrahedral structures observed experimentally around the Cu centre for all the studied complexes. Compared with the values from X-ray diffraction, the Cu–N and Cu–P bond distances and

the P–Cu–P and N–Cu–N chelating angles are calculated with errors below 0.05 Å and 2°, respectively. The angle formed by the P–Cu–P and N–Cu–N planes, which can be used as an indication of the deviation from the orthogonal disposition of the P^P and N^N ligands, has values lying between 82 and 89°, in good agreement with those observed experimentally and with those computed in previous works for similar complexes.[83,84,127] The N–C–C–N torsion angles remain in a small range between −10 and 14° indicating that the bpy ligand is essentially planar in all the cations. In contrast to the experimental results (**Table 4.1**), the cations containing the xantphosMes$_2$ ligand do not feature significantly more twisted bpy ligands (**Table 4.4**), suggesting that the packing forces play an important role in determining the structure in the crystal. However, theoretical calculations correctly reproduce the longer Cu–P bond distances observed for these complexes, and the spatial proximity of the equatorial mesityl group to the bpy unit shown in **Figure 4.5**. The differences in the torsion angles between theoretical and X-ray geometries are probably due to the fact that the former are obtained for an isolated molecule optimized in solution and do not take into account the packing forces and intermolecular interactions acting in the solid state.

Two geometry minima were found for [Cu(6-Mebpy)(xantphosMes$_2$)]$^+$, which show a different relative orientation of the 6-Mebpy ligand and correspond to the two conformations observed in the single-crystal structure determination (**Figure 4.10**). They possess close energies, the conformation with the 6-methyl group lying over the xanthene bowl being more stable than that with the Me group away from the xanthene unit by only 0.28 kcal mol$^{-1}$. This is in good agreement with the occupancy of 50% experimentally found for each conformation as discussed above.

The geometry of the first triplet excited state ($T_1$) was also optimized at the UB3LYP level for all the [Cu(N^N)(P^P)]$^+$ cations, and the most significant geometry parameters are also included in **Table 4.4**. The molecular geometries in the $T_1$ state significantly differ from those in the ground state $S_0$. As discussed below, the $T_1$ state implies a charge transfer from a molecular orbital that mainly involves a *d* orbital of the Cu atom to a molecular orbital spreading over the bpy ligand. Consequently, the metal atom is partially oxidized and tends to adopt the square-planar coordination sphere expected for four-coordinate $d^9$ Cu(II) complexes, instead of the tetrahedral conformation typical of $d^{10}$ Cu(I) coordination complexes. This effect can be studied by following the changes in the angle formed by the N–Cu–N and P–Cu–P planes, which decreases in going from $S_0$ to $T_1$ as the molecule becomes more planar (**Table 4.4**). The distortion degree from the tetrahedral structure in going from $S_0$ to $T_1$ is indeed limited by the number of methyl groups in the 6,6'-positions of the bpy ligand, because substituents in these positions impede the movement of the ligands towards more planar dispositions.[83] In this way, the [Cu(bpy)($^t$Bu$_2$xantphos)]$^+$ complex, with no substituent in the 6,6'-positions, shows the largest reduction (25.6°) passing from 82.8° in $S_0$ to 57.2° in $T_1$. The [Cu(6-Mebpy)($^t$Bu$_2$xantphos)]$^+$ complex, including one Me group in the 6-position, undergoes a smaller reduction of 23.3° (from 87.9 to 64.6°), and the [Cu(6,6'-Me$_2$bpy)($^t$Bu$_2$xantphos)]$^+$ complex, featuring Me substituents in both the 6- and 6'- positions, shows a reduction of only 15.4° (from 86.1 to 70.7°). Thus, the presence of Me groups in the 6- and 6'-positions strongly affects the degree of geometrical relaxation of the $T_1$ excited state and limits its stabilization. The energy position of the $T_1$ state relative to $S_0$, and thereby the emission properties of the complexes, therefore depend not only on the electron-donating or

electron-withdrawing character of the substituent groups present in the ligands but also on the positions where the substituents are introduced and on the structural effects they induce.

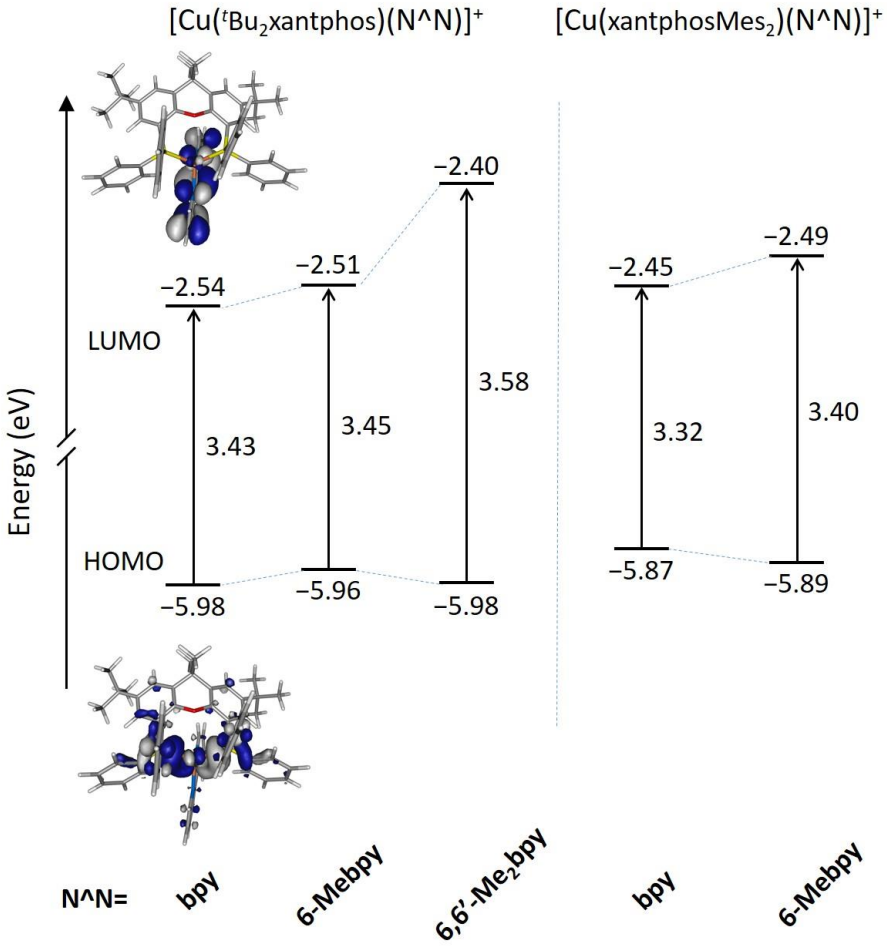


***Figure 4.20*** *Energy diagram showing the energies calculated for the HOMO and LUMO of [Cu(N^N)($^t$Bu$_2$xantphos)]$^+$ and [Cu(N^N)(xantphosMes$_2$)]$^+$ complexes. The HOMO–LUMO energy gap is also quoted. Isovalue contour plots (±0.03 a.u.) are shown for the HOMO and LUMO of [Cu(bpy)($^t$Bu$_2$xantphos)]$^+$.*

**Figure 4.20** shows the evolution of the energy calculated for the highest-occupied (HOMO) and lowest-unoccupied molecular orbital (LUMO) of the five complexes. The atomic orbital composition of the molecular orbitals remains almost unchanged along the series and only the contour plots computed for [Cu(bpy)($^t$Bu2xantphos)]$^+$ are displayed as a representative example. As reported previously for similar copper(I) complexes,[83,84,127] the HOMO appears mainly centred on the metal with a small contribution from the phosphorus atoms, and the LUMO spreads over the bpy ligand. The addition of $^t$Bu groups to the xantphos moiety has a negligible effect on the energy of the HOMO, and the [Cu(N^N)($^t$Bu$_2$xantphos)]$^+$ (N^N = bpy, 6-Mebpy and 6,6'-Me$_2$bpy) complexes have a slightly higher HOMO energy, around −5.97 eV (**Figure 4.20**), than that calculated for the reference complex [Cu(bpy)(xantphos)]$^+$ (−6.00 eV) at the same theoretical level.[127] Replacement of PPh$_2$ moieties by PPhMes groups in the xantphos ligand has a more significant effect moving up the HOMO of [Cu(bpy)(xantphosMes$_2$)]$^+$ and [Cu(6-Mebpy)(xantphosMes$_2$)]$^+$ to −5.81 and −5.89 eV, respectively. There are small

changes in this energy within each series, as the structural changes introduced in the complexes are made in regions where the HOMO is not centred. The HOMO energies, even considering the small changes described, are quite close, in good agreement with the close $E^{ox}_{1/2}$ values reported for the complexes in the Electrochemistry Section. The LUMO undergoes a small destabilization when a Me group (a weak electron donor) is added to the bpy ligand, a destabilization that becomes more pronounced when a second group is added. The HOMO–LUMO energy gap increases in the [Cu(N^N)($^t$Bu$_2$xantphos)]$^+$ series with the number of Me substituents of the bpy ligand in agreement with the experimental CV data (**Table 4.3**). It is therefore expected that excited states described by HOMO→LUMO transitions appear at lower wavelengths as more Me groups are attached to the N^N ligand.

***Table 4.4*** *Selected structural parameters calculated at the B3LYP-D3/(def2svp+def2tzvp) level in $CH_2Cl_2$ solution for [Cu(N^N)(P^P)]$^+$ complexes in their electronic ground state $S_0$ and in their first triplet excited state $T_1$.*

| Complex cation | Cu–P distance / Å (Cu1–P1; Cu1–P2) | Cu–N distance / Å (Cu1–N1; Cu1–N2) | P–Cu–P chelating angle / deg | N–Cu–N chelating angle / deg | Angle between P–Cu–P and N–Cu–N planes / deg | N–C–C–N torsion angle /deg |
|---|---|---|---|---|---|---|
| **Ground State ($S_0$)** | | | | | | |
| [Cu(bpy)(xantphos)]$^{+a}$ | 2.269; 2.270 | 2.104; 2.068 | 114.40 | 79.75 | 86.94 | 3.23 |
| [Cu(bpy)($^t$Bu$_2$xantphos)]$^+$ | 2.271; 2.274 | 2.119; 2.068 | 114.01 | 79.61 | 82.75 | −9.79 |
| [Cu(6-Mebpy)($^t$Bu$_2$xantphos)]$^+$ | 2.280; 2.281 | 2.100; 2.092 | 113.17 | 79.62 | 87.96 | −1.94 |
| [Cu(6,6'-Me$_2$bpy)($^t$Bu$_2$xantphos)]$^+$ | 2.272; 2.313 | 2.120; 2.118 | 118.83 | 79.44 | 86.12 | 8.62 |
| [Cu(bpy)(xantphosMes$_2$)]$^+$ | 2.333; 2.356 | 2.156; 2.147 | 114.77 | 77.84 | 83.39 | 14.29 |
| [Cu(6-Mebpy)(xantphosMes$_2$)]$^{+b}$ | 2.323; 2.365 | 2.152; 2.138 | 114.40 | 77.80 | 81.74 | 5.81 |
| [Cu(6-Mebpy)(xantphosMes$_2$)]$^{+c}$ | 2.308; 2.371 | 2.138; 2.132 | 114.49 | 78.04 | 88.58 | −0.06 |
| **Triplet Excited State ($T_1$)** | | | | | | |
| [Cu(bpy)(xantphos)]$^{+a}$ | 2.350; 2.399 | 1.997; 1.981 | 105.92 | 83.06 | 57.53 | 1.99 |
| [Cu(bpy)($^t$Bu$_2$xantphos)]$^+$ | 2.354; 2.392 | 1.989; 1.969 | 105.64 | 83.29 | 57.18 | 3.15 |
| [Cu(6-Mebpy)($^t$Bu$_2$xantphos)]$^+$ | 2.359; 2.379 | 1.992; 1.969 | 104.87 | 83.53 | 64.62 | −3.15 |
| [Cu(6,6'-Me$_2$bpy)($^t$Bu$_2$xantphos)]$^+$ | 2.381; 2.392 | 2.018; 1.981 | 106.82 | 83.84 | 70.68 | −3.10 |
| [Cu(bpy)(xantphosMes$_2$)]$^+$ | 2.398; 2.427 | 2.034; 1.968 | 105.92 | 82.85 | 65.14 | −5.31 |
| [Cu(6-Mebpy)(xantphosMes$_2$)]$^{+b}$ | 2.438; 2.474 | 2.074; 1.974 | 104.49 | 82.65 | 77.90 | −4.63 |
| [Cu(6-Mebpy)(xantphosMes$_2$)]$^{+c}$ | 2.408; 2.487 | 2.062; 1.991 | 103.62 | 81.86 | 64.59 | 8.44 |

[a] Values from reference 127. [b, c] Two different conformations were optimized for the [Cu(6-Mebpy)(xantphosMes$_2$)]$^+$ complex representing the two different conformers described in the "Single crystal structure Section" in the main text. The structure labelled with "b" is that with the methyl substituent of the 6-Mebpy ligand lying over the xanthene 'bowl', whereas the structure labelled with "c" is that where the methyl is remote from the xantphos. See the main text for more details about these structures.

### *4.4.3 Absorption and Emission properties*

The solution absorption spectra of the [Cu(N^N)(P^P)][$PF_6$] complexes in $CH_2Cl_2$ are shown in **Figure 4.21**. The intense bands below 330 nm are assigned to ligand-based $\pi^*\leftarrow n$ and $\pi^*\leftarrow\pi$ transitions and vary little within a series of a certain phosphane ligand. The broad absorption at around 380 nm (**Table 4.6**) arises from a metal-to-ligand charge transfer (MLCT) excitation. In the series [Cu(N^N)($^t$Bu$_2$xantphos)][$PF_6$], the MLCT absorption slightly shifts to higher energies on going from bpy to 6-Mebpy and to 6,6'-$Me_2$bpy (see **Figure 4.21** inset) as has previously been observed for the analogous [Cu(N^N)(xantphos)][$PF_6$] series.[84] This behaviour is also observed in passing from [Cu(bpy)(xantphosMes$_2$)][$PF_6$] to [Cu(6-Mebpy)(xantphosMes$_2$)][$PF_6$], and is in good agreement with the electrochemical properties discussed above.

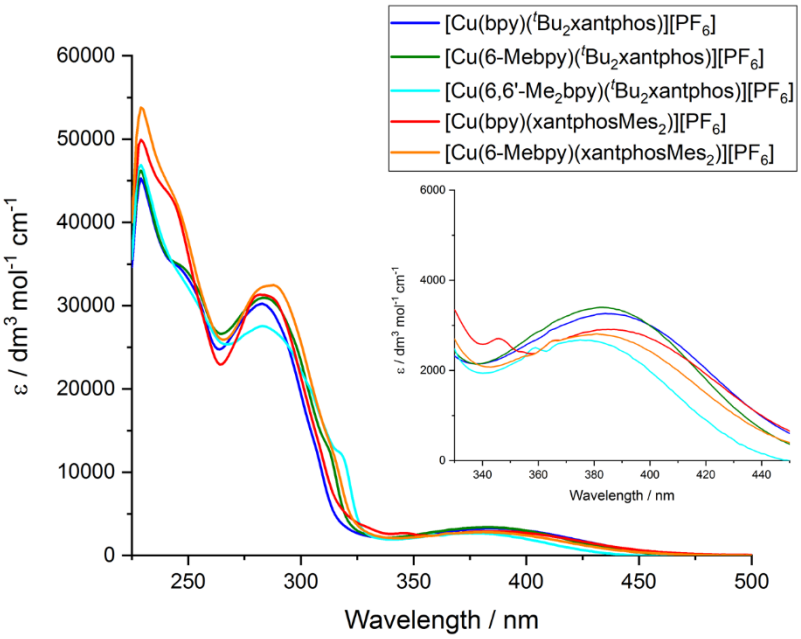


***Figure 4.21*** *Solution absorption spectra of Cu(P^P)(N^N)][$PF_6$] complexes ($CH_2Cl_2$, 2.5 $10^{-5}$ mol $dm^{-3}$). Inset: expansion of the MLCT absorption region.*

To get a better understanding of the nature of the electronic excited states involved in the absorption spectra, the time-dependent DFT (TD-DFT) approach was used to study the lowest lying singlet ($S_n$) and triplet ($T_n$) excited states. **Table 4.5** collects the energies and oscillator strengths ($f$) computed for the $S_1$ and $T_1$ states of all the complexes, together with those obtained for [Cu(bpy)(xantphos)]$^+$ included as a reference. In all cases, both the $S_1$ and the $T_1$ state result from the HOMO→LUMO monoexcitation, with a contribution exceeding 95%. This excitation implies an electron transfer from the Cu(P^P) moiety of the complex to the bpy ligand, supporting the MLCT character of $S_1$ and $T_1$. The broad absorption band observed experimentally at around 380 nm therefore originates in the $S_0\rightarrow S_1$ transition, and the calculated values, although somewhat displaced to the red, reproduce the experimentally observed shift of the absorption maxima to higher wavelengths as the number of Me substituents of the bpy ligand increases. This is also in

good accord with the increase of the HOMO–LUMO gap along each series of complexes predicted above (**Figure 4.20**).

***Table 4.5*** *Vertical excitation energies (E) calculated at the TD-DFT B3LYP/(def2svp+ def2tzvp) level for the lowest singlet ($S_1$) and triplet ($T_1$) excited states of complexes [Cu(N^N)(P^P)]$^+$ in $CH_2Cl_2$ solution. Oscillator strengths (f) are given within parentheses for the $S_0 \rightarrow S_1$ transition.*

| Complex cation | $S_1$ | $T_1$ |
|---|---|---|
| | *E* (eV/nm) (*f*) | *E* (eV) |
| [Cu(bpy)(xantphos)]$^+$ | 2.816 / 440 (0.08) | 2.569 |
| [Cu(bpy)($^t$Bu$_2$xantphos)]$^+$ | 2.803 / 442 (0.09) | 2.554 |
| [Cu(6-Mebpy)($^t$Bu$_2$xantphos)]$^+$ | 2.823 / 439 (0.10) | 2.577 |
| [Cu(6,6'-Me$_2$bpy)($^t$Bu$_2$xantphos)]$^+$ | 2.923 / 424 (0.07) | 2.694 |
| [Cu(bpy)(xantphosMes$_2$)]$^+$ | 2.664 / 465 (0.06) | 2.470 |
| [Cu(6-Mebpy)(xantphosMes$_2$)]$^+$ | 2.750 / 451 (0.06) | 2.582 |

The powder and solution emission spectra are displayed in **Figure 4.22 a) and c)**, respectively, and data are given in **Table 4.6**. Upon excitation into the MLCT region ($\lambda_{exc}$ = 365 nm), all the compounds show an emission in the orange to yellow region. On going from [Cu(bpy)($^t$Bu$_2$xantphos)][PF$_6$] to [Cu(6-Mebpy)($^t$Bu$_2$xantphos)][PF$_6$] to [Cu(6,6'-Me$_2$bpy)($^t$Bu$_2$xantphos)][PF$_6$], or from [Cu(bpy)(xantphosMes$_2$)][PF$_6$] to [Cu(6-Mebpy)(xantphosMes$_2$)][PF$_6$], the introduction of additional methyl groups in the bpy ligand shifts the emission to higher energies (**Table 4.6**). Additionally, the photoluminescence quantum yield (PLQY) increases for solution and especially for powder emission along the series (**Table 4.6**). [Cu(bpy)($^t$Bu$_2$xantphos)][PF$_6$] and [Cu(bpy)(xantphosMes$_2$)][PF$_6$], just like [Cu(bpy)(xantphos)][PF$_6$],[83] exhibit low PLQY values, especially in solution. This is most probably due to the accessibility of the copper centre, which leads to solvent quenching of the excited state. Consequently, PLQY values in the powder samples are higher than in solution. The emission in the solid state is in all cases blue-shifted compared to the solution emission. This trend has also been observed for related complexes containing DPEPhos or xantphos.[84,129]

The theoretical results reproduce the trends observed in the experimental emission spectra. The emitting $T_1$ state shifts to higher energies as more methyl groups are added to the bpy ligand (**Table 4.5**). The [Cu(6,6'-Me$_2$bpy)($^t$Bu$_2$xantphos)]$^+$ complex is predicted to have the higher energy $T_1$, followed by [Cu(6-Mebpy)($^t$Bu$_2$xantphos)]$^+$ and [Cu(6-Mebpy)(xantphosMes$_2$)]$^+$, and finally by the complexes with no methyl substituent. This is in good agreement with the emission wavelengths observed in experimental spectra (**Table 4.6**). The broad and mostly unstructured shape of the emission band (**Figure 4.22**) is also in accord with the MLCT nature predicted for the emitting HOMO→LUMO $T_1$ state.

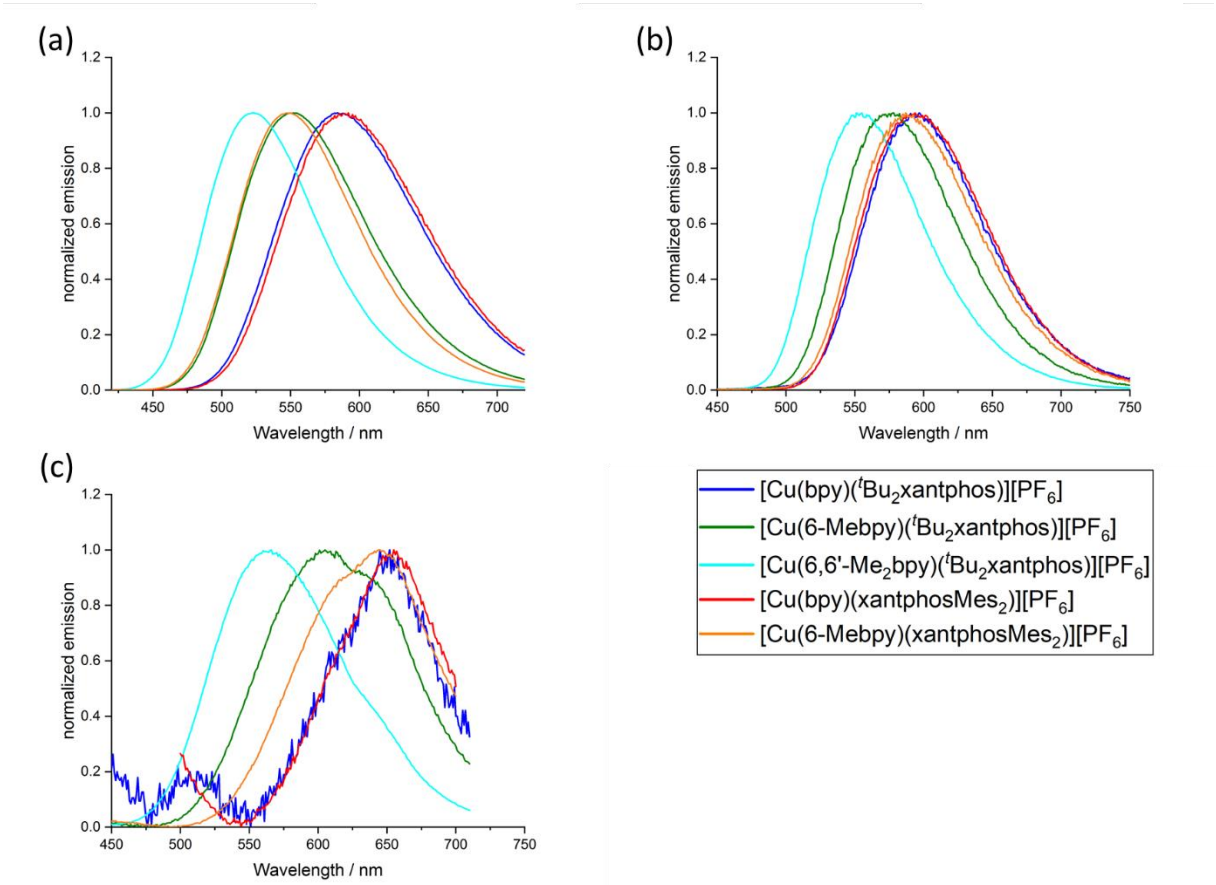


***Figure 4.22*** *Normalized emission spectra ($\lambda_{exc}$ = 365 nm) of [Cu(N^N)(P^P)][PF$_6$] complexes in (a) solid state, (b) frozen Me-THF matrix at 77 K and (c) $CH_2Cl_2$ solution (2.5 x $10^{-5}$ mol $dm^{-3}$ for [Cu(bpy)($^t$Bu$_2$xantphos)][PF$_6$], [Cu(6-Mebpy)($^t$Bu$_2$xantphos)][PF$_6$] and [Cu(6,6'-Me$_2$bpy)($^t$Bu$_2$xantphos)][PF$_6$] and 5.0 x $10^{-5}$ mol $dm^{-3}$ for [Cu)(bpy)(xantphosMes$_2$][PF$_6$] and [Cu(6-Mebpy)(xantphosMes$_2$)][PF$_6$].*

As discussed above, the geometry relaxation of the emitting $T_1$ state leads to the flattening of the tetrahedral coordination environment. This flattening is more hindered as the number of methyl substituents attached to positions 6 and 6' of the bpy ligand is increased, and the relaxation of the $T_1$ triplet is impeded thus leading to higher emission energies. Inspection of **Table 4.6** and **Table 4.7** shows that increasing the steric hindrance of the bpy ligand is beneficial for the emissive properties. Less flattening of the tetrahedral coordination environment of the copper centre gives rise to higher emission energies and, as expected, longer excited state lifetimes and higher PLQYs. The same is true for the series of [Cu(N^N)(xantphos)][PF$_6$] (**Table 4.6**).[83,84] However, from a synthetic point of view, the unsuccessful attempt to [Cu(6,6'-Me$_2$bpy)(xantphosMes$_2$)][PF$_6$] demonstrates a limitation in the combined steric properties of the xantphosMes$_2$ and 6,6'-Me$_2$bpy ligands.

***Table 4.6*** *Photophysical properties of [Cu(N^N)(P^P)][PF$_6$] complexes compared to [Cu(N^N)(xantphos)][PF$_6$]( N^N = bpy, 6-Mebpy, 6,6'-Me$_2$bpy).*

| Complex cation | $CH_2Cl_2$ solution[a,b] | | | | Powder[b] | | |
|---|---|---|---|---|---|---|---|
| | UV-Vis MLCT $\lambda_{max}$/nm | $\lambda_{em}^{max}$/nm | PLQY (non-degassed/ degassed)% | $\tau_{1/2}$(av)(non-degassed/ degassed)/µs | $\lambda_{em}^{max}$/nm | PLQY/% | $\tau_{1/2}$(av)[c]/µs |
| [Cu(bpy)(tBu$_2$xantphos)]+ | 384 | 652 | 0.3/0.4 | - | 584 | 3.0 | 1.95[f] |
| [Cu(6-Mebpy)(tBu$_2$xantphos)]+ | 382 | 605, 628sh | 0.4/0.9 | 0.205/0.581 | 552 | 16 | 6.32[f] |
| [Cu(6,6'-Me$_2$bpy)(tBu$_2$xantphos)]+ | 375 | 566[c] | 0.6/2.4[c] | 0.222/1.05[c] | 522 | 59 | 13.8[f] |
| [Cu(bpy)(xantphosMes$_2$)]+ | 385 | 655[c] | 0.2/0.2[c] | - | 589 | 1.9 | 1.19[f] |
| [Cu(6-Mebpy)(xantphosMes$_2$)]+ | 381 | 645, 623sh[c] | 0.3/0.4[c] | 0.115/0.213 | 547 | 26 | 6.62[f] |
| [Cu(bpy)(xantphos)]+[d] | 383 | 620, 650 | 0.5/0.5 | 0.075/0.104 | 587 | 1.7 | 1.3 |
| [Cu(6-Mebpy)(xantphos)]+[e] | 379 | 635, 605 | 1.0/1.8 | 0.27/0.78 | 547 | 34 | 9.6 |
| [Cu(6,6'-Me$_2$bpy)(xantphos)]+[e] | 378 | 635, 606 | 1.6/10 | 0.45/3.4 | 539 | 37 | 11 |

[a] Solution concentration = 2.5 x $10^{-5}$ mol dm$^{-3}$ unless stated otherwise. sh = shoulder. [b] $\lambda_{exc}$ = 365 nm. [c] Solution concentration = 5.0 x $10^{-5}$ mol dm$^{-3}$. [d] Values taken from reference 83. [e] Values taken from reference 127. [f] Biexponential fit using the equation $\tau_{1/2}(av) = \Sigma A_i\tau_i/\Sigma A_i$ where $A_i$ is the pre-exponential factor for the lifetime.

***Table 4.7*** *Photophysical properties of [Cu(N^N)(P^P)][PF$_6$] complexes compared to [Cu(N^N)(xantphos)][PF$_6$]( N^N = bpy, 6-Mebpy, 6,6'-Me$_2$bpy) in frozen solution and thin film.*

| Complex cation | Me-THF at 77 K | | | Thin film | |
|---|---|---|---|---|---|
| | $\lambda_{em}^{max}$/nm | PLQY/% | $\tau_{1/2}$(av)[a,b]/µs | $\lambda_{em}^{max}$/nm | PLQY/% |
| [Cu(bpy)(tBu$_2$xantphos)]+ | 597 | 7 | 27.6 | - | <1 |
| [Cu(6-Mebpy)(tBu$_2$xantphos)]+ | 578 | 25 | 56.3 | 569 | 6 |
| [Cu(6,6'-Me$_2$bpy)(tBu$_2$xantphos)]+ | 555 | 46 | 92.1 | 550 | 23 |
| [Cu(bpy)(xantphosMes$_2$)]+ | 594 | 11 | 20.0 | 594 | <1 |
| [Cu(6-Mebpy)(xantphosMes$_2$)]+ | 587 | 19 | 19.7 | 584 | 6 |
| [Cu(bpy)(xantphos)]+[d] | 613 | - | 11 | - | - |
| [Cu(6-Mebpy)(xantphos)]+[e] | - | - | - | 574 | 9.7 |
| [Cu(6,6'-Me$_2$bpy)(xantphos)]+[e] | - | - | - | 555 | 21.8 |

[a] Solution concentration = 2.5 x $10^{-5}$ mol dm$^{-3}$ unless stated otherwise. sh = shoulder. [b] $\lambda_{exc}$ = 365 nm. [c] Solution concentration = 5.0 x $10^{-5}$ mol dm$^{-3}$. [d] Values taken from reference 83. [e] Values taken from reference 127.

The photophysical properties of [Cu(bpy)($^t$Bu$_2$xantphos)][PF$_6$] and [Cu(bpy)(xantphosMes$_2$)][PF$_6$] are similar both in solution and in the solid state (**Table 4.6**). In the case of the two [Cu(6-Mebpy)(P^P)][PF$_6$] complexes, a similar behaviour is observed in the solid state emission. Both complexes are blue shifted compared to their [Cu(bpy)(P^P)][PF$_6$] analogues but the emission profile is still very similar and the difference in peak position is again low ($\Delta\lambda$ = 5 nm). It is notable that the shift difference when going from [Cu(bpy)(P^P)][PF$_6$] to [Cu(6-Mebpy)(P^P)][PF$_6$] complexes is larger in the complexes containing xantphosMes$_2$ ($\Delta\lambda$ = 42 nm) compared to $^t$Bu$_2$xantphos complexes ($\Delta\lambda$ = 32 nm). On the other hand, the solution emission profiles differ significantly for the two [Cu(6-Mebpy)(P^P)][PF$_6$] complexes (**Figure 4.22c**). The emission maximum of [Cu(6-Mebpy)($^t$Bu$_2$xantphos)] is blue shifted compared to [Cu(bpy)($^t$Bu$_2$xantphos)] ($\Delta\lambda$ = 47 nm) as expected but in case of [Cu(6-Mebpy)(xantphosMes$_2$)][PF$_6$] the emission maximum is blue-shifted very little compared to [Cu(bpy)(xantphosMes$_2$)][PF$_6$] ($\Delta\lambda$ = 10 nm). Both [Cu(6-Mebpy)($^t$Bu$_2$xantphos)][PF$_6$] and [Cu(6-Mebpy)(xantphosMes$_2$)][PF$_6$] also show a second unstructured emission feature at 628 nm and 623 nm respectively, which is not observed in the solid-state emission profile.

To investigate whether the compounds showed thermally activated delayed fluorescence (TADF) at room temperature, low temperature emission spectra and excited state lifetimes were recorded in frozen Me-THF at 77 K (**Table 4.7** and **Figure 4.22b**). All

complexes show a red shift in emission of 5–40 nm compared to the solid-state emission and a greatly enlarged excited state lifetime. This indicates the possibility that all complexes are TADF emitters at room temperature. The energy difference between the lowest energy singlet and triplet excited states has been calculated to lie between 0.17 and 0.25 eV (**Table 4.5**), and is small enough to allow for the occurrence of TADF processes.[189]

Low temperature data further support the idea that the position of the emission bands of the [Cu(N^N)($^t$Bu$_2$xantphos)] complexes is strongly affected by the flattening of the tetrahedral environment in the $T_1$ state. In solution, this flattening is not impeded and the difference in peak position between [Cu(bpy)($^t$Bu$_2$xantphos)][PF$_6$] and [Cu(6-Mebpy)($^t$Bu$_2$xantphos)][PF$_6$] is 86 nm (0.30 eV) (**Table 4.6**). In powder, the flattening is more restricted and the difference decreases to 62 nm (0.25 eV). Finally, at 77 K, where the relaxation is even more impeded for all the complexes, the emission maxima range between 597 and 555 nm, in a window of just 42 nm (0.15 eV).

### *4.4.4 Device performance*

The results and discussion in the following section were provided in collaboration with Dr. Henk J. Bolink and Dr. Michele Sessolo (University of Valencia).

The series of compounds was tested in LECs using ITO/PEDOT:PSS as the anode, an emitting layer consisting of the complex in the presence of [Emim][PF$_6$] (4:1 molar ratio) and an aluminium cathode. Devices were tested monitoring the electroluminescence and voltage over time and were driven with a pulsed current (100 A m$^{-2}$ average, 50% duty cycle, 1 kHz). The main device parameters obtained for the entire series of samples are reported in **Table 4.8**. The time evolution of the voltage and luminance for the LECs are reported in **Figure 4.23**, together with the electroluminescence spectra. All LECs based on copper(I) complexes with $^t$Bu$_2$xantphos as the P^P ligand show a fast luminescence turn-on time ($t_{on}$, defined here as the time to reach the maximum luminance), ranging from 1 minute for the complex with 6,6'-Me$_2$bpy to 4.5 minutes for the one with 6-Mebpy (**Figure 4.23b**). The maximum luminance registered for these compounds increases with increasing substitution to the N^N ligand, going from 20 cd/m$^2$ for the complex with unsubstituted bpy, to 230 cd/m$^2$ and 370 cd/m$^2$ for the ones containing 6-Mebpy and 6,6'-Me$_2$bpy, respectively. This trend follows that of the PLQY registered for the same compounds (**Table 4.6** and **Table 4.7**) and is consistent with an augmented steric hindrance of the N^N ligand, resulting in a higher stabilization of the tetrahedral complex geometry. The highest efficiency of 3.7 cd/A for the LECs using [Cu(6,6'-Me$_2$bpy)($^t$Bu$_2$-xantphos)][PF$_6$] corresponds to an external quantum efficiency of 1.0%, which is substantially lower compared to the PLQY of the same compound in thin-film (23%). This implies that even in such a bright device, non-radiative losses dominate the recombination of the injected electrons and holes. Interestingly, the quantum efficiencies for photo- and electro-luminescence of the [Cu(6,6'-Me$_2$bpy)($^t$Bu$_2$-xantphos)][PF$_6$] are very close to the unsubstituted xantphos analogue (PLQY = 22% and maximum EQE = 1.0%),[84] highlighting the dominant role of the N^N ligands on the optical and optoelectronic properties of these compounds.

***Table 4.8*** *Main device parameters obtained from LECs at 100 A m⁻².*

| [Cu(N^N)(P^P)]⁺ | $t_{on}$ (min) | $Lum_{max}$ (cd/m²) | $t_{1/2}$ (min) | Eff. (cd/A) |
|---|---|---|---|---|
| [Cu(bpy)(ᵗBu₂-xantphos)]⁺ | 1.1 | 20 | 5.1 | 0.2 |
| [Cu(6-Mebpy)(ᵗBu₂-xantphos)]⁺ | 4.5 | 230 | 53.8 | 2.3 |
| [Cu(6,6'-Me₂bpy)(ᵗBu₂-xantphos)]⁺ | 1.0 | 370 | 4.9 | 3.7 |
| [Cu(6-Mebpy)(xantphosMes₂)]⁺ | 0.7 | 50 | 34.6 | 0.5 |

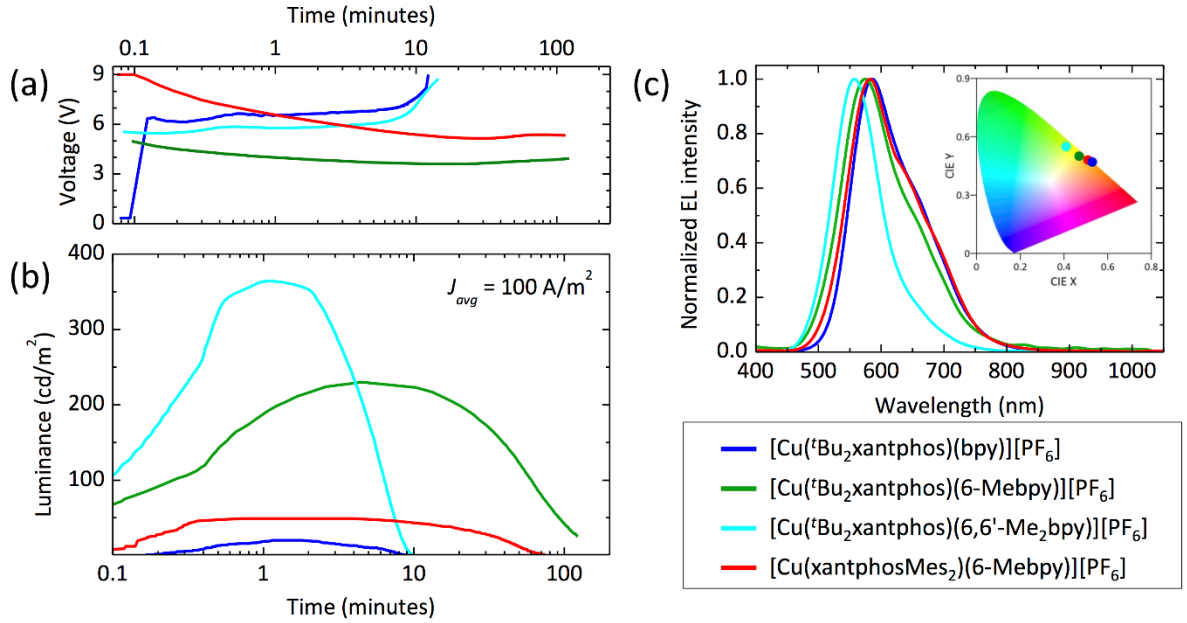


***Figure 4.23*** *Time evolution of the (a) voltage and (b) the luminance for a series of LECs driven at an average current density of 100 A/m². (c) Electroluminescence spectra for the same device series with the corresponding colour coordinates in the CIE 1931 colour space (inset).*

In general, the device lifetime ($t_{1/2}$, time to decay to one-half of the peak luminance) for complexes containing ᵗBu₂-xantphos was found to be low, approximately 5 minutes in the cases of bpy and 6,6'-Me₂bpy and above 50 minutes for the LECs with [Cu(6-Mebpy)(ᵗBu₂-xantphos)][$PF_6$]. The low lifetime of the complexes with bpy and 6,6'-Me₂bpy might be due to a reduced stability of the materials toward charge transport, as seen from the corresponding LECs voltage profile which drastically increases after only a few minutes of operation (**Figure 4.23a**).

The optoelectronic performance of complexes containing the xantphosMes₂ ligand were in general lower as compared to those involving ᵗBu₂-xantphos. We could not observe any electroluminescence from [Cu(bpy)(xantphosMes₂)][$PF_6$], perhaps due to its low PLQY both in solution and in the solid state. Moderate electroluminescence was measured for [Cu(6-Mebpy)(xantphosMes₂)][$PF_6$], with fast turn-on (<1 minute) and a maximum luminance of 50 cd/m².

The spectral shape and position of the electroluminescence (EL, **Figure 4.23c**) signals correlate with the PL maxima observed for the complexes in solution and in the solid state. For the ᵗBu₂xantphos-containing complexes, the EL maxima blue-shift from 584 nm to 575 and 557 nm when increasing the substitution at the bpy, *i.e.* going from bpy to 6-Mebpy and 6,6'-Me₂bpy, respectively. As highlighted in the inset of **Figure 4.23c**, this shift corresponds to a colour variation from the orange to the green region of the CIE 1931

colour space. The EL spectrum of [Cu(6-Mebpy)(xantphosMes$_2$)][PF$_6$] peaks at 582 nm, in agreement with the PL signal of the thin-film (**Table 4.7**).

## 4.5 Conclusion

We were able to prepare five new [Cu(N^N)(P^P)][PF$_6$] complexes bearing two new modified xantphos type ligands. XantphosMes$_2$ carries two stereogenic centre on the phosphorus atoms and the *(rac)*-form is observed in the crystal structure. Solution studies reveal that this is the dominant form, which leaves the ligand preorganized for complexation. Only the *(rac)*-form reacted with copper to form heteroleptic complexes. The complex shows interesting structural solution dynamic properties when combined with an asymmetric N^N ligand that were investigated by NMR spectroscopy with two interchangeable conformers present at 50% each. The crystal structure of xantphosMes$_2$ shows a flattened backbone which is in contrast to crystal structures of the corresponding copper complexes, where the xanthene backbone adapts a 'bowl' conformation. The photophysical properties of all five copper complexes were investigated and all show yellow emission in solid state and yellow-orange emission in frozen Me-THF, suggesting a TADF nature of the emissive state. This was confirmed by DFT-calculations that predict a low energy difference of the $S_1$ and $T_1$ state. With more sterically demanding 2,2'-bipyridine ligand the HOMO-LUMO energy gap as well as the PLQY increases, which was confirmed by emission spectroscopy, cyclic voltammetry and DFT calculations and is in good agreement with the literature.[83,84,129] This is due to less flattening of the triplet excited state. Introducing sterically demanding groups on the P^P ligand did not alter the emissive properties significantly, as was expected. However, a large steric bulk around the copper centre prevented the formation of [Cu(6,6'-Me$_2$bpy)(xantphosMes$_2$)][PF$_6$]. The introduction of $^t$Bu-groups on the xanthene backbone did not alter the photophysical properties, but the device lifetime of [Cu(6-Mebpy)($^t$Bu$_2$-xantphos)][PF$_6$] is a factor of 1.5 larger than the one of [Cu(6-Mebpy)(xantphosMes$_2$)][PF$_6$], indicating the beneficial effect of sterically demanding groups in the xanthene backbone of [Cu(N^N)(xantphos)][PF$_6$] type complexes. The brightest LEC device was prepared using [Cu(6,6'-Mebpy)($^t$Bu$_2$xantphos)][PF$_6$] which showed a peak brightness of 370 cd cm$^{-2}$ and an efficiency of 3.7 cd A$^{-1}$. However, LEC devices showed a trade-off with bright devices being shorter lived than devices with slightly lower maximum luminance.

## 4.6 Experimental

### *4.6.1 6-Methyl-2,2'bipyridine (6-Mebpy)*

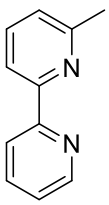

The compound was prepared by an adapted literature method.[190] A microwave flask was charged with [Pd(PPh$_3$)$_4$] (342 mg, 0.296 mmol, 0.05 eq.), then evacuated and backfilled with N$_2$ three times. 2-Pyridylzinc bromide in a solution of THF (0.5 M, 18.0 mL, 9.0 mmol, 1.4 eq.) and 2-chloro-6-methylpyridine (0.70 mL, 6.44 mmol, 1.0 eq.) were added and the mixture was degassed with N$_2$ for 20 min. The reaction was performed in a microwave reactor at 110 °C for 2 h. A saturated solution of NaHCO$_3$ (30 mL) was added and the mixture was extracted with CH$_2$Cl$_2$ (3 × 40 mL). The combined organic layers were washed with water (3 × 30 mL) and dried over MgSO$_4$. The solvent was removed and the

crude material was purified by flash chromatography (Alox, cyclohexane : ethyl acetate 20 : 1) to give 6-Mebpy as a pale yellow oil. The NMR spectroscopic data were in agreement with the literature. ESI MS: *m/z* 171.0 $[M + H]^+$ (base peak, calc. 171.1).

### *4.6.2 4,5-Bis(dimesityl-phosphino)-9,9-dimethylxanthene (xantphosMes$_4$)*

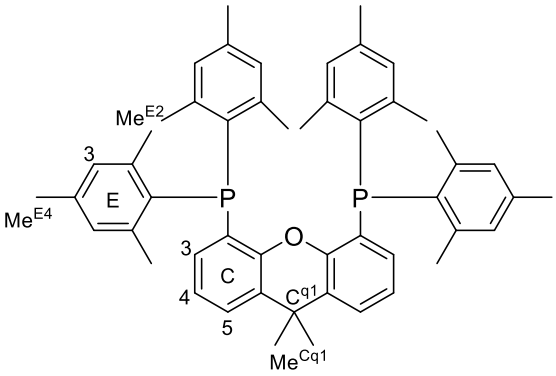


The compound was prepared by adapting a literature procedure.[183] 9,9-Dimethylxanthene (265 mg, 1.26 mmol, 1.0 eq.) was dissolved in dry heptane (30 mL) under inert conditions. A solution of $^n$BuLi (1.6 M in hexane, 1.97 mL, 3.15 mmol, 2.5 eq.) and tetramethylethylenediamine (475 µL, 3.15 mmol, 2.5 eq.) were added and the mixture was stirred at reflux for 30 min. The mixture was cooled to room temperature and added slowly to a solution of $Mes_2PCl$ (1.00 g, 3.28 mmol, 2.6 eq.) in THF (10 mL) at 0 °C. After stirring for 1 h at 0 °C, the reaction mixture was allowed to warm up over 50 h, diluted with ethyl acetate (20 mL) and washed with water (30 mL). The aqueous phase was extracted with ethyl acetate (2 × 50 mL) and the combined organic layers were dried over $MgSO_4$ and the solvent was removed. The resulting crude oil was sonicated with ethyl acetate (2 mL) until white crystals precipitated. Crystalline xantphosMes$_4$ was collected by filtration (232 mg, 0.31 mmol, 24.7%). $^1$H NMR (500 MHz, $CD_2Cl_2$) $\delta$/ppm: 7.38 (d, $J$ = 7.7 Hz, 2H, H$^{C5}$), 6.87 (t, $J$ = 7.6 Hz, 2H, H$^{C4}$), 6.75–6.67 (overlapping m, 10H, H$^{C3+E3}$), 2.21 (s, 12H, H$^{MeE4}$), 1.89 (s, 24H, H$^{MeE2}$), 1.67 (s, 6H, H$^{MeCq1}$). $^{13}$C{$^1$H} NMR (126 MHz, $CD_2Cl_2$) $\delta$/ppm: 153.4 (C$^{C1}$), 143.3 (t, $J_{PC}$ = 8.5 Hz, C$^{E1}$), 137.7 (C$^{E4}$), 131.88 (C$^{C3}$), 131.87 (C$^{E2}$), 130.1 (C$^{E3}$), 129.9 (C$^{C6}$), 126.7 (C$^{C5}$), 123.4 (C$^{C4}$), 34.7 (C$^{Cq1}$), 33.0 (C$^{MeE4}$), 22.7 (t, $J_{PC}$ = 8.3 Hz, C$^{MeE2}$), 21.2 (C$^{MeCq1}$), C2 not resolved. $^{31}$P{$^1$H} NMR (202 MHz, $CD_2Cl_2$) $\delta$/ppm: –36.2. ESI-MS: *m/z* 747.3 $[M+H]^+$ (base peak, calc. 747.4).

### *4.6.3 Chloro(mesityl)phenylphosphane*

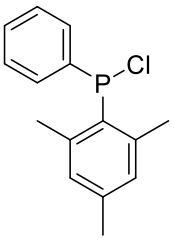


Bromomesitylene (3.38 g, 17.0 mmol, 1.0 eq.) was dissolved in dry THF (10 mL) under inert conditions. Part of this solution (2 mL) was added to a round bottomed flask with Mg turnings (455 mg, 18.7 mmol, 1.1 eq.) and heated to reflux. To initiate the reaction, a small amount of *t*-BuMgCl (1 M solution in THF) and iodine were added and after the reaction had started, the rest of the bromomesitylene solution was added slowly. The mixture was stirred at reflux for 3 h. After cooling to room temperature, the mixture was added dropwise over 1 h to a solution of $PhPCl_2$ (2.30 mL, 17.0 mmol, 1.0 eq.) at –78 °C. After warming to room temperature, the mixture was stirred for 2 h. The solvent was removed under Schlenk conditions and the crude material was used in the next step without further purification.

### *4.6.4 4,5-Bis(mesitylphenylphosphino)-9,9-dimethylxanthene (xantphosMes$_2$)*

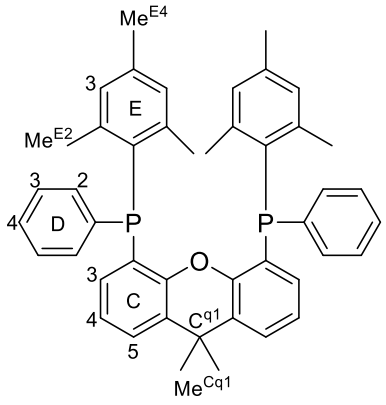


The compound was prepared by adapting a literature procedure.[183] 9,9-Dimethylxanthene (1.32 g, 6.30 mmol, 1.0 eq.) was dissolved in dry heptane (30 mL) under inert conditions. A solution of $^{n}$BuLi (1.6 M in hexane, 9.84 mL, 15.8 mmol, 2.5 eq.) and tetramethylethylenediamine (2.38 mL, 15.8 mmol, 2.5 eq.) were added and the mixture was stirred at reflux for 20 min. The mixture was cooled to room temperature and added slowly to a solution of crude chloro(mesityl)phenylphosphane in THF (10 mL) at 0 °C. After stirring for 1 h at 0 °C, the reaction mixture was diluted with ethyl acetate (20 mL) and washed with water (30 mL). The aqueous phase was extracted with ethyl acetate (2 × 50 mL) and the combined organic layers were dried over $MgSO_4$ and the solvent was removed. The crude material was purified by column chromatography (silica, ethyl acetate : cyclohexane 1:2 + 1% triethylamine). The resulting material was dissolved in a little ethyl acetate and precipitated and washed with EtOH to give xantphosMes$_2$ (874 mg, ≈1.32 mmol, ≈21%, analytically pure xantphosMes$_2$ could not be obtained) as a white powder. $^{1}$H NMR (500 MHz, acetone-$d_6$) $\delta$/ppm: 7.59 (d, $J$ = 7.8 Hz, 2H, H$^{C5}$), 7.19–7.15 (overlapping m, 6H, H$^{D3+D4}$), 7.08 (m, 4H, H$^{D2}$), 7.02 (t, $J$ = 7.6 Hz, 2H, H$^{C4}$), 6.78 (s, 4H, H$^{E3}$), 6.67 (m, 2H, H$^{C3}$), 2.21 (s, 6H, H$^{MeE4}$), 1.94 (s, 12H, H$^{MeE2}$), 1.78 (s, 6H, H$^{MeCq1}$). $^{13}$C{$^{1}$H} NMR (126 MHz, acetone-d$_6$) $\delta$/ppm: 152.8 (t, 9.6 Hz, C$^{C1}$), 145.9 (t, 8.7 Hz, C$^{E2}$), 140.1 (C$^{E4}$), 132.6 (t, 10.5 Hz, C$^{D2}$), 131.2 (C$^{C3}$), 130.7 (C$^{C6}$), 130.6 (t, 2.0 Hz, C$^{E3}$), 130.1 (C$^{E1}$), 128.4 (t, 3.3 Hz, C$^{D3}$), 127.49 (C$^{D4}$), 127.46 (C$^{C5}$), 124.4 (C$^{C4}$), 124.3 (C$^{C2}$), 35.2 (C$^{Cq1}$), 32.9 (C$^{MeCq1}$), 23.9 (C$^{MeE2}$), 21.1 (C$^{MeE4}$), C$^{D1}$ not resolved. $^{31}$P{$^{1}$H} NMR (202 MHz, acetone-$d_6$) $\delta$/ppm: –25.8. ESI-MS: $m/z$ 663.5 [M+H]$^{+}$ (base peak, calc. 663.3). Satisfactory elemental analysis could not be obtained.

### *4.6.5 [Cu(bpy)($^{t}$Bu$_2$xantphos)][PF$_6$]*

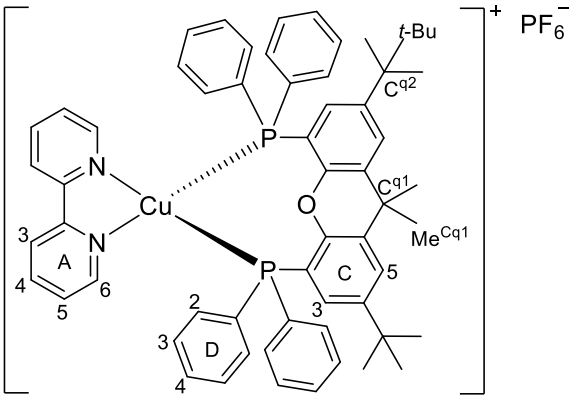


[Cu(MeCN)$_4$][PF$_6$] (93.2 mg, 0.25 mmol, 1.0 eq.) was dissolved in $CH_2Cl_2$ (15 mL). A solution of $^{t}$Bu$_2$xantphos (174 mg, 0.25 mmol, 1.0 eq.) and bpy (39.0 mg, 0.25 mmol, 1.0 eq.) was added and the mixture was stirred for 1 h at room temperature during which time it turned orange. This colour indicated the presence of homoleptic [Cu(bpy)$_2$][PF$_6$] and therefore additional $^{t}$Bu$_2$xantphos (33.0 mg, 0.05 mmol, 0.2 eq.) was added. The solution was stirred for another 2.5 h during which time it turned yellow. The solution was filtered and the solvent was removed from the filtrate under reduced pressure. The solid product was washed with $Et_2O$ (3 × 40 mL) and dried under vacuum. [Cu(bpy)($^{t}$Bu$_2$xantphos)][PF$_6$] (226 mg, 0.21 mmol, 85.6%) was isolated as a yellow solid. $^{1}$H NMR (500 MHz, acetone-$d_6$) $\delta$/ppm: 8.61 (dt, $J$ = 8.2, 1.0 Hz, 1H, H$^{A3}$), 8.24 (ddd, $J$ = 5.1, 1.6, 0.8 Hz, 1H, H$^{A6}$), 8.16 (td, $J$ = 7.8, 1.7 Hz, 1H, H$^{A4}$), 7.86 (d, $J$ = 2.2 Hz, 2H, H$^{C5}$), 7.44 (ddd, $J$ = 7.6, 5.1, 1.1 Hz, 1H, H$^{A5}$), 7.35 (m, 4H, H$^{D4}$), 7.22 (m, 8H, H$^{D3}$), 7.02 (m, 8H, H$^{D2}$),

6.59 (m, 2H, $H^{C3}$), 1.82 (s, 6H, $H^{MeCq1}$), 1.11 (s, 18 H, $H^{t\text{-}Bu}$). $^{13}C\{^1H\}$ NMR (126 MHz, acetone-$d_6$) $\delta$/ppm: 154.2 ($C^{C1}$), 152.8 ($C^{A2}$), 150.1 ($C^{A6}$), 148.5 ($C^{C4}$), 139.9 ($C^{A4}$), 133.7 (t, 8.0 Hz, $C^{D2}$), 132.8 ($C^{C6}$), 132.6 ($C^{D1}$), 130.9 ($C^{D4}$), 129.7 (t, 4.7 Hz, $C^{D3}$), 128.6 ($C^{C3}$), 127.1 ($C^{A5}$), 125.2 ($C^{C5}$), 123.8 ($C^{A3}$), 119.7 ($C^{C2}$), 37.6 ($C^{Cq1}$), 35.5 ($C^{Cq2}$), 31.5 ($C^{t\text{-}Bu}$), 28.2 ($C^{MeCq1}$). $^{31}P\{^1H\}$ NMR (202 MHz, acetone-$d_6$) $\delta$/ppm: –11.3 (broad, FWHM = 230 Hz), –144.3 (septet, $J_{PF}$ = 707 Hz, $[PF_6]^-$). ESI MS: *m/z* 909.2 $[M–PF_6]^+$ (base peak, calc. 909.3). UV-Vis ($CH_2Cl_2$, 2.5 × $10^{-5}$ mol $dm^{-3}$): $\lambda$/nm ($\varepsilon$/$dm^3$ $mol^{-1}$ $cm^{-1}$) 229 (44300), 244sh (34300), 283 (30000), 385 (3200). Found: C 64.47, H 6.17, N 2.38; $C_{57}H_{56}CuF_6N_2OP_3$ requires C 64.86, H 5.35, N 2.65%.

### *4.6.6 [Cu(6-Mebpy)($^t$Bu$_2$xantphos)][PF$_6$]*

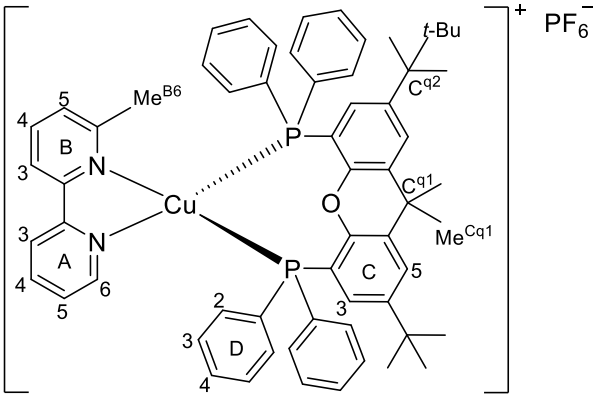


[Cu(6-Mebpy)($^t$Bu$_2$xantphos)][$PF_6$] was prepared using the procedure described for [Cu(bpy)($^t$Bu$_2$xantphos)][$PF_6$] starting with [Cu(MeCN)$_4$][$PF_6$] (93.2 mg, 0.25 mmol, 1.0 eq.), $^t$Bu$_2$xantphos (207 mg, 0.30 mmol, 1.2 eq.) and 6-Mebpy (42.6 mg, 0.25 mmol, 1.0 eq.). [Cu(6-Mebpy)($^t$Bu$_2$xantphos)][$PF_6$] was isolated as a yellow powder (226 mg, 0.21 mmol, 84.5%). $^1H$ NMR (500 MHz, acetone-$d_6$) $\delta$/ppm: 8.51 (dt, *J* = 8.3, 1.0 Hz, 1H, $H^{A3}$), 8.44–8.41 (overlapping m, 2H, $H^{A6+B3}$), 8.12 (t, *J* = 7.9 Hz, 1H, $H^{B4}$), 8.09 (m, 1H, $H^{A4}$), 7.84 (d, *J* = 2.2 Hz, 2H, $H^{C5}$), 7.49 (d, *J* = 7.7 Hz, 1H, $H^{B5}$), 7.46 (ddd, *J* = 7.6, 5.1, 1.1 Hz, 1H, $H^{A5}$), 7.40 (m, 2H, $H^{D4}$), 7.35 (m, 2H, $H^{D4'}$), 7.27 (m, 4H, $H^{D3}$), 7.23–7.16 (overlapping m, 8H, $H^{D2+D3'}$), 6.96 (m, 4H, $H^{D2'}$), 6.65 (m, 2H, $H^{C3}$), 2.01 (s, 3H, $H^{MeB6}$), 1.91 (s, 3H, $H^{MeCq1}$), 1.71 (s, 3H, $H^{MeCq1'}$), 1.12 (s, 18H, $H^{t\text{-}Bu}$). $^{13}C\{^1H\}$ NMR (126 MHz, acetone-$d_6$) $\delta$/ppm: 159.4 ($C^{B6}$), 154.3 ($C^{C1}$), 153.4 ($C^{A2}$), 152.5 ($C^{B2}$), 149.9 ($C^{A6}$), 148.8 ($C^{C4}$), 140.2 ($C^{B4}$), 139.8 ($C^{A4}$), 134.7 ($C^{C6}$), 133.8 (t, 7.9 Hz, $C^{D2'}$), 133.6 (t, 7.9 Hz, $C^{D2}$), 131.0 ($C^{D4'}$), 130.9 ($C^{D4}$), 129.8 (t, 4.4 Hz, $C^{D3}$), 129.6 (t, 4.4 Hz, $C^{D3'}$), 128.2 ($C^{C3}$), 126.89 ($C^{B5}$), 126.86 ($C^{A5}$), 125.2 ($C^{C5}$), 123.8 ($C^{A3}$), 121.0 ($C^{B3}$), 37.5 ($C^{Cq1}$), 35.5 ($C^{Cq2}$), 31.5 ($C^{t\text{-}Bu}$), 29.1 ($C^{MeCq'}$), 26.4 ($C^{MeCq1}$), 26.0 ($C^{MeB6}$), $C^{C2}$ not resolved. $^{31}P\{^1H\}$ NMR (202 MHz, acetone-$d_6$) $\delta$/ppm: –11.6 (broad, FWHM = 250 Hz), –144.3 (septet, $J_{PF}$ = 707 Hz, $[PF_6]^-$). ESI MS: *m/z* 923.2 $[M–PF_6]^+$ (base peak, calc. 923.3). HR ESI MS: *m/z* 923.3327 $[M–PF_6]^+$ (calc. 923.3315). UV-Vis ($CH_2Cl_2$, 2.5 × $10^{-5}$ mol $dm^{-3}$): $\lambda$/nm ($\varepsilon$/$dm^3$ $mol^{-1}$ $cm^{-1}$) 228 (45900), 244sh (34700), 284 (30000), 311sh (13600), 383 (3400). Found: C 64.95, H 6.44, N 2.70; $C_{58}H_{58}CuF_6N_2OP_3$ requires C 65.13, H 5.47, N 2.62%.

### *4.6.7 [Cu(6,6'-Me$_2$bpy)($^t$Bu$_2$xantphos)][PF$_6$]*

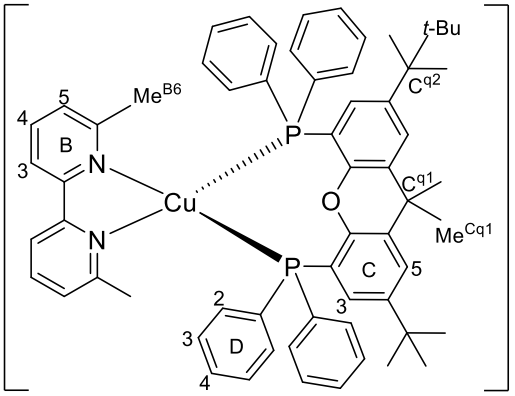


$PF_6^-$

[Cu(6,6'-Me$_2$bpy)($^t$Bu$_2$xantphos)][PF$_6$] was prepared according to the procedure described for [Cu(bpy)($^t$Bu$_2$xantphos)][PF$_6$] using [Cu(MeCN)$_4$][PF$_6$] (93.2 mg, 0.25 mmol, 1.0 eq.), $^t$Bu$_2$xantphos (207 mg, 0.30 mmol, 1.2 eq.) and 6,6'-Mebpy (46.1 mg, 0.25 mmol, 1.0 eq.). [Cu(6,6'-Me$_2$bpy)($^t$Bu$_2$xantphos)][PF$_6$] was isolated as a yellow powder (118 mg, 0.11 mmol, 43.6%). $^1$H NMR (500 MHz, acetone-$d_6$) $\delta$/ppm: 8.16 (d, $J$ = 8.0 Hz, 2H, H$^{B3}$), 7.97 (t, $J$ = 7.8 Hz, 2H, H$^{B4}$), 7.82 (d, $J$ = 2.2 Hz, 2H, H$^{C5}$), 7.41 (m, 4H, H$^{D4}$), 7.37 (d, $J$ = 7.4 Hz, 2H, H$^{B5}$), 7.25 (m, 8H, H$^{D3}$), 7.20 (m, 8H, H$^{D2}$), 6.95 (m, 2H, H$^{C3}$), 2.09 (s, 6H, H$^{MeB6}$), 1.79 (s, 6H, H$^{MeCq1}$), 1.16 (s, 18H, H$^{t\text{-}Bu}$). $^{13}$C{$^1$H} NMR (126 MHz, acetone-d$_6$) $\delta$/ppm: 159.3 (C$^{B6}$), 154.2 (C$^{C1}$), 153.1 (C$^{B2}$), 148.8 (C$^{C4}$), 139.8 (C$^{B4}$), 134.6 (C$^{C6}$), 134.0 (t, 7.7 Hz, C$^{D2}$), 132.7 (C$^{D1}$), 130.9 (C$^{D4}$), 129.6 (t, 4.4 Hz, C$^{D3}$), 127.9 (C$^{C3}$), 126.3 (C$^{B5}$), 125.3 (C$^{C5}$), 121.0 (C$^{B3}$), 37.5 (C$^{Cq1}$), 35.6 (C$^{Cq2}$), 31.5 (C$^{t\text{-}Bu}$), 28.5 (C$^{MeCq1}$), 26.8 (C$^{MeB6}$), C$^{C2}$ not resolved. $^{31}$P{$^1$H} NMR (202 MHz, acetone-$d_6$) $\delta$/ppm: –12.6 (broad, FWHM = 280 Hz), –144.3 (septet, $J_{PF}$ = 707 Hz, [PF$_6$]$^-$). ESI MS: $m/z$ 937.2 [M–PF$_6$]$^+$ (base peak, calc. 923.4). UV-Vis (CH$_2$Cl$_2$, 2.5 × 10$^{-5}$ mol dm$^{-3}$): $\lambda$/nm ($\varepsilon$/dm$^3$ mol$^{-1}$ cm$^{-1}$) 229 (46700), 244sh (34500), 283 (27000), 317sh (12100), 377 (2700). Found: C 64.88, H 5.78, N 2.41; C$_{59}$H$_{60}$CuF$_6$N$_2$OP$_3$ requires C 65.40, H 5.58, N 2.59%.

### *4.6.8 [Cu(bpy)(xantphosMes$_2$)][PF$_6$]*

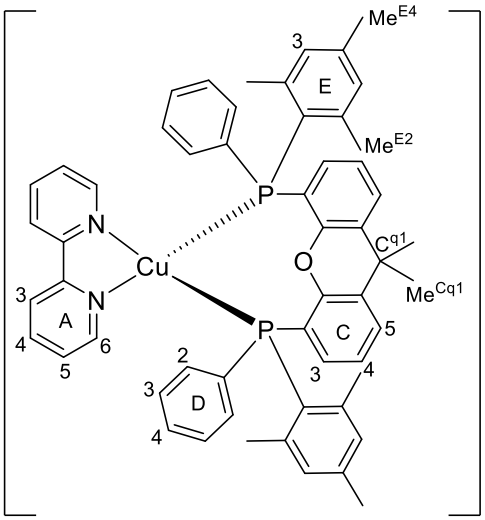


$PF_6^-$

[Cu(bpy)(xantphosMes$_2$)][PF$_6$] was prepared using the procedure described for [Cu(bpy)($^t$Bu$_2$xantphos)][PF$_6$] starting with [Cu(MeCN)$_4$][PF$_6$] (93.2 mg, 0.25 mmol, 1.0 eq.), xantphosMes$_2$ (199 mg, 0.30 mmol, 1.2 eq.) and bpy (39.0 mg, 0.25 mmol, 1.0 eq.). [Cu(bpy)(xantphosMes$_2$)][PF$_6$] was isolated as a yellow powder (224 mg, 0.22 mmol, 87.2%). $^1$H NMR (500 MHz, acetone-$d_6$) $\delta$/ppm: 8.70 (dt, $J$ = 8.3, 1.0 Hz, 2H, H$^{A3}$), 8.17 (td, $J$ = 7.8, 1.7 Hz, 2H, H$^{A4}$), 7.95 (d, $J$ = 4.9 Hz, 2H, H$^{A6}$), 7.89 (dd, $J$ = 7.8, 1.4 Hz, 2H, H$^{C5}$), 7.36 (ddd, $J$ = 7.8, 5.2, 1.1 Hz, 2H, H$^{A5}$), 7.21 (t, $J$ = 7.7 Hz, 2H, H$^{C4}$), 7.16 (t, $J$ = 7.4 Hz, 2H, H$^{D4}$), 7.01 (m, 4H, H$^{D3}$), 6.91 (m, 4H, H$^{D2}$), 6.71 (s, 4H, H$^{E3}$), 6.49 (m, 2H, H$^{C3}$), 2.24 (s, 6H, H$^{MeE4}$), 1.92 (s, 6H, H$^{MeCq1}$), 1.82 (s, 12H, H$^{MeE2}$). $^{13}$C{$^1$H} NMR (126 MHz, acetone-d$_6$) $\delta$/ppm: 156.0 (t, 6.2 Hz, C$^{C1}$), 152.8 (C$^{A2}$), 149.8 (C$^{A6}$), 144.0 (t, 5.7 Hz, C$^{E2}$), 140.9 (C$^{E4}$), 140.1 (C$^{A4}$), 134.7 (C$^{C6}$), 133.8 (t, 16.7 Hz, C$^{D1}$), 132.1 (t, 7.4 Hz, C$^{D2}$), 131.93 (C$^{E3}$), 131.88 (C$^{C3}$), 129.8 (C$^{D4}$), 129.3 (t, 4.4 Hz, C$^{D3}$), 128.3 (C$^{C5}$), 126.9 (C$^{A5}$), 126.3 (t, 2.3 Hz, C$^{C4}$), 124.8 (t, 14.1 Hz, C$^{E1}$), 124.1 (C$^{A3}$), 121.4 (t, 11.5 Hz, C$^{C2}$), 36.8 (C$^{Cq1}$), 28.3 (C$^{MeCq1}$), 23.7 (C$^{MeE2}$), 20.9 (C$^{MeE4}$). $^{31}$P{$^1$H} NMR (202 MHz, acetone-$d_6$) $\delta$/ppm: –21.7 (broad, FWHM = 360 Hz), –144.3

(septet, $J_{PF}$ = 707 Hz, $[PF_6]^-$). ESI MS: *m/z* 725.4 $[Cu(xantphosMes_2)]^+$ (base peak, calc. 725.2), 881.5 $[M–PF_6]^+$ (calc. 881.3). UV-Vis ($CH_2Cl_2$, 2.5 × $10^{-5}$ mol $dm^{-3}$): $\lambda$/nm ($\varepsilon$/$dm^3$ $mol^{-1}$ $cm^{-1}$) 230 (50000), 240sh (44000), 285 (30000), 386 (2900). Found: C 63.53, H 5.56, N 2.95; $C_{55}H_{52}CuF_6N_2OP_3$ requires C 64.29, H 5.10, N 2.73%.

### *4.6.9 [Cu(6-Mebpy)(xantphosMes$_2$)][PF$_6$]*

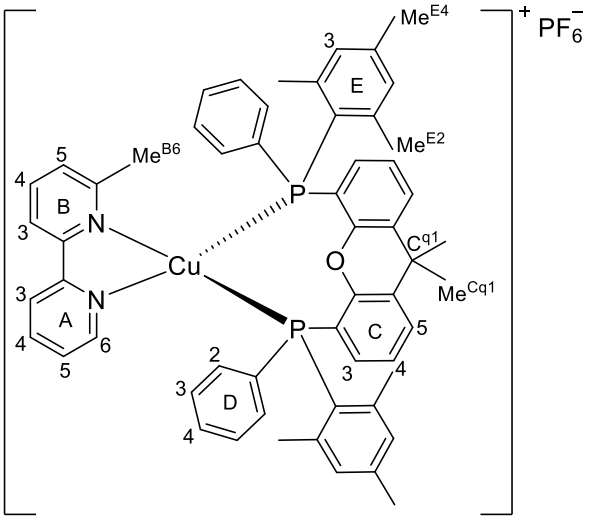


$[Cu(6\text{-}Mebpy)(xantphosMes_2)][PF_6]$ was prepared by the same procedure as for $[Cu(bpy)(^tBu_2xantphos)][PF_6]$ starting with $[Cu(MeCN)_4][PF_6]$ (93.2 mg, 0.25 mmol, 1.0 eq.), $xantphosMes_2$ (199 mg, 0.30 mmol, 1.2 eq.) and 6-Mebpy (42.6 mg, 0.25 mmol, 1.0 eq.). $[Cu(6\text{-}Mebpy)(xantphosMes_2)][PF_6]$ was isolated as a yellow powder (241 mg, 0.23 mmol, 92.6%). $^1H$ NMR (500 MHz, acetone-$d_6$) $\delta$/ppm: 8.63 (ddd, $J$ = 5.2, 1.6, 0.9 Hz, 1H, $H^{A6}$), 8.59 (d, $J$ = 8.2 Hz, 1H, $H^{A3}$), 8.55 (d, $J$ = 7.9 Hz, 1H, $H^{B3}$), 8.18–8.12 (overlapping m, 2H, $H^{A4+B4}$), 7.85 (m, 2H, $H^{C5+C5'}$), 7.51 (ddd, $J$ = 7.6, 5.2, 1.1 Hz, 1H, $H^{A5}$), 7.44 (d, $J$ = 7.7 Hz, 1H, $H^{B5}$), 7.29–7.18 (overlapping m, 5H, $H^{C4+C4'+D4+D2'}$), 7.14 (m, 1H, $H^{D4'}$), 7.04 (m, 4H, $H^{D3+D3'}$), 6.74 (s, 2H, $H^{E3}$), 6.72–6.66 (overlapping m, 3H, $H^{E3'+C3}$), 6.62 (m, 2H, $H^{D2}$), 6.48 (m, 1H, $H^{C3'}$), 2.27 (s, 3H, $H^{MeE4'}$), 2.22 (s, 3H, $H^{MeE4}$), 1.94 (s, 3H, $H^{MeCq1}$), 1.83 (s, 6H, $H^{MeE2'}$), 1.76 (s, 3H, $H^{MeB6}$), 1.75 (s, 3H, $H^{MeCq1'}$), 1.69 (s, 6H, $H^{MeE2}$). $^{13}C\{^1H\}$ NMR (126 MHz, acetone-$d_6$) $\delta$/ppm: 159.9 ($C^{B6}$), 156.4 ($C^{C1}$), 155.4 ($C^{C1'}$), 153.6 ($C^{A2}$), 152.9 ($C^{B2}$), 150.6 ($C^{A6}$), 144.7 ($C^{E2}$), 143.2 ($C^{E2'}$), 141.2 ($C^{E4}$), 140.4 ($C^{B4}$), 140.3 ($C^{E4'}$), 140.2 ($C^{A4}$), 134.9 ($C^{D1}$), 134.5 ($C^{C6}$), 134.1 ($C^{C6'}$), 132.9 ($C^{D2}$), 133.7 ($C^{D1'}$), 132.3 ($C^{C3'}$), 132.0 ($C^{E3'}$), 131.95 ($C^{D2'}$), 131.90 ($C^{C3}$), 131.8 ($C^{E3}$), 130.5 ($C^{D4}$), 129.6 (m, $C^{D3+D3'+D4'}$), 128.5 ($C^{C5+C5'}$), 127.2 ($C^{B5}$), 126.8 ($C^{A5}$), 126.3 ($C^{C4}$), 126.1 ($C^{C4'}$), 125.3 ($C^{E1}$), 124.8 ($C^{E1'}$), 123.87 ($C^{A3}$), 121.3 ($C^{B3}$), 36.6 ($C^{Cq1}$), 30.9 (broadened, $C^{MeCq1'}$), 26.6 (broadened, $C^{MeCq1}$), 25.6 ($C^{MeB6}$), 23.9 ($C^{MeE2'}$), 23.5 ($C^{MeE2}$), 20.8 ($C^{MeE4+MeE4'}$), $C^{C2}$ not resolved. $^{31}P\{^1H\}$ NMR (202 MHz, acetone-$d_6$) $\delta$/ppm: –21.2 (broad, FWHM = 280 Hz), –144.3 (septet, $J_{PF}$ = 707 Hz, $[PF_6]^-$). ESI MS: *m/z* 725.4 $[Cu(xantphosMes_2)]^+$ (base peak, calc. 725.2), $[M–PF_6]^+$ not observed. UV-Vis ($CH_2Cl_2$, 2.5 × $10^{-5}$ mol $dm^{-3}$): $\lambda$/nm ($\varepsilon$/$dm^3$ $mol^{-1}$ $cm^{-1}$) 230 (53000), 240sh (45000), 287 (32000), 381 (2800). Found: C 64.54, H 5.89, N 2.90; $C_{56}H_{54}CuF_6N_2OP_3$ requires C 64.58, H 5.23, N 2.69%.

# Chapter 5: Connected ligand - Combining N^N and P^P

## 5.1 Motivation

In Chapter 2 and Chapter 3 we focused our attention on the modification of the N^N ligands in [Cu(N^N)(P^P)][$PF_6$] complexes, effectively altering the LUMO level of the complex and/or tuning the steric environment around the copper(I) coordination sphere. The results show that a stabilization of the tetrahedral geometry by substitution in the 6-position of a 2,2'-bipyridine ligand is needed to yield luminescent copper(I) complexes, but the steric bulk and electronic nature of the substituent needs to be considered carefully. These steric effects are well established in 1,10-phenanthroline analogues and this carries through to 2,2'-bipyridine.[191] In Chapter 4 we focused our attention on the modification of the P^P ligands. Since the HOMO is mostly localized on the copper and phosphorus atoms, remote modifications do not affect the emissive properties. However, it was observed that modifications close to the copper influence the ability to coordinate other ligands.

With these investigations we were able to alter the emissive and excited state properties of copper(I) complexes. But one major challenge for their application in LECs remains the stability of the cell itself. Factors that affect device stability such as electrode materials, charge imbalances, film morphology, contamination and others are discussed in detail in section 1.4.2. The major aspect where the device stability can be improved by chemical modification lies in the electrochemical and photophysical stability of the complex itself. Excitation of an MLCT level, which occurs by the absorption of visible light, as well as the electrochemical oxidation of the complex taking place by biasing a LEC during operation, both lead to the formation of an intermediate copper(II) species. A reversible and fast recovery to the original copper(I) state is crucial for the long-term stability of the complex as well as the device.[177] It is especially important, that no ligand redistribution or detachment can occur while this oxidized state is present. Heteroleptic copper(I) complexes of the type $[Cu(N^N)(P^P)]^+$ are thermodynamically stable but kinetically instable with respect towards their corresponding homoleptic $[Cu(N^N)_2]^+$ and $[Cu(P^P)_2]^+$ complexes.[192] Poor ligand design, steric or electronic repulsion of the ligands or poor choice of solvents during device preparation can lead to the formation of some homoleptic complexes.[83] These act as quenchers in the device, which lowers the LEC efficiency and lifetime.[49] To prevent ligand redistribution and generally increase the complex stability, we present here synthetics approaches to prepare a tetradentate ligand for copper(I) complexation. Only a few examples of copper complexes containing tetradentate nitrogen-phosphorus-ligand are known in literature. Ishitani *et al.* presented tetradentate P^N^N^P type ligands, with a phenanthroline N^N moiety and two diphenyl phosphane substituents linked over aliphatic chains. The ligand formed a dinuclear structure when coordinated to copper(I) (**Scheme 5.1** left). The complexes were used as photosensitizer in Fe(II) photocatalyzed $CO_2$ reduction and showed decent performance.[193] Recently, Luo *et al.* presented different mononuclear [Cu(P^N^N^P)][$PF_6$] complexes with a shorter spacer between the phenanthroline and phosphorus moiety (**Scheme 5.1** right). These complexes were investigated with regards to their photophysical properties and show emission quantum yields of <4% in solution.[194]

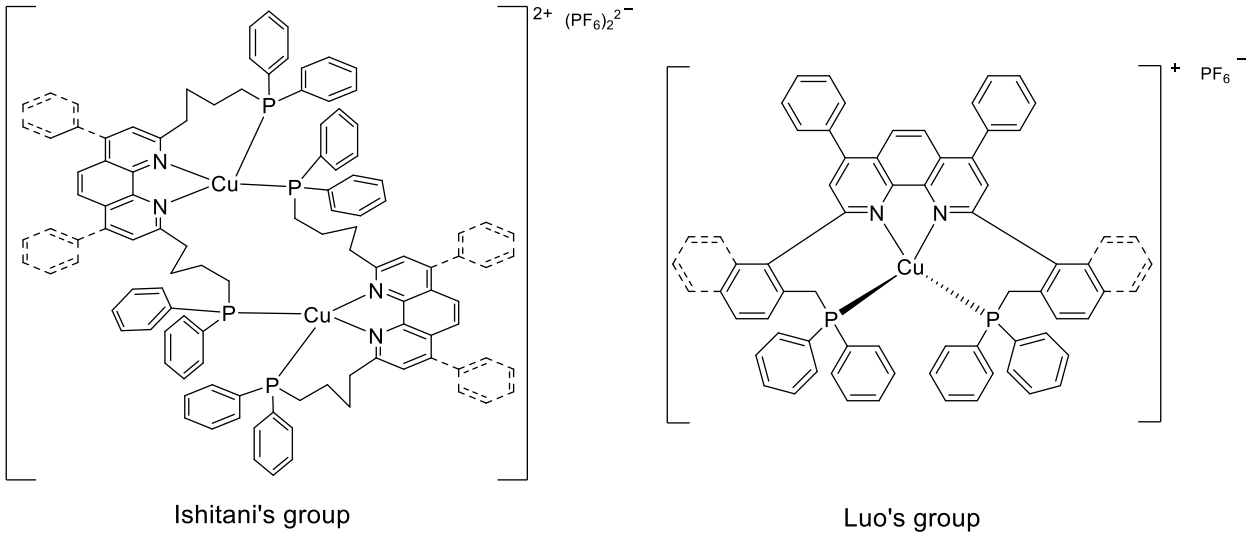


***Scheme 5.1*** *Chemical structures of copper(I) complexes incorporating different P^N^N^P ligands.*

The ligands presented above do not feature a P^P moiety. To fully incorporate the beneficial luminescent properties of the previously investigated [Cu(N^N)(P^P)][$PF_6$] complexes, we aimed our strategy towards the development of an N^N^P^P type ligand rather than the P^N^N^P type ligands presented in the literature. Our aim was to introduce a rather "flexible" connection between the N^N and P^P moieties to allow for an optimal fit of the copper atom without predefined rigid cavities, that could hinder the coordination. At the same time, we needed to preserve the spatial separation of the HOMO and LUMO within the complex scaffold. To achieve this, our linker had to incorporate at least some aliphatic units to prevent an electronic coupling of the N^N and P^P subunits. A schematic representation of an N^N^P^P ligand is shown in **Scheme 5.2**.

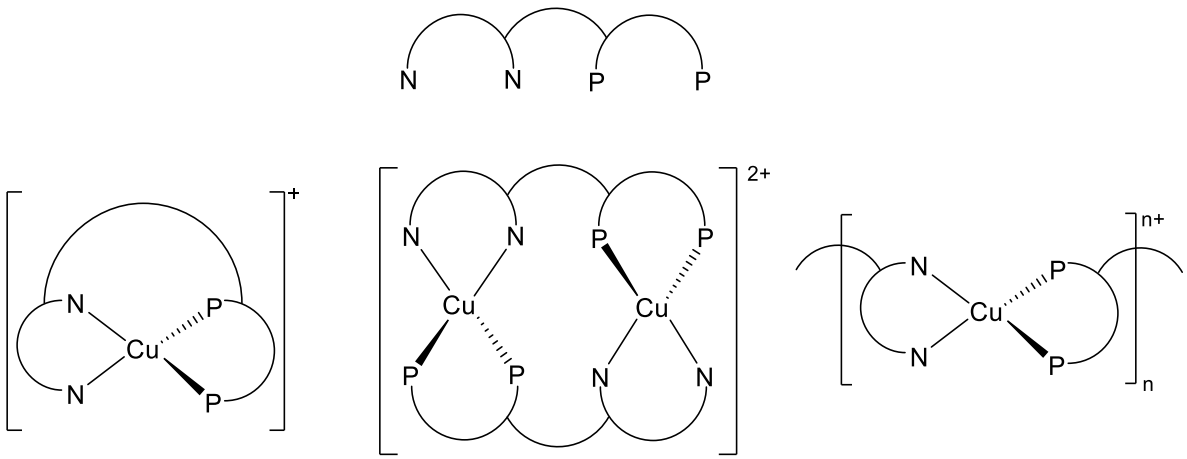

***Scheme 5.2*** *Top: Schematic structure of a N^N^P^P ligand. Bottom: Examples of possible copper(I) complexes in a mononuclear (left), dinuclear (middle) and coordination polymer (right) structure.*

The utilization of a flexible linker between the N^N and P^P moiety with little preorganization opens up the possibility of forming different complex types. Our aim was the preparation of a mononuclear copper(I) complex as shown in **Scheme 5.2** in the bottom left. The formation of a dinuclear complex similar to Ishitani's findings or polymeric structures is also possible. Higher nuclearity complexes are not necessarily

disadvantageous as long as the emissive properties of the [Cu(N^N)(P^P)]-core are not disrupted. However, larger molecules are expected to be less mobile in the active layer of a LEC device, which could be disadvantageous for the ionic mobility and therefore increase the turn-on time. To our knowledge, there is no literature report of a copper(I) coordination polymer-based light emitting device. Such a device would be very interesting and is expected to combine properties of polymer LECs with the ones of iTMC-LECs. Our first target was the preparation of a suitable N^N^P^P ligand to form a mononuclear copper(I) complex. This was believed to be achievable by designing the ligand with enough flexibility to not disturb the coordination but keeping the linker short to disfavour the formation of multi-nuclear species due to steric constrains. Different attempts and synthetic outlines to prepare such a tetradentate ligand are presented in this chapter.

## 5.2 Generation 1 - Triazole connected ligand

In a first attempt to synthesize a tetradentate N^N^P^P ligand, we planned to use a triazole moiety to connect the bpy and xantphos sub-units. Although this connection seems fairly complex in the target molecule (**Scheme 5.3**), the main advantage of this route is the easy and well established click reaction[195–198] to connect the N^N and P^P units at the very end of the synthetic route. Semi-empirical MO calculation on a PM3 level showed that a tetradentate N^N^P^P ligand as shown in **Scheme 5.3** can coordinate copper(I) (**Figure 5.1**). The calculation shows that $CH_2$-$CH_2$ as a spacer group between the 2,2'-bipyridine and the triazole ring allows for the stable coordination of a copper(I) ion without significant strain within the structure and was therefore chosen as an appropriate linker length. The triazole moiety is turned away from the copper centre, so it is expected to not interfere with the copper coordination. A crucial property that the proposed ligand needs to possess is the electronically decoupled nature of the N^N and P^P moiety. This is achieved by using an alkyl spacer between the 2,2'-bipyridine and triazole moiety.

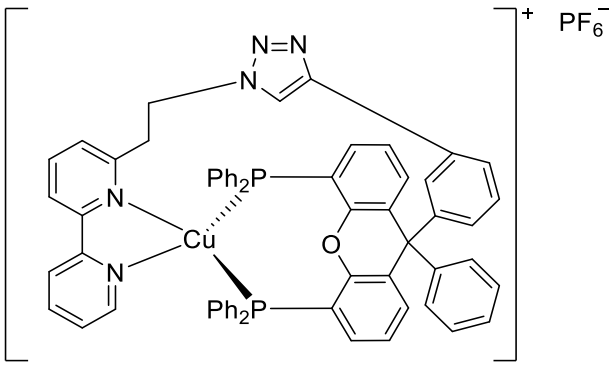


***Scheme 5.3*** *Target complex with triazole connection between xantphos and bpy ligand.*

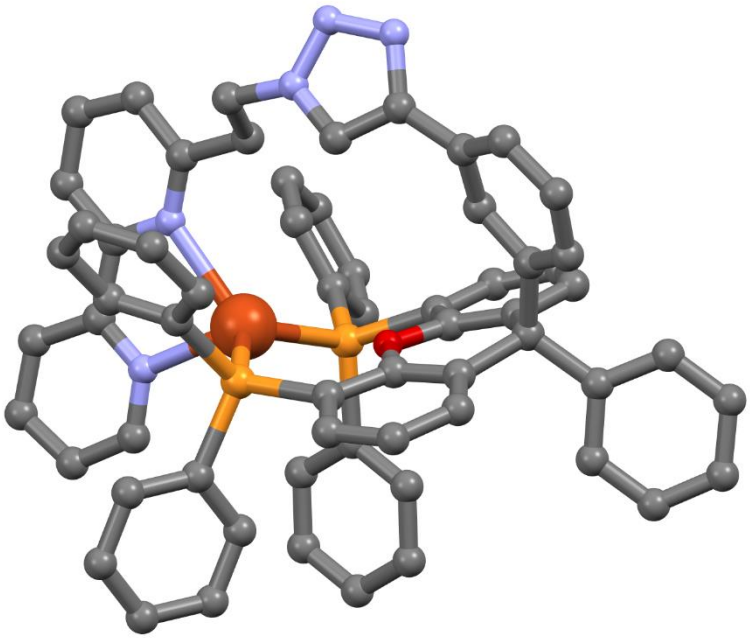

***Figure 5.1*** *Geometry optimized calculated structure of [Cu(N^N^P^P)]⁺ cation. Structures were optimized at the semi-empirical PM3 level using Spartan '18 v. 1.3 (Spartan '18, Wavefunction Inc., Irvine, CA 92612, US).*

## *5.2.1 Benchmark complexes*

To investigate the influence of the newly added substituents on the stability and photophysical behaviour of their copper(I) complexes, two benchmark complexes were prepared. The retrosynthetic routes for the new ligands are shown in **Scheme 5.4**.

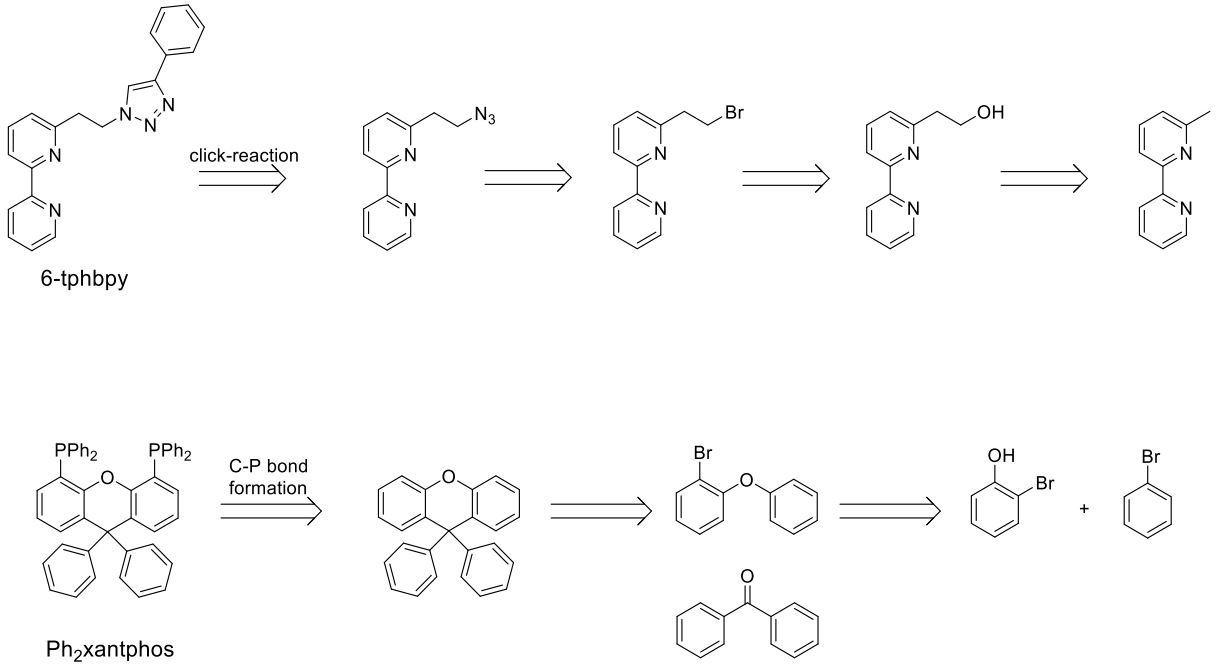


***Scheme 5.4*** *Retrosynthetic analysis of benchmark ligands.*

### 5.2.1.1 Bromo-functionalized 2,2'-bipyridine synthesis

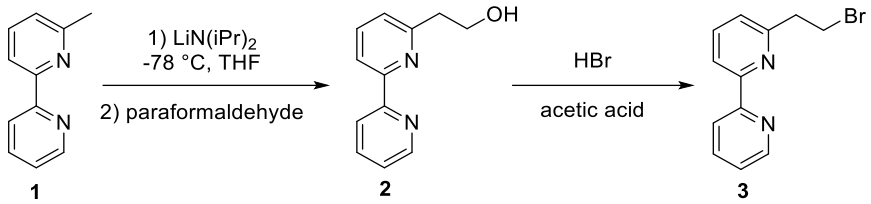


***Scheme 5.5*** *Preparation of 6-(2-bromoethyl)-2,2'-bipyridine (**3**).*

6-Mebpy (**1**) was prepared as described in section 4.6.1. Compound **3** was synthesized by adapting literature procedures according to references 199 and 195. Selective lithiation of the methyl position was achieved by using freshly prepared LDA solution as the lithiation reagent at low temperature. The immediate colour change to dark blue after addition of ligand **1** indicated a fast hydrogen-lithium exchange. A suspension of paraformaldehyde was used to quench the reaction and form a C–C bond. Compound **2** was isolated in moderate yield of 45%. Hydroxy-bromine exchange was achieved under harsh conditions by treating compound **2** with HBr (33% in acetic acid) at 100 °C for 18 h. Although this procedure is described in literature,[199] the reaction was discovered to be more sensitive than expected. Slight iron impurities (*e.g.* from needles) in the acid mixture, or the purification over basic substrates lead to the formation of the elimination product 6-vinyl-2,2'-bipyridine as was discovered by NMR spectroscopy (**Figure 5.2**). After exclusion of these disadvantageous conditions, compound **3** was isolated in a yield of 60%.

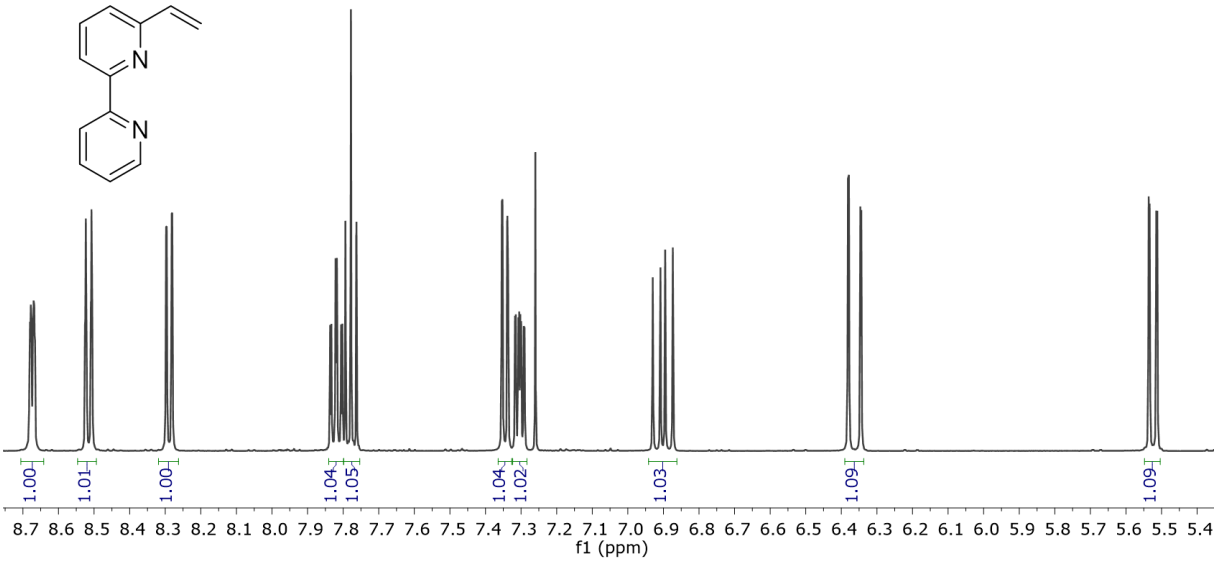


***Figure 5.2*** *$^1$H NMR (500 MHz, $CDCl_3$, 298 K) spectrum of 6-vinyl-2,2'-bipyridine created as an unwanted side product of the preparation of compound **3**.*

### 5.2.1.2 6-Tphbpy synthesis by click reaction

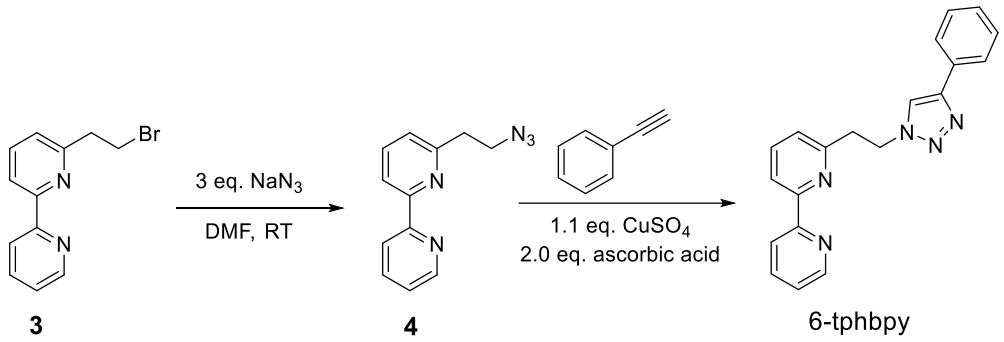


***Scheme 5.6*** *Preparation of 6-tphbpy by halogen azide exchange followed by click reaction.*

The azide modification as well as the click reaction were performed in two consecutive steps without purification of compound **4**. After modification with sodium azide, the 2,2'-bipyridine ligand was treated with a stoichiometric amount of copper catalyst, because the red colour of the reaction mixture indicated poisoning of the catalyst by bpy coordination. To remove any residual copper impurities, the reaction mixture was dissolved in $CH_2Cl_2$ and washed with an aqueous mixture of hydrogen peroxide, $H_4EDTA$ and sodium hydroxide. The 2,2'-bipyridine intermediates and product were mostly purified by column chromatography with basic alumina, since TLCs with silica showed smearing and poor separation.

### 5.2.1.3 Xanthene-backbone formation

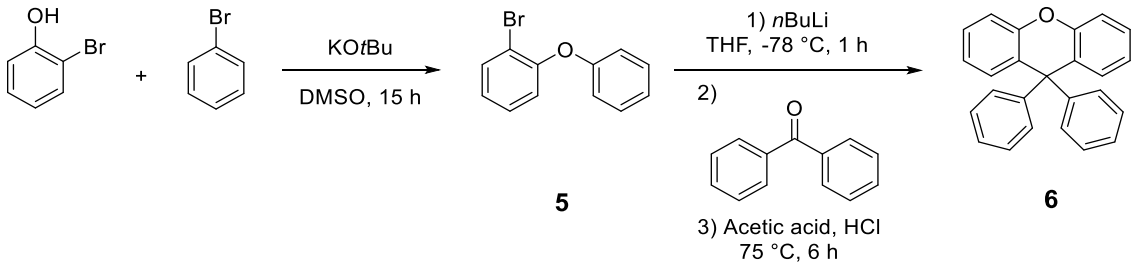


***Scheme 5.7*** *Preparation of the phenyl-modified xanthene backbone.*

The modified xanthene backbone was prepared according to a literature[200] and patent[201] procedure. Preparation of **5** yielded the product in only 11% which was substantially lower than the yield of 62% described in literature.[200] However, because the reaction was easy to perform on large scale it was not optimized further. Treatment of compound **5** with *n*BuLi followed by benzophenone according to a patent procedure[201] yielded the desired modified xanthene in good yield of 89%.

### 5.2.1.4 C-P bond formation

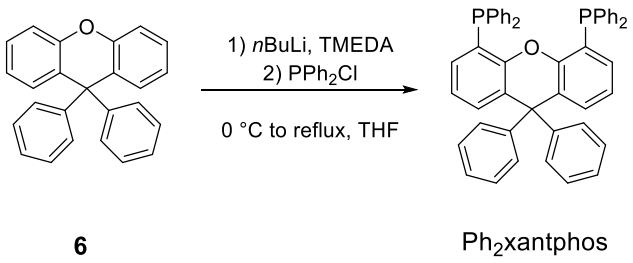


***Scheme 5.8*** *C–P bond formation reaction by lithiation of xanthene ortho to the oxygen atom.*

The C–P bond formation was performed according to a modified literature procedure[183] by selective lithiation of the xanthene backbone at the *ortho* position to the oxygen atom. The ligand $Ph_2$xantphos was used without purification in a degassed solution of $CH_2Cl_2$ because the ligand was oxygen sensitive towards most purification methods. An attempt to reduce the phosphane oxide with methyldiethoxysilane and bis(4-nitrophenyl) phosphate as catalyst according to literature[202] failed. Since impurities in the crude mixture were expected to be mainly unreacted xanthene, monofunctionalized xanthene or oxidized phosphanes, these side products were not expected to interfere with copper coordination.

### *5.2.1.5 Preparation of the benchmark complexes*

Preparation of the benchmark complexes was carried out by the standard procedure described in previous chapters and the literature.[84] The complexes were washed with $Et_2O$ and isolated as yellow powders. The structures are shown in **Scheme 5.9**.

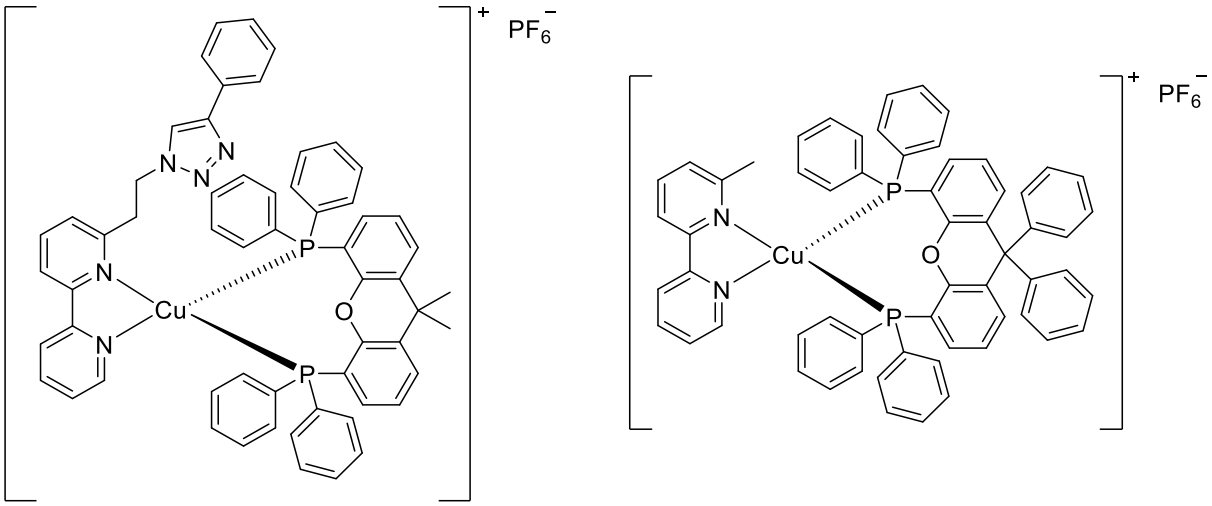


[Cu(6-tphbpy)(xantphos)][$PF_6$] [Cu(6-Mebpy)($Ph_2$xantphos)][$PF_6$]

***Scheme 5.9*** *Benchmark complexes for first generation N^N^P^P ligand complexes.*

### *5.2.1.6 Crystal structures of the benchmark complexes*

Both benchmark complexes crystallize in the triclinic space group *P*–1. ORTEP representations of both structures are shown in **Figure 5.4** and **Figure 5.5** and relevant crystal parameters are given in **Table 5.1**. The phenyl ring on the triazole moiety of [Cu(6-tphbpy)(xantphos)]$^+$ is disordered and was modelled over two positions with relative occupancies of 70% and 30%. The major occupancy structure is shown in **Figure 5.4**. Side view representations of both the cations from Scheme 5.9 are shown in **Figure 5.3**. The xantphos backbone adopts a boat conformation as is expected and has been discussed in previous chapters. The bite angle of $Ph_2$xantphos is 115.90° (**Figure 5.5**) and therefore very similar to the one of xantphos with 114.33° (**Figure 5.4**), indicating that two phenyl substituents in the xanthene backbone do not alter the coordination properties of the ligand. [Cu(6-tphbpy)(xantphos)]$^+$ shows face to face π-stacking interaction[203] of the equatorial phenyl rings, with a centroid…centroid distance of 3.85 Å and angle of 10.0° between the ring planes. These findings are similar to the findings of Keller *et al.* for [Cu(6-Mebpy)(xantphos)]$^+$.[84] The equatorial phenyl rings of [Cu(6-Mebpy)($Ph_2$xantphos)]$^+$ show a larger centroid…centroid distance of 4.14 Å and the rings are more twisted with

respect towards each other with an angle of 21.0° between the ring planes. In both structures, the sterically demanding substituents in the 6-position of the 2,2'-bipyridine ligand are positioned beneath the xanthene bowl. This is expected for [Cu(6-Mebpy)(Ph$_2$xantphos)]$^+$ due to the structural similarity to [Cu(6-Mebpy)(xantphos)]$^+$[84] but is surprising for [Cu(6-tphbpy)(xantphos)]$^+$ with its large ethyl-triazole-phenyl substituent in the 6-position. Keller *et al.* observed two conformers when a phenyl group was in the 6-position of the 2,2'-bipyridine ligand in a [Cu(N^N)(xantphos)][PF$_6$] complex, one located close to, and one remote from the xanthene backbone.[84] We reported similar findings for large aromatic substituents in 6-position of a 2,2'-bipyridine ligands in Chapter 2. It seems that the added flexibility of an ethyl-spacer allows large substituents to be positioned beneath the xanthene bowl. This was also observed for Cu(6-Etbpy)(xantphos)]$^+$ (where 6-Etbpy is 6-ethyl-2,2'-bipyridine).[84] The steric arrangement observed in both complexes confirms the finding of the geometry optimization calculations described above (**Figure 5.1**) and leads to the conclusion that the targeted connection structure of the N^N and P^P moiety is sterically suitable.

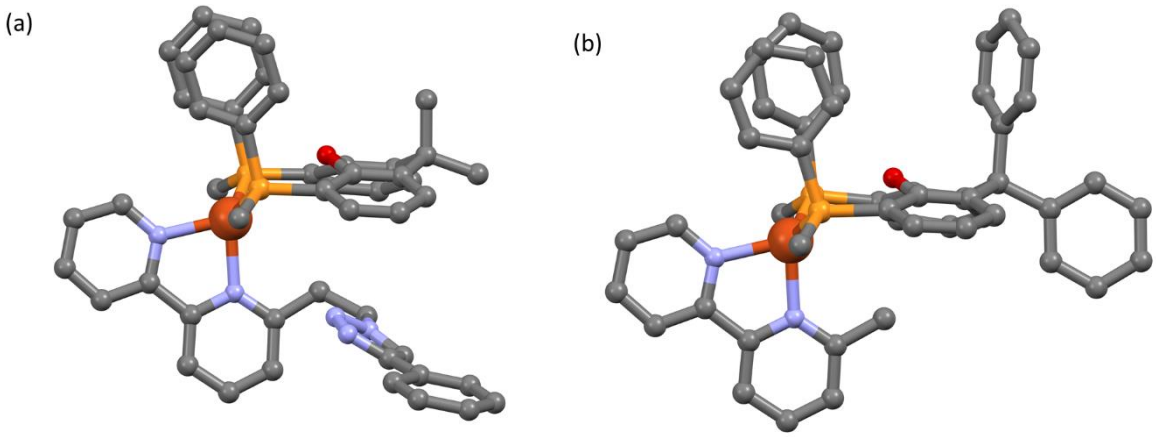


***Figure 5.3*** *Side view of [Cu(6-tphbpy)(xantphos)]$^+$ and [Cu(6-Mebpy)(Ph$_2$xantphos)]$^+$ cations. Only ipso-C of the equatorial phenyl rings are shown. Hydrogens are omitted for clarity.*

***Table 5.1*** *Crystallographic parameters of benchmark [Cu(N^N)(P^P)][$PF_6$] complexes.*

| Compound | [Cu(6-tphbpy)(xantphos)][$PF_6$] ·0.5$Et_2O$ | [Cu(6-Mebpy)($Ph_2$xantphos)][$PF_6$] ·1.5$Et_2O$ |
|---|---|---|
| Formula | $C_{61}H_{54}CuF_6N_2O_{1.5}P_3$ | $C_{66}$ $H_{51}CuF_6N_2O_{2.5}P_3$ |
| Formula weight | 1151.59 | 1192.68 |
| Crystal colour and habit | Yellow block | Yellow block |
| Crystal system | Triclinic | Triclinic |
| Space group | *P*–1 | *P*–1 |
| *a, b, c* / Å | 10.9834(7)<br>15.5458(9)<br>18.6079(11) | 10.9811(5)<br>14.0848(6)<br>18.7099(8) |
| $\alpha, \beta, \gamma$ / ° | 110.395(2)<br>94.433(2)<br>110.363(2) | 93.662(2)<br>93.723(2)<br>92.765(2) |
| *U* / Å$^3$ | 2719.7(3) | 2877.8(2) |
| *Dc* / Mg m$^{-3}$ | 1.41 | 1.376 |
| *Z* | 2 | 2 |
| $\mu$(Cu-K$\alpha$) / mm$^{-1}$ | 1.981 | 1.889 |
| *T* / K | 123 | 123 |
| Refln. collected ($R_{int}$) | 36022 (0.029) | 38013 (0.029) |
| Unique refln. | 10070 | 10633 |
| Refln. for refinement | 9303 | 9499 |
| Parameters | 682 | 736 |
| Threshold | 2$\sigma$ | 2$\sigma$ |
| *R*1 (*R*1 all data) | 0.0628 (0.0660) | 0.0533 (0.0585) |
| *wR*2 (*wR*2 all data) | 0.1619 (0.1626) | 0.1305 (0.1317) |
| Goodness of fit | 1.0476 | 1.0275 |
| CCDC deposition | - | - |

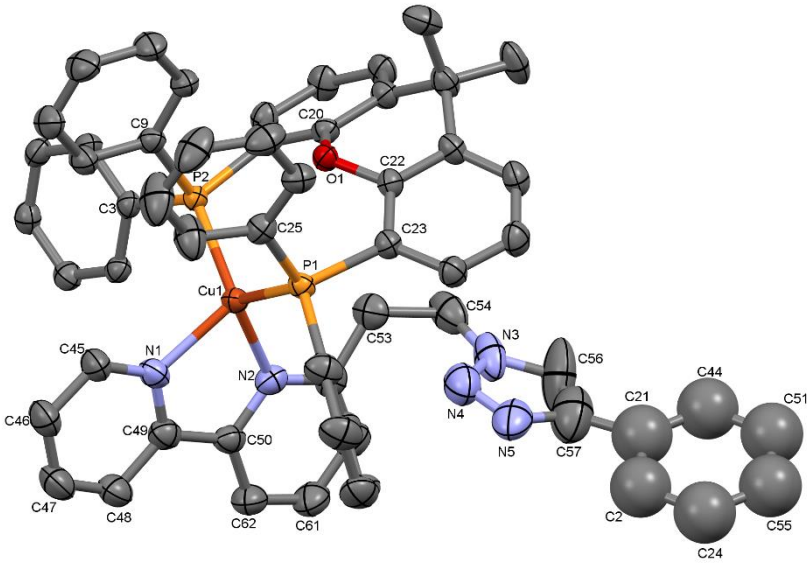


***Figure 5.4*** *Structure of the [Cu(6-tphbpy)(xantphos)]$^+$ cation in [Cu(6tphbpy)(xantphos)][$PF_6$]·0.5$Et_2O$ with ellipsoids plotted at 50% probability level. H atoms and solvent molecules omitted for clarity. Selected bond parameters: Cu1–P2 = 2.2590(8), Cu1–P1 = 2.2674(8), Cu1–N2 = 2.063(2), Cu1–N1 = 2.065(3) Å; P2–Cu1–P1 = 114.33(3), P2–Cu1–N2 = 118.78(8), P1–Cu1–N2 = 113.80(8), P2–Cu1–N1 = 111.67(8), P1–Cu1–N1 = 113.50(8), N2–Cu1–N1 = 80.2(1)°. The phenyl ring is disordered and was modelled over two positions with relative occupancies of 70% to 30%. Only the major conformer is structure.*

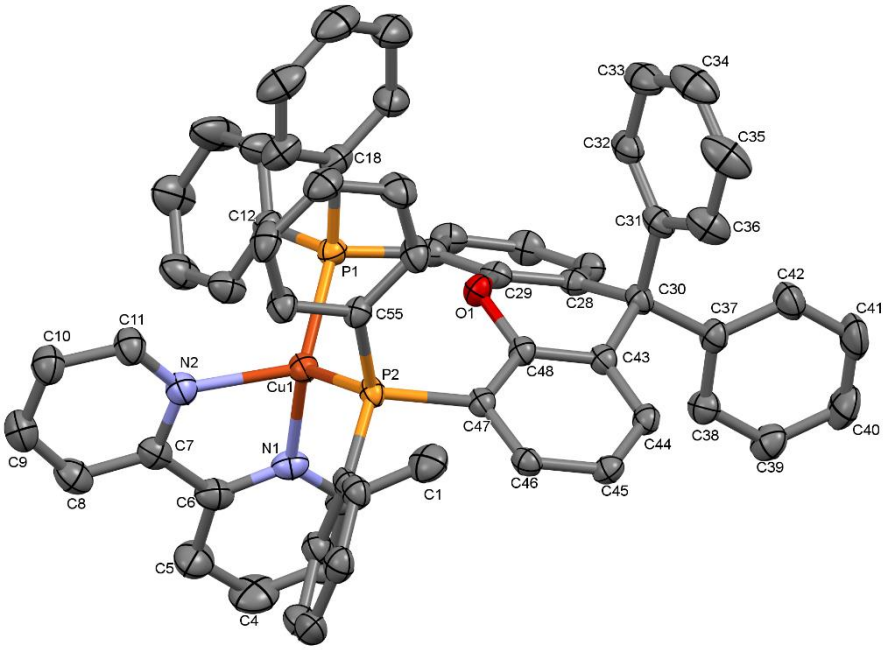


***Figure 5.5*** *Structure of the [Cu(6-Mebpy)(Ph$_2$xantphos)]$^+$ cation in [Cu(6-Mebpy)(Ph$_2$xantphos)][PF$_6$]·1.5Et$_2$O with ellipsoids plotted at 50% probability level. H atoms and solvent molecules omitted for clarity. Selected bond parameters: Cu1–P2 = 2.2686(7), Cu1–P1 = 2.2611(6), Cu1–N2 = 2.069(2), Cu1–N1 = 2.073(2) Å; P2–Cu1–P1 = 115.90(2), P2–Cu1–N2 = 112.10(6), P1–Cu1–N2 = 113.97(6), P2–Cu1–N1 = 115.59(6), P1–Cu1–N1 = 113.99(6), N2–Cu1–N1 = 80.32(8)°.*

### *5.2.1.7 Photophysical and electrochemical properties of the benchmark complexes*

To investigate the influence of the newly introduced substituents, photophysical and electrochemical investigations of [Cu(6-tphbpy)(xantphos)][PF$_6$] and [Cu(6-Mebpy)(Ph$_2$xantphos)][PF$_6$] were performed. The results are summarized in **Table 5.2**. **Figure 5.6** shows the solution absorption spectra of [Cu(6-tphbpy)(xantphos)][PF$_6$] and [Cu(6-Mebpy)(Ph$_2$xantphos)][PF$_6$]. The absorption profiles are similar, but [Cu(6-tphbpy)(xantphos)][PF$_6$] shows more intense absorption bands below 330 nm, most likely due to the additional aromatic moiety of the triazole-phenyl substituent. The MLCT absorptions of [Cu(6-Mebpy)(Ph$_2$xantphos)][PF$_6$] and [Cu(6-tphbpy)(xantphos)][PF$_6$] occur in the same range.

***Table 5.2*** *Photophysical properties of benchmark and comparison [Cu(N^N)(P^P)][PF$_6$] complexes*

| Complex cation | $CH_2Cl_2$ solution[a,b] | | | | Powder | | |
|---|---|---|---|---|---|---|---|
| | UV-Vis MLCT $\lambda_{max}$/nm | $\lambda_{em}^{max}$ /nm | PLQY (non-degassed/ degassed)% | $\tau_{1/2}$(av)(non-degassed/ degassed)/µs | $\lambda_{em}^{max}$/nm | PLQY/% | $\tau_{1/2}$(av)[c]/µs |
| [Cu(6-tphbpy)(xantphos)]$^+$ | 383 | 608, 633 | >1/>1 | 0.07/0.08 | 548 | 25 | 7.1 |
| [Cu(6-Mebpy)(Ph$_2$xantphos)]$^+$ | 386 | 602, 633 | >1/1 | 0.29/0.93 | 543 | 22 | 7.9 |
| [Cu(6-Mebpy)(xantphos)]$^+$ [d] | 379 | 605, 635 | 1.0/1.8 | 0.272/0.784 | 547 | 33.8 | 9.7 |
| [Cu(6-Etbpy)(xantphos)]$^+$ [d] | 390 | 603, 635 | 0.8/1.9 | 0.282/0.833 | 557 | 23.6 | 7.2 |

[a] Solution concentration = 2.5 x 10$^{-5}$ mol dm$^{-3}$. [b] $\lambda_{exc}$ = 365 nm. [c] Biexponential fit using the equation $\tau_{1/2}(av) = \Sigma A_i\tau_i/\Sigma A_i$ where $A_i$ is the pre-exponential factor for the lifetime. [d] Values taken from reference 174.

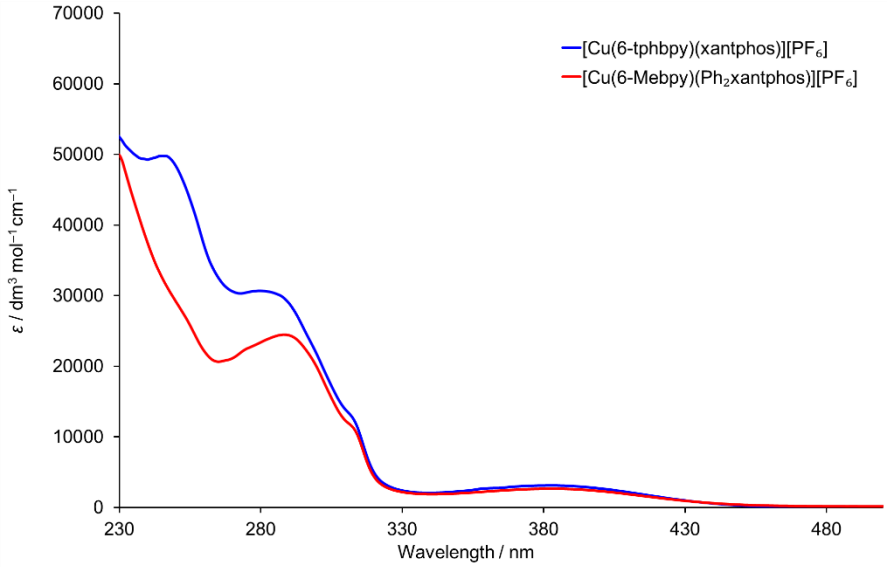


***Figure 5.6*** *Absorption spectra of [Cu(6-tphbpy)(xantphos)][PF$_6$] and [Cu(6-Mebpy)(Ph$_2$xantphos)][PF$_6$] (CH$_2$Cl$_2$, 2.5 x 10$^{-5}$ mol dm$^{-3}$).*

The solution emission spectra of both compounds show a weak yellow-orange emission around 605 nm with a shoulder at 633 nm (**Figure 5.7**). The emission bands are weak and unstructured with low quantum yields of 1% or lower in aerated and deaerated solutions (**Table 5.2**). In the solid state, both complexes show a much more intense emission that is blue shifted with respect to the solution emission. The PLQY is greatly increased to 25% for [Cu(6-tphbpy)(xantphos)][PF$_6$] and 22% [Cu(6-Mebpy)(Ph$_2$xantphos)][PF$_6$] with long excited state lifetimes of 7.1 and 7.9 µs respectively. All emission properties of [Cu(6-tphbpy)(xantphos)][PF$_6$] and [Cu(6-Mebpy)(Ph$_2$xantphos)][PF$_6$] are very similar to the ones of [Cu(6-Mebpy)(xantphos)][PF$_6$] and [Cu(6-Etbpy)(xantphos)][PF$_6$], with the exception of [Cu(6-Mebpy)(xantphos)][PF$_6$] having a higher solid state PLQY of 33.8% and longer excited state lifetime of 9.7 µs in solid state[174] (**Table 5.2**). The fact that the photophysical properties of [Cu(6-tphbpy)(xantphos)][PF$_6$] and [Cu(6-Mebpy)(Ph$_2$xantphos)][PF$_6$] are almost identical to the ones of [Cu(6-Mebpy)(xantphos)][PF$_6$] and [Cu(6-Etbpy)(xantphos)][PF$_6$] leads to the conclusion, that the newly introduced substituents do not disrupt the emissive behaviour of the complex. Therefore it is expected that the linkage between the 2,2'-bipyridine and xantphos units via an ethyl-triazole-phenyl bridge as proposed in **Scheme 5.3** and **Figure 5.1**, does not have a detrimental effect on the emissive behaviour of the newly formed complex.

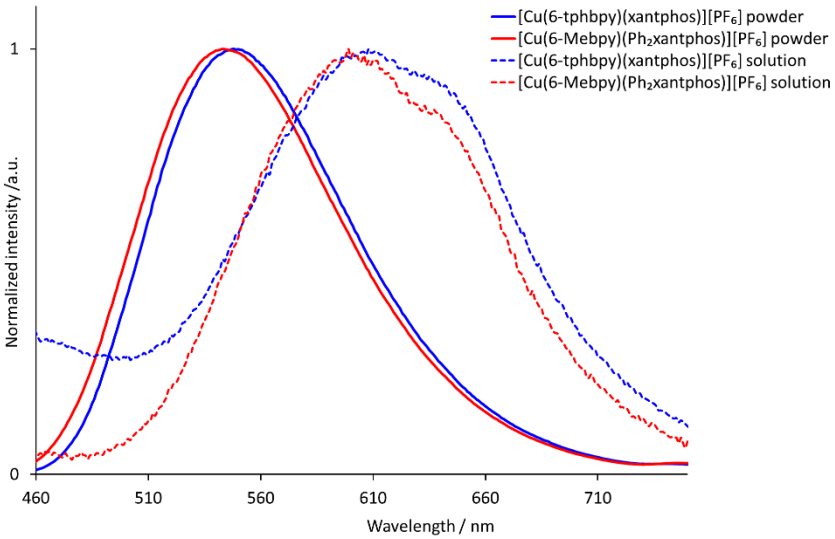


***Figure 5.7*** *Emission spectra of [Cu(6-tphbpy)(xantphos)][$PF_6$] and [Cu(6-Mebpy)($Ph_2$xantphos)][$PF_6$] in solid state (solid lines) and solution (dashed lines, $CH_2Cl_2$, 2.5 x $10^{-5}$ mol $dm^{-3}$).*

Cyclic voltamogramms of [Cu(6-tphbpy)(xantphos)][$PF_6$] and [Cu(6-Mebpy)($Ph_2$xantphos)][$PF_6$] are shown in **Figure 5.8** and the results are summarized in **Table 5.3**. Both complexes show an N^N ligand-based quasi-reversible reduction at around −2.03 V. This is expected, because DFT calculations for related complexes showed that the LUMO is located on the N^N moiety of the nitrogen ligand.[83,84] In the case of 6-Mebpy and 6-tphbpy the nature of this moiety does not change except for the bulky substituent in 6-position, which is not expected to alter the LUMO energy level significantly. Both complexes show an irreversible copper oxidation process where the oxidation potential of [Cu(6-Mebpy)($Ph_2$xantphos)]$^+$ is 100 mV higher than the oxidation potential of [Cu(6-tphbpy)(xantphos)]$^+$. The signals of [Cu(6-Mebpy)($Ph_2$xantphos)]$^+$ are poorly defined because of the low concentration of the complex due to the limited supply of compound. Keller *et al.* observed oxidation potentials of +0.85 V and +0.86 V for [Cu(6-Mebpy)(xantphos)][$PF_6$] and [Cu(6-Etbpy)(xantphos)][$PF_6$] respectively, obtained in $CH_2Cl_2$ solution.[174]

***Table 5.3*** *Cyclic voltammetric data for [Cu(6-tphbpy)(xantphos)][$PF_6$] and [Cu(6-Mebpy)($Ph_2$xantphos)][$PF_6$] referenced to internal $Fc/Fc^+$ = 0 V; propylene carbonate solutions with [$^nBu_4N$][$PF_6$] as supporting electrolyte and scan rate of 0.1 V $s^{-1}$.*

| Complex cation | $E_{pc}^{ox}$ / V | $E_{1/2}^{red}$ / V ($E_{pa}$ − $E_{pc}$ / mV) |
|---|---|---|
| [Cu(6-tphbpy)(xantphos)]$^+$ | +0.81 | −2.02 (90) |
| [Cu(6-Mebpy)($Ph_2$xantphos)]$^+$ | +0.91 | −2.05 (100) |

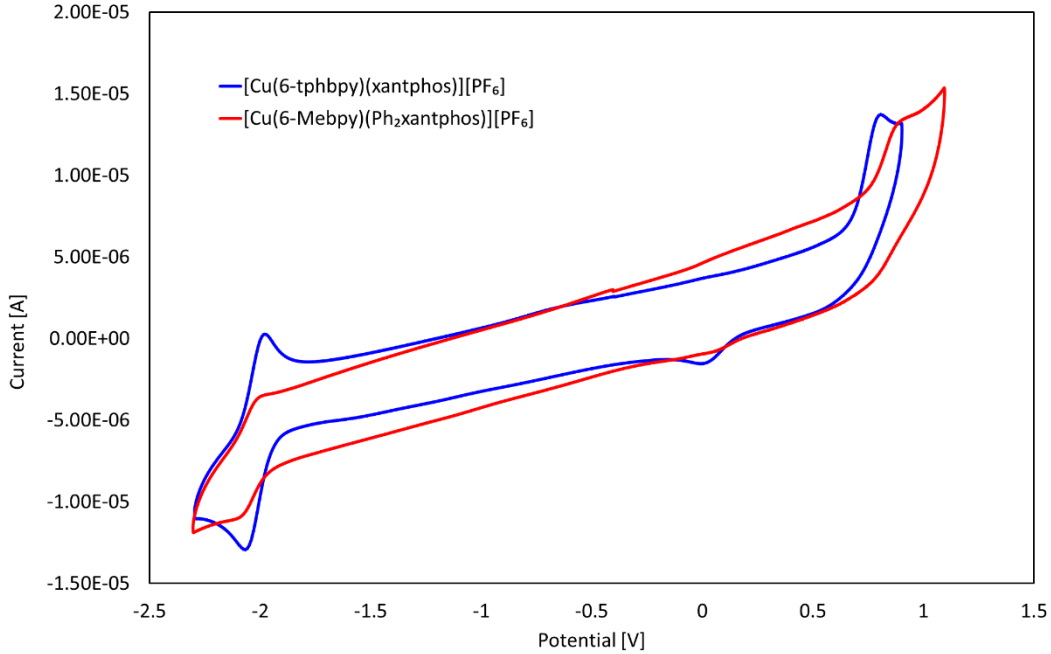


***Figure 5.8*** *Cyclic voltammogram of [Cu(6-tphbpy)(xantphos)][PF$_6$] and [Cu(6-Mebpy)(Ph$_2$xantphos)][PF$_6$] in propylene carbonate at a scan rate of 0.1 V s$^{-1}$ referenced to internal Fc/Fc$^+$ = 0V. The second of three reproducible cycles is shown.*

## *5.2.2 Target ligand synthesis*

The characterization of [Cu(6-tphbpy)(xantphos)][PF$_6$] and [Cu(6-Mebpy)(Ph$_2$xantphos)][PF$_6$] demonstrated, that a ethyl-triazole-phenyl connection between 2,2'-bipryridine and xantphos can lead to a tetradentate ligand, that gives enough structural flexibility and preorganization to form the respective [Cu(N^N^P^P)][PF$_6$] complex while maintaining the tetrahedral geometry of the copper centre. The photophysical analysis showed the conservation of the emissive properties and their similarities to [Cu(6-Mebpy)(xantphos)][PF$_6$] and [Cu(6-Etbpy)(xantphos)][PF$_6$].[174] Electrochemical analysis was in good agreement with the benchmark complexes [Cu(6-Mebpy)(xantphos)][PF$_6$] and [Cu(6-Etbpy)(xantphos)][PF$_6$]. This leads to the conclusion, that an ethyl-triazole-phenyl bridged N^N^P^P ligand is suitable to form a copper(I) complex applicable for LEC application. Therefore, a synthetic plan was developed as shown in **Scheme 5.10**

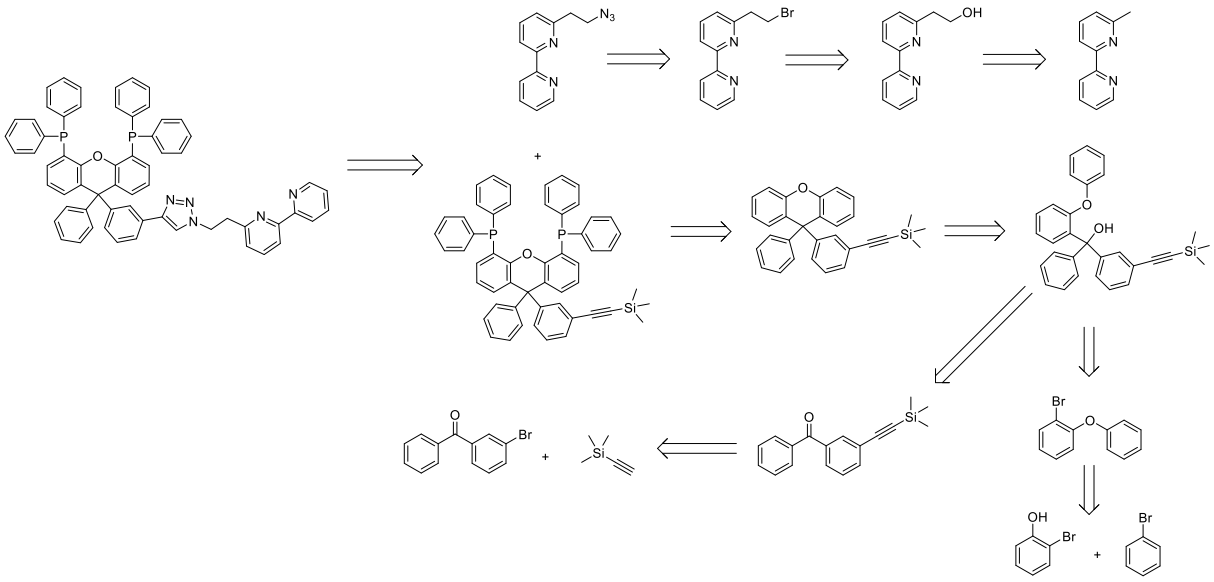

***Scheme 5.10*** *First-generation retrosynthetic analysis of the target N^N^P^P ligand.*

The preparation of 6-(2-bromoethyl)-2,2'-bipyridine (**3**) was performed according to literature[199] and is described above for the preparation of 6-tphbpy. 1-Bromo-2-diphenyl ether (**5**) was prepared according to literature[200] and is described in the previous section.

### *5.2.2.1 Sonogoshira cross-coupling*

Compound **7** was prepared via Pd/Cu-catalysed Sonogashira coupling of 3-bromobenzophenone and ethylene trimethylsilane according to an adapted literature procedure with a good yield of 90%.[204]

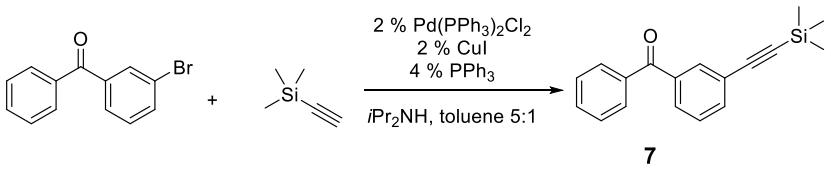


***Scheme 5.11*** *Sonogoshira coupling for preparation of* ***7****.*

### *5.2.2.2 Xanthene preparation*

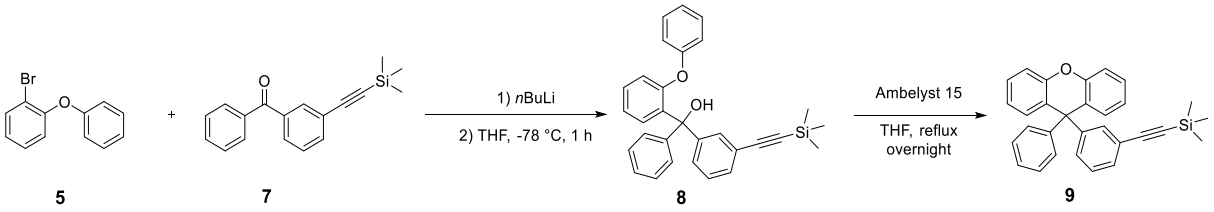


***Scheme 5.12*** *Stepwise approach for build-up of the xanthene backbone.*

Different synthetic attempts for the preparation of compound **9** were performed and are summarized in **Table 5.4**. In an attempt to build up the xanthene backbone in one step according to the patent procedure[201] described for $Ph_2$xantphos (see section 5.9.6). Compound **5** was lithiated with *n*BuLi at −78 °C before compound **7** was added to form the C-C bond and corresponding alcohol **8**. After removal of the solvent, the crude material was treated with a 3:1 mixture of acetic acid and fuming HCl and heated to 75 °C for several hours. Purification of the crude material did not yield the desired product. To

avoid disturbance of the reaction by impurities, a stepwise approach was chosen for a second attempt (**Scheme 5.12**). The C–C bond formation was performed as described above. The tertiary alcohol **8** was purified by column chromatography and isolated as a colourless oil. To perform the dehydrogenation reaction to form the xanthene moiety, different reaction conditions were tested (**Table 5.4**). Treatment with a 3:1 mixture of acetic acid and fuming HCl as described in literature[201] and above yielded the corresponding ring closure product, but also cleaved the TMS protecting group which lead to the hydrolysis of the acetylene moiety and, therefore, the corresponding ketone was isolated. Treatment of the tertiary alcohol with an organic acid such as trifluoracetic acid in a water-free environment yielded the same decomposition product. Reduction of the ketone with diethyl chlorophosphite and LDA according to literature[205] failed. It seemed that the water that is released during the dehydrogenation reaction destroys the TMS protected acetylene moiety, even when the reaction is performed in water-free media. To avoid this, a solid-state acid was used to catalyse the reaction. Therefore, the reaction was performed in water-free conditions in the presence of the acidic ion exchange resin Ambelyst 15. The desired xanthene product was isolated in moderately good yield of 65% with the TMS protected acetylene moiety intact.

***Table 5.4*** *Investigated reaction conditions for preparation pf compound* ***9****.*

| Attempt | Isolation of intermediate **8** | Acid used | Isolated product |
|---|---|---|---|
| 1 | no | acetic acid : HCl 3:1 | ? |
| 2 | yes | acetic acid : HCl 3:1 | phenyl ketone |
| 3 | yes | trifluoro acetic acid | phenyl ketone |
| 4 | yes | Ambelyst 15 | **9** |

### *5.2.2.3 C-P bond formation reaction*

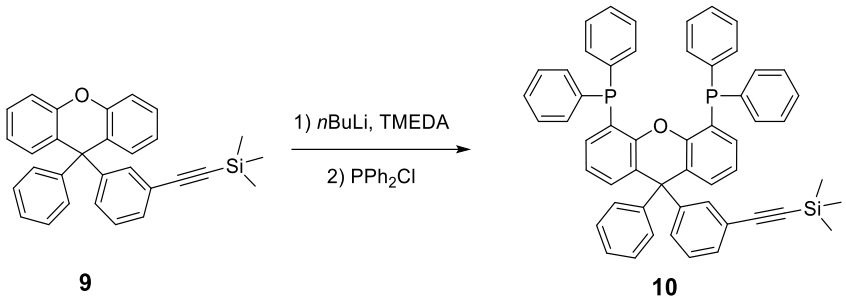


**9** **10**

***Scheme 5.13*** *C–P bond formation reaction by lithiation of the xantphos moiety ortho to the oxygen atom.*

An established method to introduce the $PPh_2$ groups is the double deprotonation of xanthene with *n*BuLi and TMEDA *ortho* to the oxygen atom, which acts as *ortho*-directing group for the lithiation.[183] A rigorous exclusion of water and oxygen is needed in this type of C–P bond formation reaction. For the lithiation, the xanthene molecule (**9**) was treated with *n*BuLi and TMEDA and stirred for 16 h at room temperature. After the addition of $PPh_2Cl$ and further reaction time, only oxidised phosphane signals were observed in the $^{31}P\{^1H\}$ NMR (**Figure 5.9b**). In a first attempt THF was used as solvent. Changing the solvent to heptane to increase the stability of the lithiated xanthene species did not yield the desired product. Using stronger lithiation reagents such as *sec*-butyllithium and performing the reaction at lower temperatures gave the same results. Rigorous degassing of the solvents by sonication under reduced pressure and work up under inert conditions

did not give the desired results. The different reaction conditions are summarized in **Table 5.5**. Additionally, $^{1}H$ NMR spectra indicated that the TMS protection group was partially lost during the reaction or workup (**Figure 5.9a**). Because of all these difficulties, it was decided to alter original synthetic outline to a second-generation scheme.

***Table 5.5*** *Reaction parameters for attempted C–P bond formation reactions.*

| Attempt | Lithiation reagent | Solvent | Temperature [°C] | Reaction time [h] |
|---|---|---|---|---|
| 1 | *n*BuLi | THF | +25 | 16 |
| 2 | *n*BuLi | heptane | +25 | 16 |
| 3 | *sec*BuLi | $Et_2O$ | −78 to +25 | 16 |
| 4 | *n*BuLi | THF/heptane | reflux | 1 |

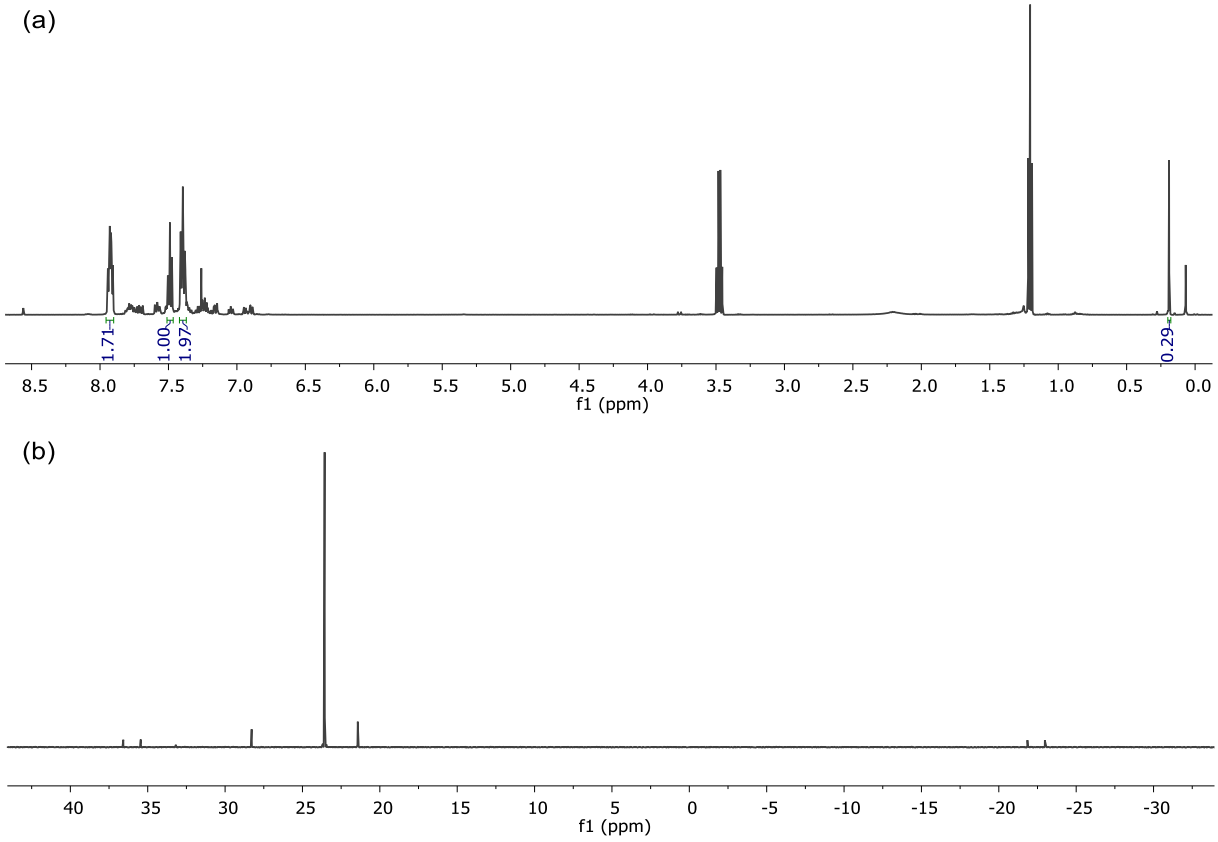


***Figure 5.9*** *(a) $^{1}H$ (500 MHz, $CDCl_3$, 298 K) and (b) $^{31}P\{^{1}H\}$ (202 MHz, $CDCl_3$, 298 K) NMR spectra of C-P bond formation reaction after work-up under inert conditions. The TMS signal at 0.19 ppm (a) is greatly diminished and the $^{31}P\{^{1}H\}$ NMR spectrum shows mainly oxidised phosphane signals.*

## 5.3 Generation 2 - Triazole connected ligand by late C-P bond formation

In the first-generation reaction scheme the synthetic route could be optimized up to the C-P bond formation reaction. Upon lithiation and reaction of the xanthene backbone with $PPh_2Cl$, signals arising from oxidized phosphanes were observed in the $^{31}P\{^{1}H\}$ NMR spectra. Additionally, the methyl signal for the TMS protection group was diminished in the crude NMR spectra after workup of the reaction. These findings indicate that the TMS protected acetylene group interferes with the C–P bond formation reaction. To avoid this, a second-generation synthetic scheme was developed (**Scheme 5.14**). The assembly of

the modified xanthene backbone as well as the modification of the 2,2'-bipyridine in the 6-position are identical to those in the first-generation reaction scheme (**Scheme 5.10**) and the synthetic steps were discussed in detail in the previous section. However, in contrast to the first-generation attempt, the linkage of the two backbone moieties by the click reaction is performed earlier in the sequence, leaving the C–P bond formation reaction as the last step. This shortens the number of reaction steps in which the air sensitive bis-phosphane ligand needs to be handled. In a best-case scenario, a one pot reaction for C–P bond formation and complex formation could be possible, eliminating the necessity for purification of the air sensitive N^N^P^P ligand entirely. Once complexed, the compound is believed to no longer be sensitive to oxygen, as has been observed for similar compounds before.[83,84,128,129]

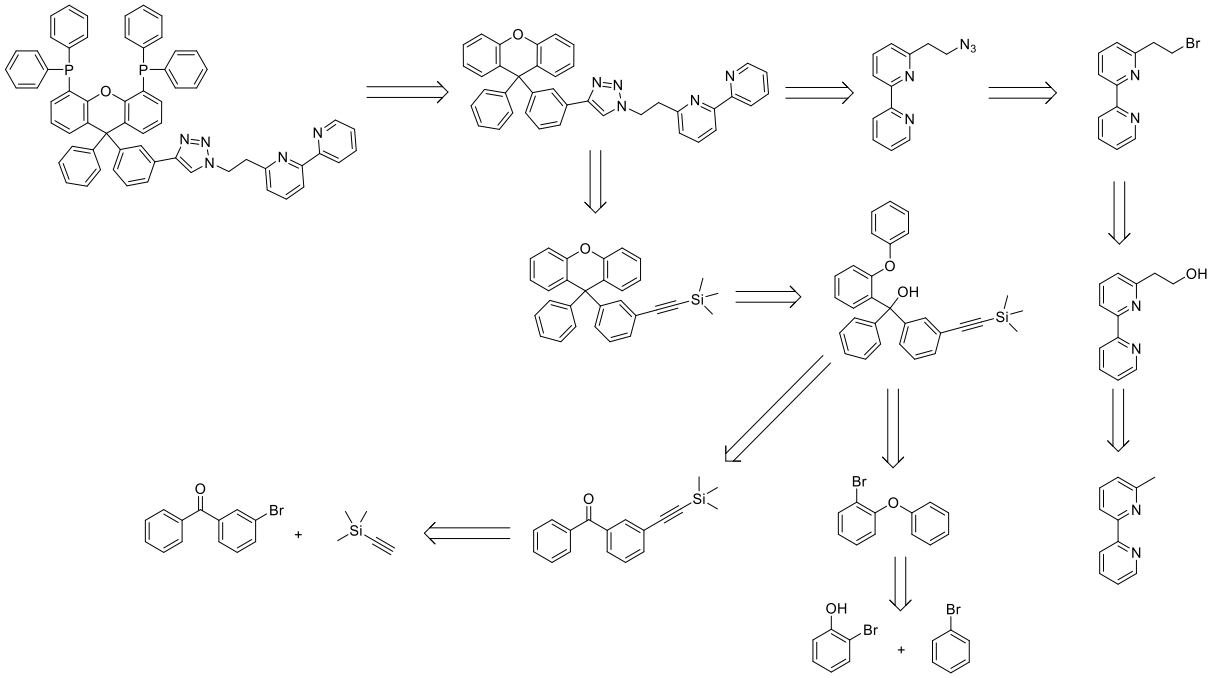

***Scheme 5.14*** *Second-generation retrosynthetic approach for the preparation of a N^N^P^P ligand with the C–P bond formation as the last step.*

## *5.3.1 Click reaction*

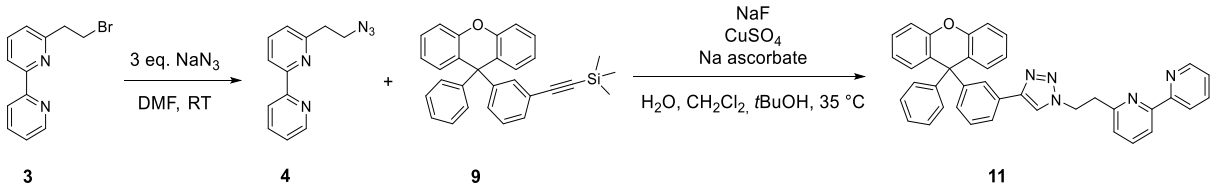


***Scheme 5.15*** *Click reaction for the connection of the 2,2'-bipyridine and xanthene moiety.*

To connect the 2,2'-bipyridine to the xanthene backbone, removal of the TMS protection on the acetylene and click reaction were all performed in a one pot synthesis. Compound **3** was treated with sodium azide in DMF, extracted and used as crude. The click reaction was performed in a mixture of $CH_2Cl_2$, water and *tert*-butanol. Sodium fluoride was added to the reaction to remove the TMS functionalization of the acetylene moiety in situ. The catalytically active copper(I) species was generated in situ from copper(II) sulfate and sodium ascorbate. Because the bipyridine was expected to bind to the catalyst and

therefore poison it (see section 5.2.1), an excess of copper(II) sulfate and sodium ascorbate was used. To remove the excess of copper in the product, the crude material was washed with an aqueous mixture of $H_2O_2$, $H_4EDTA$ and sodium hydroxide. The formation of the desired product was confirmed by NMR and ESI-MS.

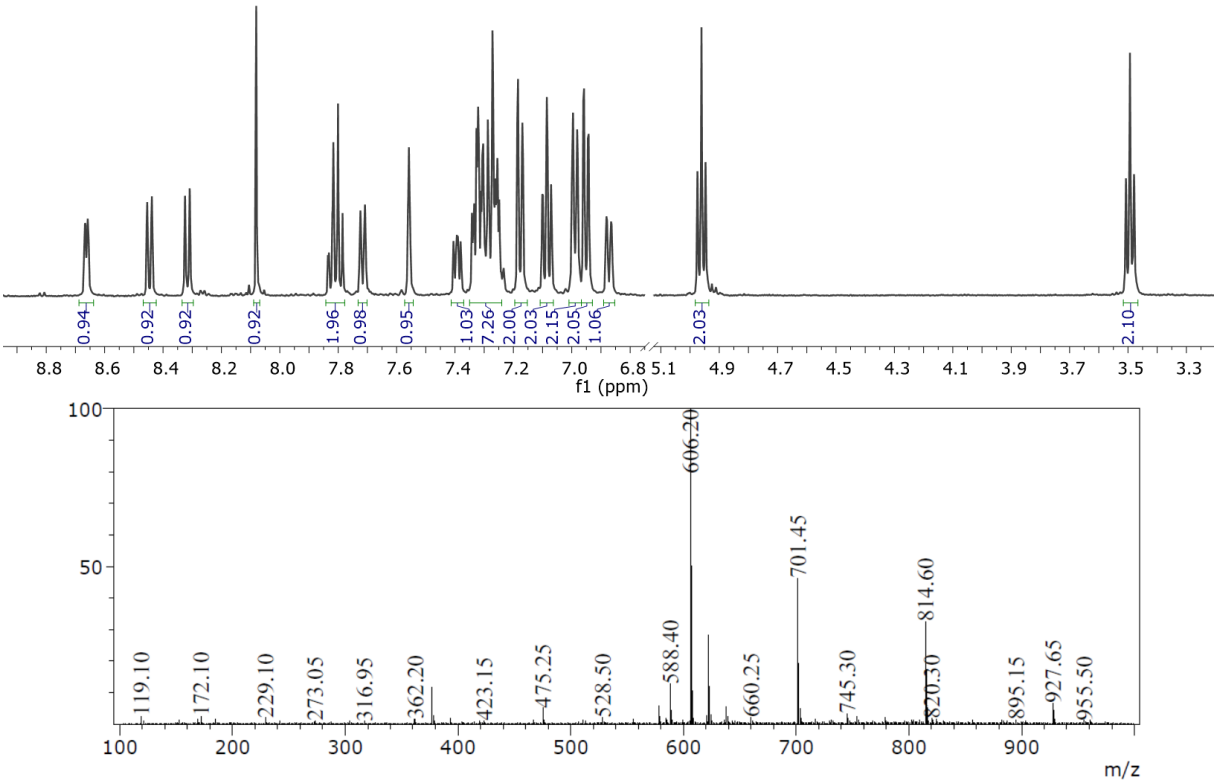


***Figure 5.10*** *Parts of the $^1H$ NMR spectrum (top, 500 MHz, acetone-$d_6$, 298 K) and ESI-MS (bottom) of the purified of the xanthene-phenyl-triazole-ethyl-bpy molecule. The ESI-MS shows the $[M+Na]^+$ signal at m/z 606.*

## *5.3.2 C-P bond formation*

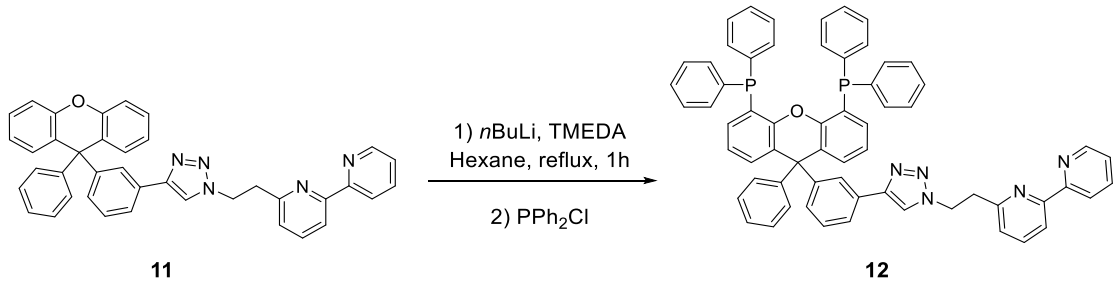


***Scheme 5.16*** *C-P bond formation reaction on the modified xanthene backbone.*

The C–P bond formation reaction was performed as described in section 5.2.2. A crude $^{31}P\{^1H\}$ NMR spectrum of the crude mixture from a test reaction showed only signals downfield of $\delta$ 20 ppm, consistent with the presence of phosphane oxide species. There were no significant signals at higherfield than $\delta$ −13 ppm in the region expected for the target compound (**Figure 5.11**). Additionally, ESI-MS indicated decomposition of the compound, since only peaks with masses below *m/z* 775 were detected.

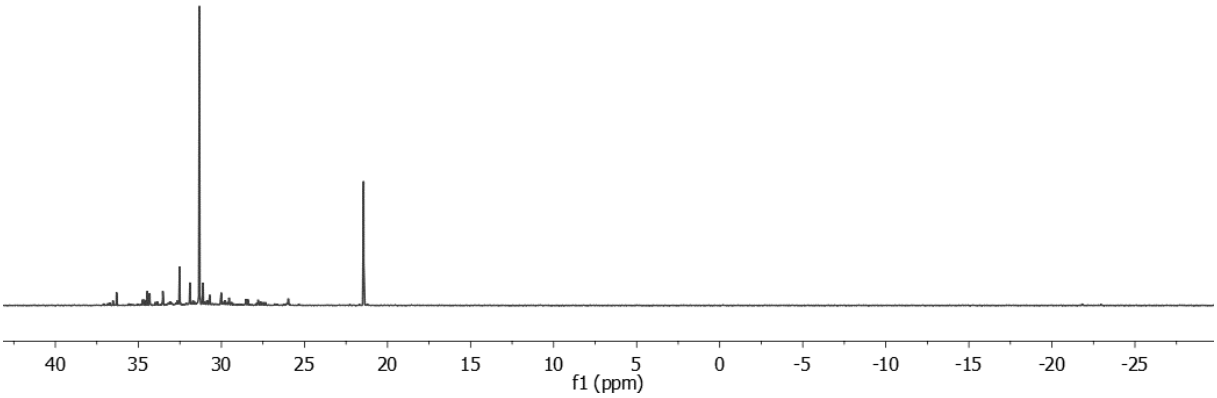


***Figure 5.11*** *Parts of the $^{31}P$ NMR spectrum (202 MHz, $CDCl_3$, 298 K) of the C–P bond formation reaction under inert conditions. Only signals for oxidised phosphanes are observed.*

To further investigate possible decomposition reactions, a test-lithiation reaction was performed (**Scheme 5.17**). Compound **11** was treated with *n*BuLi at low temperature as described above. Since the lithiation position cannot be observed directly, the reaction was quenched with an excess of methyl iodide. The methyl group replaced the lithium and allowed the investigation of the lithiation position by NMR. ESI-MS showed a peak at *m/z* 634.3, which corresponds to a double methylation product. Comparison of the $^{1}H$ NMR spectra before and after the reaction shows the disappearance of the triazole proton, indicating a lithiation and then methylation in this position (**Figure 5.12**). This means, that the triazole proton is competing with the ortho protons on the xanthene backbone, leading to a lithiation in an undesired position. To overcome this problem, protection of the triazole is needed. Therefore, a third-generation reaction sequence was developed.

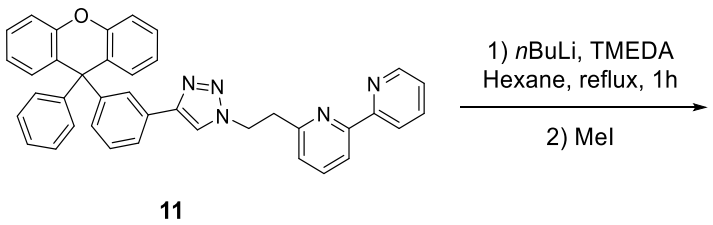


**11**

***Scheme 5.17*** *Test reaction to investigate the modification position of the lithiation reaction.*

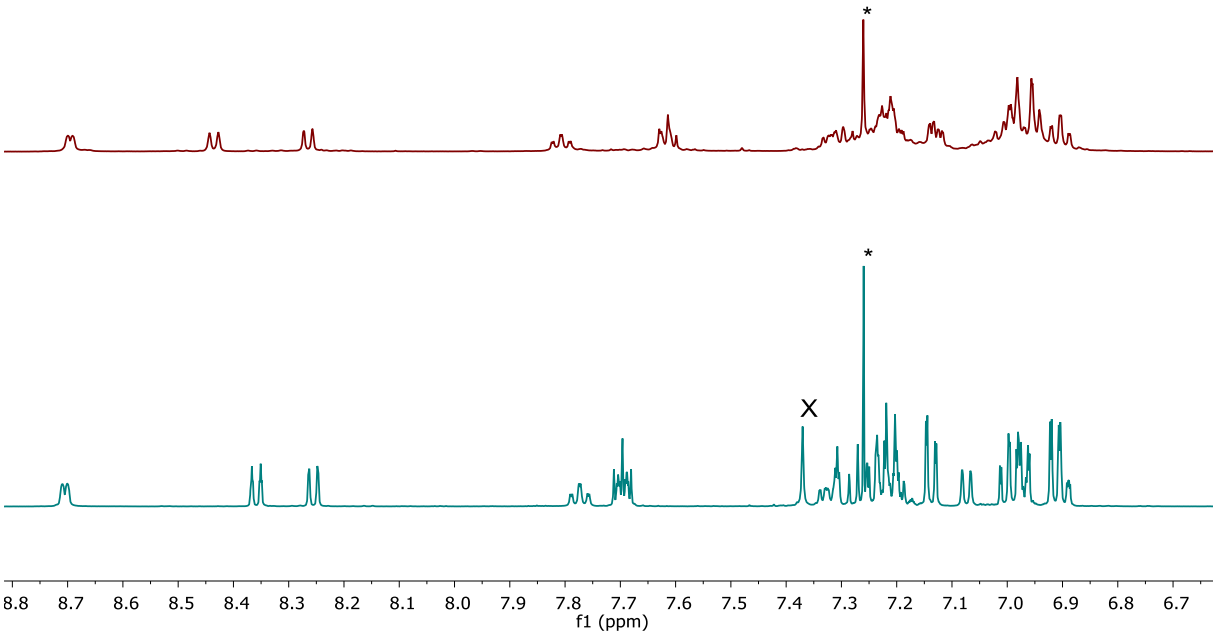


***Figure 5.12*** *Parts of $^1$H NMR spectra (500 MHz, $CDCl_3$, 298 K) for comparison of the methylation test reaction (top) to the starting material (6-(ethyl-triazole-phenyl-xanthene)-2,2'-bipyridine, bottom. The triazole proton (= X in bottom spectrum) is missing after the reaction, indicating a methylation in this position.*

## 5.4 Generation 3 - Triazole connected ligand with increased chain length

The connection of the N^N and P^P moieties through a triazole unit brings the disadvantage of introducing an acidic proton at the triazole ring that competes in lithiation reactions, as discussed in the previous section. Therefore, protection of this position is needed. Test reactions showed that a methyl functionalization in this position is possible by treatment with iodomethane. Geometry optimization at a semi-empirical level showed that the N^N^P^P ligand with two $CH_2$ units between 2,2'-bipyridine and triazole moiety and with a methyl group attached to the triazole ring, is flexible enough and is not too sterically demanding to coordinate to a copper(I) centre (**Figure 5.13a**). However, the structure is highly strained, indicated by the fact, that the N-C bond between the triazole and neighbouring $CH_2$ group is strongly bent out of plane of the triazole ring with an angle of 28.3° (calculated by 180° − [C-N-centroid$_{N\text{-}N\text{-}N\text{-}C\text{-}C}$ angle]). Although the xanthene adopts the expected boat conformation, the two phenyl rings are twisted with respect towards each other. This twist affects the position of the phosphorus atoms and distorts the coordination geometry at the copper centre. When the length of the spacer is increased to three $CH_2$ groups, the N-C bond to plane angel is reduced to 18.9° and the xanthene backbone shows less distortion(**Figure 5.13b**). Therefore, the synthetic strategy was altered again to prepare an N^N^P^P ligand able to accommodate a methyl substituent at the triazole ring, so this position is blocked and should not interfere in the

C–P bond formation reaction. The third-generation retrosynthetic reaction scheme is shown in **Scheme 5.18**.

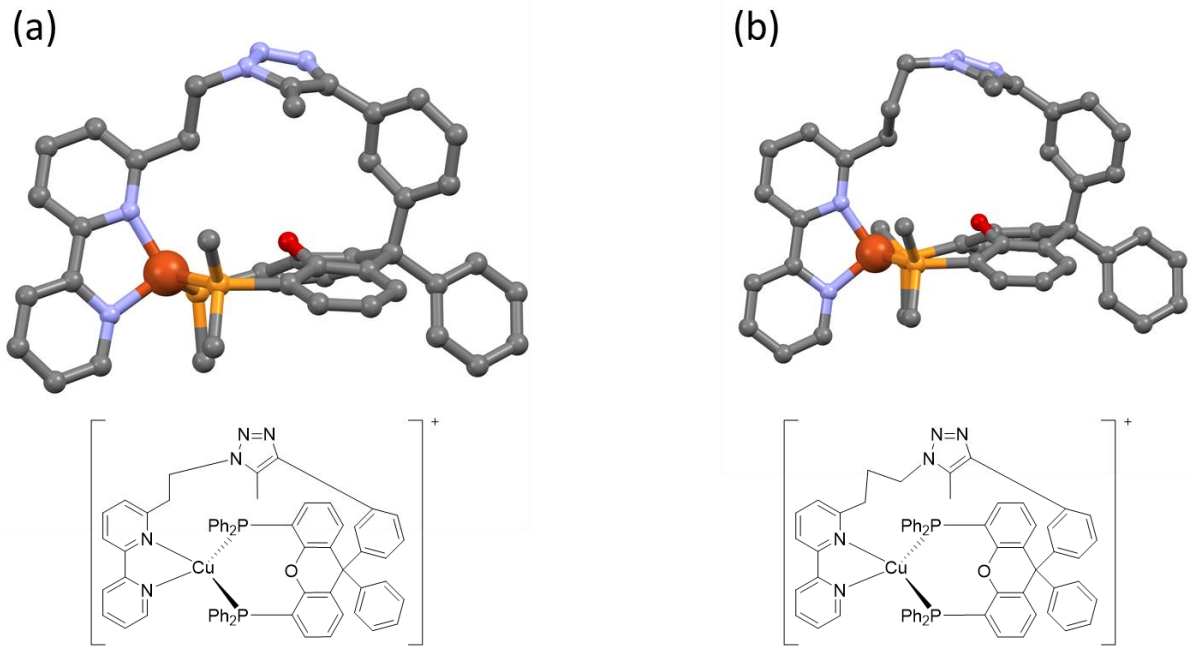


***Figure 5.13*** *Symmetry optimized calculated structures of triazole bridged N^N^P^P ligand complexating a copper(I) ion with a ligand in which the spacer length has two (a) and three (b) $CH_2$ units between the 2,2'-bipyridine and triazole moiety. Hydrogen atoms are omitted for clarity. Only the ipso-C of the phenyl rings are shown. Structures were optimized at the semi-empirical PM3 level using Spartan '18 v. 1.3 (Spartan '18, Wavefunction Inc., Irvine, CA 92612, US).*

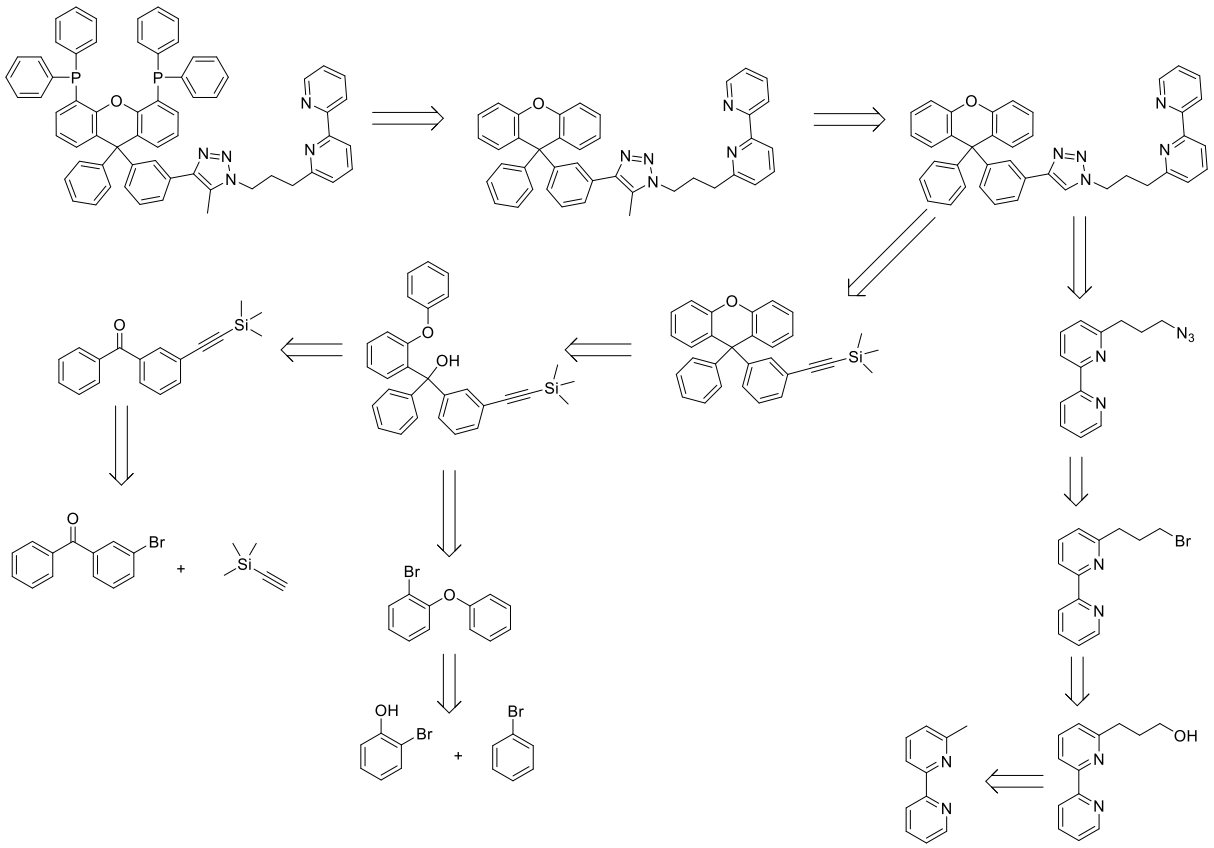

***Scheme 5.18*** *Third-generation retrosynthetic strategy for the preparation of a N^N^P^P ligand with an elongated $CH_2$ chain between 2,2'-bipyridine and the triazole moiety, with an additional methylation step to protect the triazole from unwanted functionalization during the C-P bond formation reaction.*

The third-generation reaction scheme features an elongated chain between the 2,2'-bipyridine and triazole ring and adds an methylation step after the click reaction where a methyl group is introduced in the acidic position of the triazole moiety to prevent it from interfering in the C-P bond formation reaction. Preparation of compound **9** was discussed in section 5.2.2 and remains unchanged.

## *5.4.1 2,2'-bipyridine with longer chain*

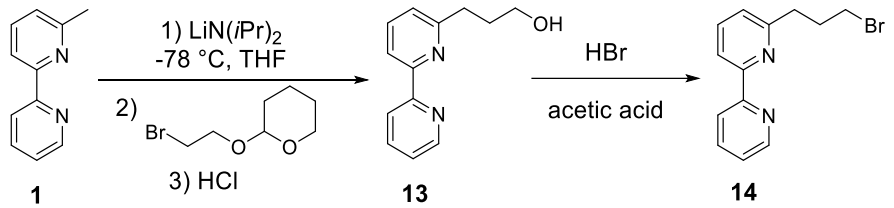


***Scheme 5.19*** *Synthetic strategy for the introduction of an elongated alkyl chain to the 2,2'-bipyridine moiety.*

To introduce a longer $(CH_2)_n$ chain in the 6-position of the bipyridine, a similar synthetic approach as in the first- and second-generation approach was performed. 6-Mebpy was treated with LDA at low temperature to selectively deprotonate at the methyl position. Quenching of the reaction with 2-(2-bromoethoxy)tetrahydro-2H-pyran followed the treatment with acid lead to the formation of the primary alcohol as is described in the literature.[206] Surprisingly, the transformation of a hydroxy into a bromo group by

treatment with HBr in acetic acid according to literature,[199] as was successful for the first- and second-generation approach, did not succeed in forming compound **14**. As an alternative, treatment of the primary alcohol with $PBr_3$ was performed, but also did not yield the desired terminal bromo-product. ESI-MS spectra did not show a typical bromine isotope pattern as expected for a single bromine functionalization. Instead, the products of both reactions showed a base peak at *m/z* 197.1. The $^1H$ NMR spectrum of the product of the reaction of 6-(3-hydroxybutyl)-2,2'-bipyridine with $PBr_3$ shows a set of new signals, that indicate a significantly altered bipyridine environment (**Figure 5.14**). These findings indicate the formation of a product other than that desired. The structure of two possible products are shown in **Figure 5.15**. For the elimination product an $[M+H]^+$ peak is expected while the cyclization product is positively charged and would be detected as the $[M]^+$ peak.

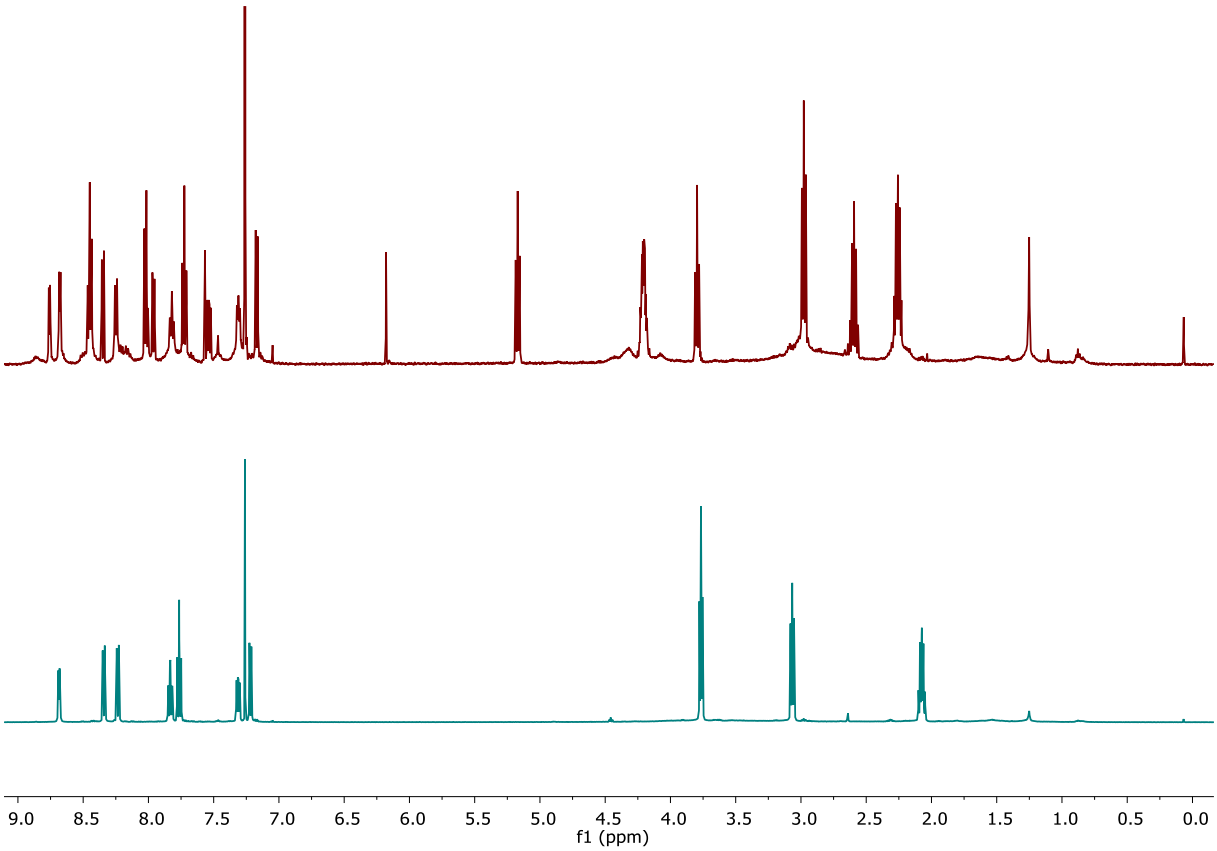


***Figure 5.14*** *Comparison of $^1H$ NMR spectra (500 MHz, $CDCl_3$, 298 K) of 6-(3-hydroxypropyl)-2,2'-bipyridine (**13**) (bottom) and its treatment with $PBr_3$ (top). A new set of bipyridine signals arise and the alkyl region is significantly altered, which does not agree with a simple bromine substitution.*

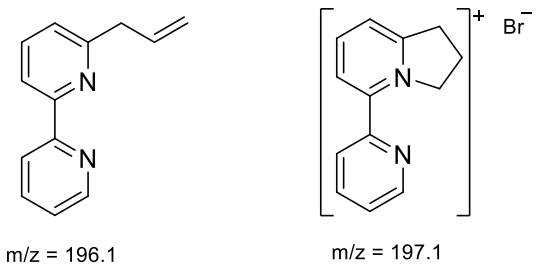


***Figure 5.15*** *Two possible products of the bromination attempts of 6-(3-hydroxybutyl)-2,2'-bipyridine.*

The failure of introducing a bromo substituent at the 3-position of a propyl chain attached to a 2,2'-bipyridine prohibits the preparation of the corresponding azide-propyl bipyridine intermediate. A possible solution could be the use of different leaving groups, such as other halo or tosylate substituents, but a more strongly attached substituent is also expected to disrupt the azide formation when the molecule is treated with sodium azide.

After the development of three generations of reaction schemes for a triazole bridged N^N^P^P tetradentate ligand, we decided to shift our strategy towards other connection methods. Although the click reaction itself is very robust and might appear to be an ideal reaction for such a linkage, the interference of different functional groups along the synthesis pathway complicated things to a significant extent. Since a solution for a problem, that creates two new problems cannot be seen as a solution, we abandoned the triazole connection and therefore developed a synthetic outline for a chemically simpler linkage: an alkyl chain.

## 5.5 Generation 4 - Direct xantphos modification with 2,2'-bipyridine

After the first three generations of attempted linkages between an N^N and P^P moiety of the target tetradentate ligand, it became clear, that the connection mode should be an easy to establish C–C bond formation reaction of which the product should be chemically innocent towards further reactions and copper(I) complexation. A possible candidate for such a reaction was found to be the Friedel-Crafts-acylation. Kamer *et al.* demonstrated that the modification of 9,9-dimethylxanthene with long alkyl chains in the 2- and 7-positions via a Friedel-Crafts reaction is possible.[135,207,208] The 2- and 7-position of the xanthene are the easiest to modify and were therefore chosen as the point of connection on the xanthene side. For the N^N ligand, different aspects needed to be considered. Firstly, a substituent in the 6-position of the 2,2'-bipyridine ligand is needed to stabilize the tetrahedral geometry of the copper(I) complex upon excitation, as was observed by Keller *et al.*[83,84,129] as well as in our previous findings. Secondly, the connection should not influence the energy levels of the target complex. To achieve this, an alkyl chain in the 6-position was chosen both as the linkage and for the required steric bulk to stabilize the copper(I) coordination geometry. In order to gain an idea of an appropriate length of the alkyl linker which would allow the N^N^P^P ligand to coordinate copper(I), geometry optimizations at the PM3 level were performed for chain lengths of six, seven, eight, nine and ten $CH_2$ units between the N^N and P^P moieties. The structures of the copper(I) complexes containing the ligands with six and ten $CH_2$ units in the linkers are shown in **Figure 5.16**. Although six $CH_2$ units in the chain were initially thought to be too short, the calculation shows an undistorted coordination geometry in the copper(I) complex. Longer chains would allow for more flexibility. However, the six $CH_2$ chain was chosen for the target molecule to minimize the risk of vibrational quenching of the excited state due to an increased number of C–H bonds in close proximity of the copper centre as was observed by Keller *et al.*[180]

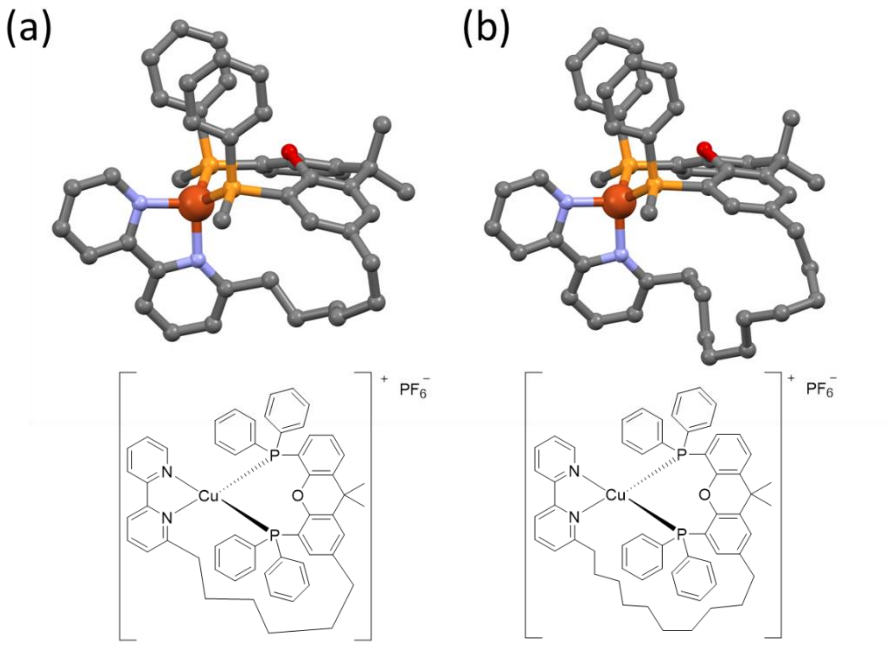


***Figure 5.16*** *Geometry optimized structures of an alkyl chain-linked N^N^P^P ligand complexing a copper(I) ion with a spacer length of six (a) and ten (b) $CH_2$ units between the 2,2'-bipyridine and xanthene backbone. Hydrogen atoms are omitted for clarity. Only the ipso-C of the equatorial phenyl rings are shown. Structures were optimized at the semi-empirical PM3 level using Spartan '18 v. 1.3 (Spartan '18, Wavefunction Inc., Irvine, CA 92612, US).*

The target N^N^P^P ligand and its retrosynthetic analysis are shown in **Scheme 5.20**. Previous attempts showed that the C–P bond formation via a selective lithiation *ortho* to the oxygen atom, is difficult to perform and isolate. Therefore, we decided to attempt the direct modification of xantphos, instead of xanthene. This brings the advantage that there is no C–P bond formation reaction necessary. Additionally, treatment of a carbonyl containing compound with *n*BuLi was expected to direct the lithiation position towards the α-position of the carbonyl, instead the desired *ortho* position to the xanthene moiety. Using xantphos as an already prepared bisphosphane scaffold makes the lithiation step obsolete and therefore no protection of the carbonyl functionalization is needed.

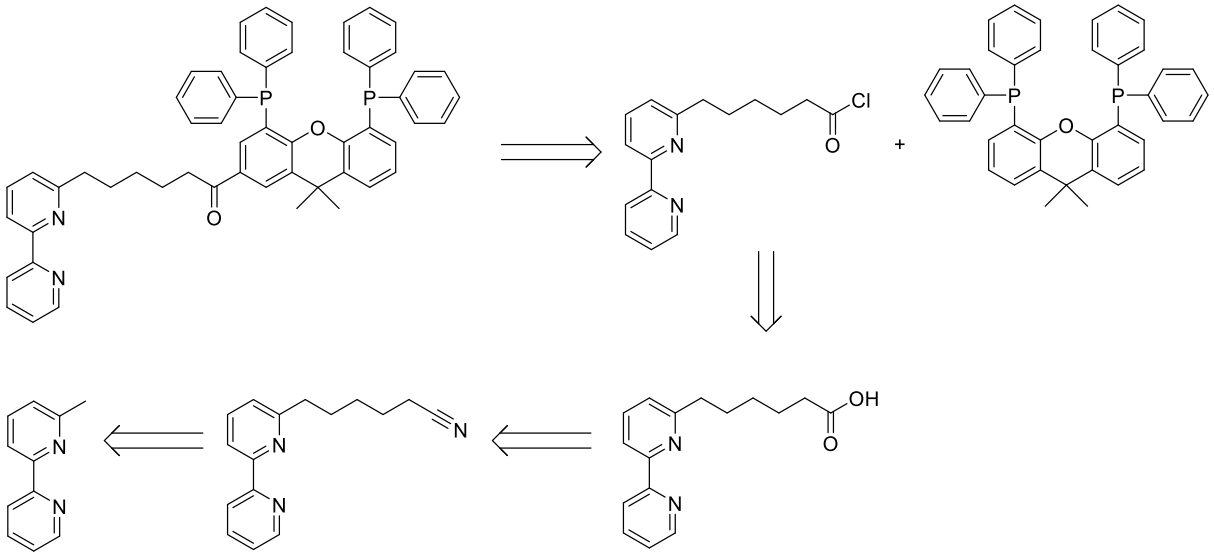


***Scheme 5.20*** *Fourth-generation retrosynthetic strategy for the preparation of a N^N^P^P by direct modification of xantphos by Friedel-Crafts-acylation.*

## 5.5.1 Carboxylic acid preparation

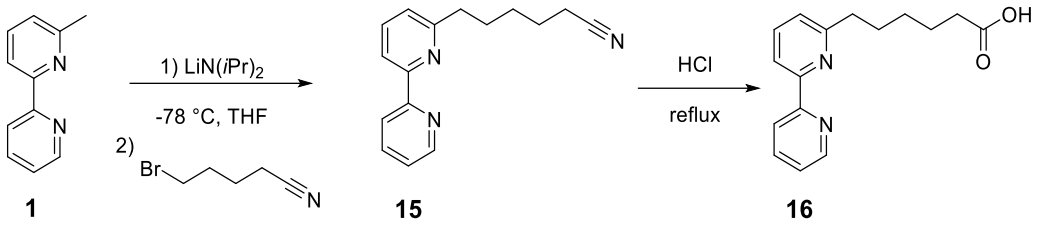


***Scheme 5.21*** *Synthetic route for the preparation of carboxylic acid functionalized 2,2'-bipyridine.*

Compound **16** was prepared according to literature procedure[209] by selective lithiation of the methyl position of compound **1** similar to the N^N modifications described in previous ligand generations. Treatment of the nitrile group with acid leads to the formation of the corresponding carboxylic acid.

## 5.5.2 Direct xantphos modification

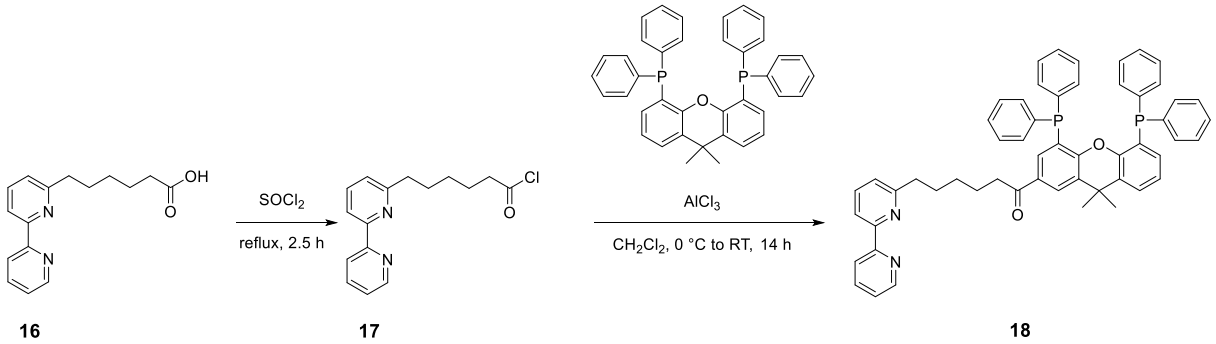


***Scheme 5.22*** *Direct functionalization of xantphos by Friedel-Crafts-acylation with acid chloride functionalized 2,2'-bipyridine.*

To perform a Friedel-Crafts-acylation reaction directly on the xantphos backbone, compound **16** was refluxed in an excess of thionyl chloride to form the corresponding acid chloride (**17**). Residual thionyl chloride was removed under vacuum before degassed solvent, $AlCl_3$ and xantphos were added and the mixture was stirred at room temperature under inert conditions. Multiple attempts of the reaction were performed, and the reaction conditions are summarized in **Table 5.6**. None of the attempts showed the desired reaction product by ESI-MS. To exclude the possibility of the N^N^P^P ligand not being accessible by ESI-MS due to ionization issues, test extractions were treated with $[Cu(MeCN)_4][PF_6]$. It was expected, that a copper(I) complex would form (although not necessarily four coordinated) which is easily traceable by ESI-MS. However, no such signal was observed. In the case of attempt 3, no acid chloride was prepared and compound **16** was reacted directly with xantphos. ESI-MS only showed a signal for $[Cu(Xantphos)]^+$. To investigate if the N^N moiety was interfering with the direct Friedel-Crafts-acylation reaction, direct functionalization of xantphos was attempted with 5-phenylvaleric acid instead of compound **16** with and without the previous formation of the corresponding acid chloride. Pure xantphos was recovered from both reactions. This led to the conclusion, that direct Friedel-Crafts-acylation of xantphos is not possible under standard conditions.

***Table 5.6*** *Reaction conditions for direct xantphos modification by Friedel-Crafts-acylation.*

| Attempt | Carboxylic acid used | Solvent | Addition of $AlCl_3$ and xantphos | Acid chloride formation | Reaction time | Reaction temperature |
|---|---|---|---|---|---|---|
| 1 | **16** | dichloromethane | consecutive | yes | 24 h | 0 °C to RT |
| 2 | **16** | dichloroethane | simultaneous | yes | 24 h | 0 °C to RT |
| 3 | **16** | dichloroethane | simultaneous | no | 5 days | RT to reflux |
| 4 | Phenylvaleric acid | dichloromethane | consecutive | no | 24 h | 0 °C to RT |
| 5 | Phenylvaleric acid | dichloromethane | simultaneous | yes | 24 h | 0 °C to RT |

## *5.5.3 Carboxylic acid-2,2'-bipyridine complexes*

Although the direct functionalization of xantphos was not successful, experimental confirmation of the stability of heteroleptic copper(I) complexes with long alkyl substituent in 6-position of the 2,2'-bipyridine ligand was still needed for further attempts to prepare a tetradentate N^N^P^P ligand. Therefore compound **16** was used to prepare heteroleptic complexes (**Scheme 5.23**). These were prepared by a stepwise and simultaneous ligand addition for [Cu(**16**)(DPEPhos)][$PF_6$] and [Cu(**16**)(xantphos)][$PF_6$] respectively similar to the preparation described in section 2.2.2. Both complexes were isolated as yellow powders and their photophysical and electrochemical properties were investigated.

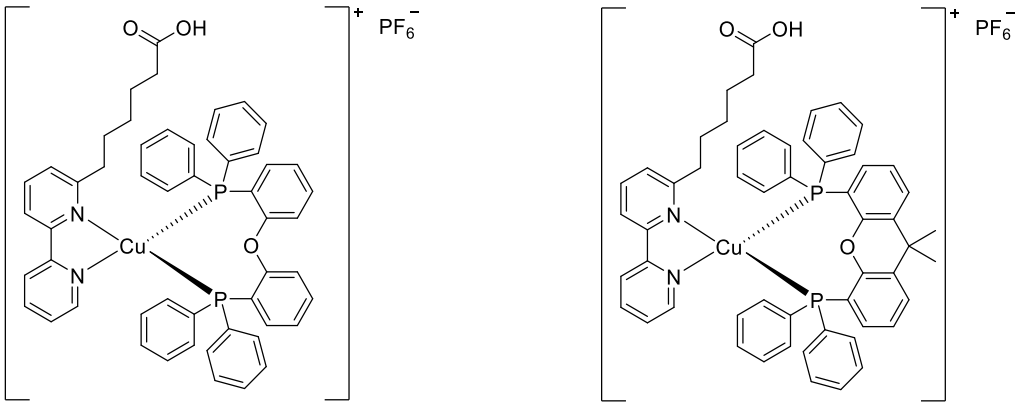


***Scheme 5.23*** *Chemical structures of [Cu(**16**)(DPEPhos)][$PF_6$] (left) and [Cu(**16**)(Xantphos)][$PF_6$] (right).*

### *5.5.3.1 Photophysical and electrochemical properties of [Cu(**16**)(P^P)][$PF_6$] complexes*

The photophysical properties of [Cu(**16**)(DPEPhos)][$PF_6$] and [Cu(**16**)(xantphos)][$PF_6$] are summarized in **Table 5.7**. Both complexes show intense absorption bands below 330 nm that can be assigned to ligand-based absorption. In addition, the complexes show an MLCT absorption around 382 nm (**Figure 5.17**). Upon excitation on an MLCT level both complexes show an emission in the yellow region in solid state and an orange-yellow emission in deaerated solution (**Figure 5.18**). Photoluminescence quantum yields are low in solution for both complexes. In solid state [Cu(**16**)(DPEPhos)][$PF_6$] shows a moderate PLQY of 17% while [Cu(**16**)(xantphos)][$PF_6$] shows a good quantum yield of 28%. This value is slightly lower than the solid state quantum yield of 37% observed for [Cu(Etbpy)(xantphos)][$PF_6$] by Keller *et al.*[84] Our findings indicate that the emissive properties of the complex are not significantly disrupted by the introduction of a long alkyl substituent in 6-position of the 2,2'-bipyridine ligand. It is possible that the terminal

carboxylic acid has an influence on the emission, but since this will not be contained in the target N^N^P^P ligand, it is of low relevance.

***Table 5.7*** *Photophysical properties of [Cu(**16**)(P^P)][$PF_6$] complexes*

| Complex cation | $CH_2Cl_2$ solution[a,b] | | | | Powder | | |
|---|---|---|---|---|---|---|---|
| | UV-Vis MLCT $\lambda_{max}$/nm | $\lambda_{em}^{max}$ /nm | PLQY (non-degassed/ degassed)% | $\tau_{1/2}$(av)(non-degassed/ degassed)/µs | $\lambda_{em}^{max}$/nm | PLQY/% | $\tau_{1/2}$(av)[c]/µs |
| [Cu(**16**)(xantphos)]$^+$ | 383 | 613, 636 | >1/>1 | 0.18/0.32 | 552 | 17 | 5.4 |
| [Cu(**16**)(DPEPhos)]$^+$ | 381 | 607, 628 | >1/1 | 0.28/0.78 | 542 | 28 | 7.2 |

[a] Solution concentration = 2.5 x $10^{-5}$ mol $dm^{-3}$. [b] $\lambda_{exc}$ = 365 nm. [c] Biexponential fit using the equation $\tau_{1/2}(av) = \Sigma A_i\tau_i/\Sigma A_i$ where $A_i$ is the pre-exponential factor for the lifetime. [d] Values taken from reference 174.

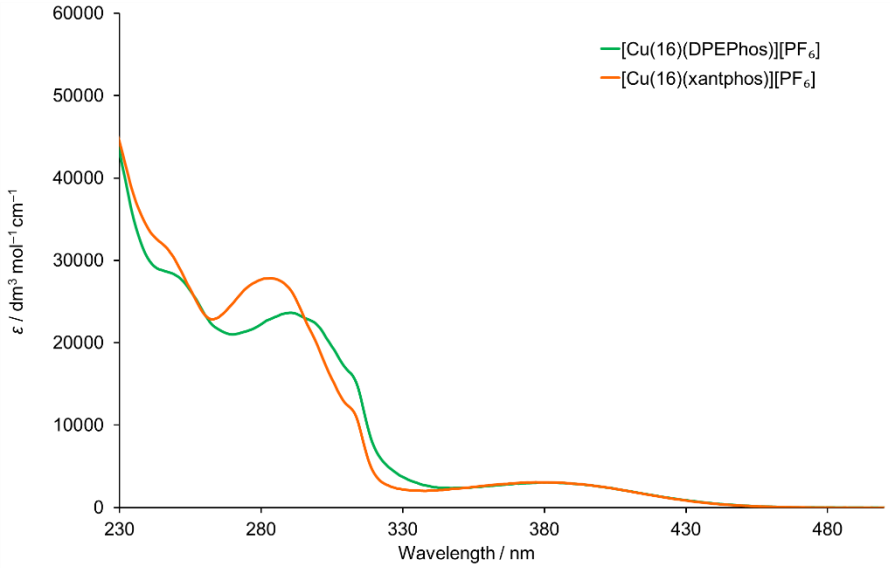


***Figure 5.17*** *Absorption spectra of [Cu(**16**)(DPEPhos)][$PF_6$] and [Cu(**16**)(xantphos)][$PF_6$] ($CH_2Cl_2$, 2.5 x $10^{-5}$ mol $dm^{-3}$).*

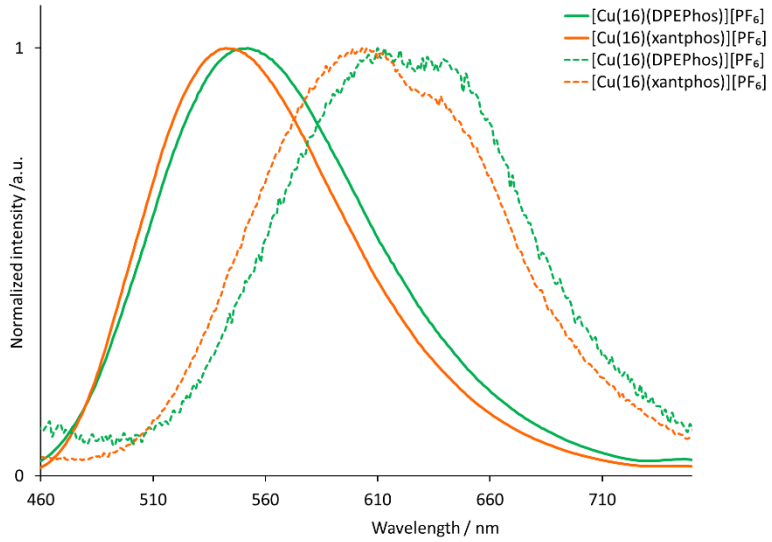


***Figure 5.18*** *Emission spectra of [Cu(**16**)(DPEPhos)][$PF_6$] and [Cu(**16**)(xantphos)][$PF_6$] in solid state (solid lines) and solution (dashed lines, $CH_2Cl_2$, 2.5 x $10^{-5}$ mol $dm^{-3}$).*

**Figure 5.19** shows the cyclic voltammograms of [Cu(**16**)(DPEPhos)][$PF_6$] and [Cu(**16**)(xantphos)][$PF_6$] in propylene carbonate and the results of the electrochemical

analysis are summarized in **Table 5.8**. The complexes show an irreversible oxidation at +0.85 V for [Cu(**16**)(DPEPhos)][$PF_6$] and +0.93 V for [Cu(**16**)(xantphos)][$PF_6$]. Both complexes show a quasi-reversible reduction signal at −2.07 V. This process is most likely based on the N^N ligand and therefore occurs at the same potential for both complexes. In addition, a second re-oxidation signal is visible on the back-oxidation wave at −1.65 V. This signal is only observed when scanning to −2.4 V. When scanning to more negative potentials, only the reversible reduction signal is shown. Only scanning to −1.8 V renders no reduction signal at all. This leads to the conclusion that the signal at −1.65 V is coupled to the reversible reduction process. One possible explanation would be that after an initial ligand reduction the back-oxidation occurred in two consecutive steps.

***Table 5.8*** *Cyclic voltammetric data for [Cu(**16**)(DPEPhos)][$PF_6$] and [Cu(**16**)(xantphos)][$PF_6$] referenced to internal $Fc/Fc^+$ = 0 V; propylene carbonate solutions with [$^nBu_4N$][$PF_6$] as supporting electrolyte and scan rate of 0.1 V $s^{-1}$.*

| Complex cation | $E_{pc}^{ox}$ / V | $E_{1/2}^{red}$ / V ($E_{pa}$ − $E_{pc}$ / mV) | $E_{pa}^{red}$ / V |
|---|---|---|---|
| [Cu(**16**)(DPEPhos)]$^+$ | +0.85 | −2.07 (80) | −1.65 |
| [Cu(**16**)(xantphos)]$^+$ | +0.93 | −2.06 (90) | −1.65 |

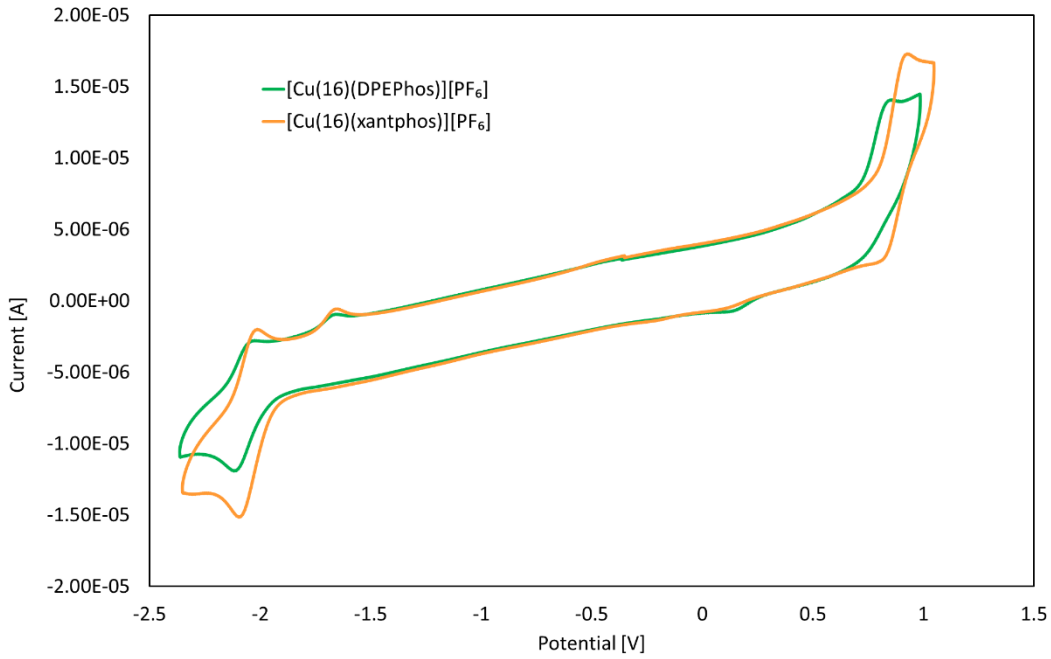


***Figure 5.19*** *Cyclic voltammogram of [Cu(**16**)(DPEPhos)][$PF_6$] and [Cu(**16**)(xantphos)][$PF_6$] in propylene carbonate at a scan rate of 0.1 V $s^{-1}$ referenced to internal $Fc/Fc^+$ = 0V and an initially positive scan direction. The second of three reproducible cycles is shown.*

## 5.6 Generation 5 - Stepwise xanthene backbone modification

This generation of ligand design was performed in close collaboration with Dr. Paola Andrea Forero Cortés. The fourth generation of ligand design demonstrated that a direct modification of xantphos was not possible via a Friedel-Crafts-acylation. Therefore, we decided to modify our synthetic strategy. In the fifth generation of ligand design we build up the connection moiety on the xanthene backbone, introduce the N^N moiety and form C−P bonds at the xanthene as the last step. The corresponding retrosynthetic analysis is shown in **Scheme 5.24**. The asymmetric modification of xanthene was demonstrated by

Kamer *et al.*[135] In principle, only one modified alkyl chain on the xanthene backbone would be necessary for our target N^N^P^P ligand. However, since previous test reactions had shown that the 2 and 7-position of xanthene are more reactive than the 4 and 5-positions *ortho* to the oxygen atom, we intended to modify both the 2 and 7-positions by Friedel-Crafts-acylation. For simplicity, both chains in the target molecule were chosen to be the same length with six carbon atoms. The protons in α-position to the carbonyl groups were expected to interfere with the lithiation needed for the C–P bond formation later in the synthesis. Therefore, deactivation of this position was needed. The carbonyl group was protected with an acetal formation. This was expected to be innocent in terms of copper(I) coordination and therefore deprotection would not be needed. Previous generations showed that the C–P bond formation reaction was difficult to perform quantitatively by only utilization of the *ortho* directing effect of the oxygen atom for lithiation. Therefore, we decided to introduce bromo-groups in the desired position. Since the double bromo-compound would not be sensitive towards oxygen, purification was expected to be possible by standard procedures, leaving the C–P bond formation as the only oxygen sensitive reaction step. Halogen-lithium exchange was expected to be straight forward and require relatively short reaction time, limiting the risk of unwanted oxidation during the reaction.

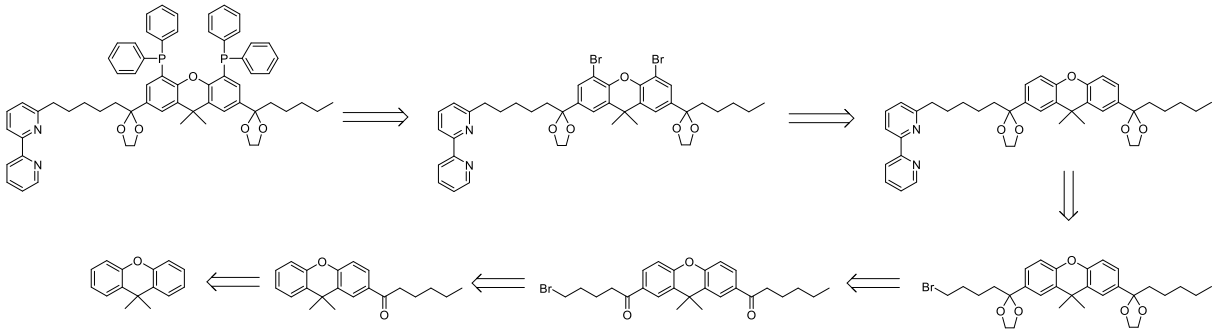

***Scheme 5.24*** *Fifth-generation retrosynthetic strategy for the preparation of a N^N^P^P ligand by direct Friedel-Crafts-acylation of xanthene, acetal protection of ketones and functionalization by C–P bond formation.*

## *5.6.1 Friedel-Crafts-acylation of xanthene*

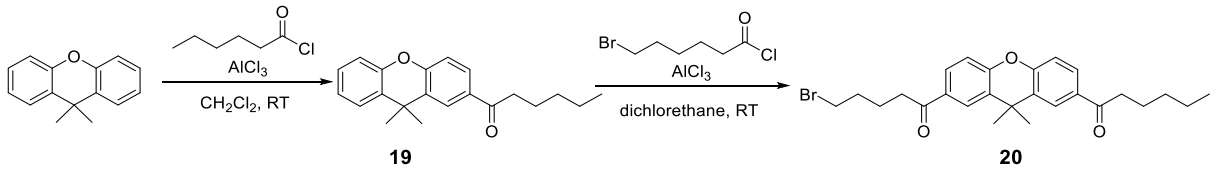


***Scheme 5.25*** *Stepwise Friedel-Crafts-acylation for the preparation on an asymmetrically modified xanthene backbone.*

The preparation of the asymmetrically modified xanthene was attempted according to literature procedure.[135] Preparation of compound **19** was performed under standard Friedel-Crafts conditions and yielded the product in high yield which was in agreement with the literature. The second modification however did not give the expected result when performed under the same standard conditions in dichloromethane at room temperature. To increase the reactivity, the reaction temperature was increased. Therefore 1,2-dichloroethane was chosen as a solvent, but this attempt led to decomposition of compound **19**. The preparation of compound **20** was successful by

performing the reaction under standard room temperature Friedel-Crafts condition using 1,2-dichloroethane as solvent and an excess of $AlCl_3$ and acid chloride, although not in quantitative yield due to challenging purification. The reaction parameters are summarized in **Table 5.9**.

***Table 5.9*** *Reaction conditions for preparation of compound **20**.*

| Attempt | Equivalents of $AlCl_3$ and acid chloride | Solvent | Reaction time | Reaction temperature |
|---|---|---|---|---|
| 1 | **1.2/1.1** | dichloromethane | 72 h | 0 °C to RT |
| 2 | **1.7/1.7** | dichloroethane | 24 h | 0 °C to reflux |
| 3 | **3.5/3** | dichloroethane | 24 h | 0 °C to RT |

## *5.6.2 Carbonyl protection*

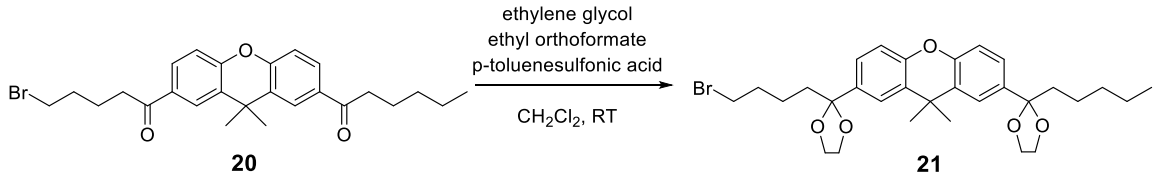


***Scheme 5.26*** *Carbonyl protection by acetal formation reaction.*

This reaction step was optimized by Dr. Paola Andrea Forero Cortés. Protection of the carbonyl groups was necessary due to the acidity of the corresponding α-protons that were expected to disturb the lithiation reaction needed in the C–P bond formation reaction later in the synthesis. Deactivation of these positions by protecting the carbonyl with an acetal functionalization with ethylene glycol was successful and compound **21** was isolated quantitative yield.

## *5.6.3 Terminal bipyridine functionalization*

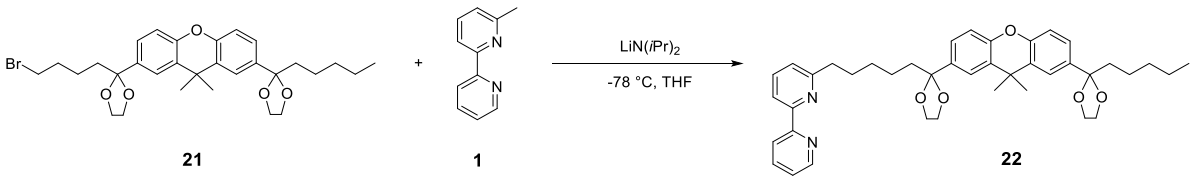


***Scheme 5.27*** *Terminal bipyridine functionalization of the alkyl modified xanthene.*

Introduction of the N^N moiety was performed similar to the procedure described in section 5.2.1. Compound **1** was treated with freshly prepared lithium diisopropylamine to lithiate selectively on the methyl group. Quenching of the lithiated species with compound **21** gave the target molecule **22** which was purified by column chromatography and isolated in moderate yield of 52%. The intermediate was fully characterized by $^{1}H$ (**Figure 5.20**) and $^{13}C\{^{1}H\}$ NMR spectroscopies, elemental analysis and high resolution ESI-MS to confirm the successful preparation of this key intermediate. For detailed characterization see section 5.9.21.

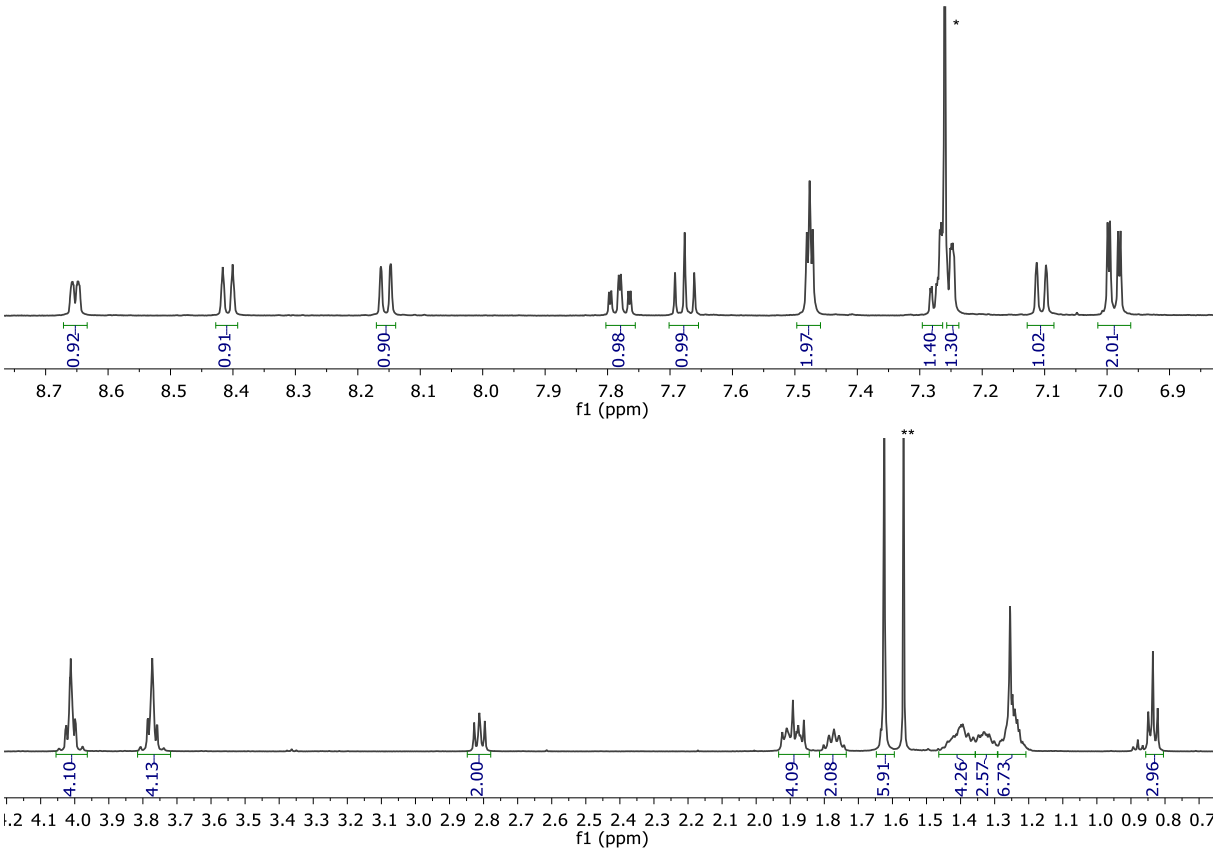


***Figure 5.20*** *Aromatic (top) and aliphatic (bottom) $^1$H NMR spectra (500 MHz, $CDCl_3$, 298 K) of compound **22** after purification. * residual $CHCl_3$, ** residual $H_2O$.*

## *5.6.4 C–P bond formation reaction*

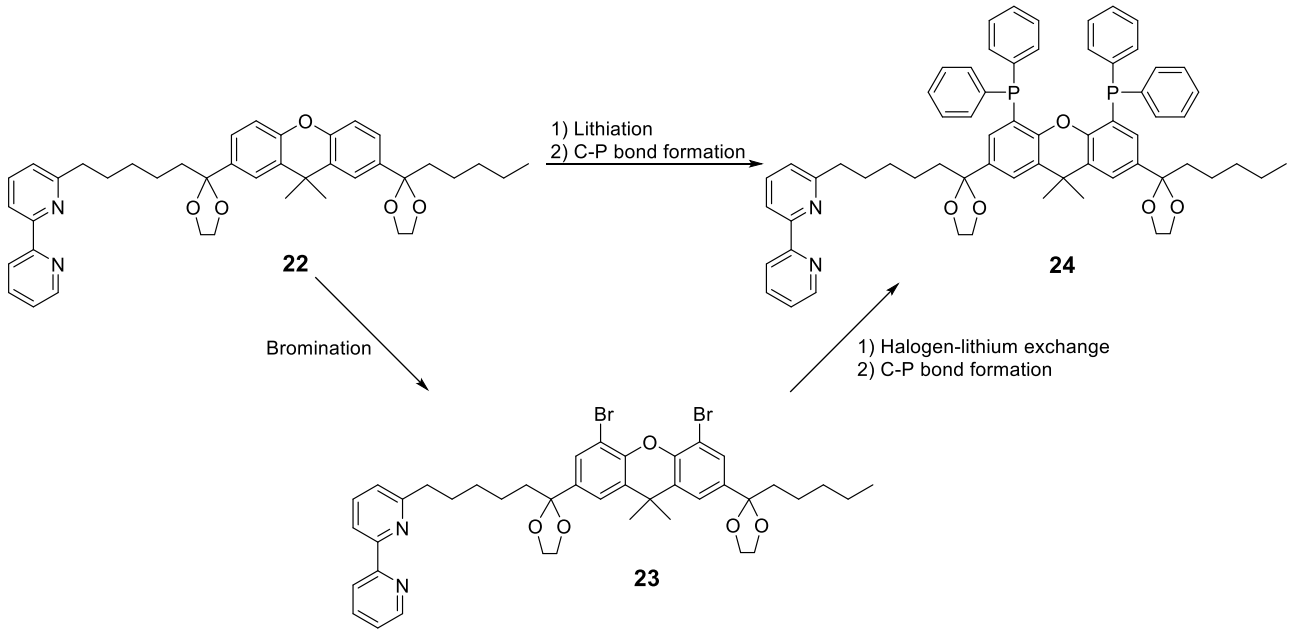


***Scheme 5.28*** *Possible strategies for direct and indirect C–P bond formation in 4 and 5-position of the xanthene moiety.*

Previous attempts of C–P bond formation reactions by directly treating xanthene derivate with *n*BuLi had not been successful and often yielded complex mixtures and/or oxidized phosphane. Nevertheless, we attempted direct litiation on the newly prepared compound

**22**. Test reactions were performed, where compound **22** was treated with *n*BuLi under different reaction conditions and the lithiated species was quenched with deuterium oxide. Reaction parameters are summarized in **Table 5.10**. Performing this test reaction gives the advantage, that both unreacted starting material as well as partially and/or fully deuterated product, can still be used for further reactions, since deuterium is expected to react the same as hydrogen in C−P bond formation reactions. Additionally, the desired product is easily observable by ESI-MS. Unfortunately, none of the attempted lithiation reactions gave the desired product.

***Table 5.10*** *Reaction parameter for direct lithiation with 2.4 eq. nBuLi and TMEDA, followed by quenching with deuterium oxide of compound **22**.*

| Attempt | Solvent | Reaction time | Reaction temperature |
|---|---|---|---|
| 1 | diethyl ether | 72 h | −78 to 40 °C |
| 2 | diethyl ether | 18 h | −78 °C to RT |
| 3 | THF | 3 h | −65 °C |

As a solution for the unreliability of directly lithiating the xanthene moiety, we decided to attempt to bromo-functionalize the xanthene moiety in the 4 and 5-postions. If successful, we planned to follow this with a halogen-lithium exchange. Reaction parameters are summarized in **Table 5.11**. For the first attempt compound **22** was treated with 2.2 eq. of bromine at reflux overnight. ESI-MS indicated the presence of some desired product, but also deprotection of the acetal groups (**Figure 5.21**). In an attempt to re-introduce the cleaved acetal protection group the isolated material was treated with the carbonyl protection procedure described in section 5.6.2. NMR spectrum and ESI-MS indicated that reintroduction of the protecting group was not successful. We suspected that protons released during the bromination could remove the protective acetal group. Therefore, attempts to perform the bromination reaction with the addition of base to capture released protons were made. Reaction with DBU gave only starting material. The addition of 2,6-luthidine gave some signals of product in ESI-MS, but also mono-brominated species. After the addition of up to 6 eq. bromine the ESI-MS showed mainly double bromination pattern signals, but deprotection of the acetal group was still observed (**Figure 5.22**). Purification of the target dibrominated product was not possible. When NBS was used as bromination reagent instead of bromine, there was no reaction observed in dichloromethane, acetonitrile or DMF when the reaction was stirred overnight at room temperature. The reaction in dioxane gave a monobrominated species identified by ESI-MS, but NMR spectroscopy indicated that the bromination did not occur in the desired position. Heating compound **22** to 160 °C with NBS in DMF over 40 h yielded decomposition of the starting material. Treatment of compound **22** with bromine in tetrachloromethane with and without a catalytic amount of iron powder yielded monobrominated product, identified by ESI-MS. When using NIS to introduce iodine atoms in 4 and 5 position of the xanthene moiety the results were similar to the NBS test reactions with no observable product. Treatment of compound **22** in THF at low or high temperature as well as in chloroform at room temperature gave similar results as previous attempts.

***Table 5.11*** *Reaction parameters for the halogenation of compound* ***22****.*

| Attempt | Halogenation reagent | Solvent | Reaction time | Reaction temperature | Additives/comments |
|---|---|---|---|---|---|
| 1 | 2.2 eq. $Br_2$ | Chloroform | 14 h | reflux | Acetal reprotection attempted after workup |
| 2 | 2.6 eq. $Br_2$ | Chloroform | 14 h | reflux | DBU |
| 3 | 6.0 eq. $Br_2$ | Chloroform | 72 h | reflux | 2,6-Luthidine |
| 4 | 2.3 eq. NBS | Dichloromethane | 14 h | 0 °C to RT | |
| 5 | 2.3 eq. NBS | Acetonitrile | 40 h | RT | |
| 6 | 2.3 eq. NBS | Dioxane | 40 h | RT | |
| 7 | 2.3 eq. NBS | DMF | 40 h | RT | |
| 8 | 2.3 eq. NBS | DMF | 40 h | 160 °C | |
| 9 | 3.0 eq. $Br_2$ | Tetrachloromethane | 14 h | −78 °C to RT | |
| 10 | 3.0 eq. $Br_2$ | Tetrachloromethane | 14 h | −78 °C to RT | 0.15 eq. iron powder |
| 11 | NIS | Tetrachloromethane | 14 h | RT | |
| 12 | 3.0 eq. $Br_2$ | THF | 14 h | −78 °C to reflux | |
| 13 | 2.5 eq. NBS | Dichloromethane | 14 h | 0 °C to RT | |
| 14 | 2.5 eq. $Br_2$ | Chloroform | 14 h | RT | |

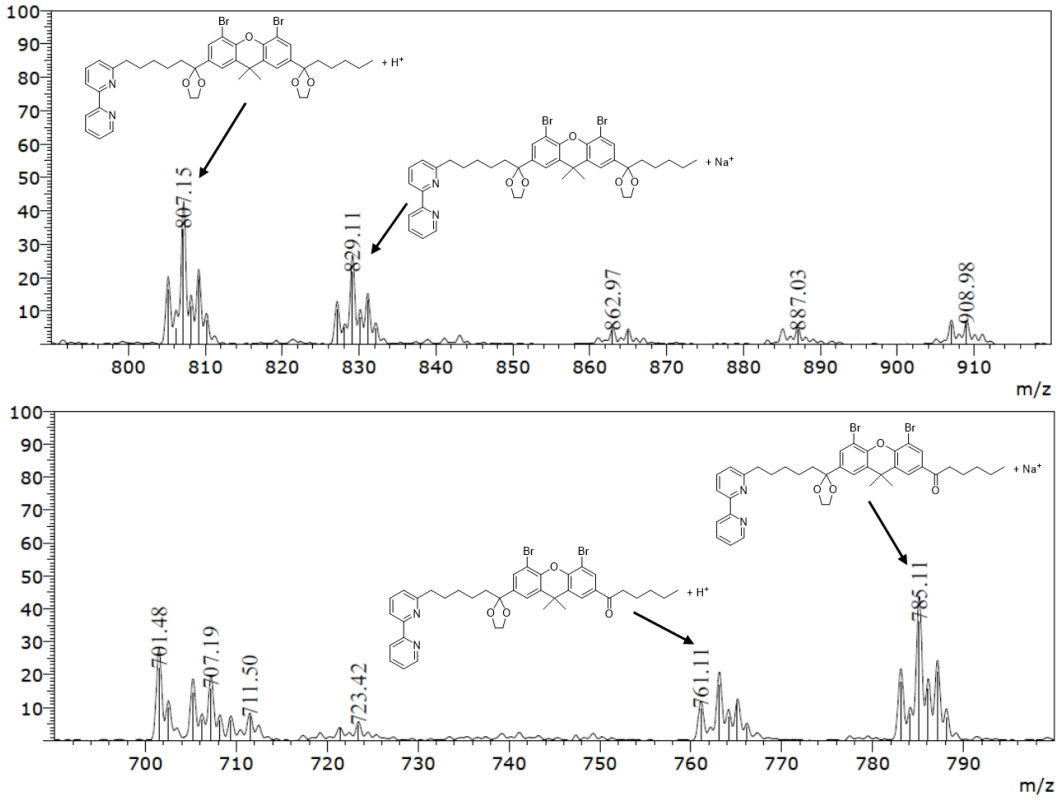


***Figure 5.21*** *Parts of the ESI-MS of bromination attempt 1 after purification by column chromatography. Exact position of acetal deprotection cannot be distinguished by MS. Structures in the bottom spectrum are only shown for illustration.*

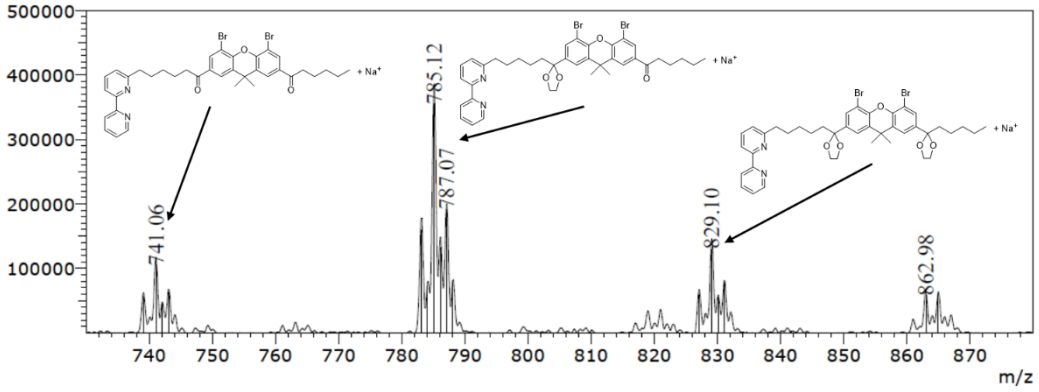


***Figure 5.22*** *Parts of the ESI-MS of bomination attempt 3 with the addition of 2,6-luthidine as base and an increased amount of bromine. Exact position of acetal deprotection cannot be distinguished by MS. The structure assigned to the signal at 785.1 m/z is only shown for illustration.*

In conclusion we observed partial bromination of compound **22** under certain conditions. In some cases, a double brominated species was observable by ESI-MS, but never in decent amount and always in combination with mono brominated species. Separation of these species was not successful. Additionally, ESI-MS indicated that the acetal protection group was lost in many cases and reintroduction was not possible. We conclude from this, that protection of the carbonyl group is not sufficient for our synthetic approach. Although it is expected to be of no significant relevance in the target N^N^P^P ligand in terms of coordination chemistry, it introduces synthetic challenges along the way. Therefore, we decided to change our synthetic strategy once more.

## 5.7 Generation 6 - Deoxygenated stepwise xanthene backbone modification

This generation of ligand design was performed in close collaboration with Dr. Paola Andrea Forero Cortés. Since interference of the acetal and/or carbonyl group was believed to be the major problem in the previous synthetic approach, we shifted our strategy towards the removal of this group. Kamer *et al.* prepared multiple functionalized xantphos derivates by stepwise Friedel-Crafts-acylation, followed by deoxygenation with indium(III) chloride and chlorodimethylsilane. Bromine was used to functionalize the 4 and 5-positions of the xanthene moiety before a C–P bond was established via a lithiation reaction.[135,207,208] In our sixth-generation synthetic attempt, we aimed to follow Kamer's strategy up to the deoxygenation step. After the ketone reduction we aimed to introduce the 2,2'-bipyridine moiety before bromination of the 4 and 5-positin of the xanthene unit. This order of reaction was chosen, because xanthene bromination before bipyridine introduction would lead to a tribromo species. Since introduction of the bipyridine moiety involves a lithiated bipyridine intermediate, it was expected that the tribromo species would lead to selectivity problems for the introduction of the N^N moiety. The sixth-generation retrosynthetic strategy for the preparation of a N^N^P^P ligand is shown in **Scheme 5.29**. Synthetic details for the preparation of Friedel-Crafts acylated xanthene (compound **20**) are given in the literature[135] and discussed in detail in the previous section.

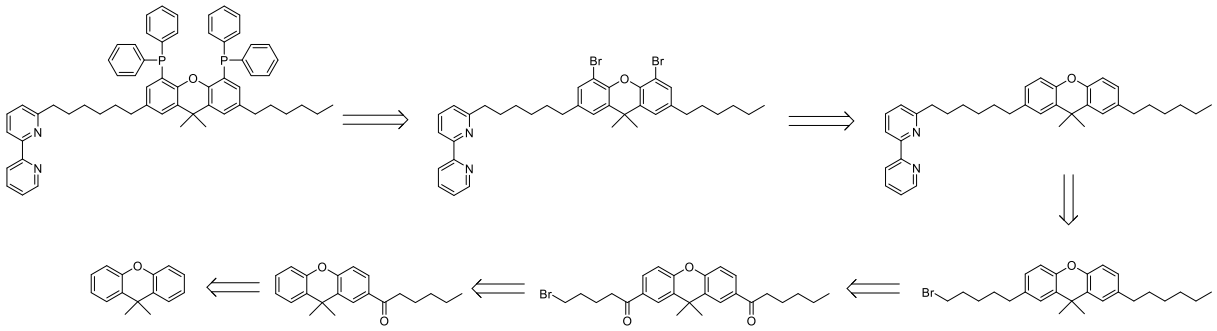

***Scheme 5.29*** *Sixth-generation retrosynthetic strategy for the preparation of a N^N^P^P ligand by direct Friedel-Crafts-acylation of xanthene, deoxygenation of carbonyl groups and functionalization by C–P bond formation.*

## *5.7.1 Deoxygenation reaction*

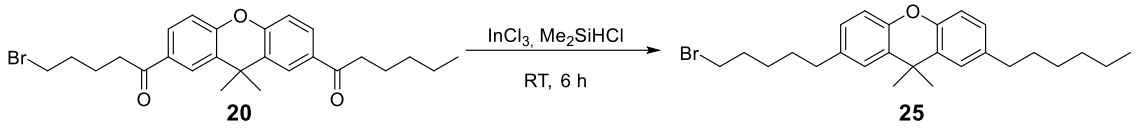


***Scheme 5.30*** *Deoxygenation reaction for the complete reduction of the carbonyl groups.*

Deoxygenation of compound **20** was performed according to literature procedure[135] using indium(III) chloride as catalyst and an excess of chlorodimethylsilane as reducing agent. After purification by column chromatography the product was isolated in good yield of 86%. Although the alkyl region of the $^1$H NMR spectrum was not in perfect agreement with the literature, it was consistent with the formation of compound **25** (**Figure 5.23**)

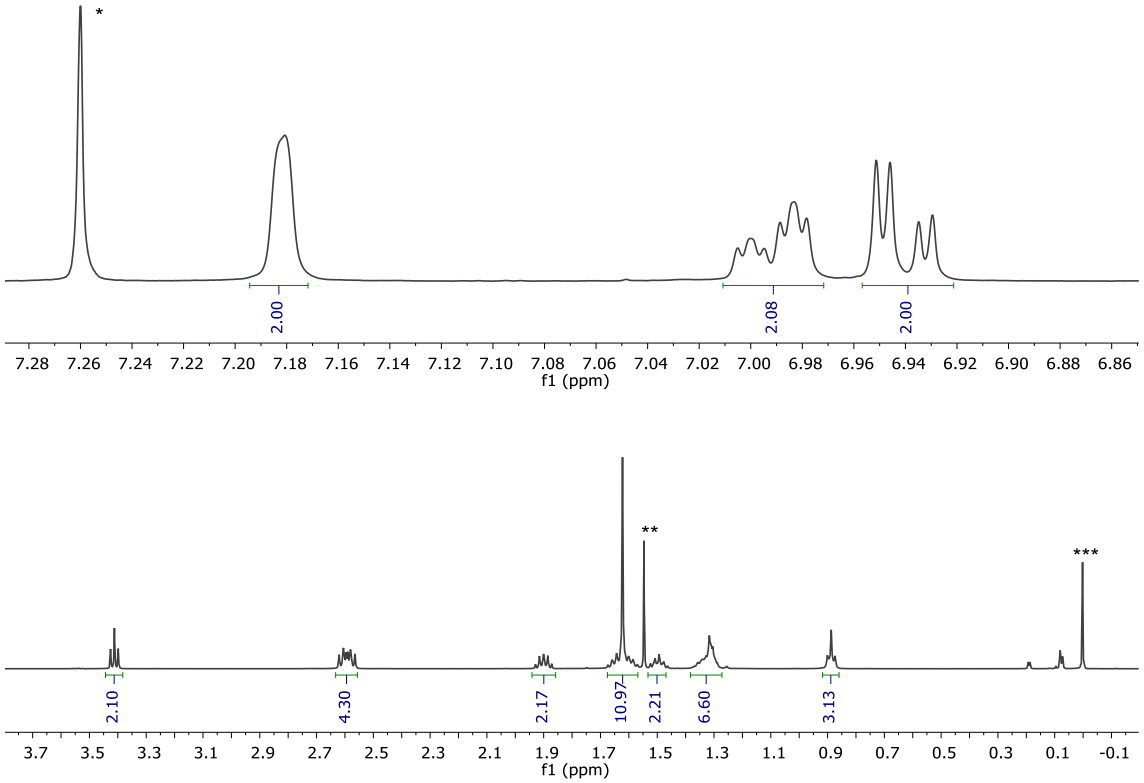


***Figure 5.23*** *Aromatic (top) and aliphatic (bottom) $^1$H NMR spectra (500 MHz, $CDCl_3$, 298 K) of compound **25** after purification. * residual $CHCl_3$, ** residual $H_2O$, *** TMS.*

## *5.7.2 Terminal bipyridine fictionalization*

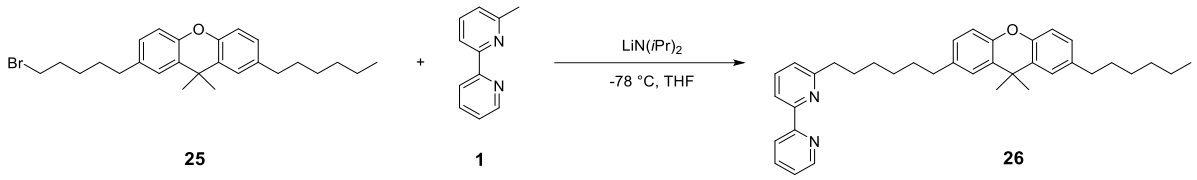


***Scheme 5.31*** *Terminal bipyridine functionalization of the alkyl modified xanthene.*

Introduction of the N^N moiety was performed in a similar manner as the procedure described in section 5.2.1. Compound **1** was treated with freshly prepared lithium diisopropylamine to lithiate selectively on the methyl group. Quenching of the lithiated species with compound **25** gave the target molecule **26** in good yield of 72%. The product was identified by $^{1}$H NMR spectroscopy (**Figure 5.24**) as well as ESI-MS.

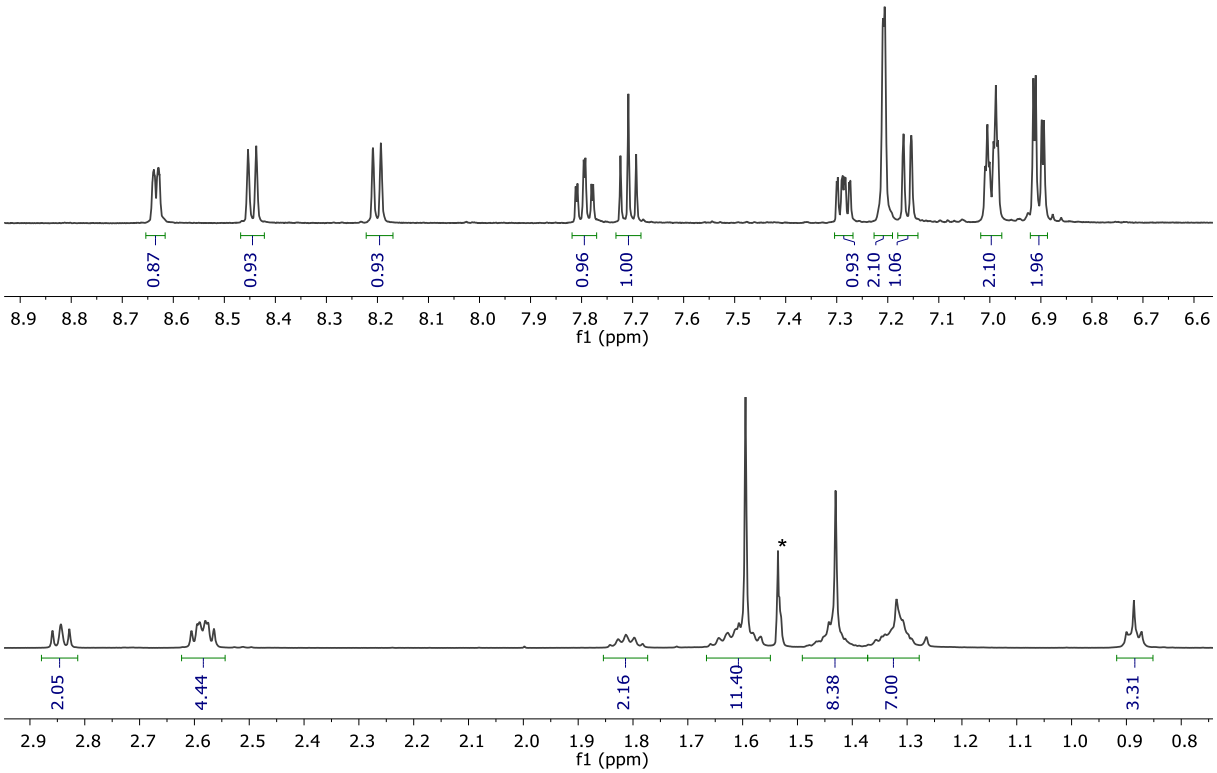


***Figure 5.24*** *Aromatic (top) and aliphatic (bottom) $^{1}$H NMR spectra (500 MHz, $CD_2Cl_2$, 298 K) of compound **26** after purification. * residual $H_2O$.*

## *5.7.3 Bromination of xanthene moiety*

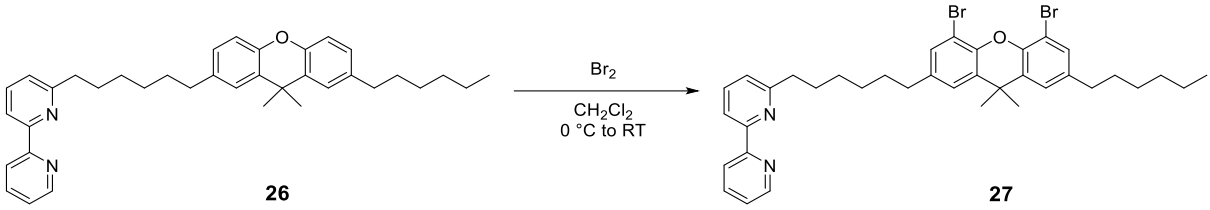


***Scheme 5.32*** *Bromination of the deoxygenated xanthene molecule.*

Direct lithiation of the 4 and 5-positions of the xanthene moiety had been attempted for previous ligand generations but had not been successful (see section 5.6.4). Nevertheless, one attempt to perform a direct lithiation ortho to the oxygen atom was made, using *n*BuLi and TMEDA at low temperature, followed by quenching of the reaction with $D_2O$. $^1H$ NMR spectra showed a new set of bipyridine signals and ESI-MS indicated the addition of a butyl group instead of the desired deuteration at the 4 and 5-positions of the xanthene moiety. Therefore, the direct lithiation method was discarded. Bromination of the 4 and 5 position of the xanthene moiety had proven itself to be difficult in the presence of a 2,2'-bipyridine moiety (see section 5.6.4). Several attempts to prepare compound **27** were made using bromine in different solvents at various temperatures (**Table 5.12**, attempt 1 to 4). All these reactions showed a mixture of mono- and dibrominated product. These species were inseparable by conventional purification methods and therefore the target molecule could not be isolated. However, the presence of some dibrominated species indicated, that the bromination had partly been successful. We suspect that either bromine was consumed by unwanted side reactions and/or the iron catalyst was poisoned during the reaction. Therefore, we decided to drop conventional conservative methods and attempt a bromination reactions under rather harsh conditions. Compound **26** was treated with 8 equivalents of bromine in the presence on a stochiometric amount of iron powder at 0 °C up to room temperature. Test extraction ESI-MS showed only dibrominated species. The reaction was quenched by aqueous sodium thiosulfate and sodium hydrogen carbonate solution, extracted with dichloromethane and the combined organic layers were washed with basic $H_4EDTA$ solution to remove all residual metal impurities. Filtration of the crude material over basic Alox gave the desired product compound **27** in excellent yield of 95%. The product was characterized by $^1H$ (**Figure 5.25**) and $^{13}C\{^1H\}$ NMR spectroscopy as well as ESI-MS (**Figure 5.26**).

***Table 5.12*** *Reaction parameters for the bromination of compound **26**.*

| Attempt | Halogenation reagent | Solvent | Reaction time | Reaction temperature | Additives/comments |
|---|---|---|---|---|---|
| 1 | 2.5 to 3.5 eq. $Br_2$ | Dichloromethane | 14 h | −78 °C to RT | - |
| 2 | 3.5 eq. $Br_2$ | Tetrachloromethane | 14 h | −78 °C to RT | - |
| 3 | 3.5 eq. $Br_2$ | Tetrachloromethane | 14 h | 50 °C | - |
| 4 | 3.5 eq. $Br_2$ | Tetrachloromethane | 14 h | RT | ca. 1 eq. iron powder |
| 5 | 8.0 eq. $Br_2$ | Dichloromethane | 14 h | 0 °C to RT | 1.3 eq. iron powder |

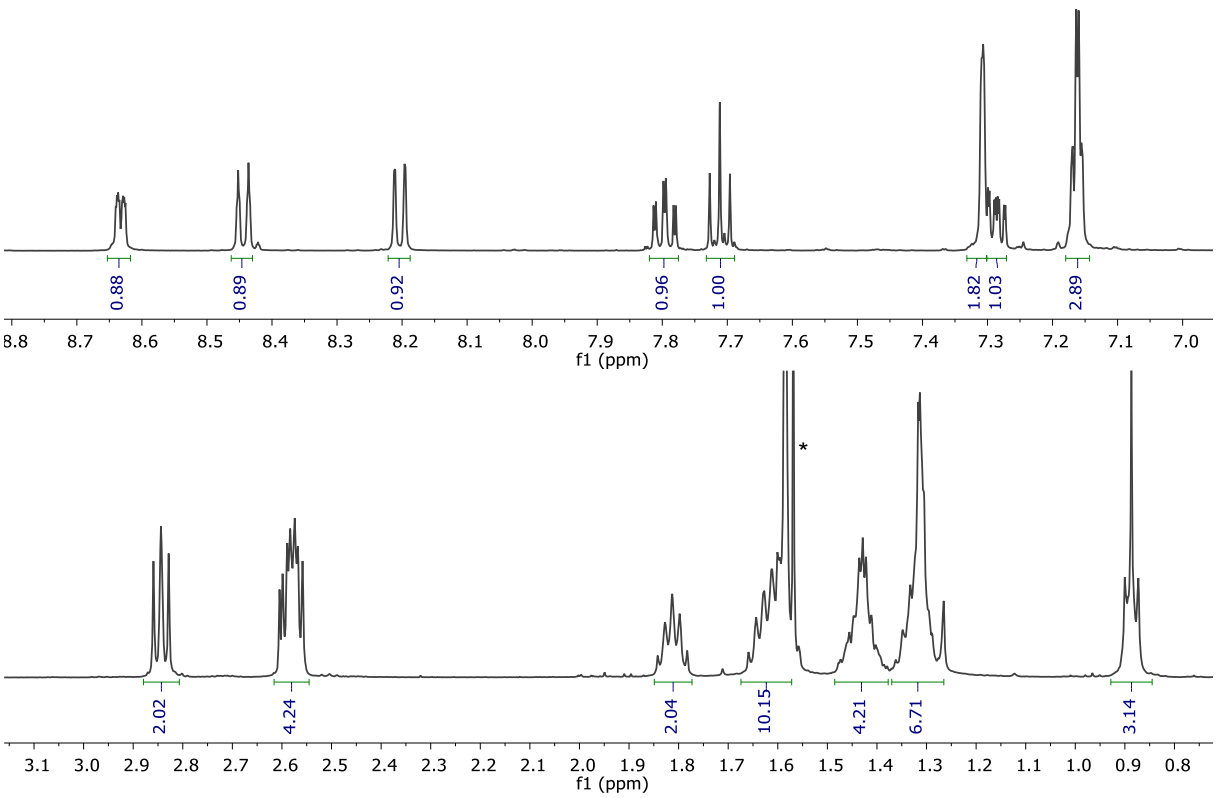


***Figure 5.25*** *Aromatic (top) and aliphatic (bottom) $^1$H NMR spectra (500 MHz, $CD_2Cl_2$-$d_2$, 298 K) of compound **27** after filtration. * residual $H_2O$.*

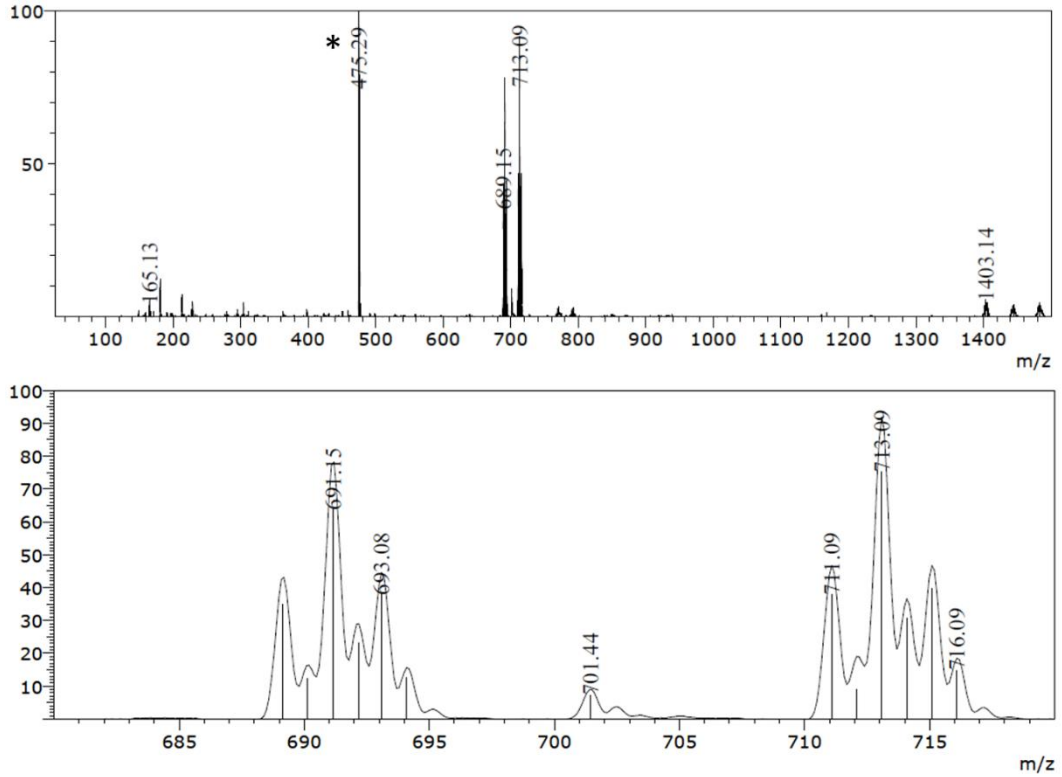


***Figure 5.26*** *Full ESI-MS (top) of compound **27**. The zoomed vie (bottom) shows a double bromine pattern. No monobrominated species is observed. * President impurity in the mass spectrometer.*

## *5.7.4 C–P bond formation*

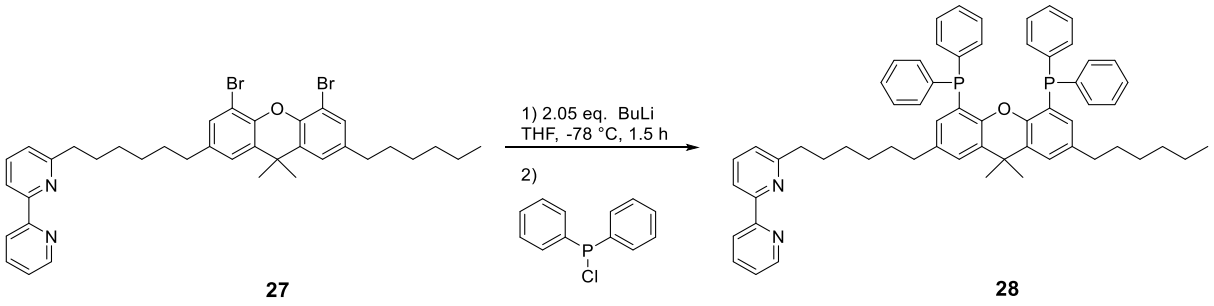


***Scheme 5.33*** *C–P bond formation reaction by halogen lithium exchange.*

Previous trials had shown that the C–P bond formation is challenging to perform. However, the introduction of two bromo functionalization in 4 and 5-position of the xanthene moiety was successful, and the halogen lithium exchange was expected to occur much faster than a hydrogen lithium exchange. To avoid side reactions the C–P bond formation attempts were performed under rigorous exclusion of water and oxygen. All solvents were dry and degassed using a stream of argon. Compound **27** was azeotropically dried by dissolving it in toluene and removing the solvent under vacuum 5 times. Quenching and workup of the reactions were performed under inert conditions on the Schlenk line and NMR samples were taken inside the glovebox. Reaction parameters are summarized in **Table 5.13**. In the first attempt *sec*BuLi was used as lithiation reagent and after $PPh_2Cl$ had been added, diluted aqueous HCl was used to quench the reaction. Surprisingly the $^{31}P\{^1H\}$ NMR spectrum of the crude mixture showed only signals above δ +20 ppm. This indicates the presence of oxidized phosphane species. No signal in the region of δ −12 to −25 ppm was observed; this would be a typical region for a phosphane. ESI MS shows the presence of a peak that corresponds to [**28**+2×O+H]$^+$. Additionally, a signal for [**28**+2×O+H+$^i$Bu]$^+$ can be observed (**Figure 5.27**). Sine ESI MS gives no structural information we cannot conclusively prove, that the C–P bond formation occurred in the desired position. One possible reason for side reactions could be the slightly elevated lithiation temperature, long reaction time and the nucleophilic nature of the iso-butyl group. To counteract this, a second reaction attempt was made, using $^t$BuLi at lower temperature for a shorter period of time. This time, the $^{31}P\{^1H\}$ NMR spectrum of the crude material showed some signals in the desired regions, but still mayor peaks above +20 ppm (**Figure 5.28**). In both attempts, oxygen was excluded rigorously during the reaction, workup and NMR sample preparation.

***Table 5.13*** *Reaction Parameters for the C–P bond formation.*

| Attempt | Lithiation reagent | Solvent | Lithiation time | Reaction temperature | Comments |
|---|---|---|---|---|---|
| 1 | *sec*BuLi | THF | 2.5 h | −68 to −78 °C | warm up overnight, acidic workup |
| 2 | $^t$BuLi | THF | 1.5 h | −78 °C | warm up overnight, acidic workup |
| 3 | $^t$BuLi | THF | 1.5 h | −78 °C | acidic workup, evaporation of solvent in low temperatures, part of reaction used for copper(I) workup |

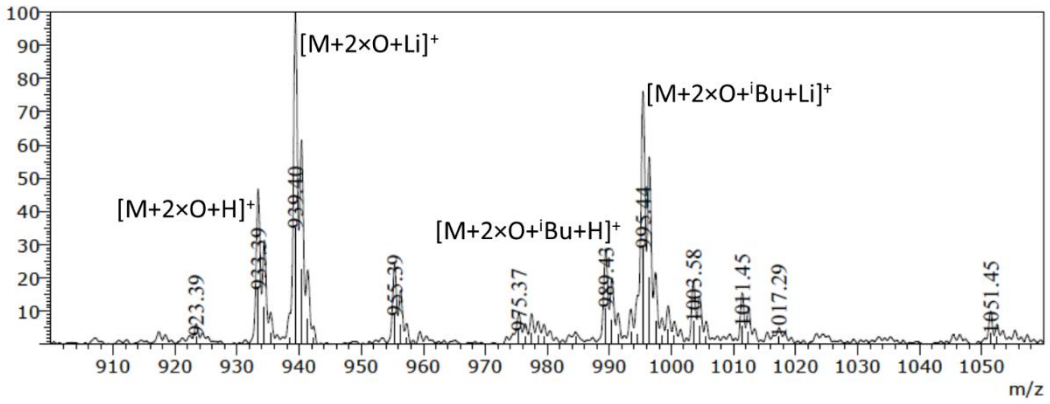


***Figure 5.27*** *Part of the ESI-MS spectrum of the crude reaction mixture of the first attempt, using secBuLi as lithiation reagent.*

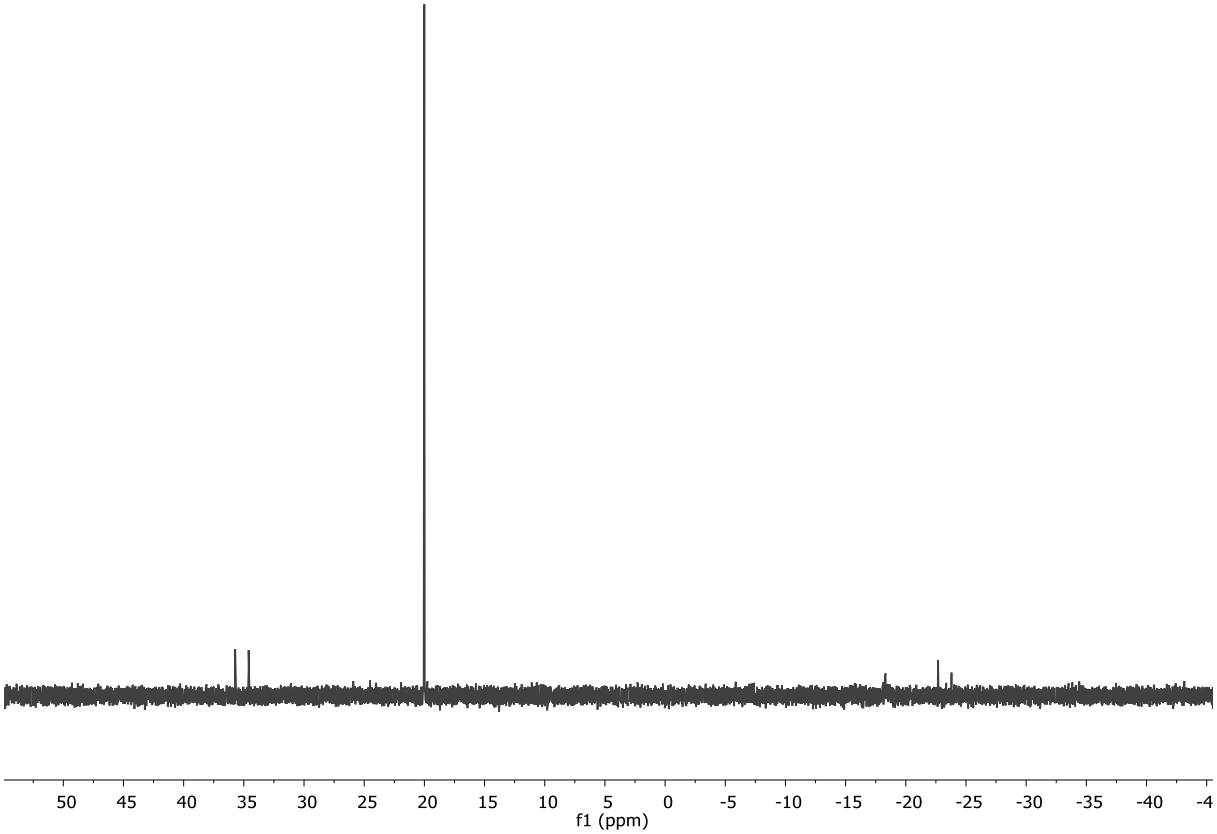


***Figure 5.28*** *$^{31}P\{^{1}H\}$ NMR spectrum (500 MHz, $CD_2Cl_2$, 298 K) of the crude material of attempt 2. Only minor signals in the desired region between $\delta$ –12 and – 25 ppm are observed.*

The fact, that we still observed oxidized species lead us to the conclusion, that there were either unexpected side reactions occurring during the reaction, or the product was destroyed during the workup. Therefore, a third attempt was made to prepare the target ligand using the reaction protocol of the previous attempt. The only difference was that after the reaction, the solvent (THF) was evaporated slowly in low temperatures. The crude material was then re-dissolved in $CH_2Cl_2$ and split in two batches. The first half was worked up under inert conditions like in attempt 1 and 2. NMR and ESI MS gave similar results to attempt 2 and were therefore declared not successful. The second half was treated with a solution of $[Cu(MeCN)_4][PF_6]$ in degassed $CH_2Cl_2$ and stirred for 2 h. This approach was chosen, to coordinate copper(I) to the possibly formed N^N^P^P ligand,

which would prevent the phosphorus oxidation in air. After stirring, the mixture was removed from the inert atmosphere, filtered and the solvent was removed in vacuo. The $^{31}P\{^{1}H\}$ NMR spectrum showed a signal for $PF_6^-$ at δ −144.5 ppm, as well as three broadened signals at δ +33, +28 and −18 ppm (**Figure 5.29**). The latter possibly corresponds to the desired $[Cu(N^N^P^P)]^+$ complex. The ESI-MS of the crude copper quenched attempt shows a signal for $[M+Cu]^+$ that fits the isotopic pattern of a coper containing complex (**Figure 5.30**). Although this does not give any information about the exact chemical nature of the complex, the absence of oxidized phosphane signals in the $^{31}P\{^{1}H\}$ NMR spectrum and ESI MS indicates, that our approach to quench the reaction with copper(I) therefore preventing phosphane oxidation was partly successful.

Several attempts of purifying the $[Cu(N^N^P^P)][PF_6]$ complex were made. Layer crystallization in various solvent mixtures ($CH_2Cl_2/Et_2O$, THF/hexane, THF/$Et_2O$, acetone/hexane, $CH_2Cl_2$/hexane and acetone/$Et_2O$) were not successful. Purification by column chromatography with cellulose as well as preparative HPLC failed.

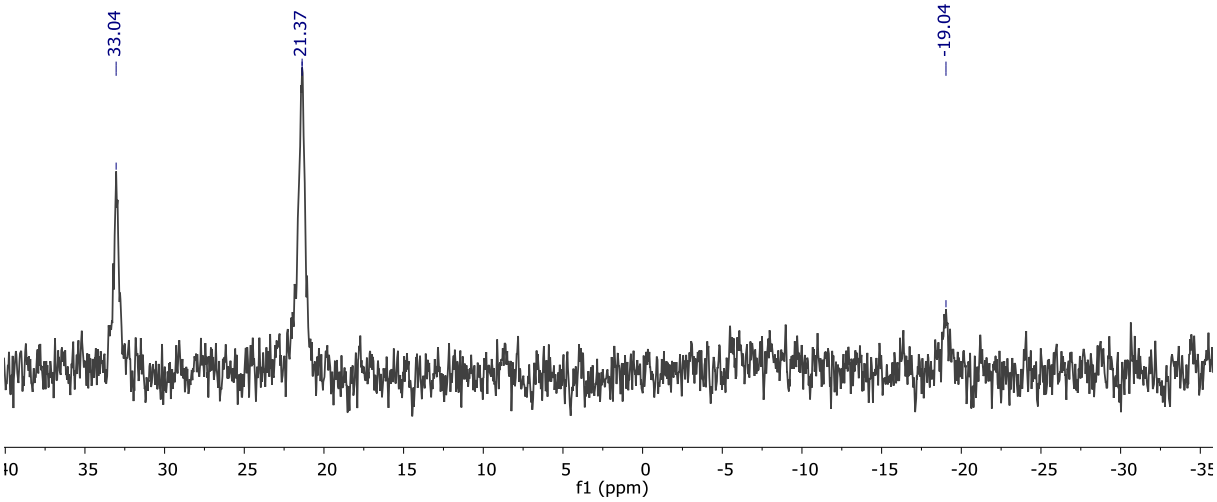


***Figure 5.29*** *Part of the $^{31}P\{^{1}H\}$ NMR spectrum (500 MHz, $CD_2Cl_2$, 298 K) of attempt 3 quenched with copper(I) solution.*

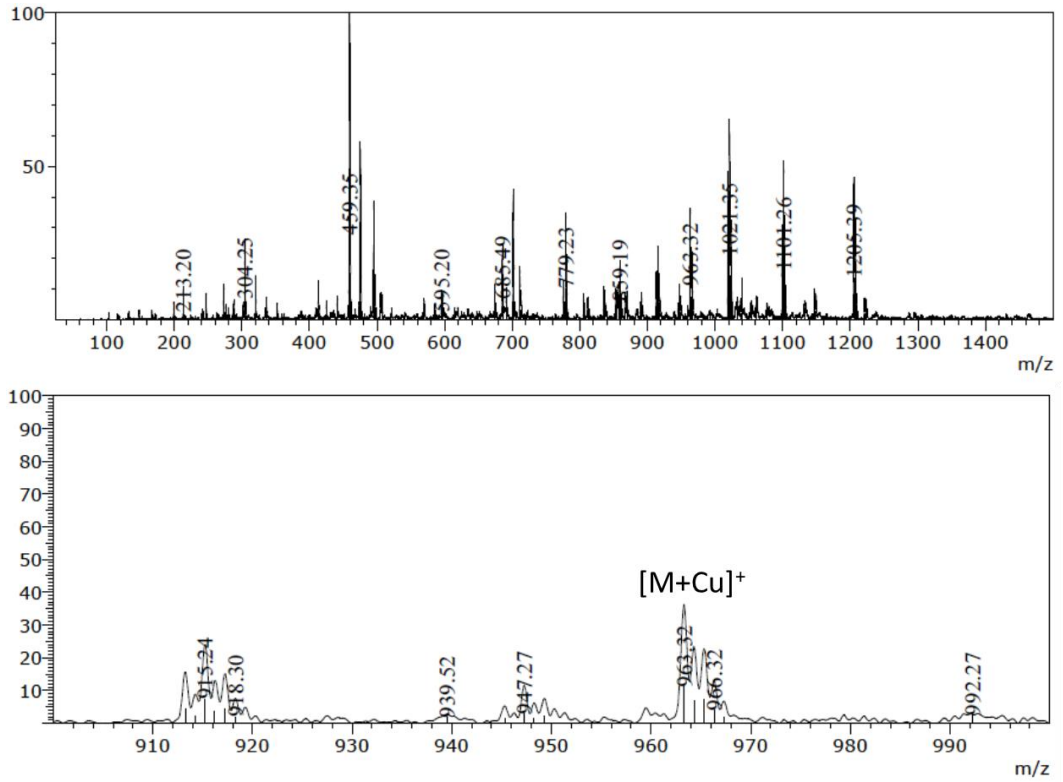


***Figure 5.30*** *Crude ESI MS of the third C–P bond formation attempt quenched with* $[Cu(MeCN)_4][PF_6]$ *solution.*

## 5.8 Conclusion

In this chapter we presented six attempts to prepare a tetradentate N^N^P^P ligand. Preparation of copper(I) complexes with such a ligand was expected to result in chemically more stable luminescent compound. Implementation of such complexes in LECs has the potential of increasing the device lifetime by lowering the amount of emitter degradation in the active layer. While designing such a tetradentate ligand, several factors needed to be considered carefully. The N^N and P^P moiety need to be electronically decoupled to maintain a spatial separation of the HOMO and the LUMO within a complex. The steric demand of substituents close to the copper centre needs to be able to stabilize the tetrahedral geometry upon excitation while still allowing for stable copper coordination. And the linkage between the N^N and P^P moiety needs to be long and flexible enough to allow stable coordination of one copper(I) atom while being as short as possible to limit the probability of multinuclear coordination.

In the first three generation we aimed towards the preparation of a triazole linked tetradentate ligand. This motive was chosen because of the reliable and robust nature of the click reaction used to create the linkage between the N^N and P^P moiety. Benchmark complexes were prepared to investigate the influence of the linkage substructures on the luminescent properties of the complex. Although the photoluminescent quantum yield of the benchmark complexes was slightly lower than comparable literature complexes, it was concluded that the luminescent properties were still sufficient for application in light-emitting electrochemical cells. However, during the preparation of the target triazole linked tetradentate ligand we faced several unexpected synthetic difficulties. Two major obstacles were the instability of the TMS protected acetylene moiety as well as the acidity

of the triazole proton. After the development of three generation of triazole bridged ligand this strategy was abandoned due to its complexity and unpredictability during a multi-step synthesis.

After these initial difficulties we decided to aim towards a tetradentate ligand with chemically less complex structures and a simple alkane linkage between the N^N and P^P moiety. The literature showed, that building up modified xantphos derivates is possible by Friedel-Crafts-acylation[135,207,208] and we combined this approach with our strategies of introducing an 2,2'-bipyridine moiety by lithiation on a terminal alkane position. The fourth generation of ligand design aimed to perform Friedel-Crafts-acylation directly on xantphos, which would have spared us from C−P bond formation reactions. This was not successful; however, we were able to prepare alkyl modified bipyridine derivates, which allowed us to investigate the influence of long alkyl chains on the emissive behaviour of copper(I) complexes. It was found that this new connection motive was suitable for our target complex. In the fifth and sixth generation of complex preparation we aimed to perform stepwise modification of the xanthene unit and introducing the phosphane moieties as the last step. This step proved itself to be the most difficult part of the synthesis. Unwanted oxidation was observed multiple times. In the sixth generation of ligand design we were able to capture the target molecule by the unconventional method of quenching the C−P bond formation reaction with a copper(I) salt, effectively forming the target complex. However, purification of this complex was not successful, most likely due to the complex mixture and amount of impurities from the reaction. We still believe that our attempts suggest that the preparation of a $[Cu(N^N^P^P)]^+$ complex is possible with further optimization of the ligand design and synthetic strategy. Further development of these approached are needed. A possible strategy would be to follow the sixth-generation synthetic strategy but using a short alkyl chain to block the 7-position of the xanthene unit. Fewer flexible alkyl chains in the target molecule increase the chance of crystallizing the target molecule from complex mixtures. Another possible strategy would be to prepare a xantphos derivate with a terminal bromine functionalization, allowing for the late introduction of a bipyridine moiety. However, this approach would need a carefully optimized C−P bond formation step, because the synthetic route would involve a tri-brominated intermediate that could interfere with the lithiation step involved in this procedure.

## 5.9 Experimental

### *5.9.1 Density functional theory (DFT) calculations*

Ground state DFT calculations were carried out using Spartan 18 (v. 1.3) at the B3LYP level with a 6-31G* basis set in vacuum. We have previously demonstrated that for bis(diimine)copper(I) complexes, the choice of atomic orbital basis set (6-311++G** basis set on all atoms, 6-311++G** on Cu and 6-31G* basis set on C, H and N, or 6-31G* basis set on all atoms) has negligible effect on the calculated MO compositions, while significantly influencing the calculated absorption spectra.[187] Hence, a 6-31G* basis set on all atoms was chosen to optimize computer time.

### 5.9.2 6-(2-Bromoethyl)-2,2'-bipyridine (**3**)

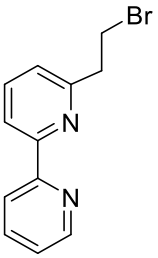


6-(2-bromoethyl)-2,2'-bipyridine was synthesized according to literature[199] and isolated in good yield of 60%. NMR ESI-MS data were in agreement with the literature.

### 5.9.3 6-[(4-Phenyl-1,2,3-triazol-1-yl)ethyl]-2,2'-bipyridine (6-tphbpy)

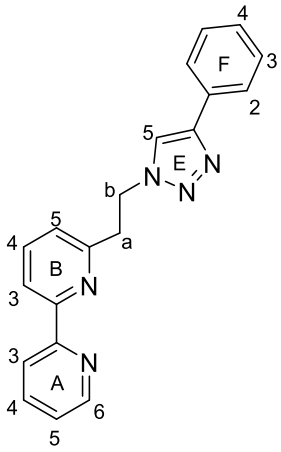


6-[(4-Phenyl-1,2,3-triazol-1-yl)ethyl]-2,2'-bipyridine (6-tphbpy) was synthesized according to an adapted literature procedure.[195] 6-(2-bromoethyl)-2,2'-bipyridine (**3**) (130 mg, 0.49 mmol, 1.0 eq.) was dissolved in DMF (2ml). Sodium azide (48.2 mg, 0.74 mmol, 1.5 eq.) was added and the mixture was stirred overnight. Water (5 ml) was added and the mixture was extracted with $CH_2Cl_2$ (4 × 15 ml). The solvent volume was reduced under vacuo. Phenyl acetylene (101 mg, 0.99 mmol, 2.0 eq.), water (1 ml) and *t*-BuOH (5ml) were added, followed by copper sulfate (12.3 mg, 0.05 mmol, 0.1 eq.) and sodium ascorbate (97.9 mg, 0.49 mmol, 1.0 eq.). The mixture was stirred at 35 °C for 72 h. NMR indicated an incomplete conversion. Therefore more copper sulfate (123 mg, 0.49 mg, 1.0 eq.) and sodium ascorbate (97.9 mg, 0.49 mmol, 1.0 eq.) were added and the reaction was stirred at 35 °C for 5 more h. Water (10 ml) was added and the mixture was extracted with $CH_2Cl_2$ (3 × 20 ml). The combined organic layers were washed with water (2 × 30 ml) and dried over $MgSO_4$. The solvent was removed *in vacuo*. Since NMR indicated the presence of copper impurities, the material was dissolved in $CH_2Cl_2$ (10 ml) and the organic layer was washed with a mixture (2x 20 ml) of aqueous $H_2O_2$ (ca 1%) And $H_4EDTA$ (ca. 1% in 2 M NaOH(aq.). The organic layer was dried over $MgSO_4$ and the solvent was removed *in vacuo*. The product was purified by column chromatography (Alox 90 basic, cyclohexane : ethyl acetate 2 : 1) to give 6-[(4-phenyl-1,2,3-triazol-1-yl)ethyl]-2,2'-bipyridine (87.0 mg, 0.27 mmol, 54%) as a white solid. $^1$H NMR (500 MHz, Chloroform-*d*) $\delta$/ppm: 8.69 (d, $J$ = 4.1 Hz, 1H, $H^{A6}$), 8.41 (d, $J$ = 7.9 Hz, 1H, $H^{A3}$), 8.28 (d, $J$ = 7.9 Hz, 1H, $H^{B3}$), 7.79 (t, $J$ = 7.7 Hz, 1H, $H^{A4}$), 7.74 (d, $J$ = 7.9 Hz, 2H, $H^{F2}$), 7.71 (t, $J$ = 7.8 Hz, 1H, $H^{B4}$), 7.62 (s, 1H, $H^{E5}$), 7.37 (t, $J$ = 7.6 Hz, 2H, $H^{F3}$), 7.34–7.27 (ov. m, 2H, $H^{A5+F4}$), 7.09 (d, $J$ = 7.6 Hz, 1H, $H^{B5}$), 4.98 (t, $J$ = 6.9 Hz, 2H, $H^b$), 3.50 (t, $J$ = 6.9 Hz, 2H, $H^a$). $^{13}$C{$^1$H} NMR (126 MHz, $CDCl_3$) $\delta$/ppm: 156.5 ($C^{B6}$), 156.1 ($C^{A2}$), 156.0 ($C^{B2}$), 149.4 ($C^{A6}$), 147.6 ($C^{E4}$), 137.8 ($C^{B4}$), 137.0 ($C^{A4}$), 130.8 ($C^{F1}$), 128.9 ($C^{F3}$), 128.1 ($C^{F4}$), 125.8 ($C^{F2}$), 124.0 ($C^{A5}$), 123.8 ($C^{B5}$), 121.2 ($C^{A3}$), 120.2 ($C^{E5}$), 119.5 ($C^{B3}$), 49.5 ($C^b$), 38.4 ($C^a$). ESI MS: *m/z* 328.1 $[M+H]^+$ (base peak calc. 328.2).

### 5.9.4 2-(2-Bromophenoxy)benzene (**5**)

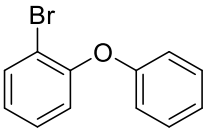


2-(2-Bromophenoxy)benzene (**5**) ether was prepared according to literature procedure.[200] 2-Bromophenol (17.3 g, 100 mmol, 1.0 eq.) and bromobenzene (31.4 g, 200 mmol, 2.0 eq.) were dissolved in DMSO (100 ml) and stirred for 5 min. Potassium tert-butoxide (28.1 g, 150 mmol,

2.5 eq.) was added portion wise and the mixture was stirred at 45 °C for 15 h. The reaction mixture was poured into water and extracted with ethyl acetate (3 × 100 ml) The combined organic layers were dried over $MgSO_4$ and the solvent was removed in vacuo. The product was purified by flash chromatography (silica, cyclohexane to cyclohexane + 1% ethyl acetate.) to give 2-(2-bromophenoxy)benzene (**5**, 2.76 g, 11.1 mmol, 11%) as white solid. NMR data was in agreement with the literature.[200]

### *5.9.5 9,9-Diphenylxanthene (**6**)*

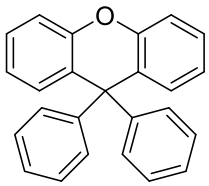

9,9-Diphenylxanthene (**6**) was prepared according to a patent procedure.[201] 2-(2-Bromophenoxy)benzene (**5**, 2.50 g, 10.0 mmol, 1.1 eq.) was dissolved in dry THF (30 ml) under inert conditions. The solution was cooled to −78 °C. *n*BuLi (6.84 ml, 1.6 M in hexane, 10.9 mmol, 2.2 eq.) was added dropwise and the mixture was stirred for 1 h. A solution of benzophenone (1.66 g, 9.12 mmol, 1.0 eq.) in THF (10 ml) was added dropwise. The mixture was allowed to warm to room temperature before sat. aqueous $NH_4Cl$ solution was added to quench the reaction. The volume of the mixture was reduced under vacuo. Acetic acid (30 ml) and fuming HCl (5 ml) were added and the mixture was heated to 75 °C for 6 h. After cooling to room temperature, the white precipitate was filtered off and washed with methanol to yield 9,9-diphenylxanthene (**6**, 2.54 g, 7.58 mmol, 83%) as white solid. $^1$H NMR (500 MHz, $CDCl_3$) δ 7.28 – 7.19 (m, 8H), 7.16 (dd, *J* = 8.1, 1.3 Hz, 2H), 7.04 (td, *J* = 7.5, 1.3 Hz, 2H), 7.01 – 6.97 (m, 4H), 6.92 (dd, *J* = 7.9, 1.7 Hz, 2H).

### *5.9.6 9,9-Diphenyl-9H-xanthene-4,5-diyl)bis(diphenylphosphane) (Ph$_2$xantphos)*

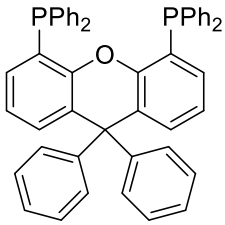

Ph$_2$xantphos was prepared by a modified literature procedure.[183] 9,9-Diphenylxanthene (**6**, 500 mg, 1.50 mmol, 1.0 eq.) was dissolved in dry hexane (30 ml) under inert conditions. *n*BuLi (2.34 ml, 1.6 M in hexane, 3.75 mmol, 2.5 eq.) and TMEDA (436 mg, 3.75 mmol, 2.5 eq.) were added and the mixture was heated to reflux for 60 min while the colour changed to pale orange. The mixture was cooled to 0 °C and a solution of chlorodiphenylphosphine (0.70 ml, 3.9 mmol, 2.6 eq.) in dry THF (10 ml) was added slowly to quench the reaction. The reaction mixture was stirred at 0°C for 1 h before allowed to warm up to RT, while stirred overnight (16 h) it turned from red to yellow. The mixture was diluted with ethyl acetate and washed with $H_2O$. The aqueous phase was extracted with $CH_2Cl_2$ (2 × 15 ml). The combined organic layers were dried over $MgSO_4$ and the solvent was removed under vacuo. $^{31}$P{$^1$H} NMR showed mainly oxidised product. An attempt to reduce the phosphane oxide with methyldiethoxysilane and bis(4-nitrophenyl) phosphate as catalyst according to literature[202] failed. Since the crude $^{31}$P{$^1$H} NMR showed a signal in the expected region at −16.1 ppm, the presence of the desired product was assumed. The concentration of product vs. impurities was estimated to be ca. 30% by NMR. Therefore, the crude material was dissolved in deoxygenated $CH_2Cl_2$ and used for complexation. (section 5.2.1).

## *5.9.7 [Cu(6-tphbpy)(xantphos)][PF$_6$]*

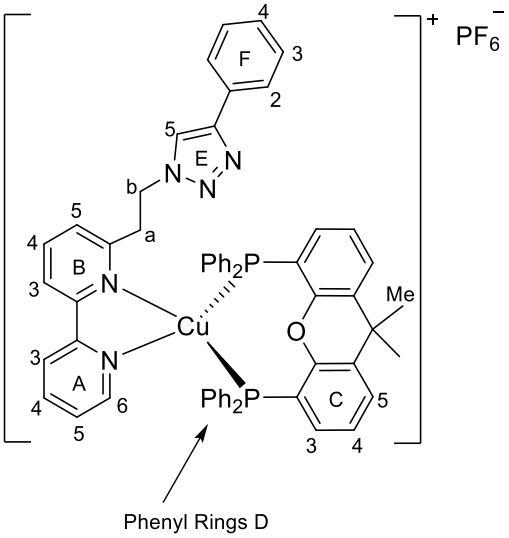


[Cu(MeCN)$_4$][PF$_6$] (42.1 mg, 0.11 mmol, 1.0 eq.) was dissolved in $CH_2Cl_2$ (15 ml). A solution of xantphos (65.4 mg, 0.11 mmol, 1.0 eq.) and 6-tphbpy (37.0 mg, 0.11 mmol, 1.0 eq.) was added and the mixture turned red then yellow while it was stirred for 2 h at room temperature. The yellow solution was filtered and the solvent was removed from the filtrate. The solid material was washed with $Et_2O$ (4 × 10 ml) by sonication and dried under vacuum. [Cu(6-tphbpy)(xantphos)][PF$_6$] (125 mg, 0.11 mmol, 99%) was isolated as a yellow solid. $^1$H NMR (500 MHz, acetone-*d*$_6$) $\delta$/ppm: 8.56 (d, *J* = 8.2 Hz, 1H, H$^{A3}$), 8.49 (d, *J* = 7.9 Hz, 1H, H$^{B3}$), 8.32 (br s, 1H, H$^{A6}$), 8.14(t, *J* = 7.9 Hz, 1H, H$^{B4}$), 8.11 (t, *J* = 7.9 Hz, 1H, H$^{A4}$), 7.87 (d, *J* = 7.8 Hz, 2H, H$^{C5}$), 7.73 (d, *J* = 7.7 Hz, 2H, H$^{F2}$), 7.68 (s, 1H, H$^{E5}$), 7.45 (dd, *J* = 7.6, 5.3 Hz, 1H, H$^{A5}$), 7.43–7.36 (ov. m, 5H, H$^{B5+D4+F3}$), 7.34 (d, *J* = 7.4 Hz, 1H, H$^{F4}$), 7.32–7.27 (ov. m, 4H, H$^{C4+D4'}$), 7.25 (t, *J* = 7.6 Hz, 4H, H$^{D3'}$), 7.18–7.09 (ov. m, 8H, H$^{D2'+D3}$), 6.97 (q, *J* = 6.1 Hz, 4H, H$^{D2}$), 6.70 (m, 2H, H$^{C3}$), 4.20 (t, *J* = 6.9 Hz, 2H, H$^{b}$), 3.31 (t, *J* = 6.1 Hz, 3H, H$^{a}$), 1.87 (s, 3H, H$^{Me}$), 1.75 (s,3H, H$^{Me'}$). $^{13}$C{$^1$H} NMR (126 MHz, acetone-*d*$_6$) $\delta$/ppm: 158.6(C$^{B6}$), 155.7 (t, *J* = 6.3 Hz, C$^{C1}$), 153.3(C$^{A2}$), 153.0(C$^{B2}$), 149.8(C$^{A6}$), 147.9(C$^{E4}$), 140.5(C$^{B4}$), 140.0(C$^{A4}$), 135.1 (t, *J* = 1.6 Hz, C$^{C6}$), 133.9 (t, *J* = 8.0 Hz, C$^{D2}$), 133.5 (t, *J* = 7.9 Hz, C$^{D2'}$), 132.5 (t, *J* = 16.9 Hz, C$^{D1'}$), 132.0 (t, *J* = 17.6 Hz, C$^{D1}$), 131.9 (C$^{F1}$), 131.7 (C$^{C3}$), 131.11 (C$^{D4'}$), 131.06 (C$^{D4}$), 129.92 (t, *J* = 4.8 Hz, C$^{D3'}$), 129.88 (t, *J* = 4.8 Hz, C$^{D3}$), 129.7 (C$^{F3}$), 128.9 (C$^{F4}$), 128.8 (C$^{C5}$), 127.1 (C$^{A5}$), 126.5 (t, *J* = 2.2 Hz, C$^{C4}$), 126.3 (C$^{F2}$), 126.0 (C$^{B5}$), 124.1 (C$^{A3}$), 122.4 (C$^{B3}$), 121.23 (t, *J* = 13.5 Hz, C$^{C2}$), 121.17 (C$^{E5}$), 48.1 (C$^{b}$), 40.9 (C$^{a}$), 37.0 (C$^{q}$), 29.6 (br, C$^{Me'}$), 27.2 (br, C$^{Me}$). $^{31}$P{$^1$H} NMR (202 Hz, acetone-*d*$_6$) $\delta$/ppm: −12.7 (broad, FWHM = 220 Hz), −144.3 (septet, $J_{PF}$ = 707 Hz, [PF$_6$]$^-$). ESI MS 968.2 [M − PF$_6$]$^+$ (calc. 968.3). UV-Vis ($CH_2Cl_2$, 2.5 × 10$^{-5}$ mol dm$^{-3}$): $\lambda$/nm ($\varepsilon$/dm$^3$ mol$^{-1}$ cm$^{-1}$) 248 (50000), 283 (30000), 383 (3000). Found: C 63.24, H 4.63, N 6.19; $C_{59}H_{49}CuF_6N_5OP_3$ requires C 63.58, H 4.43, N 6.28%.

## *5.9.8 [Cu(6-Mebpy)(Ph$_2$xantphos)][PF$_6$]*

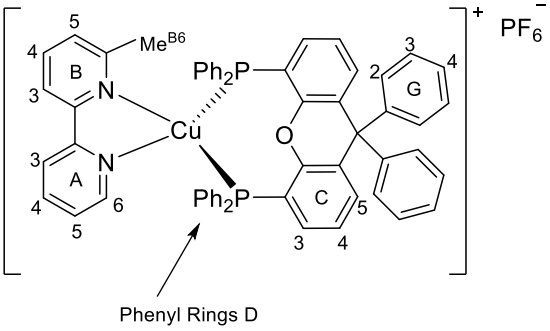


[Cu(MeCN)$_4$][PF$_6$] (55.9 mg, 0.15 mmol, 1.0 eq.) was dissolved in $CH_2Cl_2$ (15 ml). A solution of Ph$_2$xantphos (127 mg, 0.18 mmol, 1.1 eq.) and 6-Mebpy (25.5 mg, 0.15 mmol, 1.0 eq.) was added and the mixture turned red then yellow while it was stirred for 2 h at room temperature. The yellow solution was filtered and the solvent was removed from the filtrate. The solid material was washed with $Et_2O$ (3 × 10 ml) by sonication and dried under vacuum. [Cu(6-Mebpy)(Ph$_2$xantphos)][PF$_6$] (119 mg, 0.11 mmol, 73%) was isolated as a yellow solid. $^1$H NMR (500 MHz, acetone-*d*$_6$) $\delta$/ppm: 8.65 (d, *J* = 4.6 Hz, 1H, H$^{A6}$), 8.61 (d, *J* = 8.1 Hz, 1H, H$^{A3}$), 8.53 (d, *J* = 7.9 Hz, 1H, H$^{B3}$), 8.20 (t, *J* = 7.9 Hz, 1H, H$^{B4}$), 8.15 (t, *J* = 7.6 Hz, 1H, H$^{A4}$), 7.61 – 7.55 (ov. m, 2H, H$^{A5+B5}$), 7.50

– 7.37 (ov. m, 6H, $H^{G3+G3'+G4+G4'}$), 7.34 – 7.25 (ov. m, 6H, $H^{C4+D4+D4'}$), 7.20 (d, *J* = 6.7 Hz, 2H, $H^{C5}$), 7.14 – 7.05 (ov. m, 12H, $H^{D3+D3'+G2+G2'}$), 7.00 (q, *J* = 6.1 Hz, 4H, $H^{D2'}$), 6.85 (q, *J* = 6.1 Hz, 4H , $H^{D2}$), 6.67 (m, 2H , $H^{C3}$), 2.16 (s, 2H , $H^{MeB6}$). $^{13}C\{^1H\}$ NMR (126 MHz, acetone-$d_6$) $\delta$/ppm: 159.6 ($C^{B6}$), 156.1(t, *J* = 6.2 Hz, $C^{C1}$), 153.4 ($C^{A2}$), 152.5 ($C^{B2}$), 150.0 ($C^{A6}$), 140.5 ($C^{B4}$), 140.0 ($C^{A4}$), 134.6 (t, *J* = 1.8 Hz, $C^{C6}$), 134.0 (t, *J* = 8.1 Hz, $C^{D2}$), 133.2 (t, *J* = 7.7 Hz, $C^{D2'}$), 132.8 ($C^{C5}$), 132.1 ($C^{C3}$), 131.3 ($C^{G1}$), 131.2 ($C^{D4}$), 130.8 ($C^{D4'}$), 130.3 ($C^{G2}$), 129.7 (m, $C^{D3+D3'}$), 129.24 ($C^{G3'}$), 129.22 ($C^{G3}$), 128.4 ($C^{G4}$), 128.2 ($C^{G4'}$), 127.23 ($C^{B5}$), 127.16 ($C^{A5}$), 125.8 (t, *J* = 2.4 Hz, $C^{C4}$), 123.9 ($C^{A3}$), 121.8 ($C^{C2}$), 121.3 ($C^{B3}$), 56.7 ($C^{q}$), 26.4 ($C^{MeB6}$). $^{31}P\{^1H\}$ NMR (202 Hz, acetone-$d_6$) $\delta$/ppm: −13.3 (broad, FWHM = 230 Hz), −144.3 (septet, $J_{PF}$ = 707 Hz, $[PF_6]^-$). ESI MS: *m/z* 935.2 $[M - PF_6]^+$ (base peak, calc. 935.2). UV-Vis ($CH_2Cl_2$, 2.5 × $10^{-5}$ mol $dm^{-3}$): $\lambda$/nm ($\varepsilon$/$dm^3$ $mol^{-1}$ $cm^{-1}$) 250 (28000), 291 (24500), 313sh (12000) 386 (2600). Found: C 64.80, H 4.56, N 2.17; $C_{60}H_{46}CuF_6N_2OP_3$ requires C 66.64, H 4.29, N 2.59%.

### *5.9.9 Phenyl[3-(2-trimethylsilylethynyl)phenyl]methanone (**7**)*

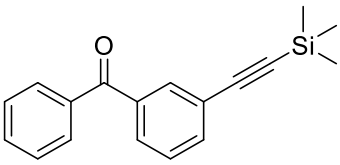


3-Bromobenzophenone (2.00 g, 7.65 mmol, 1.0 eq.), Bis(triphenylphosphine)palladium(II) dichloride (107 mg, 0.153 mmol, 0.02 eq.), triphenylphosphine (80.3 mg, 0.306 mmol, 0.04 eq.) and copper(I) iodide (29.1 mg, 0.153 mmol, 0.02 eq.) were added to a flame dried two neck flask and evacuated and nitrogen refilled three time. A 5:1 mixture of toluene and diisopropylamine (25 ml) was added and argon was bubbled through the solution for 10 min. Trimethylsilylacetylene (1.27 ml, 9.18 mmol, 1.2 eq.) was added and the mixture was stirred at 35 °C for 24 h. The reaction was quenched by addition of aqueous $NH_4Cl$ and the mixture was extracted with $CH_2Cl_2$ (3 × 30 ml), dried over $MgSO_4$ and the solvent was removed in vacuo. The product was purified by column chromatography (silica, toluene : cyclohexane 1:1) and Kugelrohr distillation to yield Phenyl[3-(2-trimethylsilylethynyl)phenyl]methanone (**7**, 1.91 g, 6.85 mmol, 90 %) as yellow oil. $^1H$ NMR (500 MHz, $CDCl_3$) $\delta$/ppm: 7.87 (t, *J* = 1.7 Hz, 1H), 7.82 – 7.77 (m, 2H), 7.74 (dt, *J* = 7.8, 1.5 Hz, 1H), 7.67 (dt, *J* = 7.7, 1.4 Hz, 1H), 7.61 (dt, *J* = 7.4, 1.3 Hz, 1H), 7.50 (t, *J* = 7.7 Hz, 2H), 7.43 (t, *J* = 7.7 Hz, 1H), 0.25 (s, 9H).

### *5.9.10 (2-Phenoxyphenyl)(phenyl)[3-(2-trimethylsilylethynyl)phenyl]methanol (**8**)*

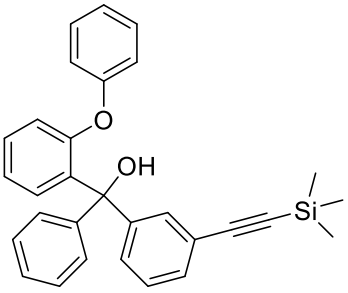


(2-Phenoxyphenyl)(phenyl)[3-(2-trimethylsilylethynyl)phenyl]methanol (**8**) was prepared according to an adapted patent procedure.[201] 2-(2-Bromophenoxy)benzene (**5**, 586 mg, 2.37 mmol, 1.1 eq.) was dissolved in dry THF (10 ml) and cooled to −78 °C. *n*BuLi (2.15 ml, 1.6 M in hexane, 3.44 mmol, 1.6 eq.) was added dropwise and the mixture was stirred for 1.5 h. A solution of phenyl[3-(2-trimethylsilylethynyl)phenyl]methanone (**7**, 599 mg, 2.15 mmol, 1.0 eq.) in THF (10 ml) was added slowly and the mixture was allowed to warm to room temperature overnight. The reaction was quenched by addition of aqueous $NH_4Cl$ and the mixture was extracted with $CH_2Cl_2$ (3 × 30 ml) and the combined organic layer were washed with water (2 × 50 ml). The wash fractions were extracted with toluene (2

× 40 ml), the combined organic layers were dried over $MgSO_4$ and the solvent was removed in vacuo. The product was purified by column chromatography (silica, cyclohexane : $CH_2Cl_2$ 3:1) to yield (2-phenoxyphenyl)(phenyl)[3-(2-trimethylsilylethynyl)phenyl]methanol (**8**, 570 mg, 1.27 mmol, 59 %) as colourless oil. $^1$H NMR (500 MHz, $CDCl_3$) $\delta$/ppm: 7.55 – 7.53 (m, 1H), 7.38 – 7.35 (m, 1H), 7.32 – 7.27 (m, 5H), 7.25 – 7.21 (m, 4H), 7.19 (ddd, *J* = 8.1, 7.3, 1.7 Hz, 1H), 7.09 (ddt, *J* = 7.9, 7.0, 1.1 Hz, 1H), 6.91 (td, *J* = 7.6, 1.2 Hz, 1H), 6.77 – 6.74 (m, 2H), 6.72 (dd, *J* = 8.2, 1.2 Hz, 1H), 6.64 (dd, *J* = 7.8, 1.7 Hz, 1H), 4.97 (s, 1H), 0.22 (s, 8H). ESI MS: *m/z* 431.1 $[M - H_2O]^+$ (base peak, calc. 431.2).

### *5.9.11 9-Phenyl-9-[3-(2-trimethylsilylethynyl)phenyl]xanthene (**9**)*

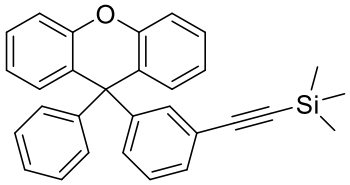


Ambelyst 15 (1.00 g) was placed in a flame dried reaction flask and evacuated for 2 h. A solution of (2-phenoxyphenyl)(phenyl)[3-(2-trimethylsilylethynyl)phenyl]methanol (**8**, 364 mg, 0.811 mmol 1.0 eq.) in dry THF (15 ml) was added and the mixture was heated to reflux overnight. The solution was filtered under a nitrogen stream and the solvent was removed under vacuo. The product was purified by column chromatography (silica, cyclohexane : $CH_2Cl_2$ to give 9-phenyl-9-[3-(2-trimethylsilylethynyl)phenyl]xanthene (**9**, 225 mg, 0.522 mmol, 64 %) as colourless oil. $^1$H NMR (500 MHz, $CDCl_3$) $\delta$/ppm: 7.34 (dt, *J* = 7.7, 1.3 Hz, 1H), 7.30 – 7.27 (m, 2H), 7.24 – 7.19 (m, 3H), 7.18 – 7.14 (m, 4H), 7.05 (ddd, *J* = 7.9, 7.2, 1.3 Hz, 2H), 6.96 – 6.93 (m, 2H), 6.93 – 6.91 (m, 1H), 6.90 (dd, *J* = 7.8, 1.6 Hz, 2H), 0.19 (s, 9H).

### *5.9.12 6-(2-[4-([3-(9-Phenylxanthen-9-yl)phenyl]-1,2,3-triazol-1-yl)]ethyl)-2,2'-bipyridine (**11**)*

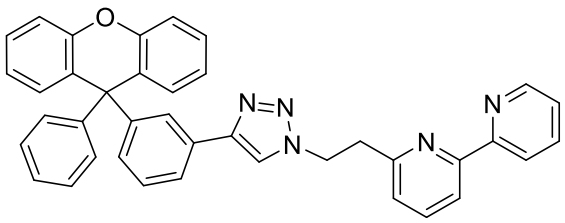


6-(2-[4-([3-(9-Phenylxanthen-9-yl)phenyl]-1,2,3-triazol-1-yl)]ethyl)-2,2'-bipyridine (**11**) was synthesized according to an adapted literature procedure.[195] 6-(2-Bromoethyl)-2,2'-bipyridine (**3**) was used with some impurities of the elimination product 6-vinyl-2,2'-bipyridine. 6-(2-Bromoethyl)-2,2'-bipyridine (**3**, 32.3 mg, 0.12 mmol, 1.0 eq.) was dissolved in DMF (2ml). Sodium azide (10.5 mg, 0.19 mmol, 1.5 eq.) was added and the mixture was stirred overnight. Water (5 ml) was added and the mixture was extracted with $CH_2Cl_2$ (4 × 10 ml). The solvent volume was reduced under vacuo. 9-Phenyl-9-[3-(2-trimethylsilylethynyl)phenyl]xanthene (**9**, 80.1 mg, 0.19 mmol, 1.4 eq.), water (1 ml) and *t*-BuOH (5ml) were added, followed by sodium fluoride (8.33 mg, 0.20 mmol, 1.6 eq.), copper sulfate (21.8 mg, 0.14 mmol, 1.1 eq.) and sodium ascorbate (54.0 mg, 0.27 mmol, 2.2 eq.). The mixture was stirred at 35 °C overnight. Water (10 ml) was added and the mixture was extracted with $CH_2Cl_2$ (3 × 20 ml). The combined organic layers were washed with water (2 × 30 ml) and dried over $MgSO_4$. The solvent was removed *in vacuo*. Since NMR indicated the presence of copper impurities, the material was dissolved in $CH_2Cl_2$ (10 ml) and the organic layer was washed with a mixture (2x 20 ml) of aqueous $H_2O_2$ (ca 1%) and $H_4$EDTA (ca. 1% in 2 M NaOH(aq.). The organic layer was dried over $MgSO_4$ and the solvent was removed *in vacuo*. The product was purified by column chromatography

(silica, cyclohexane : ethyl acetate 5:1, then ethyl acetate) to give 6-(2-[4-([3-(9-phenylxanthen-9-yl)phenyl]-1,2,3-triazol-1-yl)]ethyl)-2,2'-bipyridine (**11**, 65.0 mg, 0.12 mmol, 90%) as white solid. $^1$H NMR (500 MHz, Acetone-$d_6$) $\delta$/ppm: 8.66 (dt, $J$ = 4.8, 1.1 Hz, 1H), 8.45 (d, $J$ = 7.9 Hz, 1H), 8.32 (d, $J$ = 7.8 Hz, 1H), 8.08 (s, 1H), 7.85 – 7.77 (m, 2H), 7.72 (dt, $J$ = 7.7, 1.5 Hz, 1H), 7.56 (s, 1H), 7.39 (ddd, $J$ = 7.4, 4.8, 1.2 Hz, 1H), 7.36 – 7.23 (m, 9H), 7.18 (dd, $J$ = 8.2, 1.3 Hz, 2H), 7.09 (td, $J$ = 7.5, 1.3 Hz, 2H), 7.02 – 6.97 (m, 2H), 6.95 (dd, $J$ = 7.8, 1.6 Hz, 2H), 6.87 (dt, $J$ = 7.2, 1.2 Hz, 1H), 4.96 (t, $J$ = 7.0 Hz, 2H), 3.49 (t, $J$ = 6.9 Hz, 2H). ESI MS: *m/z* 606.2 $[M + Na]^+$ (base peak, calc. 606.2).

### *5.9.13 6-(2-[4-([3-(9-Phenylxanthen-9-yl)phenyl]-1,2,3-triazol-1-yl)]ethyl)-2,2'-bipyridine iodization*

6-(2-[4-([3-(9-Phenylxanthen-9-yl)phenyl]-1,2,3-triazol-1-yl)]ethyl)-2,2'-bipyridine (**11**, 12.7 mg, 0.02 mmol, 1.0 eq.) was dissolved in dry THF (3 ml) under inert conditions. *n*BuLi (10.5 µl, 2.5 M in hexane, 0.02 mmol, 1.2 eq.) was added and the mixture turned dark blue while it was stirred at −78 °C for 20 min. A solution of iodomethane (5.43 µl, 0.08 mmol, 4.0 eq.) in dry THF (2 ml) was added slowly to quench the reaction. The reaction mixture was stirred at −78 °C for 1h before allowed to warm up to room temperature. Water was added and the mixture was extracted with $CH_2Cl_2$, dried over $MgSO_4$ and the solvent was removed in vacuo. Part of the $^1$H NMR spectrum is shown in **Figure 5.12**. ESI-MS: *m/z* 634.2 [starting material double methylated + Na]$^+$ (base peak, calc. 606.3).

### *5.9.14 3-(2,2'-Bipyridiny-6-yl)propanol (**13**)*

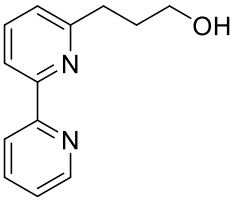


3-(2,2'-Bipyridiny-6-yl)propanol was synthesized according to literature[206]. NMR ESI-MS data were in agreement with the literature.

### *5.9.15 6-(2,2'-Bipyridin-6-yl)hexanoic acid (**16**)*

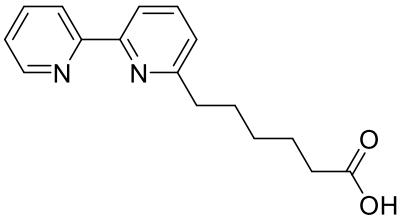


6-(2,2'-Bipyridin-6-yl)hexanoic acid (**16**) was prepared according to literature procedure.[209]

## *5.9.16[Cu(**16**)(DPEPhos)][PF$_6$]*

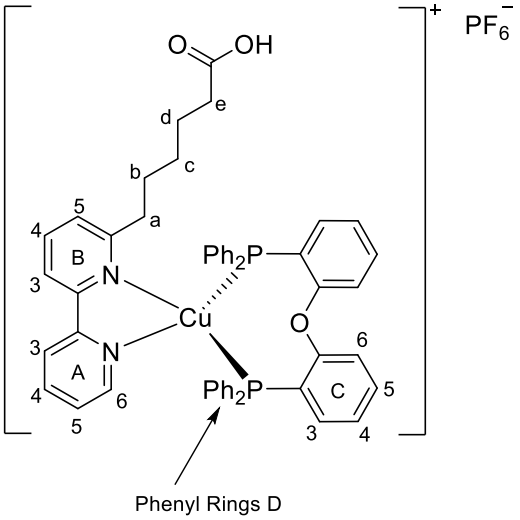


[Cu(MeCN)$_4$][PF$_6$] (93.2 mg, 0.25 mmol, 1.0 eq.) and DPEPhos (148 mg, 0.28 mmol, 1.1 eq.) were dissolved in $CH_2Cl_2$ (30 ml) and the mixture stirred for 1 h. 6-(2,2'-bipyridyl)hexanoic acid (**16**, 67.6 mg, 0.25 mmol, 1.0 eq.) was added and the mixture turned red, then orange while it was stirred for 1 h. The colour indicated the presence of homoleptic [Cu(**16**)$_2$][PF$_6$] and therefore additional DPEPhos (26.9 mg, 0.05 mmol, 0.2 eq.) was added. The mixture turned yellow while it was stirred for 1.5 h. The solution was filtered and the volume was reduced *in vacuo*. The product was precipitated by addition of $Et_2O$ and the solid material was washed by sonication in $Et_2O$ (4x 15 ml). Drying in vacuo yielded [Cu(**16**)(DPEPhos)][PF$_6$] (213 mg, 0.21 mmol, 84%) as a yellow solid. $^1$H NMR (500 MHz, acetone-$d_6$) $\delta$/ppm: 10.45 (br s, 1H, $H^{COOH}$), 8.71 (d, $J$ = 5.0 Hz, 1H, $H^{A6}$), 8.50 (d, $J$ = 8.1 Hz, 1H, $H^{A3}$), 8.43 (d, $J$ = 7.9 Hz, 1H, $H^{B3}$), 8.16 (t, $J$ = 7.9 Hz, 1H, $H^{B4}$), 8.07 (td, $J$ = 7.8, 1.6 Hz, 1H, $H^{A4}$), 7.54 (d, $J$ = 7.9 Hz, 1H, $H^{B5}$), 7.46 − 7.35 (ov. m, 7H, $H^{A5+C5+D4+D4'}$), 7.28 (t, $J$ = 7.6 Hz, 8H, $H^{D3+D3'}$), 7.21 (m, 2H, $H^{C6}$), 7.18 − 7.13 (ov. m, 6H, $H^{C4+D2'}$), 7.07 (m, 4H, $H^{D2}$), 6.88 (dtd, $J$ = 7.8, 4.0, 1.7 Hz, 2H, $H^{C3}$), 2.81 (t, $J$ = 8.2 Hz, 2H, $H^a$), 2.12 (t, $J$ = 7.4 Hz, 2H, $H^e$), 1.31 (m, 2H, $H^d$), 1.25 (m, 2H, $H^b$), 0.85 (m, 3H, $H^c$). $^{13}$C{$^1$H} NMR (126 MHz, acetone-$d_6$) $\delta$/ppm: 174.5 ($C^f$), 163.7 ($C^{B6}$), 158.8 (t, $J$ = 6.0 Hz, $C^{C1}$), 153.6 (t, $J$ = 2.1 Hz, $C^{A2}$), 152.4 (t, $J$ = 1.8 Hz, $C^{B2}$), 150.3 ($C^{A6}$), 140.1 ($C^{B4}$), 139.7 ($C^{A4}$), 134.9 ($C^{C3}$), 134.2 (t, $J$ = 7.7 Hz, $C^{D2'}$), 133.7 (t, $J$ = 7.9 Hz, $C^{D2}$), 133.2 ($C^{C5}$), 132.1 (t, $J$ = 17.2 Hz, $C^{D1}$), 131.1 ($C^{D4'}$), 131.0 ($C^{D4}$), 129.8 (t, $J$ = 4.7 Hz, $C^{D3}$), 126.7 ($C^{A5}$), 126.1 (t, $J$ = 2.3 Hz, $C^{C2}$), 125.3 ($C^{B5}$), 125.1 (t, $J$ = 14.5 Hz, $C^{C2}$), 123.6 ($C^{A3}$), 121.4 (t, $J$ = 1.8 Hz, $C^{C6}$), 121.2 ($C^{B3}$), 40.8 ($C^a$), 34.0 ($C^e$), 29.5 ($C^c$), 28.7 ($C^b$), 25.5 ($C^d$). $^{31}$P{$^1$H} NMR (202 Hz, acetone-$d_6$) $\delta$/ppm: −13.1 (broad, FWHM = 260 Hz), −144.3 (septet, $J_{PF}$ = 707 Hz, [PF$_6$]$^-$). ESI MS: $m/z$ 871.2 [M − PF$_6$]$^+$ (base peak, calc. 871.2). UV-Vis ($CH_2Cl_2$, 2.5 × 10$^{-5}$ mol dm$^{-3}$): $\lambda$/nm ($\varepsilon$/dm$^3$ mol$^{-1}$ cm$^{-1}$) 250 (28000), 292 (23500), 380 (3000). Found: C 61.28, H 4.71, N 2.66; $C_{52}H_{46}CuF_6N_2O_3P_3$ requires C 61.39, H 4.56, N 2.75%.

## *5.9.17 [Cu(**16**)(xantphos)][PF$_6$]*

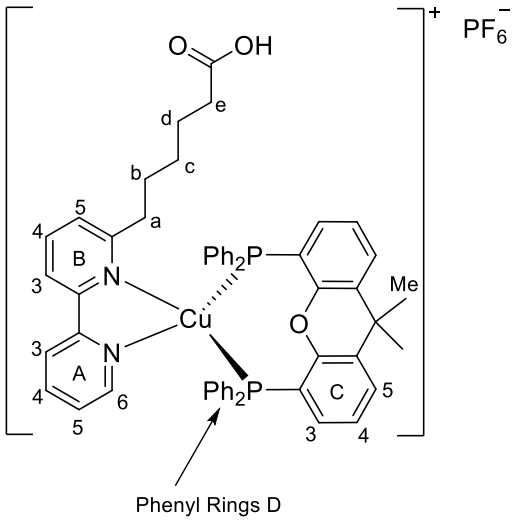


[Cu(**16**)(xantphos)][PF$_6$] was prepared according to the procedure described for [Cu(6-tphbpy)(xantphos)][PF$_6$] using [Cu(MeCN)$_4$][PF$_6$] (93.2 mg, 0.25 mmol, 1.0 eq.), xantphos (145 mg, 0.25 mmol, 1.0 eq.) and 6-(2,2'-bipyridyl)hexanoic acid (**16**, 67.6 mg, 0.25 mmol, 1.0 eq.). The product [Cu(**16**)(xantphos)][PF$_6$] (259 mg, 0.25 mmol, 98%) was isolated as a yellow solid. $^1$H NMR (500 MHz, acetone-$d_6$) $\delta$/ppm: 10.41 (s, 1H, H$^{COOH}$), 8.62 (s, 1H, H$^{A6}$), 8.50 (d, $J$ = 8.2 Hz, 1H, H$^{A3}$), 8.43 (d, $J$ = 7.9 Hz, 1H, H$^{B3}$), 8.20 (t, $J$ = 7.9 Hz, 1H, H$^{B4}$), 8.10 (td, $J$ = 7.8, 1.6 Hz, 1H, H$^{A4}$), 7.87 (dd, $J$ = 7.8, 1.5 Hz, 2H, H$^{C5}$), 7.61 (d, $J$ = 7.8 Hz, 1H, H$^{B5}$), 7.53 (dd, $J$ = 7.6, 5.1 Hz, 1H, H$^{A5}$), 7.40 (t, $J$ = 7.4 Hz, 2H, H$^{D4'}$), 7.36 – 7.29 (ov. m, 4H, H$^{C4+D4}$), 7.27 (t, $J$ = 7.5 Hz, 4H, H$^{D3'}$), 7.20 (m, 4H, H$^{D2'}$), 7.16 (t, $J$ = 7.8 Hz, 4H, H$^{D3}$), 6.90 (m, 4H, H$^{D2}$), 6.71 (m, 2H, H$^{C3}$), 2.48 (t, $J$ = 7.6 Hz, 2H, H$^{a}$), 2.02 (t, $J$ = 7.7 Hz, 2H, H$^{e}$), 1.95 (s, 3H, H$^{Me}$), 1.64 (s, 3H, H$^{Me'}$), 1.23 – 1.12 (ov. m, 4H, H$^{b+c}$), 0.51 (m, 2H, H$^{d}$). $^{13}$C{$^1$H} NMR (126 MHz, acetone-$d_6$) $\delta$/ppm: 174.3 (C$^{f}$),163.0 (C$^{B6}$), 155.9 (t, $J$ = 6.2 Hz, C$^{C1}$), 153.5 (t, $J$ = 2.2 Hz, C$^{A2}$), 152.3 (t, $J$ = 1.9 Hz, C$^{B2}$), 150.0 (C$^{A6}$), 140.3 (C$^{B4}$), 139.9 (C$^{A4}$), 135.1 (t, $J$ = 1.7 Hz, C$^{C6}$), 134.0 (t, $J$ = 8.1 Hz, C$^{D2}$), 133.4 (t, $J$ = 7.7 Hz, C$^{D2'}$), 132.8 (m, C$^{D1'}$), 132.3 (m, C$^{D1}$), 131.5 (C$^{C3}$), 131.1 (C$^{D4}$), 130.9 (C$^{D4'}$), 129.9 (t, $J$ = 4.7 Hz, C$^{D3'}$), 129.7 (t, $J$ = 4.7 Hz, C$^{D3}$), 128.6 (C$^{C5}$), 127.0 (C$^{A5}$), 126.3 (t, $J$ = 2.4 Hz, C$^{C4}$), 125.5 (C$^{B5}$), 123.8 (C$^{A3}$), 121.50 (dd, $J$ = 13.5 Hz, C$^{C2}$), 121.46 (C$^{B3}$), 41.2 (C$^{a}$), 37.0 (t, $J$ = 1.5 Hz, C$^{q}$), 33.8 (br, C$^{e}$), 30.9 (br, C$^{Me'}$), 28.8 (C$^{d}$), 28.5 (C$^{b}$), 25.7 (br, C$^{Me}$), 25.5 (C$^{c}$). $^{31}$P{$^1$H} NMR (202 Hz, acetone-$d_6$) $\delta$/ppm: −13.1 (broad, FWHM = 220 Hz), −144.2 (septet, $J_{PF}$ = 708 Hz, [PF$_6$]$^-$). ESI MS: $m/z$ 641.2 [Cu(Xantphos)]$^+$ (base peak, calc. 641.1), 911.3 [M − PF$_6$]$^+$ (calc. 911.3). UV-Vis ($CH_2Cl_2$, 2.5 × 10$^{-5}$ mol dm$^{-3}$): $\lambda$/nm ($\varepsilon$/dm$^3$ mol$^{-1}$ cm$^{-1}$) 248sh (31500), 285 (28000), 381 (3100). Found: C 60.88, H 5.06, N 2.45; $C_{55}H_{50}CuF_6N_2O_3P_3$ requires C 62.47, H 4.77, N 2.65%.

## *5.9.18 1-(9,9-Dimethylxanthen-2-yl)hexanone (**19**)*

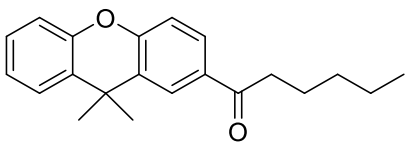

1-(9,9-Dimethylxanthen-2-yl)hexanone (**19**) was prepared according to literature procedure.[135] NMR date fit the literature and the crude material was used for the second Friedel-Crafts-acylation without further purification as was done in literature.

## *5.9.19 1-[7-(5-Bromo-1-oxopentyl)]-9,9-dimethylxanthen-2-yl)hexanone (**20**)*

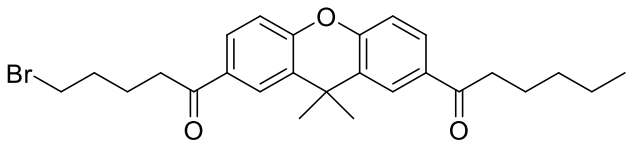


1-[7-(5-Bromo-1-oxopentyl)]-9,9-dimethylxanthen-2-yl)hexanone (**20**) was prepared by via an adapted literature procedure.[135] 1-(9,9-Dimethylxanthen-2-yl)hexanone (**19**, 10.2 g, 33.1 mmol, 1.0 eq.) was used as crude from the previous reaction was dissolved in $CH_2Cl_2$ (120 ml) and cooled to 0 °C. 5-Bromopentanoyl chloride (13.3 ml, 99.3 mmol, 3.0 eq.) was added. $AlCl_3$ (11.8 g, 116

mmol, 3.5 eq.) was added portion wise and the mixture turned greenish black while it was stirred overnight and let to warm to room temperature. The mixture was poured on ice, stirred for 2 h and extracted with $CH_2Cl_2$ (3 × 50 ml). The combined layers were washed with sat. $NaHCO_3$ (aq.) and the wash fraction was extracted once more with $CH_2Cl_2$. Combining all organic layer yielded a slurry mixture, that was treated with a large amount of $MgSO_4$ until the $CH_2Cl_2$ solution could be separated by decantation and filtration over a celite plug. Evaporation of the solvent yielded a yellow-brownish oil. Purification was attempted by crystallization from hexane or cyclohexane, but yielded only little product, due to phase separation of the mixture. The crude material was purified by column chromatography (Silica, toluene with 0 to 20 % $CH_2Cl_2$) followed by two crystallization steps from hexane and pentane to separate the gained white crystalline solid from residual yellow gum. The product was isolated as pale yellow crystalline solid (**20**, 6.53 g, 13.8 mmol, 42%). The $^1$H NMR date fit the literature.

### *5.9.20 1-[7-(5-Bromo-1-oxopentyl)]-9,9-dimethylxanthen-2-yl)hexanone bis((ethane-1,2-diyl)acetal (**21**)*

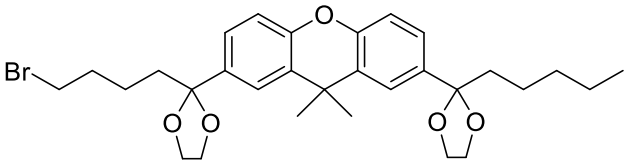

1-[7-(5-Bromo-1-oxopentyl)]-9,9-dimethylxanthen-2-yl)hexanone (**20**, 2.30 g, 4.88 mmol, 1.0 eq.) was dissolved in $CH_2Cl_2$ (20 ml) under inert conditions. Ethylene glycol (2.48 ml, 48.8 mmol, 10 eq.), ethyl orthoformate (1.62 ml, 9.76 mmol, 2.0 eq) and toluene-2-sulphuric acid monohydrate (15.0 µl, 0.15 eq.) were added and the mixture was stirred at room temperature overnight. Saturated $NaHCO_3$ (aq.) was added and the mixture was extracted with $CH_2Cl_2$ (3 × 40 ml), the combined organic layers were washed with brine (2 × 30 ml), dried over $MgSO_4$, filtered and the solvent was removed in vacuo. 1-[7-(5-Bromo-1-oxopentyl)]-9,9-dimethylxanthen-2-yl)hexanone bis((ethane-1,2-diyl)acetal was isolated as colourless oil (**21**, 2.62 g, 4.69 mmol, 96 %) without further purification. $^1$H NMR (500 MHz, $CDCl_3$) $\delta$/ppm: 7.48 (d, $J$ = 2.1 Hz, 2H), 7.27 – 7.24 (m, 2H), 7.00 (dd, $J$ = 8.4, 2.6 Hz, 2H), 4.05 – 3.99 (m, 4H), 3.80 – 3.75 (m, 4H), 3.36 (t, $J$ = 6.8 Hz, 2H), 1.95 – 1.80 (m, 6H), 1.63 (s, 6H), 1.55 – 1.47 (m, 2H), 1.38 – 1.30 (m, 2H), 1.31 – 1.20 (m, 4H), 0.84 (t, $J$ = 6.9 Hz, 3H). MALDI-TOF MS: 559.2 $[M+H]^+$ (calc. 559.2).

### *5.9.21 1-(7-[6-(2,2'-bipyridin-6-yl)-1-oxohexyl]-9,9-dimethylxanthen-2-yl)hexanone bis((ethane-1,2-diyl)acetal (**22**)*

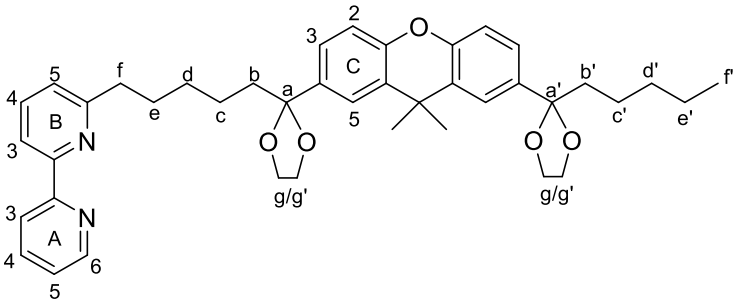

Compound **22** was prepared by an adapted literature procedure.[209] Diisopropylamine (0.79 ml, 5.62 mmol, 1.2 eq.) was dissolved in THF (15 ml) and cooled to −78 °C under inert conditions. *n*BuLi (2.25 ml, 2.5 M in hexane, 5.62 mmol, 1.2 eq.) was added dropwise and the mixture was stirred at −78 °C for 1 h. A solution of 6-Mebpy (**1**, 0.80 g, 4.67 mmol, 1.0 eq.) in THF (10 ml) was added dropwise and the solution turned dark blue while it was stirred at −78 °C for 80 min. A solution of 1-[7-(5-Bromo-1-

oxopentyl)]-9,9-dimethylxanthen-2-yl)hexanone bis((ethane-1,2-diyl)acetal (**21**, 2.62 g, 4.68 mmol, 1.0 eq.) in THF (15 ml) was added slowly and the mixture was stirred while warming to room temperature overnight. The colour changed from dark blue to orange. Sat. $NH_4Cl$ (aq.) and $NaHCO_3$ (aq.) were added to quench the reaction. The mixture was extracted with $CH_2Cl_2$ (3 × 40 ml), the combined organic layers were washed with brine (2 × 30 ml), dried over $MgSO_4$, filtered and the solvent was removed in vacuo. The crude material was filtered through basic Alox with hexane, then $CH_2Cl_2$ : Toluene 1 : 1 and purified by column chromatography (Silica C18, $H_2O$ + 1% formic acid : acetonitrile 5% to 90 %) to give 1-(7-[6-(2,2'-bipyridin-6-yl)-1-oxohexyl]-9,9-dimethylxanthen-2-yl)hexanone bis((ethane-1,2-diyl)acetal (**22**, 1.59 g, 2.45 mmol, 52%) as colourless oil. $^1$H NMR (500 MHz, Chlorodorm-*d*$_3$) $\delta$/ppm: 8.65 (ddd, *J* = 4.8, 1.8, 0.9 Hz, 1H, $H^{A6}$), 8.41 (dt, *J* = 8.0, 1.1 Hz, 1H, $H^{A3}$), 8.16 (dd, *J* = 7.9, 1.0 Hz, 1H, $H^{B3}$), 7.78 (td, *J* = 7.7, 1.8 Hz, 1H, $H^{A4}$), 7.68 (t, *J* = 7.7 Hz, 1H, $H^{B4}$), 7.48 (t, *J* = 2.4 Hz, 2H, $H^{C5}$), 7.29 – 7.24 (m, 3H, $H^{A5+C3}$), 7.11 (dd, *J* = 7.6, 1.0 Hz, 1H, $H^{B5}$), 6.99 (dd, *J* = 8.4, 2.0 Hz, 2H, $H^{C2}$), 4.03 – 3.99 (m, 4H, $H^{g/g'}$), 3.80 – 3.75 (m, 4H, $H^{g/g'}$), 2.81 (t, *J* = 7.7 Hz, 2H, $H^{f}$), 1.94 – 1.84 (m, 4H, $H^{b+b'}$), 1.77 (m, 2H, $H^{e}$), 1.62 (s, 6H, $H^{Me}$), 1.46 – 1.36 (m, 4H, $H^{c+d}$), 1.33 (m, 2H, $H^{c'}$), 1.29 – 1.21 (m, 4H, $H^{d'+e'}$), 0.84 (t, *J* = 6.9 Hz, 3H, $H^{f}$). $^{13}$C{$^1$H} NMR (126 MHz, $CDCl_3$) $\delta$/ppm: 161.9 ($C^{B6}$), 156.8 ($C^{A2}$), 155.6 ($C^{B2}$), 150.14 ($C^{C1/C1'}$), 150.10 ($C^{C1/C1'}$), 149.2 ($C^{A6}$), 137.5 ($C^{C4/C4'}$), 137.4 ($C^{C4/C4'}$), 137.1 ($C^{B4}$), 137.0 ($C^{A4}$), 129.71 ($C^{C6/C6'}$), 129.66 ($C^{C6/C6'}$), 125.1 ($C^{C3}$), 123.63 ($C^{C5/C5'}$), 123.62 ($C^{C5/C5'}$), 123.6 ($C^{A5}$), 122.8 ($C^{B5}$), 121.4 ($C^{A3}$), 118.3 ($C^{B3}$), 116.08 ($C^{C2/C2'}$), 116.1 ($C^{C2/C2'}$), 110.71 ($C^{a/a'}$), 110.65 ($C^{a/a'}$), 64.60 ($C^{g/g'}$), 64.59 ($C^{g/g'}$), 40.8 ($C^{b/b'}$), 40.7 ($C^{b/b'}$), 38.4 ($C^{f}$), 34.3 ($C^{Cq}$), 32.5 ($C^{Me}$), 32.0 ($C^{d'}$), 29.7 ($C^{e}$), 29.5 ($C^{d}$), 23.7 ($C^{c}$), 23.4 ($C^{c'}$), 22.7 ($C^{e'}$), 14.1 ($C^{f}$). HR-ESI MS: *m/z* 649.3641 $[M+H]^+$ (base peak, calc. 649.3636). Found: C 75.27, H 7.67, N 4.25; $C_{41}H_{48}N_2O_5$ requires C 75.88, H 7.48, N 4.32%.

### *5.9.22 2-(5-Bromopentyl)-7-hexyl-9,9-dimethylxanthene (**25**)*

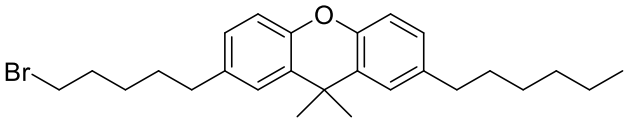


2-(5-Bromopentyl)-7-hexyl-9,9-dimethylxanthene was prepared by an adapted literature procedure.[135] 2-(hexan-1-on)-7-(5-bromopentan-1-on)-9,9-dimethyl xanthene (**20**, 2.33 g, 4.94 mmol, 1.0 eq.) was added to a stirring suspension of indium(III) chloride (109 mg, 0.49 mmol, 0.1 eq.) and chlorodimethylsilane (2.80 ml, 25.2 mmol, 5.1 eq.) in dry $CH_2Cl_2$ (20 ml) under inert conditions. The reaction was stirred at room temperature for 6 h. The reaction was quenched by the addition of water (20 ml) and the mixture was extracted with $CH_2Cl_2$ (3 × 30 ml). The combined organic layers were dried over $MgSO_4$, filtered and the solvent was removed in vacuo. The crude product was purified by column chromatography (silica cyclohexane : ethyl acetate 0 to 10 %). Some fractions still showed crude yellow impurities and were filtered through a silica plug with pure hexane to yield 2-(5-Bromopentyl)-7-hexyl-9,9-dimethylxanthene (**25**, 1.89 g, 4.26 mmol, 86%) as colourless oil. The $^1$H NMR spectrum differed slightly from the literature in the aliphatic region but could still confirm the presence of the desired product. $^1$H NMR (500 MHz, $CDCl_3$) $\delta$/ppm: 7.18 (m, 2H), 6.99 (ddd, *J* = 8.3, 3.2, 2.1 Hz, 2H), 6.94 (dd, *J* = 8.2, 2.7 Hz, 2H), 3.41 (t, *J* = 6.8 Hz, 2H), 2.59 (dt, *J* = 12.5, 7.8 Hz, 4H), 1.90 (dq, *J* = 9.3, 7.0 Hz, 2H), 1.70 – 1.57 (m, 10H), 1.53 – 1.45 (m, 2H), 1.39 – 1.28 (m, 6H), 0.89 (t, *J* = 6.9 Hz, 3H).

### *5.9.23 2-[6-(2,2'-Bipyridin-6-yl)hexyl]-7-hexyl-9,9-dimethylxanthene (**26**)*

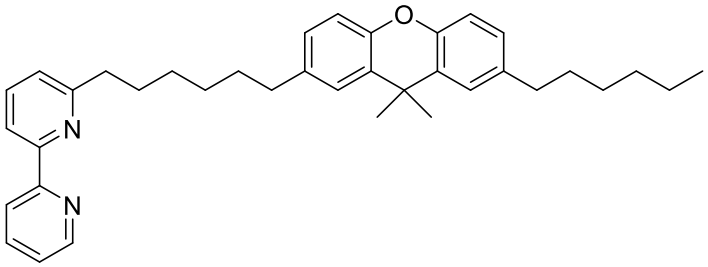

2-[6-(2,2'-Bipyridin-6-yl)hexyl]-7-hexyl-9,9-dimethylxanthene was prepared by an adapted literature procedure.[209] Diisopropylamine (0.70 ml, 5.00 mmol, 1.2 eq.) was dissolved in THF (10 ml) and cooled to −78 °C under inert conditions. *n*BuLi (2.00 ml, 2.5 M in hexane, 5.00 mmol, 1.2 eq.) was added dropwise and the mixture was stirred at −78 °C for 1 h. A solution of 6-Mebpy (**1**, 0.71 g, 4.17 mmol, 1.0 eq.) in THF (5 ml) was added dropwise and the solution turned dark blue while it was stirred at −78 °C for 90 min. A solution of 2-(5-Bromopentyl)-7-hexyl-9,9-dimethylxanthene (**25**, 1.85 g, 4.17 mmol, 1.0 eq.) in THF (5 ml) was added slowly and the mixture was stirred while warming to room temperature overnight. The colour changed from dark blue to orange. Sat. $NH_4Cl$ (aq.) and $NaHCO_3$ (aq.) were added to quench the reaction. The mixture was extracted with $CH_2Cl_2$ (3 × 30 ml), the combined organic layers were washed with brine (2 × 30 ml), dried over $MgSO_4$, filtered and the solvent was removed in vacuo. The crude material was purified by column chromatography (silica, cyclohexane : ethyl acetate 10 to 20 %) followed by filtration with cyclohexane through a plug of basic Alox. 2-[6-(2,2'-Bipyridin-6-yl)hexyl]-7-hexyl-9,9-dimethylxanthene (**26**, 1.61 g, 3.01 mmol, 72%) was isolated as yellow oil with minor impurities. $^1$H NMR (500 MHz, $CD_2Cl_2$) $\delta$/ppm: 8.63 (m, 1H), 8.45 (d, $J$ = 7.9 Hz, 1H), 8.20 (d, $J$ = 7.8 Hz, 1H), 7.79 (td, $J$ = 7.7, 1.8 Hz, 1H), 7.71 (t, $J$ = 7.7 Hz, 1H), 7.29 (ddd, $J$ = 7.5, 4.7, 1.2 Hz, 1H), 7.21 (d, $J$ = 2.1 Hz, 2H), 7.16 (dd, $J$ = 7.7, 1.0 Hz, 1H), 7.00 (dt, $J$ = 8.3, 2.3 Hz, 2H), 6.90 (dd, $J$ = 8.2, 2.3 Hz, 2H), 2.84 (t, $J$ = 7.6 Hz, 2H), 2.59 (td, $J$ = 7.8, 5.1 Hz, 4H), 1.81 (p, $J$ = 7.3 Hz, 2H), 1.66 – 1.56 (m, 10H), 1.46 – 1.39 (m, 8H), 1.33 (m, 7H), 0.92 – 0.86 (m, 3H). (Integration of aliphatic region indicates the presence of some impurities). ESI MS: *m/z* 533.3 $[M+H]^+$ (base peak, calc. 533.4).

### *5.9.24 2-[6-(2,2'-Bipyridin-6-yl)hexyl]-4,5-dibromo-7-hexyl-9,9-dimethylxanthene (**27**)*

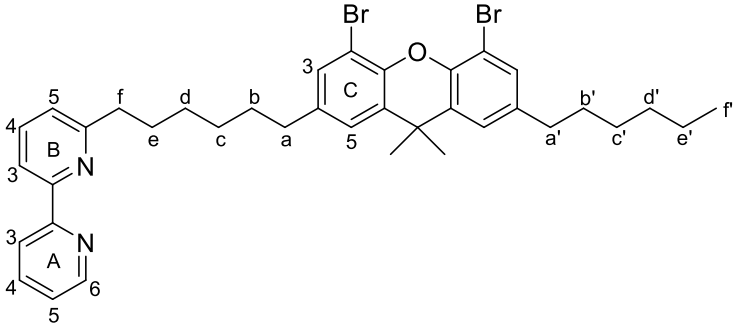

2-[6-(2,2'-Bipyridin-6-yl)hexyl]-7-hexyl-9,9-dimethylxanthene (**26**, 879 mg, 1.65 mmol, 1.0 eq.) was dissolved in 50 ml $CH_2Cl_2$ and the solution was cooled to 0 °C. Bromine (0.67 ml, 13.2 mmol, 8.0 eq.) and iron powder (15.2 mg, 2.15 mmol, 1.3 eq.) were added. The reaction vessel was covered in tinfoil to exclude light. The mixture was stirred overnight and allowed to warm to room temperature. An aqueous solution of sodium thiosulfate and sodium hydrogen carbonate was added to quench the reaction. The mixture was extracted with $CH_2Cl_2$ (2 × 30 ml), and the combined organic layers were washed with an aqueous solution of $H_4EDTA$ and sodium hydroxide to remove any metal impurities before being dried over $MgSO_4$, filtered and the solvent was removed in vacuo. The rust red crude material was

dissolved in $CH_2Cl_2$ and filtered through a plug of basic Alox. Evaporation of the solvent gave 2-(5-(-6-(2,2'-Bipyridine))hexyl)-4,5-dibromo-7-hexyl-9,9-dimethylxanthene (**27**, 1.08 g, 1.56 mmol, 95%) as brown oil. $^1$H NMR (500 MHz, $CD_2Cl_2$) $\delta$/ppm: 8.63 (ddd, $J$ = 4.7, 1.8, 0.9 Hz, 1H, $H^{A6}$), 8.44 (dt, $J$ = 8.1, 1.1 Hz, 1H, $H^{A3}$), 8.20 (dd, $J$ = 7.9, 0.5 Hz, 1H, $H^{B3}$), 7.80 (td, $J$ = 7.7, 1.8 Hz, 1H, $H^{A4}$), 7.71 (t, $J$ = 7.7 Hz, 1H, $H^{B4}$), 7.31 (s, 2H, $H^{C3}$), 7.29 (ddd, $J$ = 7.5, 4.8, 1.2 Hz, 1H, $H^{A5}$), 7.18 – 7.15 (ov. m, 3H, $H^{B5+C5}$), 2.84 (t, $J$ = 7.7 Hz, 2H, $H^{f}$), 2.61 – 2.55 (ov. m, 4H, , $H^{a+a'}$), 1.81 (p, $J$ = 7.5 Hz, 2H, $H^{e}$), 1.67 – 1.57 (ov. m, 4H, $H^{b+b'}$), 1.59 (s, 6H, $H^{Me}$), 1.48 – 1.39 (ov. m, 4H, $H^{c+d}$), 1.37 – 1.28 (ov. m, 6H, $H^{c'+d'+e'}$), 0.89 (m, 3H, $H^{f'}$). $^{13}$C{$^1$H} NMR (126 MHz, $CD_2Cl_2$) $\delta$/ppm: 162.4 ($C^{B6}$), 157.1 ($C^{A2}$), 155.9, ($C^{B2}$) 149.6 ($C^{A6}$), 145.90 ($C^{C1/C1'}$), 145.88 ($C^{C1/C1'}$), 139.8 ($C^{C4/C4'}$), 139.7 ($C^{C4/C4'}$), 137.5 ($C^{B4}$), 137.2 ($C^{A4}$), 132.13 ($C^{C6/C6'}$), 132.11 ($C^{C6/C6'}$), 131.5 ($C^{C3}$), 125.6 ($C^{C5}$), 124.0 ($C^{A5}$), 123.2 ($C^{B5}$), 121.4 ($C^{A3}$), 118.5 ($C^{B3}$), 110.69 ($C^{C2/C2'}$), 110.67 ($C^{C2/C2'}$), 38.8 ($C^{f}$), 35.9 ($C^{Cq}$), 35.74 ($C^{a/a'}$), 35.71 ($C^{a/a'}$), 32.22 ($C^{Me}$), 32.2 ($C^{d'}$), 32.0 ($C^{b/b'}$), 31.9 ($C^{b/b'}$), 30.1 ($C^{e}$), 29.7 ($C^{c/d}$), 29.6 ($C^{c/d}$), 29.4 ($C^{e'}$), 23.2 ($C^{c'}$), 14.4 ($C^{f'}$). ESI MS: *m/z* 691.2 $[M+H]^+$ (base peak, calc. 691.2), 713.1 $[M+Na]^+$ (base peak, calc. 713.2).

### *5.9.25 2-[6-(2,2'-bipyridin-6-yl)hexyl]-7-hexyl-9,9-dimethyl-9H-xanthene-4,5-diyl)bis(diphenylphosphane) (**28**)*

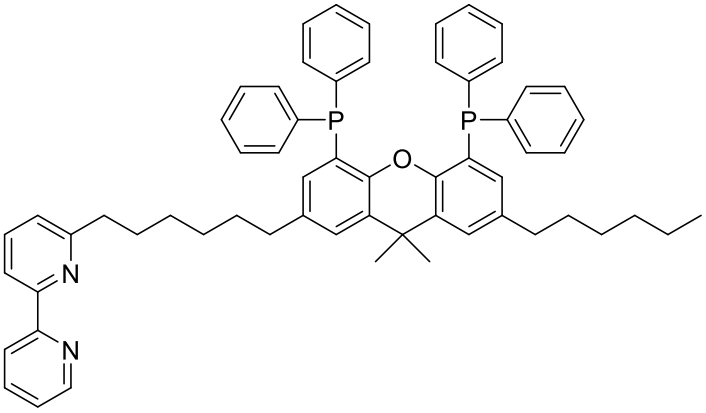


All solvents were dry (over molecular sieve) and degassed by bubbling argon through them. 2-[6-(2,2'-Bipyridin-6-yl)hexyl]-4,5-dibromo-7-hexyl-9,9-dimethylxanthene (**27**, 272 mg, 0.39 mmol, 10. eq.) was placed in a round bottom flask and dried by adding toluene and removing the solvent under vacuum on the Schlenk line 5 times. Dry THF (15 ml) was added and the solution was cooled to −78 °C. $^t$BuLi (0.48 ml, 1.7 M, 0.80 mmol, 2.1 eq.) was added dropwise and the mixture turned red while it was stirred for 1.5 h. A solution of chlorodipehnylphosphane (0.15 ml, 0.82 mmol, 2.1 eq.) in THF (3 ml) was added dropwise and the colour changed from red to orange, then pale yellow. After stirring for 10 min the solvent was removed under vacuo while the setup was still connected to the Schlenk line and in the cooling bath (acetone/dry ice) to maintain low temperatures. The crude material was dissolved in dry $CH_2Cl_2$ and split in two batches. The first batch was worked up as described in section 5.7.4. $^{31}$P{$^1$H} NMR and ESI MS indicated that the majority of the material was oxidised phosphane species. To the second batch a solution of $[Cu(MeCN)_4][PF_6]$ (88.1 mg, 0.236 mmol, 0.6 eq.) in degassed $CH_2Cl_2$ (5 ml) was added and the mixture was stirred for 2 h at room temperature. The solution was filtered under ambient atmosphere and the solvent was removed. $^{31}$P{$^1$H} NMR and ESI MS indicated the presence of a [Cu(N^N^P^P)][$PF_6$] complex. Purification attempts were not successful (see section 5.7.4). $^{31}$P{$^1$H} NMR (202 Hz, acetone-$d_6$) $\delta$/ppm: −19.1 (broad), 21.4, 33.0, −144.5 (septet, $J_{PF}$ = 711 Hz, $[PF_6]^-$). ESI MS: *m/z* 963.3 $[M+Cu]^+$ (calc. 963.4).

# Chapter 6: Conclusion and Outlook

In this thesis different systematic approaches were used to develop and investigate new heteroleptic copper(I) complexes for the application in light-emitting electrochemical cells. Building on the excellent pioneering work of Dr. Sarah Keller, the influence of different functional groups on the 2,2'-bipyridine ligand in [Cu(N^N)(P^P)][$PF_6$] complexes were investigated. It was shown that the 6-position of a 2,2'-bipyridine ligand can accommodate large aromatic groups and still form stable heteroleptic copper(I) complexes, when combined with DPEPhos or xantphos as the P^P ligand. In the case of a naphthalene functionalization, the complex showed photoluminescent properties in solid state and reversible redox behaviour. When incorporating larger aromatic substituents such as pyrene, the emissive properties are lost, most likely due to the quenching effect of a low-lying triplet excited state localized on the pyrene moiety on the $^3$MLCT state of the copper(I) complex. However, the asymmetric nature that these large substituents imposed on the complex revealed interesting structural properties. Two conformers were observable by variable temperature NMR spectroscopy for the complexes [Cu(1-Naphbpy)(xantphos)]$^+$ and [Cu(1-Pyrbpy)(xantphos)]$^+$. These conformers are interchangeable by inversion of the xanthene moiety in solution. It was observed that the coordination environment close to the copper centre can accommodate unexpectedly large substituents. However, the electronic nature of these groups needs to be taken into consideration, since large aromatic moieties can enable unwanted non-radiative relaxation pathways.

In a follow up study possibilities for optimization of methyl substitution pattern on the 2,2'-bipyridine ligand in [Cu(N^N)(P^P)][$PF_6$] complexes were investigated. Keller *et al.* had shown that methyl substitution in 6- and/or 6'-position of the bpy ligand in copper(I) complexes was beneficial for the luminescence properties as well as device performance. They found a general trend with [Cu(6,6'-$Me_2$bpy)(xantphos)][$PF_6$] containing LECs having a high peak brightness while [Cu(6-Mebpy)(xantphos)][$PF_6$] containing LECs giving decent device lifetimes.[84] Building on this knowledge, a new 5,6'-$Me_2$bpy ligand was designed to give a middle ground between 6-Mebpy and 6,6'-$Me_2$bpy in terms of steric demand. Copper(I) complexes incorporating this new 5,6'-$Me_2$bpy ligand show decent luminescence properties, that are similar to 6-Mebpy containing complexes. Methyl substitution in 5-position does not disturb the coordination geometry of the complex, but the improvement of the luminescent properties is less than expected, compared to 6-Mebpy containing complexes. Testing in LECs is needed to investigate if the additional substitution in 5-position of the 2,2'-bipyridine ligand has a beneficial effect on the device lifetime.

DFT calculations had previously shown that structural and electronic alteration of the N^N ligand affects the LUMO energy level of [Cu(N^N)(P^P)][$PF_6$] complexes. The HOMO is located mainly on the copper(I) centre with some contribution of the coordinated phosphorus atoms and their substituents. After different modifications and tuning approaches on the diimine ligand, optimization of the bisphosphane ligand in [Cu(N^N)(P^P)][$PF_6$] complexes was attempted. Three modified xantphos derivates were prepared. $^t$Bu$_2$xantphos was prepared with *tert*-butyl substituents on the xanthene backbone of the P^P ligand. These groups were introduced to increase the spatial distance of complexes in a LEC device and therefore decrease the chance of exciton quenching of

neighbouring molecules. Copper(I) complexes were prepared in combination with bpy, 6-Mebpy and 6,6'-$Me_2$bpy. To modify the steric demand of the P^P ligand, the molecules xantphos$Mes_4$ and xantphos$Mes_2$ were prepared, carrying mesityl substituents on the phosphorus atoms. $Mes_4$xantphos proved itself to be sterically too demanding to form heteroleptic copper(I) complexes with 2,2'-bipyridine ligands. Xantphos$Mes_2$ formed stable copper(I) complexes in combination with bpy and 6-Mebpy as N^N ligand. The combination of xantphos$Mes_2$ and 6,6'-$Me_2$bpy was sterically too demanding and did not form heteroleptic copper(I) complexes. Using these P^P ligands, five new complexes were prepared and investigated in terms of their structural, photophysical, electrochemical and LEC device properties. The new xantphos$Mes_2$ ligand carries two stereogenic centres on the phosphorus atoms with the *(rac)*-form being the dominant species. Therefore, the ligand is preorganized to give particular diastereoisomers upon complexation with copper(I). The asymmetric nature of 6-Mebpy and xantphos$Mes_2$ in [Cu(6-Mebpy)(xantphos$Mes_2$)][$PF_6$] reveals two dynamic motion events occurring in solution that are observable by NMR spectroscopy due to characteristic EXSY signals between two sets of D and E ring signals. These movements occur consecutively and are assigned to a xantphos bowl inversion, followed by a copper ring flip. All five complexes show an emission in the orange to yellow region in solid state and a red shifted emission in solution. A clear trend can be observed, where the introduction of one or two methyl groups in 6- and 6'-position of the N^N ligand leads to an increased PLQY, longer excited state lifetime and a blue shift in emission. The reason for these observations is a better stabilization of the tetrahedral geometry of the copper centre upon excitation and therefore a bigger HOMO-LUMO energy gap. This was also confirmed by cyclic voltammetry. All complexes of this series were tested in a LEC configuration. Complexes with high PLQY gave bright devices of up to 370 cd $m^{-2}$ but degraded quickly. Moderate electroluminescent devices showed a much longer lifetime. A trade-off of highly luminescent devices vs. long device lifetime is observed which is in agreement with the findings of Keller *et al.* for different copper(I) based complexes.[84] All devices showed yellow electroluminescence.

In the last chapter of this thesis one of the biggest challenges of copper-based light-emitting electrochemical cells was tackled - the poor device stability. Copper-LECs lack behind iridium based LECs in terms of device lifetime. Reasons and mechanisms of device degradation are not always obvious, but a major factor for the longevity of a LEC is the chemical and electrochemical stability of the emitting compound. Therefore, attempts to design a more stable copper(I) complex based on a tetradentate N^N^P^P ligand were made. Such a ligand was expected to decrease device decomposition and limit the chances of ligand exchange during device operation. Six generations of ligand designs are presented. The first three generations aimed to connect a 6,6'-bipyridine and a xantphos moiety by click chemistry, forming a triazole based linker. Benchmark complexes showed promising luminescent properties and therefore the target complex was thought to be suitable for LEC application. However, the synthesis of the tetradentate ligand turned out to be challenging, because of different functional groups interfering with the multi-step synthesis. After three generations of synthetic approaches it was decided to drop the triazole bridge concept because of its complexity and the synthetic challenges it brought with it. For the next approaches preparation of a tetradentate ligand with a chemically simpler structure and a robust $(CH_2)_n$ linkage between the N^N and P^P moieties was

attempted. The first approach of directly modifying xantphos to avoid a C–P bond formation reaction failed. During the fifth and sixth generational attempts synthetic strategies were developed to build up a modified xanthene scaffold that was functionalized with an N^N moiety followed by a C–P bond formation as the last step. This last reaction step proved itself to be especially challenging and purification of the target ligand was not successful. However, quenching of the last reaction with a copper(I) salt showed the desired complex observable by ESI MS.

Although isolation and characterization of the desired N^N^P^P ligand was not successful, MS analysis indicates that the preparation of such a ligand was a success. Further optimization of the synthetic preparation is needed. A possible approach would be to perform the C–P bond formation reaction before attachment of the N^N moiety. Although this route would lead over a tribromo species, which could make the C–P bond formation reaction more challenging, literature suggests that this approach could be successful. Newer strategies should also aim towards easier purification methods of the intermediates and product. One possible approach towards this would be to use shorter chain substituents where possible to enable easier crystallization of the molecules. After the successful preparation of a $[Cu(N^N^P^P)]^+$ complex, it is suggest to attempt the preparation of a fully caging ligand with two connections between the N^N and P^P moieties. This would not only prevent the possible formation of multi- or polymeric coordination structures but is also expected to largely increase the complex stability. However, careful tuning of the coordination sphere and structural flexibility is needed, and the luminescent properties of the $[Cu(N^N)(P^P)]^+$ core must always be taken into account.

Copper-based light-emitting devices have the potential to play a crucial role in the display industry as well as for large area low-tech applications. The relatively high abundance of copper as a resource material is a key advantage of this technology. However, there are still many parameters to be optimized, before these devices are ready to be commercially available. One of the most important characteristics that needs to be improved is the device lifetime. Careful optimization of the chemical properties along with device fabrication and architecture has the potential to give copper based LEC the needed longevity so they can contribute to a sustainable, more energy efficient future.

# Chapter 7: References


1 W. Bruker Analytical X-ray Systems, Inc., 2006, APEX2, version 2 User Manual, M86-E01078, Madison.

2 P. W. Betteridge, J. R. Carruthers, R. I. Cooper, K. Prout and D. J. Watkin, *J. Appl. Crystallogr.*, 2003, **36**, 1487–1487.

3 I. J. Bruno, J. C. Cole, P. R. Edgington, M. Kessler, C. F. Macrae, P. McCabe, J. Pearson and R. Taylor, *Acta Crystallogr. Sect. B Struct. Sci.*, 2002, **58**, 389–397.

4 C. F. Macrae, I. J. Bruno, J. A. Chisholm, P. R. Edgington, P. McCabe, E. Pidcock, L. Rodriguez-Monge, R. Taylor, J. van de Streek and P. A. Wood, *J. Appl. Crystallogr.*, 2008, **41**, 466–470.

5 M. J. Frisch, G. W. Trucks, H. B. Schlegel, G. E. Scuseria, M. A. Robb, J. R. Cheeseman, G. Scalmani, V. Barone, G. A. Petersson, H. Nakatsuji, X. Li, M. Caricato, A. V Marenich, J. Bloino, B. G. Janesko, R. Gomperts, B. Mennucci, H. P. Hratchian, J. V Ortiz, A. F. Izmaylov, J. L. Sonnenberg, D. Williams-Young, F. Ding, F. Lipparini, F. Egidi, J. Goings, B. Peng, A. Petrone, T. Henderson, D. Ranasinghe, V. G. Zakrzewski, J. Gao, N. Rega, G. Zheng, W. Liang, M. Hada, M. Ehara, K. Toyota, R. Fukuda, J. Hasegawa, M. Ishida, T. Nakajima, Y. Honda, O. Kitao, H. Nakai, T. Vreven, K. Throssell, J. A. Montgomery Jr., J. E. Peralta, F. Ogliaro, M. J. Bearpark, J. J. Heyd, E. N. Brothers, K. N. Kudin, V. N. Staroverov, T. A. Keith, R. Kobayashi, J. Normand, K. Raghavachari, A. P. Rendell, J. C. Burant, S. S. Iyengar, J. Tomasi, M. Cossi, J. M. Millam, M. Klene, C. Adamo, R. Cammi, J. W. Ochterski, R. L. Martin, K. Morokuma, O. Farkas, J. B. Foresman and D. J. Fox, *Gaussian 16, Revision A. 03, GaussianInc., Wallingford CT*, 2016.

6 C. Lee, W. Yang and R. G. Parr, *Phys. Rev. A*, 1988, **38**, 3098.

7 A. D. Becke, *J. Chem. Phys.*, 1993, **98**, 5648.

8 F. Weigend and R. Ahlrichs, *Phys. Chem. Chem. Phys.*, 2005, **7**, 3297–3305.

9 F. Weigend, *Phys. Chem. Chem. Phys.*, 2006, **8**, 1057–1065.

10 S. Grimme, J. Anthony, S. Ehrlich and H. Krieg, *J. Chem. Phys.*, 2010, **132**, 154104.

11 S. Grimme, S. Ehrlich and L. Goerigk, *J. Comput. Chem.*, 2011, **32**, 1456–1465.

12 M. Petersilka, U. J. Gossmann and E. K. U. Gross, *Phys. Rev. Lett.*, 1996, **76**, 1212–1215.

13 C. Jamorski, M. E. Casida and D. R. Salahub, *J. Chem. Phys.*, 1996, **104**, 5134–5147.

14 M. E. Casida, C. Jamorski, K. C. Casida and D. R. Salahub, *J. Chem. Phys.*, 1998, **108**, 4439–4449.

15 J. Tomasi and M. Persico, *Chem. Rev.*, 1994, **94**, 2027–2094.

16 J. Tomasi, B. Mennucci and R. Cammi, *Chem. Rev.*, 2005, **105**, 2999–3094.

17 O. Tapia, J. Bertrán and J. B. Bertrán, *Solvent effects and chemical reactivity*, Springer, 1996, vol. 17.

18 https://www.iea.org/statistics/, (20.11.2019).

19 https://www.iea.org/newsroom/news/2019/may/renewable-capacity-growth-worldwide-stalled-in-2018-after-two-decades-of-strong-e.html, (21.11.2019).

20 https://www.theguardian.com/technology/2019/apr/09/amazon-accused-of-abandoning-100-per-cent-renewable-energy-goal, (21.11.2019).

21 https://www.spiegel.de/international/germany/german-failure-on-the-road-to-a-renewable-future-a-1266586.html, (21.11.2019).

22 A. Kemmler, T. Spillmann, A. Piégsa, B. Notter, B. Cox, M. Jakob and G. Catenazzi, *Analyse des schweizerischen Energieverbrauchs 2000 - 2018 nach Verwendungszwecken*, Bundesamt für Energie, Bern, 2019.

23 A. Kirchner, P. Hofer, A. Kemmler, M. Keller, B. Aebischer, M. Jakob, G. Catenazzi and W. Baumgartner, *Analyse des schweizerischen Energieverbrauchs 2000 - 2006 nach Verwendungszwecken*, Bundesamt für Energie, Bern, 2008.
24 D. DiLaura, *Opt. Photonics News*, 2008, **19**, 22–28.
25 https://www.livescience.com/43424-who-invented-the-light-bulb.html, (20.11.2019).
26 C. J. Humphreys, *MRS Bull.*, 2008, **33**, 459–470.
27 https://www.brighthubengineering.com/consumer-appliances-electronics/70833-how-a-light-bulb-works/, (21.11.2019).
28 I. L. Azevedo, M. G. Morgan and F. Morgan, *Proc. IEEE*, 2009, **97**, 481–510.
29 N. Holonyak and S. F. Bevacqua, *Appl. Phys. Lett.*, 1962, **1**, 82–83.
30 A. Bergh, G. Craford, A. Duggal and R. Haitz, *Phys. Today*, 2001, **54**, 42–47.
31 R. D. Costa, E. Ortí, H. J. Bolink, F. Monti, G. Accorsi and N. Armaroli, *Angew. Chemie Int. Ed.*, 2012, **51**, 8178–8211.
32 M. Manikandan, D. Nirmal, J. Ajayan, P. Mohankumar, P. Prajoon and L. Arivazhagan, *Superlattices Microstruct.*, 2019, **136**, 106294.
33 S. Pimputkar, J. S. Speck, S. P. DenBaars and S. Nakamura, *Nat. Photonics*, 2009, **3**, 180–182.
34 https://www.fcgov.com/utilities/img/site_specific/uploads/led-efficiency.pdf, (26.11.2019).
35 C. W. Tang and S. A. VanSlyke, *Appl. Phys. Lett.*, 1987, **51**, 913–915.
36 J. H. Burroughes, D. D. C. Bradley, A. R. Brown, R. N. Marks, K. Mackay, R. H. Friend, P. L. Burns and A. B. Holmes, *Nature*, 1990, **347**, 539–541.
37 https://www.digitaltrends.com/home-theater/oled-vs-led/, (02.12.2019).
38 https://newatlas.com/lg-flexible-oled-tv/30332/, (27.11.2019).
39 https://www.oled-info.com/rollable-oleds, (27.11.2019).
40 https://www.theverge.com/2019/1/8/18174278/royole-flexpai-foldable-phone-android-ces-2019, (27.11.2019).
41 S. Ashok Kumar, J. S. Shankar, B. K Periyasamy and S. K. Nayak, *Polym. Technol. Mater.*, 2019, **58**, 1597–1624.
42 S. Reineke, M. Thomschke, B. Lüssem and K. Leo, *Rev. Mod. Phys.*, 2013, **85**, 1245–1293.
43 M. Sarma and K. T. Wong, *Chem. Rec.*, 2019, **19**, 1667–1692.
44 M. Y. Wong and E. Zysman-Colman, *Adv. Mater.*, 2017, **29**, 1605444.
45 Z. Li, W. Li, C. Keum, E. Archer, B. Zhao, A. M. Z. Slawin, W. Huang, M. C. Gather, I. D. W. Samuel and E. Zysman-Colman, *J. Phys. Chem. C*, 2019, **123**, 24772–24785.
46 A. Salehi, X. Fu, D. Shin and F. So, *Adv. Funct. Mater.*, 2019, **29**, 1808803.
47 Y.-F. Liu, J. Feng, Y.-G. Bi, D. Yin and H.-B. Sun, *Adv. Mater. Technol.*, 2019, **4**, 1800371.
48 D. Luo, Q. Chen, B. Liu and Y. Qiu, *Polymers*, 2019, **11**, 384.
49 E. Fresta and R. D. Costa, *J. Mater. Chem. C*, 2017, **5**, 5643–5675.
50 D. Volz, M. Wallesch, C. Fléchon, M. Danz, A. Verma, J. M. Navarro, D. M. Zink, S. Bräse and T. Baumann, *Green Chem.*, 2015, **17**, 1988–2011.
51 Q. Pei, G. Yu, C. Zhang, Y. Yang and A. J. Heeger, *Science*, 1995, **269**, 1086–1088.
52 K. M. Maness, R. H. Terrill, T. J. Meyer, R. W. Murray and R. M. Wightman, *J. Am. Chem. Soc.*, 1996, **118**, 10609–10616.
53 J. -K. Lee, D. S. Yoo, E. S. Handy and M. F. Rubner, *Appl. Phys. Lett.*, 1996, **69**, 1686–1688.
54 D. Tordera, S. Meier, M. Lenes, R. D. Costa, E. Ortí, W. Sarfert and H. J. Bolink, *Adv. Mater.*, 2012, **24**, 897–900.
55 S. van Reenen and M. Kemerink, in *Light-Emitting Electrochemical Cells*, Springer

International Publishing, Cham, 2017, pp. 3–45.
56 Z. Zhang, K. Guo, Y. Li, X. Li, G. Guan, H. Li, Y. Luo, F. Zhao, Q. Zhang, B. Wei, Q. Pei and H. Peng, *Nat. Photonics*, 2015, **9**, 233–238.
57 J. Wu, F. Li, Q. Zeng, C. Nie, P. C. Ooi, T. Guo, G. Shan and Z. Su, *Org. Electron.*, 2016, **28**, 314–318.
58 T. Lanz, A. Sandström, S. Tang, P. Chabrecek, U. Sonderegger and L. Edman, *Flex. Print. Electron.*, 2016, **1**, 025004.
59 A. Sandström, A. Asadpoordarvish, J. Enevold and L. Edman, *Adv. Mater.*, 2014, **26**, 4975–4980.
60 A. Asadpoordarvish, A. Sandström, C. Larsen, R. Bollström, M. Toivakka, R. Österbacka and L. Edman, *Adv. Funct. Mater.*, 2015, **25**, 3238–3245.
61 A. Sandström, H. F. Dam, F. C. Krebs and L. Edman, *Nat. Commun.*, 2012, **3**, 1002.
62 K. Sato, S. Uchida, S. Toriyama, S. Nishimura, K. Oyaizu, H. Nishide and Y. Nishikitani, *Adv. Mater. Technol.*, 2017, **2**, 1600293.
63 A. Sandström and L. Edman, *Energy Technol.*, 2015, **3**, 329–339.
64 Q. Pei, Y. Yang, G. Yu, C. Zhang and A. J. Heeger, *J. Am. Chem. Soc.*, 1996, **118**, 3922–3929.
65 J. C. deMello, N. Tessler, S. C. Graham and R. H. Friend, *Phys. Rev. B*, 1998, **57**, 12951–12963.
66 J. C. deMello, *Phys. Rev. B*, 2002, **66**, 235210.
67 J. C. deMello, J. J. M. Halls, S. C. Graham, N. Tessler and R. H. Friend, *Phys. Rev. Lett.*, 2000, **85**, 421–424.
68 T. J. Mills and M. C. Lonergan, *Phys. Rev. B*, 2012, **85**, 035203.
69 J. Gao and J. Dane, *Appl. Phys. Lett.*, 2004, **84**, 2778–2780.
70 F. Miomandre and P. Audebert, *Luminescence in Electrochemistry*, Springer International Publishing, Cham, 2017.
71 K.-Y. Lin, L. D. Bastatas, K. J. Suhr, M. D. Moore, B. J. Holliday, M. Minary-Jolandan and J. D. Slinker, *ACS Appl. Mater. Interfaces*, 2016, **8**, 16776–16782.
72 L. D. Bastatas, K. Y. Lin, M. D. Moore, K. J. Suhr, M. H. Bowler, Y. Shen, B. J. Holliday and J. D. Slinker, *Langmuir*, 2016, **32**, 9468–9474.
73 P.-C. Huang, G. Krucaite, H.-C. Su and S. Grigalevicius, *Phys. Chem. Chem. Phys.*, 2015, **17**, 17253–17259.
74 E. Bandiello, M. Sessolo and H. J. Bolink, *J. Mater. Chem. C*, 2016, **4**, 10781–10785.
75 G. Hernandez-Sosa, R. Eckstein, S. Tekoglu, T. Becker, F. Mathies, U. Lemmer and N. Mechau, *Org. Electron. physics, Mater. Appl.*, 2013, **14**, 2223–2227.
76 J. H. Shin, P. Matyba, N. D. Robinson and L. Edman, *Electrochim. Acta*, 2007, **52**, 6456–6462.
77 J. Xu, A. Sandström, E. M. Lindh, W. Yang, S. Tang and L. Edman, *ACS Appl. Mater. Interfaces*, 2018, **10**, 33380–33389.
78 D. Berner, M. Schaer, W. Leo, F. Nüesch and L. Zuppiroli, *Adv. Funct. Mater.*, 2005, **11**, 116–121.
79 W. Zhao, C.-Y. Liu, Q. Wang, J. M. White and A. J. Bard, *Chem. Mater.*, 2005, **17**, 6403–6406.
80 S. Chung, J.-H. Lee, J. Jeong, J.-J. Kim and Y. Hong, *Appl. Phys. Lett.*, 2009, **94**, 253302.
81 J. Mindemark, S. Tang, J. Wang, N. Kaihovirta, D. Brandell and L. Edman, *Chem. Mater.*, 2016, **28**, 2618–2623.
82 J. Mindemark and L. Edman, *J. Mater. Chem. C*, 2016, **4**, 420–432.
83 S. Keller, F. Brunner, J. M. Junquera-Hernández, A. Pertegás, M.-G. La-Placa, A. Prescimone, E. C. Constable, H. J. Bolink, E. Ortí and C. E. Housecroft, *ChemPlusChem*, 2018, **83**, 217–229.

84 S. Keller, A. Pertegás, G. Longo, L. Martínez, J. Cerdá, J. M. Junquera-Hernández, A. Prescimone, E. C. Constable, C. E. Housecroft, E. Ortí and H. J. Bolink, *J. Mater. Chem. C*, 2016, **4**, 3857–3871.

85 R. D. Costa, D. Tordera, E. Ortí, H. J. Bolink, J. Schönle, S. Graber, C. E. Housecroft, E. C. Constable and J. a. Zampese, *J. Mater. Chem.*, 2011, **21**, 16108.

86 E. Fresta, M. D. Weber, J. Fernandez-Cestau and R. D. Costa, *Adv. Opt. Mater.*, 2019, **7**, 1900830.

87 C.-T. Liao, H.-F. Chen, H.-C. Su and K.-T. Wong, *J. Mater. Chem.*, 2011, **21**, 17855–17862.

88 C. E. Housecroft and E. C. Constable, in *Light-Emitting Electrochemical Cells*, Springer International Publishing, Cham, 2017, pp. 167–202.

89 J. Wang, S. Tang, A. Sandström and L. Edman, *ACS Appl. Mater. Interfaces*, 2015, **7**, 2784–2789.

90 S. Tang, H. A. Buchholz and L. Edman, *ACS Appl. Mater. Interfaces*, 2015, **7**, 25955–25960.

91 S. Tang, J. Pan, H. a. Buchholz and L. Edman, *J. Am. Chem. Soc.*, 2013, **135**, 3647–3652.

92 M.-L. Wu, G.-Y. Chen, T.-A. Shih, C.-W. Lu and H.-C. Su, *Phys. Chem. Chem. Phys.*, 2018, **20**, 18226–18232.

93 C.-C. Shih, C.-W. Huang, M. Gao, C.-C. Chueh and W.-C. Chen, *J. Mater. Chem. C*, 2017, **5**, 11421–11428.

94 S. Sprouse, K. A. King, P. J. Spellane and R. J. Watts, *J. Am. Chem. Soc.*, 1984, **106**, 6647–6653.

95 A. M. Bünzli, H. J. Bolink, E. C. Constable, C. E. Housecroft, J. M. Junquera-Hernández, M. Neuburger, E. Ortí, A. Pertegás, J. J. Serrano-Pérez, D. Tordera and J. A. Zampese, *Dalton Trans.*, 2014, **43**, 738–750.

96 D. Tordera, A. M. Bünzli, A. Pertegás, J. M. Junquera-Hernández, E. C. Constable, J. A. Zampese, C. E. Housecroft, E. Ortí and H. J. Bolink, *Chem. Eur. J.*, 2013, **19**, 8597–8609.

97 B. Schmid, F. O. Garces and R. J. Watts, *Inorg. Chem.*, 1994, **33**, 9–14.

98 A. M. Bünzli, E. C. Constable, C. E. Housecroft, A. Prescimone, J. A. Zampese, G. Longo, L. Gil-Escrig, A. Pertegás, E. Ortí and H. J. Bolink, *Chem. Sci.*, 2015, **6**, 2843–2852.

99 G. E. Schneider, H. J. Bolink, E. C. Constable, C. D. Ertl, C. E. Housecroft, A. Pertegàs, J. A. Zampese, A. Kanitz, F. Kessler and S. B. Meier, *Dalton Trans.*, 2014, **43**, 1961–1964.

100 R. D. Costa, E. Ortí-, H. J. Bolink, S. Graber, S. Schaffner, M. Neuburger, C. E. Housecroft and E. C. Constable, *Adv. Funct. Mater.*, 2009, **19**, 3456–3463.

101 M. K. Nazeeruddin, R. T. Wegh, Z. Zhou, C. Klein, Q. Wang, F. De Angelis, S. Fantacci and M. Grätzel, *Inorg. Chem.*, 2006, **45**, 9245–9250.

102 D. Tordera, J. J. Serrano-Pérez, A. Pertegás, E. Ortí, H. J. Bolink, E. Baranoff, M. K. Nazeeruddin and J. Frey, *Chem. Mater.*, 2013, **25**, 3391–3397.

103 H. J. Bolink, E. Coronado, R. D. Costa, N. Lardiés and E. Ortí, *Inorg. Chem.*, 2008, **47**, 9149–9151.

104 C. D. Ertl, L. Gil-Escrig, J. Cerdá, A. Pertegás, H. J. Bolink, J. M. Junquera-Hernández, A. Prescimone, M. Neuburger, E. C. Constable, E. Ortí and C. E. Housecroft, *Dalton Trans.*, 2016, **45**, 11668–11681.

105 L. He, L. Duan, J. Qiao, R. Wang, P. Wei, L. Wang and Y. Qiu, *Adv. Funct. Mater.*, 2008, **18**, 2123–2131.

106 C. D. Sunesh, K. Shanmugasundaram, M. S. Subeesh, R. K. Chitumalla, J. Jang and Y. Choe, *ACS Appl. Mater. Interfaces*, 2015, **7**, 7741–7751.

107 Y. You, C.-G. An, J.-J. Kim and S. Y. Park, *J. Org. Chem.*, 2007, **72**, 6241–6246.
108 J. L. Rodríguez-Redondo, R. D. Costa, E. Ortí, A. Sastre-Santos, H. J. Bolink and F. Fernández-Lázaro, *Dalton Trans.*, 2009, 9787–9793.
109 B. Jiang, Y. Gu, J. Qin, X. Ning, S. Gong, G. Xie and C. Yang, *J. Mater. Chem. C*, 2016, **4**, 3492–3498.
110 A. B. Tamayo, S. Garon, T. Sajoto, P. I. Djurovich, I. M. Tsyba, R. Bau and M. E. Thompson, *Inorg. Chem.*, 2005, **44**, 8723–8732.
111 S. Graber, K. Doyle, M. Neuburger, C. E. Housecroft, E. C. Constable, R. D. Costa, E. Ortí, D. Repetto and H. J. Bolink, *J. Am. Chem. Soc.*, 2008, **130**, 14944–14945.
112 H. J. Bolink, E. Coronado, R. D. Costa, E. Ortí, M. Sessolo, S. Graber, K. Doyle, M. Neuburger, C. E. Housecroft and E. C. Constable, *Adv. Mater.*, 2008, **20**, 3910–3913.
113 L. D. Bastatas and J. D. Slinker, in *Light-Emitting Electrochemical Cells*, Springer International Publishing, Cham, 2017, pp. 93–119.
114 https://cen.acs.org/articles/94/i28/rise-OLED-displays.html, (08.12.2019).
115 https://www.it-markt.ch/news/2019-02-17/forscher-will-produktion-von-oled-displays-deutlich-billiger-machen, (08.12.2019).
116 https://www.livescience.com/39143-iridium.html, (08.12.2019).
117 http://www.infomine.com/investment/metal-prices/iridium/1-year/, (08.12.2019).
118 https://periodictable.com/Elements/029/data.html, (10.12.2019).
119 http://www.infomine.com/investment/metal-prices/copper/6-month/, (10.12.2019).
120 C. E. Housecroft and A. G. Sharpe, *Anorganische Chemie*, Pearson Studium, Munic, 2006.
121 D. R. McMillin, M. T. Buckner and B. T. Ahn, *Inorg. Chem.*, 1977, **16**, 943–945.
122 M. W. Blaskie and D. R. McMillin, *Inorg. Chem.*, 1980, **19**, 3519–3522.
123 R. E. Gamache, R. A. Rader and D. R. McMillin, *J. Am. Chem. Soc.*, 1985, **107**, 1141–1146.
124 M. T. Buckner and D. R. McMillin, *J. Chem. Soc. Chem. Commun.*, 1978, 759–761.
125 R. A. Rader, D. R. McMillin, M. T. Buckner, T. G. Matthews, D. J. Casadonte, R. K. Lengel, S. B. Whittaker, L. M. Darmon and F. E. Lytle, *J. Am. Chem. Soc.*, 1981, **103**, 5906–5912.
126 D. G. Cuttell, S. Kuang, P. E. Fanwick, D. R. McMillin and R. A. Walton, *J. Am. Chem. Soc.*, 2002, **124**, 6–7.
127 S. Keller, A. Prescimone, H. Bolink, M. Sessolo, G. Longo, L. Martínez-Sarti, J. M. Junquera-Hernández, E. C. Constable, E. Ortí and C. E. Housecroft, *Dalton Trans.*, 2018, **47**, 14263–14276.
128 F. Brunner, L. Martínez-Sarti, S. Keller, A. Pertegás, A. Prescimone, E. C. Constable, H. J. Bolink and C. E. Housecroft, *Dalton Trans.*, 2016, **45**, 15180–15192.
129 S. Keller, E. C. Constable, C. E. Housecroft, M. Neuburger, A. Prescimone, G. Longo, A. Pertegás, M. Sessolo and H. J. Bolink, *Dalton Trans.*, 2014, **43**, 16593–16596.
130 M. Elie, S. Gaillard and J.-L. Renaud, in *Light-Emitting Electrochemical Cells*, Springer International Publishing, Cham, 2017, pp. 287–327.
131 P. C. J. Kamer, P. W. N. M. van Leeuwen and J. N. H. Reek, *Acc. Chem. Res.*, 2001, **34**, 895–904.
132 E. Leoni, J. Mohanraj, M. Holler, M. Mohankumar, I. Nierengarten, F. Monti, A. Sournia-Saquet, B. Delavaux-Nicot, J.-F. Nierengarten and N. Armaroli, *Inorg. Chem.*, 2018, **57**, 15537–15549.
133 S.-P. Luo, E. Mejía, A. Friedrich, A. Pazidis, H. Junge, A.-E. Surkus, R. Jackstell, S. Denurra, S. Gladiali, S. Lochbrunner and M. Beller, *Angew. Chemie Int. Ed.*, 2013, **52**,

419–423.
134 E. Zuidema, P. Elsbeth Goudriaan, B. H. G. Swennenhuis, P. C. J. Kamer, P. W. N. M. van Leeuwen, M. Lutz and A. L. Spek, *Organometallics*, 2010, **29**, 1210–1221.
135 R. P. J. Bronger, J. P. Bermon, J. N. H. Reek, P. C. J. Kamer, P. W. N. M. van Leeuwen, D. N. Carter, P. Licence and M. Poliakoff, *J. Mol. Catal. A Chem.*, 2004, **224**, 145–152.
136 C. L. Linfoot, M. J. Leitl, P. Richardson, A. F. Rausch, O. Chepelin, F. J. White, H. Yersin and N. Robertson, *Inorg. Chem.*, 2014, **53**, 10854–10861.
137 R. Czerwieniec, M. J. Leitl, H. H. H. Homeier and H. Yersin, *Coord. Chem. Rev.*, 2016, **325**, 2–28.
138 M. Z. Shafikov, A. F. Suleymanova, R. Czerwieniec and H. Yersin, *Chem. Mater.*, 2017, **29**, 1708–1715.
139 R. Czerwieniec and H. Yersin, *Inorg. Chem.*, 2015, **54**, 4322–4327.
140 A. Kaeser, O. Moudam, G. Accorsi, I. Séguy, J. Navarro, A. Belbakra, C. Duhayon, N. Armaroli, B. Delavaux-Nicot and J. F. Nierengarten, *Eur. J. Inorg. Chem.*, 2014, 1345–1355.
141 J. Yuasa, M. Dan and T. Kawai, *Dalton Trans.*, 2013, **42**, 16096–16101.
142 M. Mohankumar, F. Monti, M. Holler, F. Niess, B. Delavaux-Nicot, N. Armaroli, J.-P. Sauvage and J.-F. Nierengarten, *Chem. Eur. J.*, 2014, **20**, 12083–12090.
143 M. Mohankumar, M. Holler, M. Schmitt, J. Sauvage and J. Nierengarten, *Chem. Commun.*, 2013, **49**, 1261–1263.
144 M.-A. Schmid, M. Rentschler, W. Frey, S. Tschierlei and M. Karnahl, *Inorganics*, 2018, **6**, 134.
145 E. Mejía, S.-P. Luo, M. Karnahl, A. Friedrich, S. Tschierlei, A.-E. Surkus, H. Junge, S. Gladiali, S. Lochbrunner and M. Beller, *Chem. Eur. J.*, 2013, **19**, 15972–15978.
146 M. Heberle, S. Tschierlei, N. Rockstroh, M. Ringenberg, W. Frey, H. Junge, M. Beller, S. Lochbrunner and M. Karnahl, *Chem. Eur. J.*, 2017, **23**, 312–319.
147 R. Giereth, I. Reim, W. Frey, H. Junge, S. Tschierlei and M. Karnahl, *Sustainable Energy Fuels*, 2019, **3**, 692–700.
148 A. Rosas-Hernández, C. Steinlechner, H. Junge and M. Beller, *Green Chem.*, 2017, **19**, 2356–2360.
149 X. Zhang, M. Cibian, A. Call, K. Yamauchi and K. Sakai, *ACS Catal.*, 2019, **9**, 11263–11273.
150 M. Claros, A. Casitas and J. Lloret-Fillol, *Synlett*, 2019, **30**, 1496–1507.
151 M. Claros, F. Ungeheuer, F. Franco, V. Martin-Diaconescu, A. Casitas and J. Lloret-Fillol, *Angew. Chemie Int. Ed.*, 2019, **58**, 4869–4874.
152 Y.-M. Wang, F. Teng, Y.-B. Hou, Z. Xu, Y.-S. Wang and W.-F. Fu, *Appl. Phys. Lett.*, 2005, **87**, 233512.
153 N. Armaroli, G. Accorsi, M. Holler, O. Moudam, J.-F. Nierengarten, Z. Zhou, R. T. Wegh and R. Welter, *Adv. Mater.*, 2006, **18**, 1313–1316.
154 M. D. Weber, M. Viciano-Chumillas, D. Armentano, J. Cano and R. D. Costa, *Dalton Trans.*, 2017, **46**, 6312–6323.
155 M. D. Weber, C. Garino, G. Volpi, E. Casamassa, M. Milanesio, C. Barolo and R. D. Costa, *Dalton Trans.*, 2016, **45**, 8984–8993.
156 M. Elie, F. Sguerra, F. Di Meo, M. D. Weber, R. Marion, A. Grimault, J.-F. Lohier, A. Stallivieri, A. Brosseau, R. B. Pansu, J.-L. Renaud, M. Linares, M. Hamel, R. D. Costa and S. Gaillard, *ACS Appl. Mater. Interfaces*, 2016, **8**, 14678–14691.
157 M. Elie, M. D. Weber, F. Di Meo, F. Sguerra, J.-F. Lohier, R. B. Pansu, J.-L. Renaud, M. Hamel, M. Linares, R. D. Costa and S. Gaillard, *Chem. Eur. J.*, 2017, **23**, 16328–16337.
158 M. D. Weber, E. Fresta, M. Elie, M. E. Miehlich, J.-L. Renaud, K. Meyer, S. Gaillard and R. D. Costa, *Adv. Funct. Mater.*, 2018, **28**, 1707423.

159 F. Brunner, S. Graber, Y. Baumgartner, D. Häussinger, A. Prescimone, E. C. Constable and C. E. Housecroft, *Dalton Trans.*, 2017, **46**, 6379–6391.
160 A. M. Bünzli, A. Pertegás, C. Momblona, J. M. Junquera-Hernández, E. C. Constable, H. J. Bolink, E. Ortí and C. E. Housecroft, *Dalton Trans.*, 2016, **45**, 16379–16392.
161 M. Montalti, A. Credi, L. Prodi and M. T. Gandolfi, *Handbook of Photochemistry*, CRC Press, 2006.
162 G. E. Schneider, A. Pertegás, E. C. Constable, C. E. Housecroft, N. Hostettler, C. D. Morris, J. A. Zampese, H. J. Bolink, J. M. Junquera-Hernández, E. Ortí and M. Sessolo, *J. Mater. Chem. C*, 2014, **2**, 7047–7055.
163 J. G. Park and Y. Jahng, *Bull. Korean Chem. Soc.*, 1998, **19**, 436–439.
164 R. D. Costa, D. Tordera, E. Ortí, H. J. Bolink, J. Schönle, S. Graber, C. E. Housecroft, E. C. Constable and J. A. Zampese, *J. Mater. Chem.*, 2011, **21**, 16108–16118.
165 M. Nishio, *CrystEngComm*, 2004, **6**, 130–158.
166 G. Tárkányi, P. Király, G. Pálinkás and A. Deák, *Magn. Reson. Chem.*, 2007, **45**, 917–924.
167 A. Pintado-Alba, H. de la Riva, M. Nieuwhuyzen, D. Bautista, P. R. Raithby, H. a Sparkes, S. J. Teat, J. M. López-de-Luzuriaga and M. C. Lagunas, *Dalton Trans.*, 2004, **2**, 3459–3467.
168 S. Keller, F. Brunner, A. Prescimone, E. C. Constable and C. E. Housecroft, *Inorg. Chem. Commun.*, 2015, **58**, 64–66.
169 I. Andrés-Tomé, J. Fyson, F. Baiao Dias, A. P. Monkman, G. Iacobellis and P. Coppo, *Dalton Trans.*, 2012, **41**, 8669–8674.
170 E. C. Constable, M. Neuburger, P. Rösel, G. E. Schneider, J. A. Zampese, C. E. Housecroft, F. Monti, N. Armaroli, R. D. Costa and E. Ortí, *Inorg. Chem.*, 2013, **52**, 885–897.
171 A. Harriman, M. Hissler and R. Ziessel, *Phys. Chem. Chem. Phys.*, 1999, **1**, 4203–4211.
172 T. Norrby, A. Börje, L. Zhang and B. Akermark, *Acta Chem. Scand.*, 1998, **52**, 77–85.
173 Y.-J. Pu, M. Miyamoto, K. Nakayama, T. Oyama, Y. Masaaki and J. Kido, *Org. Electron.*, 2009, **10**, 228–232.
174 S. Keller, PhD thesis, University of Basel, 2017.
175 F. Brunner, A. Babaei, A. Pertegás, J. M. Junquera-Hernández, A. Prescimone, E. C. Constable, H. J. Bolink, M. Sessolo, E. Ortí and C. E. Housecroft, *Dalton Trans.*, 2019, **48**, 446–460.
176 Y. Zhang, M. Schulz, M. Wächtler, M. Karnahl and B. Dietzek, *Coord. Chem. Rev.*, 2018, **356**, 127–146.
177 E. Fresta, G. Volpi, M. Milanesio, C. Garino, C. Barolo and R. D. Costa, *Inorg. Chem.*, 2018, **57**, 10469–10479.
178 E. Fresta, G. Volpi, C. Garino, C. Barolo and R. D. Costa, *Polyhedron*, 2018, **140**, 129–137.
179 S. Keller, M. Bantle, A. Prescimone, E. C. Constable and C. E. Housecroft, *Molecules*, 2019, **24**, 3934.
180 S. Keller, A. Prescimone, E. C. Constable and C. E. Housecroft, *Photochem. Photobiol. Sci.*, 2018, **17**, 375–385.
181 A. M. Johns, N. Sakai, A. Ridder and J. F. Hartwig, *J. Am. Chem. Soc.*, 2006, **128**, 9306–9307.
182 C. A. Tolman, *Chem. Rev.*, 1977, **77**, 313–348.
183 B. C. Hamann and J. F. Hartwig, *J. Am. Chem. Soc.*, 1998, **120**, 3694–3703.
184 J. Holz, K. Rumpel, A. Spannenberg, R. Paciello, H. Jiao and A. Börner, *ACS Catal.*, 2017, **7**, 6162–6169.
185 Y. Hamada, F. Matsuura, M. Oku, K. Hatano and T. Shioiri, *Tetrahedron Lett.*, 1997,

**38**, 8961–8964.
186 J. I. van der Vlugt, E. A. Pidko, D. Vogt, M. Lutz and A. L. Spek, *Inorg. Chem.*, 2009, **48**, 7513–7515.
187 B. Bozic-Weber, V. Chaurin, E. C. Constable, C. E. Housecroft, M. Meuwly, M. Neuburger, J. A. Rudd, E. Schönhofer and L. Siegfried, *Dalton Trans.*, 2012, **41**, 14157–14169.
188 C. R. Groom, I. J. Bruno, M. P. Lightfoot and S. C. Ward, *Acta Crystallogr., Sect. B Struct. Sci., Cryst. Eng. Mater.*, 2016, **72**, 171–179.
189 H. Yersin, R. Czerwieniec, M. Z. Shafikov and A. F. Suleymanova, *ChemPhysChem*, 2017, **18**, 3508–3535.
190 S.-H. Kim and R. D. Rieke, *Tetrahedron*, 2010, **66**, 3135–3146.
191 R. M. Everly, R. Ziessel, J. Suffert and D. R. McMillin, *Inorg. Chem.*, 1991, **30**, 559–561.
192 M. Holler, B. Delavaux-Nicot and J. Nierengarten, *Chem. – A Eur. J.*, 2019, **25**, 4543–4550.
193 H. Takeda, K. Ohashi, A. Sekine and O. Ishitani, *J. Am. Chem. Soc.*, 2016, **138**, 4354–4357.
194 H. Chen, L.-X. Xu, L.-J. Yan, X.-F. Liu, D.-D. Xu, X.-C. Yu, J.-X. Fan, Q.-A. Wu and S.-P. Luo, *Dyes Pigments*, 2020, **173**, 108000.
195 V. Bevilacqua, M. King, M. Chaumontet, M. Nothisen, S. Gabillet, D. Buisson, C. Puente, A. Wagner and F. Taran, *Angew. Chemie Int. Ed.*, 2014, **53**, 5872–5876.
196 D. Anandkumar, S. Ganesan, P. Rajakumar and P. Maruthamuthu, *New J. Chem.*, 2017, **41**, 11238–11249.
197 C. Kütahya, Y. Yagci and B. Strehmel, *ChemPhotoChem*, 2019, **3**, 1180–1186.
198 C. He, B. Abraham, H. Fan, R. Harmer, Z. Li, E. Galoppini, L. Gundlach and A. V. Teplyakov, *J. Phys. Chem. Lett.*, 2018, **9**, 768–772.
199 R. Ziessel, L. Toupet, S. Chardon-Noblat, A. Deronzier and D. Matt, *J. Chem. Soc. Dalton Trans.*, 1997, 3777–3784.
200 S. Kumar, A. Kumar, B. S. Bhakuni, C. D. Prasad and S. Kumar, *Tetrahedron*, 2013, **69**, 5383–5392.
201 WO2014072017 A1, 2014.
202 Y. Li, L.-Q. Lu, S. Das, S. Pisiewicz, K. Junge and M. Beller, *J. Am. Chem. Soc.*, 2012, **134**, 18325–18329.
203 C. Janiak, *J. Chem. Soc. Dalton Trans.*, 2000, 3885–3896.
204 R. Severin, J. Reimer and S. Doye, *J. Org. Chem.*, 2010, **75**, 3518–3521.
205 G. B. Hammond, T. Calogeropoulou and D. F. Wiemer, *Tetrahedron Lett.*, 1986, **27**, 4265–4268.
206 K. Maeyama, C. Okumura and N. Yonezawa, *Synth. Commun.*, 2002, **32**, 3159–3167.
207 R. P. J. Bronger, S. M. Silva, P. C. J. Kamer and P. W. N. M. van Leeuwen, *Chem. Commun.*, 2002, 3044–3045.
208 R. P. J. Bronger, J. P. Bermon, J. Herwig, P. C. J. Kamer and P. W. N. M. van Leeuwen, *Adv. Synth. Catal.*, 2004, **346**, 789–799.
209 B. Yao Liu, P. Ganzel and T. G. Traylor, *Inorganica Chim. Acta*, 1997, **254**, 407–410.